UNIVERSITY OF CALIFORNIA, SAN DIEGO

SAN DIEGO STATE UNIVERSITY

Guidance and Optimization of Planetary Entry and Powered Descent

A dissertation submitted in partial satisfaction of the
requirements for the degree Doctor of Philosophy

in

Engineering Sciences (Mechanical and Aerospace Engineering)

by

Sergio Alfonso Sandoval

Committee in charge:

University of California, San Diego

Professor John T. Hwang, Co-Chair
Professor Philip Gill
Professor Aaron Rosengren

San Diego State University

Professor Ping Lu, Co-Chair
Professor Ahmad Bani-Younes

2023

The dissertation of Sergio Alfonso Sandoval is approved, and it is acceptable in quality and form for publication on microfilm and electronically.

_____

_____

_____

_____
Co-Chair

_____
Co-Chair

University of California, San Diego
San Diego State University

2023

DEDICATION

To my wife, I cannot imagine a world without you.

EPIGRAPH

If we knew what it was we were doing, it would not be called research, would it?

—*Albert Einstein*

TABLE OF CONTENTS

LIST OF FIGURES

LIST OF TABLES

ACKNOWLEDGEMENTS

I want to start by thanking my wife, Daniela, for all of her support throughout my doctoral program. It is not always easy to balance work and life as a PhD student, and none of this would have been possible without the best partner I could have asked for. Thanks to her I could always find myself in a positive environment of love and understanding. Thanks for always going above and beyond to make my dream a reality. I also want to thank my son Nicolás, who grew up in this academic environment and helped me keep my feet on the ground. His excitement about life taught me more about life than anything else I had done before, and helped me stay motivated in the last years before graduating.

I want to thank Professor Ping Lu, the greatest mentor I have had, for taking me under his wing and sharing all of his knowledge with me. I feel honored to have learned directly from one of the greatest aerospace engineers in the field. Thanks for believing in me and taking the time to teach me about the fascinating topic of guidance and control. You were always available to meet with me to answer any questions and you were involved in every detail of my projects despite having many other things to worry about as the chair of the department. You always led by example, and I take with me many valuable lessons on discipline, professionalism and humility. I hope to take all of these lessons to continue to do great work in the future.

Thanks to Professor John Hwang, for co-chairing my committee and giving me the opportunity to be a member of his laboratory, not just as an observer, but an actual lab member. Your work ethic is something admirable that I hope to be able to replicate in my

own work. Thanks to Professors Ahmad Bani Younes, Philip Gill, and Aaron Rosengren for being part of my committee and helping me improve the way I convey my work.

To the friends that I met through my PhD that offered me their unconditional support: Paulina Diaz-Montiel, Maricruz Carrillo, Ricardo Montes, Ambar Cajigas, Marcela Sotelo, and Isabel White. Graduate school would have been miserable without you in my life. Beyond academics, your friendship offered a space of peace and comfort where I could be myself and share how I felt. Having that safe space was crucial to being able to continue all the way to the end.

I want to take the members of the "Computational Guidance and Control Lab" at San Diego State University for the great memories and the opportunity to serve as a mentor. I enjoyed having a community where we could learn together and it makes me happy to consider you my friends. Similarly, I want to thank all the members of the "Large-Scale Design Optimization Lab" at the University of California San Diego. Your help in understanding several topics in optimization was very necessary and you inspired me to keep learning more about the topic.

Many thanks to my family and extended family for their support. To my dad, Sergio Sandoval, who I admire for all his knowledge, creativity and being the greatest example of a father. To my brother, Alonso Sandoval, who was always by my side growing up and even right now is one of my greatest supporters. To my best friend, Mauricio Marquez, for starting this journey with me back in high school when both of us decided to leave Mexico and come to the United States, and for motivating me to do a PhD when I was too scared of being good enough. To my mother-in-law, Ana Camacho, for always

giving us a hand when we needed it, especially during the pandemic when the uncertain times made us end up in one of her spare rooms.

I want to thank the NASA Pathways Program and the NASA Space Technology Research Fellowship for the opportunity they gave me to go to graduate school and for exposing to this amazing academic environment. I got a lot of inspiration from my time as a Pathways Intern at the Johnson Space Center where I learned a lot from many mentors. Special thanks to Jeremy Rea, for giving me direct mentorship during my entire PhD, many of the ideas in this dissertation emerged from many discussions we had. To Daniel Matz, for helping me become a better engineer by guiding me on several projects throughout my time at NASA. Thanks to Chris D'Souza for guiding me in the right direction, without your help I wouldn't have found the right PhD program for me. Many thanks to Breanna Johnson, Jeff Gutkowski, Frank Monahan, Ron Sostaric, John Goodman, Mark Hammerschmidt, John Gowan, John Carson, Rafael Lugo, Soumyo Dutta, and many other mentors that helped me understand the NASA mission and goals through their mentorship and example.

To my closest friends from Georgia Tech: Camilo Duarte, Giovanny Güecha, Marc-Henri Bleu-Laine, Juan Sebastian Rubio, Sebastian Arroyave, and Samuel Rodríguez. My time at Georgia Tech was a very important part of my life, that is where I really learned what it means to be an engineer and the importance of having a support system to make it through the hard times.

Thanks to those friends that had an important part of my life outside my PhD, but that were significant in helping me become a better person: Atl Arredondo, José Ramírez,

Elizabeth Castrejon, Noel Naranjo, Jesús Arellano, Heli Lucas, Ana Elisa Prado Rocha, Ana Clara Prado Rocha, Carlos and Cristina Llamas, Sarai Welsh, Max Rodríguez, Bardo and Leslie Borja, Andrés Sánchez, Gabriela Vázquez, Jafet and Hercy Nuñez and Hillary Arias.

To the many people that have been part of my life, thank you for your love and friendship. To all my teachers, coaches and friends at Colegio Montessori and Preparatoria Federal Lázaro Cárdenas. To my leaders and friends at Scouts of México, especially Mirtha Santana and Rolando Segura. To Rafael Alvarez, Gerald Vanderpot, and Mariaelena Delgado from San Diego City College, for being the first ones to believe in me when all I had were dreams in my pocket. Special thanks to key people in my academic growth: Jorge Breton, Valentina de la Fe, Eugene Fiorini, and Julian Rimoli. To my professors at Georgia Tech, San Diego State University and the University of California, San Diego. To my friends in San Diego, Tijuana, Atlanta, and Houston that I hold dear to my heart. The list of people can go on and on, and I sincerely apologize if I forget somebody's name. The person I am thanks to you is a better testament to your significance. Thanks for making my life a dream come true, I share this work with all of you in gratitude.

The contents of Chapter 3 describe different supporting algorithms that will be utilized throughout the dissertation. The material provided is not a full reprint, but the author wishes to acknowledge the primary investigators of the sources cited and the contribution of their work on the progress and development of this project. The material on the Fully Numerical Predictor-Corrector Entry Guidance is referenced from Lu, P., "Entry guidance: a unified method," Journal of Guidance, Control, and dynamics, vol. 37,

no. 3, pp. 713–728, 2014. The material on the Fractional-Polynomial Powered Descent Guidance is referenced from Lu, P., "Theory of fractional-polynomial powered descent guidance," Journal of Guidance, Control, and Dynamics, vol. 43, no. 3, pp. 398–409, 2020. The material on the Universal Powered Guidance is Lu, P., "Propellant-optimal powered descent guidance," Journal of Guidance, Control, and Dynamics, vol. 41, no. 4, pp. 813–826, 2018. The material on Guidance for Propellant-Optimal Landing of A Rocket is referenced from Lu, P. and Callan, R., "Propellant-optimal powered descent guidance revisited." Journal of Guidance, Control, and Dynamics, vol. 46, no. 2, pp. 215–230, 2023.

Chapter 4, in full, is a reprint of the material as it appears in Powered Descent Guidance for a Crewed Lunar Landing Mission, 2020. Sandoval, Sergio; Lu, Ping. The dissertation author was the primary investigator and author of this paper.

Chapters 5 and 6, are currently under review for publication as Abort Guidance during Lunar Powered Descent at the Journal of Guidance, Control, and Dynamics. Sandoval, Sergio; Lu, Ping; Hwang, John. The dissertation author was the primary investigator and author of this material.

Chapter 7, in full, is a reprint of the material as it appears in Simulation Comparison of Entry and Powered Descent Guidance Algorithms for a Human-Scale Mars Mission, 2022. Sandoval, Sergio; Lugo, Rafael; Lu, Ping; Cianciolo, Alicia. The dissertation author was the primary investigator and author of this paper.

Chapter 8 is based on the paper coauthored with Lu, Ping and Davami, Christopher and under review for publication as Fast and Robust Optimization of Full Trajectory From

Entry Through Powered Descent at the Journal of Guidance, Control, and Dynamics. The dissertation author was the primary author of this chapter.

VITA

2017 B. S. in Aerospace Engineering *magna cum laude*, Georgia Institute of Technology

2018-2023 Graduate Research Assistant, San Diego State University

2023 Ph. D. in Engineering Sciences (Mechanical and Aerospace Engineering), San Diego State University and University of California San Diego

PUBLICATIONS

Sandoval, S. A. and Lu, P., "Powered Descent Guidance for a Crewed Lunar Landing Mission," AAS Guidance and Control Conference, Breckenridge, CO. AAS Paper 20-044, 2020.

Lu, P. and Sandoval, S. A., "Abort Guidance during Powered Descent for Crewed Lunar Landing Missions," AIAA SciTech Forum, Virtual Event. AIAA Paper 2021-0505, 2021.

Sandoval, S. A., Lugo, R. A., Lu, P., and Cianciolo, A. D., "Simulation Comparison of Entry and Powered Descent Guidance Algorithms for a Human-Scale Mars Mission," AAS Guidance and Control Conference, Breckenridge, CO. AAS Paper 22-106, 2022.

Sandoval, S. A., Lu, P., Hwang, J. T., Rea, J. R., and Sostaric, R. R., "Multiple Optima in Abort Ascent during Lunar Powered Descent," AIAA SciTech Forum, San Diego, CA. AIAA Paper 2022-0949, 2022.

Sandoval, S. A., Hwang, J. T., and Lu, P., "Abort Guidance during Lunar Powered Descent," Submitted to the Journal of Guidance Control and Dynamics.

Lu, P., Sandoval, S. A. and Davami, C., "Fast and Robust Optimization of Full Trajectory from Entry Through Powered Descent," Submitted to the Journal of Guidance Control and Dynamics.

ABSTRACT OF THE DISSERTATION

Guidance and Optimization of Planetary Entry and Powered Descent

by

Sergio Alfonso Sandoval

Doctor of Philosophy in Engineering Sciences (Mechanical and Aerospace Engineering)

University of California San Diego, 2023
San Diego State University, 2023

Professor Ping Lu, Co-Chair
Professor John T. Hwang, Co-Chair

Safety, precision, and efficiency are the key ingredients for successful future human-scale entry, descent, and landing (EDL) missions to the Moon and Mars. In this work, a complete investigation into each component of an EDL mission, including an emergency scenario, revealed some of the necessary techniques that need to be implemented to effectively reach these goals.

An often-ignored aspect of EDL is the requirement to have a safety protocol in

place in case of an emergency. In this work, a newly developed abort guidance technique revealed that an ascent-abort into orbit can be achieved from any point during the lunar powered descent phase. The two-phase abort methodology is inspired in the solution to the optimal ascent guidance problem and can be activated autonomously to guide the vehicle towards a safe orbit with the least amount of propellant possible.

Validation of two state-of-the-art algorithms for entry and optimal powered descent guidance in different mission scenarios and in a high-fidelity simulation environment, demonstrated that a complete non-optimized EDL trajectory can be generated quickly and reliably. With the addition of an adaptive powered descent initiation logic, based on the indirect method of optimal control, the total propellant consumption during powered descent can be greatly reduced even when the powered descent guidance is not optimal. The complexity of the end-to-end EDL problem limits the extent to which the problem can be optimized by the known optimal control techniques. Optimization using the direct method of optimal control can generate a theoretical solution, albeit in an impractical amount of time and operational limitations. Leveraging the robustness of a state-of-the-art entry guidance and an optimal powered descent guidance algorithm, a novel approach to the optimization of the end-to-end EDL problem emerged. The problem is solved with a bi-level optimization approach in which an inner loop optimizes the propellant consumption during powered descent, and an outer loop modifies the entry trajectory to provide the best PDI condition. This innovative approach results in a fast and reliable trajectory with near-optimal propellant consumption in a matter of seconds. All the results from this investigation are tested for robustness in Monte Carlo simulations.

Chapter 1

Introduction

In 1962, president John F. Kennedy dared the United States of America to accomplish the biggest challenge ever imagined. In the midst of the cold war, he believed that whoever won the Space Race would win the war. He set his expectations high and challenged the National Aeronautics and Space Administration (NASA) to land a human on the Moon by the end of the decade [1]. History showed that he was correct, whoever reached the prized Moon landing would set a precedent for the dominion of space. However, nobody ever imagined that what started as an act of war would have such a positive impact in our lives as we have seen for the past 60 years [2]. Ever since we landed the first man on the Moon, the goals have been bigger and greater. Despite not having gone back to the surface of the Moon, many accomplishments in space exploration through NASA and the private sector have been achieved [3, 4, 5].

President Kennedy would hardly have imagined that one day we would build the biggest and most complex machine and send it to space in the form of the International Space Station [6]. That we would eventually get so good at sending humans to space that we would have been living in space for more than 20 continuous years since 2000 [7]. We

have built satellites that have left our solar system and telescopes so clear that have shown us clusters of stars in perfect detail [8, 9, 10].

And all of this for what? Very simple, because as humans we want to explore and we want to understand. When we look at both of these ideas we realize that one can't live without the other. To explore is to understand and to understand you need to explore. Countless missions have shaped our society through discoveries that have changed our perspective of the universe. There is hardly anybody in the world that has not heard of NASA. With so many years of exploration, by now it would be hard to think what else to do. And yet, we have only scratched the surface of what can be achieved as humanity. The reason why space exploration is so important is because it brings hope. Each mission is so significantly challenging and complex that knowing humans can get together to accomplish such an endeavor gives us a chance to solve more dramatically important problems in our planet. Nowadays, NASA and the space community is trying to open new frontiers by planning some of the most challenging missions ever imagined. On one hand, to go back to the Moon and make it habitable to humans. On the other hand, we want to reach where no other human has before, we want to reach Mars [11, 12, 13].

Entry, Descent, and Landing is among the most challenging stages of a planetary landing mission [14]. The ability to steer a hypersonic vehicle through the atmosphere of a planet and safely descend towards a landing target requires effective and precise guidance and control algorithms. Previously, robotic landings on Mars have been accomplished with a combination of entry and powered descent guidance [15, 16, 17, 18]. The biggest spacecraft to perform EDL maneuvers have been the Mars Science Lab in 2012 and the

Mars 2020 Mission [19, 20]. In the entry guidance phase, the vehicle is guided towards the landing site and the velocity is reduced by using parachutes to take advantage of the aerodynamic forces in the atmosphere [21]. Entry uses energy dissipation. The entry phase also serves as an initial alignment phase with the landing site, reducing the crossrange distance between the vehicle and the landing site. The powered descent phase uses supersonic retropropulsion (SRP) to eliminate any remaining velocity from the entry phase before starting a vertical descent with constant velocity that ends in a soft-landing on the surface [22].

It is intended that future Mars landing missions will be performed with a crew onboard the vehicle [23, 24]. The long journey from Earth to Mars will require that the crew stays on the destination for an extended period of time. To accomplish this goal, the spacecraft must be able to carry the life support systems necessary to keep the crew safe for the duration of the mission [25]. The higher level of complexity in a crewed mission will require a larger and heavier spacecraft than previously flown. For comparison, Mars 2020 landed a total weight of 3649 kg, while a human-scale Mars mission would be in the order of 60 metric tons [26]. With a spacecraft of this magnitude, it becomes infeasible to utilize parachutes during entry [27]. Instead, control during entry can be achieved with aerodynamic surfaces on the vehicle. The motion of the aerodynamic surfaces produces three-dimensional motion with the aid of the lift and drag forces developed as the vehicle moves through the atmosphere. A combination of aerodynamic control during entry and SRP during powered descent is required to bring the vehicle safely on the ground. The heavier spacecraft will result in a larger speed at the entry interface, and powered descent

becomes a critical component of EDL in order to control the spacecraft towards the landing site and eliminate any targeting errors before touchdown. The propellant fraction of SRP will be critical for the feasibility of a mission of this kind. It is therefore very important to have entry guidance and powered descent guidance work together to use the least amount of SRP propellant. Landing within 50 meters of the predetermined target location is necessary for a successful crewed mission to Mars [25]. This allows the crew to be away from any danger and in the vicinity of available support systems flown in previous missions. New technology and engineering advances in EDL are required to meet these challenges, especially entry and powered descent guidance algorithms that are fully adaptive and not limited to predefined or stored reference trajectories. Improved propellant performance is important to reduce mission cost and maximize payload capacity.

The aforementioned concepts can be easily applied to a lunar landing mission. With the distinction that the lack of atmosphere in the Moon eliminates the need for an entry phase. The relatively close distance between the Moon and the Earth reduces the level of complexity required to perform a crewed lunar landing mission in comparison to a Mars landing mission. The Apollo program accomplished a total of 6 human landings on the surface of the Moon. Lessons learned from the Apollo missions propelled the development of new technology to land humans on the Moon once again [28]. In this new era of space exploration, going back to the Moon to create a sustainable human presence will give the opportunity to develop technology necessary for future missions to Mars [29]. Therefore, investigating how current technology can be adapted for lunar landing missions is an important component of the development of Mars EDL. In the near future, the inclusion

of a lunar outpost to perform operations in lunar proximity will allow the mission duration to be shorter than previous missions to the Moon, thus giving an advantage to the types of maneuvers that can be perform to bring the spacecraft to safety in case of a contingency.

Over the entire descent trajectory, the vehicle experiences uncertainty in the environment (atmosphere) and system dynamics that are critical to maintain the control of the vehicle. The guidance algorithms must be adaptive and robust with respect to uncertainty. In addition, the guidance solution for powered descent must be calculated onboard and within the capabilities of the spacecraft computer. The spacecraft in future missions will have the advantage of better onboard capability, allowing it to use more sophisticated numerical optimization algorithms and complex computations than the ones available in previous human landing missions; but the capability is still limited. In recent years, advances in optimal control and numerical optimization have led to the development of guidance techniques that permit a more robust solution within the limits of onboard computation [30, 22].

Over the years, different entry and powered descent guidance algorithms have been developed to improve individual aspects of EDL. These algorithms evolved to fulfill the needs of different types of spacecraft, missions, and the increase in onboard computational capability. The increase in oboard computation opens new possibilities where technologies previously considered unrealistic are now viable. In aerospace engineering, Computational Guidance and Control (CG&C) is a trend that needs to be explored further [31]. The approaches to guidance and control problems resulted from CG&C are no longer bounded by the traditional closed-form solution. Rather, the problem is solved by a numerical

algorithm onboard. CG&C has the potential to greatly increase the capability with better performance for the existing systems.

Currently, the evolution of entry guidance methods has led to methods that effectively overcome problems during entry guidance and powered descent. However, the solutions to these problems are approached separately and no current method considers both entry guidance optimization and fuel efficiency at the same time. The need for both computationally advantageous algorithms and propellant efficiency during missions to other planets are the main drivers for this investigation. In a time like this, it is desired to explore the solar system by maximizing our resources. Learning from current technology to create a new generation of optimization algorithms for guidance and control will help the development of spacecraft control in future missions.

1.1 Motivation

During the course of any interplanetary landing mission, multiple phases need to be integrated smoothly to produce a complete mission profile that would transport a payload from launch on Earth to the landing location on the target planet. The cost of the mission is one of the most important considerations for planning. An increase in weight can cost the mission hundreds of thousands of dollars. Keeping the weight as low as possible is an important, yet, difficult task to accomplish given the complexity of multiple spacecraft systems. One of the areas where most of the weight resides is in the tanks that carry the propellant for landing operations. Minimizing the propellant consumption during EDL operations is important, especially for missions to Mars where the propellant-mass

fraction of the vehicle is very high. The EDL phase is one of the most difficult segments of a mission and can be the difference between success and failure. Solving this problem optimally with respect to propellant consumption is challenging on two fronts: on one side it is required to land a vehicle safely on the ground while on the other it needs to be done as propellant-efficiently as possible. Either one of these problems is hard by itself.

Another important consideration is that guidance algorithms for the Moon and Mars need to be able to safely and precisely transport astronauts from an orbit to the landing location. In the past, successful EDL human and robotic missions have been achieved on the surface of the Moon and Mars [28, 19]. Most of them without any sort of optimization and with fragile algorithms that relied heavily on the astronauts to operate properly. Advances in numerical optimization techniques and optimal control theory have opened the doors to solve problems in an optimal sense, changing completely the paradigm of what can be achieved. In an era where computational capability is much greater, taking advantage of these techniques is imperative to develop the tools of the future.

Development of optimal or near-optimal solutions to the problem of landing a spacecraft on the surface of the Moon or Mars is necessary to achieve the desired landing site with the least amount of propellant possible while staying within the limits of on-board computer capability. In this proposal three different topics will be addressed: the problem of optimizing entry guidance to provide a fast and reliable solution on-board the vehicle, coordinating entry and powered descent to obtain the best powered descent initiation (PDI) condition available, and aborting to a safe orbit in case of an emergency that makes the landing unfeasible. Using optimal control and state-of-the-art EDL techniques, a suite

of EDL guidance algorithms will be developed for human and robotic landing missions to the Moon and Mars. The integration of these algorithms in end-to-end simulations will demonstrate the effectiveness of the algorithms in taking advantage of aerodynamic control, develop a fast fuel-optimal powered descent guidance algorithm applicable to three-dimensional powered descent, and achieve the landing accuracy required to land a human-scale vehicle to the surface of Mars. Furthermore, onboard optimization is a challenging task that has not been accomplished in real-time.

Through this work, a solution to the propellant optimization problem wants to be found while keeping the rigorous safety and accuracy standards. Robust state-of-the-art entry and powered descent guidance algorithms are utilized as the baseline of this work. The advantages in propellant efficiency and accuracy are exploited in a novel bi-level optimization approach to gain a near-optimal performance.

1.2 Previous Work

Previous Work in Entry Guidance

Entry guidance has evolved over the years to satisfy the requirements of different missions and vehicles. The first generation of entry guidance emerged of the need to control the Apollo capsule during re-entry through Earth's atmosphere [32, 33]. Capsule vehicles produce a low-lift to drag ratio vehicle and generate lift through a center of mass offset to produce a non-zero trim angle of attack [34]. A closed-form analytical solution is generated through approximations to coefficients based on a reference trajectory stored as a table. Despite having a reference trajectory, the guidance is not a tracking law, but it depends

on the reference trajectory to generate adjoint variables around the linearized dynamics of the reference trajectory. The adjoint variables serve as the sensitivity coefficients for the predicted downrange error with respect to trajectory dispersions. To generate the trajectory, a bank angle command was produced to eliminate the predicted downrange error. Bank reversals are enforced to achieve a crossrange requirement and the sign is changed whenever a velocity-dependent deadband is reached. Originally, the Apollo entry guidance was planned as a skip entry guidance, with an initial entry and a subsequent re-entry. The purpose of the skip entry was to extend the period of time that the vehicle spent on the atmosphere to mitigate more velocity. However, the low computational capacity of the time required the use of an analytical solution and approximations that made the skip entry too risky and only a direct entry was flown. The Apollo entry guidance has been a rather successful algorithm that has been implemented in contemporary missions as a modified and more advanced version of the original algorithm. Two relevant examples are the Mars Science Lab [34] and the Orion capsule of the Artemis Program [35].

Another generation of entry guidance algorithms unfolded with the introduction of the space shuttle vehicle. A shuttle-like spacecraft has a high-lift-to-drag ratio and departed from the short range achieved by a capsule vehicle [36]. In the space-shuttle guidance, the plan was to fly a long range trajectory and land the vehicle horizontally and at a supersonic speed of Mach 2.5. To this end, a small flight-path-angle was flown for most of the entry trajectory and a quasi-equilibrium glide condition assumption is utilized to simplify the entry dynamics. A tracking law followed a drag acceleration versus Earth-relative velocity profile for speeds above Mach 10.5, and a drag acceleration versus

energy profile for speeds below Mach 10.5. These profiles were linked together as drag deceleration functions to create a drag deceleration reference profile [37] that defines a longitudinal reference trajectory. The reference drag profile is followed by a linearized gain-scheduled tracking law that generates the control command. The control of the vehicle was achieved through bank angle control with a bank reversal logic similar to the Apollo entry guidance. Other vehicles that also used some version of the space shuttle entry guidance are the X-33 and X-37B hypersonic vehicles [38, 39].

In recent years, advances in computational capability allowed the use of more sophisticated techniques to calculate entry trajectories onboard a vehicle. One of the outstanding advances of entry guidance is the emergence of numerical predictor-corrector algorithms that take advantage of computational improvements to quickly calculate a solution in real-time. The advantage of these methods is that they can adapt to large trajectory dispersions without relying on a reference trajectory or a tracking law. The working principle of predictor-corrector algorithms is that based on an initial control profile, a predicted trajectory is generated from entry interface to the final condition, where a target error is calculated. The algorithm updates a parameter to modify the control profile and correct the targeting error. The iterative process continues until a threshold is met. Two state-of-the-art entry guidance algorithms are the numerical predictor-corrector entry guidance (NPCG) [40] and the Fully Numerical Predictor-Corrector Entry Guidance (FNPEG) [21]. In both cases, the algorithms achieve convergence in less than 1 second on a conventional computer. Of particular interest is FNPEG, that has unified the three previously fragmented areas of low-, mid-, and high-lift-to-drag ratio vehicles with a single

algorithm that can generate a trajectory for each case with only minor modifications on the mission and vehicle parameters [21]. Furthermore, it can easily enforce inequality constraints, a former weakness of predictor-corrector algorithms.

Previous Work in Powered Descent Guidance

A total of 21 successful landing missions on the surface of the Moon have been completed. The United States has attained 11 successful landings (6 missions were accomplished with a crew on-board), Russia has done 7, while China recently landed 3 operational missions. The more challenging goal of landing a vehicle on Mars has only been accomplished a total of 10 times. The United States has landed a combination of landers, rovers, and even a helicopter on 9 occasions, while China accomplished the task for the first time in 2020.

The first account of a landing on a different planet was accomplished by Russia with their Luna 9 lander on the Moon in 1966. On the American side, the Surveyor Program achieved the first lunar landing during the same year [41]. These efforts were propelled by the space race between the space dominant nations: the United States and Russia. The ultimate goal was to create the technology necessary to land a manned vehicle on the surface of the Moon. The lack of atmosphere on the Moon required the use of retro-rockets in all landings. Gravity on the surface of the Moon accounts for only one-sixth to that of Earth, demanding less engine power for a soft-landing. In the first landing attempts of the Surveyor Program, a solid-propellant retro-engine was ignited to decelerate the vehicle from a pre-calculated time delay using an altimeter to generate a marking signal [42]. During the burn, attitude was maintained constant with three

liquid-propellant engines. The solid motor burns for 40 seconds and is jettisoned when empty. Vernier engines were used to control the spacecraft at 0.9 lunar g's for the remainder of the descent. The attitude and thrust during the Vernier engine phase was controlled with velocity and range measurements to the lunar surface [42]. Attitude was held at the original position until the velocity radar locked on the lunar surface, then the thrust vector was aligned with the velocity vector until touchdown at 10 mph [43]. The soft-landing method employed was not very accurate, landing 18.96 km away from the target with Surveyor 1; but it was effective at landing the spacecraft on the ground [44]. The goal of the Surveyor program was to develop the technology to land humans on the Moon with Apollo. At the same time, attempts to land a vehicle on the surface of Mars were taking place. The addition of the Mars atmosphere made available the use of entry guidance. In this case, a lift control phase was used to maneuver the vehicle through the atmosphere at hypersonic speeds. To help reduce the velocity during entry even further, almost all robotic landing missions on Mars made use of supersonic parachutes. During the Viking Program, the first successful landing on Mars, retro-rockets were used to land the vehicle after parachute separation [45, 46]. Later, the Mars Pathfinder and Mars Exploration Rovers (MER) made use of retro-rockets and large airbags to cushion the impact during landing [47, 48]. Phoenix, Insight, and Tianwen-1 achieved landing using parachutes and powered deceleration with retro-rockets [49, 50]. Although some missions like the Phoenix lander had sensors for hazard detection and avoidance, these methods were not very accurate as the use of parachute caused large dispersions in the landing range and crossrange and the simple gravity turn applied failed at recovering from the error [51, 52].

The landings of the Mars Science Laboratory and Mars 2020 utilized a slightly different method for the terminal phase. AS the heaviest spacecraft flown to Mars, these vehicles required the use of retro-rockets mounted on a skycrane to lower the rovers safely on the ground [19].

The culmination of powered descent guidance development resides in two powered descent guidance algorithms that have successfully landed a crewed vehicle: E-guidance and Apollo Powered Descent Guidance (APDG) [53, 54]. These approaches were developed at the same as the two alternatives for the first human landing on the Moon. In the end, APDG was the algorithm selected for the Moon landings. Both methods solve the landing problem in closed-form solution with a thrust acceleration vector profile that is linear for E-guidance and quadratic for APDG. Although neither one of the algorithms is fuel-optimal, E-guidance generally results in lower propellant consumption. Studies showed that E-guidance is close to the fuel-optimal solution in a constant gravity field [55]. Through the years, APDG has influenced many guidance developments for landing [56, 57, 58, 59, 60]. An apparent problem with E-Guidance and APDG is their need for a PDI trigger to start the engines. This goes in hand with a proper selection of the time-to-go or total burn time from PDI to touchdown. The original algorithm developed required these values as inputs, but did not provide an easy way to calculate them. During the Apollo program, trial and error in simulations was the method that provided an acceptable solution. The importance of PDI selection has been studied with results that show the great impact it has on propellant consumption, accuracy and robustness [61, 62]. In Lu [61], a new approach at calculating a near-optimal PDI condition has been proposed with the aid

of an optimal powered descent guidance solution called the Universal Powered Guidance (UPG) [22]. The optimal solution to the soft-landing problem can be solved with UPG to obtain the optimal time-to-go. During powered descent, UPG can be activated at a predefined altitude to start testing the soft-landing solution and comparing the final range to the landing site. Once the landing site has been reached, a command is sent to start powered descent immediately with the calculated flight time. This approach solves two problems: finding a suitable time-to-go to be used as an input to APDG, and starting powered descent at a near-optimal PDI condition. A unifying approach combined both E-guidance and APDG into a single guidance equation with a tuning parameter the Tunable Apollo Powered Descent Guidance (TAPDG) [63]. TAPDG has the advantage that it provides a set of solutions that can vary the shape of the trajectory and thrust profile to provide flexibility when used with different vehicles or missions. When the adaptive PDI condition is applied with TAPDG, the guidance becomes the Augmented Apollo Powered Descent Guidance (A^2PDG), a guidance approach with improved fuel consumption [63]. Furthermore, the application of the fractional polynomial theory to powered guidance uncovered a family of guidance laws that included the Augmented Apollo Powered Descent Guidance as one of its variations when properly tuned, demonstrating increased control of fuel consumption and trajectory design in a new formulation known as the Fractional Polynomial Powered Descent Guidance (FP^2DG) [64, 65].

Recently, multiple approaches have been proposed to address the problem of landing a crewed vehicle to the surface of Mars [58]. The main focus has been on landing a vehicle as close as possible from the landing site [24]. Pinpoint landing algorithms have been at the

forefront of these efforts [30, 66, 67, 68, 59, 69]. In powered descent, aerodynamic forces are usually ignored making the optimal control problem easier to solve than the optimal entry guidance problem. Optimal solutions to the powered descent guidance problem have been developed yielding results that have the potential to be applied on-board a spacecraft [70, 71, 22, 72]. Despite being easier to solve, the number of constraints on an optimal pinpoint landing problem often results in convergence issues. Alternative methods that approximate the optimal control problem [73], or use an optimization such as successive convexification [74, 75, 76, 77] have addressed these concerns.

Previous Work in Abort Guidance

The first instance of an abort guidance implementation was during the Apollo program. The Apollo Primary Guidance Navigation and Control System (PGNCS) was used to fly the Lunar Module (LM) during descent, ascent, aborts, and rendezvous. There were two descent abort guidance programs, P70 for abort using the descent stage engine, and P71 if the ascent stage propulsion system is required to achieve orbit insertion. The targeted orbital insertion conditions were different depending on where the abort would take place during descent, because of the varying relative position between the LM and Command and Service Module (CSM) and the rendezvous requirement with CSM after abort [78]. For aborts during descent, the PGNCS would fly the vehicle using the same guidance law and logic for lunar ascent. The guidance commands only attitude, and no engine throttling is used. The abort guidance begins with the attitude pitched to the vertical (similar to the vertical rise phase in ascent from the lunar surface) until the altitude is greater than 25,000 ft (for lunar ascent the vertical rise terminates when the

altitude rate reaches +40 ft/s). During the vertical rise the LM is rotated to the desired azimuth (normally in the CSM orbital plane). The next phase, orbit insertion phase, is designed for efficient propellant usage to achieve the targeting condition [78]. The guidance command is defined by an acceleration profile which is a linear function of time. The time-to-go is determined by the velocity to be gained. Based on the current state and the targeting condition, the guidance law determines the accelerations in the radial and crossrange directions [78].

In the event of a PGNCS failure during descent, the landing would not be attempted. The backup system, the Abort Guidance System (AGS), would be used to insert the LM into a safe orbit and accomplish the rendezvous with the CSM. The AGS was not designed to support lunar landing. The early back-up powered-descent abort plans were complex because of the limited onboard capabilities in navigation, computation, guidance, and communication [79]. An early version of the AGS was to provide a pitch sequence based on the time of abort and stored constants and produces a thrust cut-off signal based on the velocity [80]. A compensation scheme compared velocity readings from an accelerometer on the thrust axis with nominal velocity values at specified time intervals, and adjusted pitch attitude and velocity at engine cut-off [80]. Later as a general-purpose computer TRW MARCO 4418 became available onboard, this open-loop guidance plus closed-loop compensation design of AGS was abandoned in favor of a simplified explicit ascent guidance algorithm [81]. According to Goodman [81], the AGS guidance algorithm is similar to that reported in Scofield [82]. The guidance method in Scofield [82] targets a particular set of final conditions specified by the final radius and radial velocity as well as

crossrange. The engine cut-off time is chosen to meet the targeting value of the total final velocity.

Ever since the Apollo Program, little effort has been done to update the abort guidance sequence for onboard operations during powered descent. The only other attempt at solving the abort guidance problem has been found in Kenny [83], and that it is likely to have been inspired by some of the work presented in this dissertation. In Kenny [83], the time-optimal abort guidance problem is solved in real-time using a feature-based learning method. A large data-set of optimal trajectories is run offline with different initial conditions. Then, the information obtained is processed with a neural network to map the relationships based on the generated data-set. The problem is solved in real-time, a requisite for future onboard operations on the Moon.

Previous Work in Optimized End-to-End Entry, Descent, and Landing

Lately, many new algorithms expand on the computational capability to solve the optimal or optimized entry guidance problem using convex optimization for trajectory tracking [84, 85], using parameter optimization [86], or even learning-based optimal control [87]. It is evident that the solutions to these problems generate solutions that are considerably close to an optimal solution at a significantly faster time than previous generations. However, some of the solutions that can be obtained with these methods require some additional modifications to be operational. For instance, the optimal solution in Wang [84] exhibits some undesirable characteristics of entry flight. Namely, the optimal bang-bang solution solves the problem in only two bank reversals, which can result in

exceeding the crossrange requirement. This is especially true when there is no control margin left towards the end, as is the case in Wang [84]. New approaches such as using learning-based methods to find the optimal solution in You [87], open a door into new possibilities that can be achieved by higher computational power. The only downside is that many times, it is still necessary to use simplified models to be able to solve the problems, thus, affecting the accuracy of the solution.

Solving the optimal entry or powered descent problem on its own is already a challenging undertaking. An end-to-end EDL optimized trajectory is an even more challenging effort. The dynamics of the problem are different and trying to add two separate optimization problems proves so difficult that it is theoretically difficult to solve with some assumptions or simplifications. The only instance known to the author of an attempt to solve a complete EDL optimization problem is in Wan [88], where the complete EDL trajectory is solved as a 2D problem with multiple assumptions. The problem is formulated as a polynomial programming problem using polynomial approximations and discretization techniques. The problem is then converted into a nonconvex quadratically constrained quadratic program (QCQP). The optimum is found using a customized alternating direction method of multipliers (ADMM). Despite being a trailblazer in this area, the solution to a 2D problem with multiple assumptions and approximations is not yet at a point to be functional for trajectories than can be flown by a vehicle. On the other hand, complete EDL optimization has been achieved by using a simulation environment on a specific guidance algorithm to produce an optimal nominal trajectory [40]. In Lugo [40], the NPCG algorithm is used to produce a complete EDL trajectory in a high-fidelity simulation

environment. The complete EDL trajectory is flown in the simulation environment multiple times with different parameters to find the optimal reference trajectory. However, in this case the optimal solution is pre-calculated and the complete simulation environment to calculate the solution cannot be implemented on-board. Clearly, technology is starting to grasp the power of optimization for end-to-end EDL trajectory generation, but new methods that maintain high-accuracy and that can produce a trajectory rapidly are still needed.

1.3 Objective and Approach

The main goal of my research is to develop a method to optimize the integrated set of guidance tools to solve the problem of entry, descent and landing. The main components required to accomplish this are the development of a fast fuel-optimal powered descent guidance algorithm applicable to three-dimensional motion and the integration with a fast and robust entry guidance algorithm for effective control during atmospheric flight. A central piece to this research will be the methodology and algorithm to integrate the entry and powered descent guidance algorithms during EDL operations. Furthermore, expanding on this integration, creating a scheme to optimize both entry and powered descent simultaneously during the generation of the EDL trajectory. There is strong evidence in current EDL research that points to significant propellant saving for a human Mars mission if the entry trajectory can be shaped for the powered descent guidance to take advantage. One of the challenges is how to best accomplish this collaboration between entry and powered descent guidance in an onboard environment based on the actual

condition. This research will implement an algorithm capable of onboard determination of the trajectory and guidance commands necessary for entry, based on the actual state and selecting an appropriate condition for PDI. It is intended to deliver an algorithm with onboard capability based on the actual condition and not requiring complex algorithms or functions other than the ones already available for entry and powered descent guidance. The development of this integrated algorithms will allow further investigation and comparison with current algorithms. The following objectives were selected in order to achieve the mentioned goals:

Objective 1. Integration of adaptive PDI prediction in powered descent of a human-scale lunar landing mission.

The starting point of this research was to use a PDI prediction logic to select the appropriate time to start powered descent on a lunar landing mission. In this objective, it desired to demonstrate that using a non-optimized powered descent guidance algorithm with the adaptive PDI logic can reduce the propellant consumption and the risk of mission failure. The FP^{2}DG was selected to demonstrate this capability as it provides a fast and reliable analytical solution and it is not optimized. Furthermore, since FP^{2}DG is closely related to the APDG used to land the first humans on the Moon, a comparison on the performance is readily available. On the Moon, powered descent starts without an entry phase at nearly orbital speed, but it was shown that the PDI logic also offers propellant reduction and safety advantages.The integration of the adaptive PDI logic is a critical step in the development of this research, as it is the transition between powered descent and the previous phase.

For Mars landing missions, both entry and powered descent phases are required. The baseline entry guidance algorithm to be used is the FNPEG algorithm [21, 31, 89]. A big advantage of this algorithm is that it provides real-time onboard computation to create the trajectory design and obtain the guidance solution. This algorithm is designed for entry flight with active modulation of bank angle. Finding a way to integrate both entry and powered descent guidance is crucial to this research since it will provide the link between both phases to improve the overall performance of the EDL mission. A methodology and algorithm to integrate the entry and powered descent guidance algorithms during the entry flight will be applied. Similar to the lunar landing mission, the goal of the PDI logic is to predict a suitable PDI condition in real-time based on the actual condition. This adaptive determination will improve reliability, precision, and propellant efficiency greatly. The condition at the PDI is critical to the powered descent phase, it determines the divert requirement, the best propellant usage possible, and the trajetory margin to accommodate dispersions. Usually, the PDI condition is chosen based on specific criteria such as time at entry interface, altitude, or velocity. Such criteria are not alwasy accurate, especially in the presence of large dispersions. It is very important that entry and powered descent algorithms work seamlessly during entry phase to predict and identify the best PDI condition, and how to determine it onboard without additional complex algorithms besides the entry and powered descent guidance algorithms already available. The development of this integrated algorithm will enable to conceive a simple but sensible logic to identify and trigger a good PDI condition, onboard and based on the actual conditions, that leads to pinpoint landing with least amount of propellant consumed. The selection of

an appropriate PDI condition can improve performance in powered descent algorithms that are not optimal. Using non-optimal algorithms with better performance gives an advantage in convergence of the solution due to their closed-form solution. For instance, the FP^{2}DG is an algorithm that is not optimal but that has shown potential when the best PDI condition is chosen. Using the adaptive PDI logic derived in Lu [61], the optimal soft-landing solution can be used to predict the best starting point for powered descent. Additionally, the initial time-to-go can be obtained from the total flight time of the optimal solution. Using this method for PDI prediction, both entry and powered descent guidance algorithms can be incorporated to achieve better propellant performance and landing accuracy.

The purpose of this objective is to demonstrate that the PDI logic offers a near-optimal transition point between entry and powered descent that will be required for a Mars mission. Testing and development of this guidance algorithm in Lunar and Martian landing missions will determine the flexibility and propellant improvement in different scenarios. Monte Carlo testing will help assess the robustness of the algorithm by using dispersions.

Objective 2. Development of abort guidance strategy and algorithm for crewed lunar landing missions

The need for abort guidance emerged as a need to ascend into a safe orbit in case landing is no longer an option for the mission. A novel abort technique demonstrated in Lu [90] has been shown to solve the optimal ascent guidance problem simply and efficiently. The same baseline algorithm used for the optimal soft-landing can be used to obtain the

solution to a fuel-optimal ascent guidance in a configuration named UPG+A [22]. However, the problem of aborting during a lunar powered descent is more challenging as it requires changing the trajectory as the vehicle is moving fast in the opposite direction. The difficult task of arresting the descent velocity during powered descent is exchanged for a method that takes advantage of the momentum available to propel the vehicle towards the final orbit. A pull-up maneuver accomplishes the difficult task of turning the velocity vector before starting ascent into a safe orbit. Incorporating UPG+A in the guidance algorithm will provide an additional safety measurement with minimum effort. The inclusion of an abort guidance method to the EDL mission will define a new category of EDL problems that take into account accuracy, robustness, and risk mitigation. The goal is to provide an algorithm with the capability of providing a solution that will always bring the crew to safety at any point during the lunar landing mission.

Objective 3. Development of a method for rapid generation of near-optimal EDL trajectories in real-time

The complete optimization of an EDL trajectory in real-time is a challenging endeavor that has not been accomplished in the past. Lunar or martian landing missions rely heavily on predefined mission profiles, assumptions, or sub-optimal solutions. To create the first real-time EDL optimization method, two fast and robust entry and powered descent guidance algorithms will be utilized to solve the complete EDL optimization problem. The problem will be formulated as a hybrid optimal control problem, where the entry, powered descent, and PDI point will be optimized simultaneously. Since solving the entry guidance problem optimally is a difficult task given the highly non-linear terms in the

entry dynamics, a non-optimized entry guidance algorithm will be used and optimized via a uni-variate optimization approach. An optimal powered descent guidance algorithms will be used to find the optimal solution to the last portion of the EDL trajectory. The robustness of the entry and powered descent guidance algorithms guarantee that a complete EDL trajectory can be found for appropriate initial conditions. Similarly, the fast convergence of algorithms will provide a complete optimization of the EDL problem in a matter of seconds. The goal of this objective is to obtain an optimized end-to-end EDL trajectory in a matter of seconds, an unprecedented achievement.

Methodology

The goal of this research is to produce a suite of guidance algorithms that can be integrated and optimized for use in planetary landing missions. The idea is to provide a set of solutions to the EDL problem in an integrated fashion. Each one of the objectives will be accomplished by a series of steps: development, simulation and testing. Development of the optimized guidance algorithms is required to solve the EDL problem. Each algorithm will be developed separately and integrated to provide a near-optimal solution. End-to-end simulations will determine the reliability of the algorithm in obtaining a solution that accurately lands a vehicle on the designating landing location. Comprehensive testing in nominal and Monte Carlo simulations will be performed to evaluate the performance and robustness of the entry and powered descent guidance algorithms.

1.4 Research Contributions

In this investigation, three critical elements that are necessary for future Moon or Mars EDL operations were uncovered. First, the use of an adaptive PDI logic to predict the optimal or near-optimal PDI condition is necessary for successful EDL missions. The results from this dissertation demonstrated that an inadequate selection of PDI can result in mission failure caused by insufficient propellant when downrange is too large or diminished thrust control when the landing site is too close. In addition, it was shown that a proper PDI condition has a large impact on the overall propellant consumption during EDL. Furthermore, it was shown in Monte Carlo simulations, that in order to account for all possible changes to the initial conditions and atmospheric uncertainty, the selection of the PDI condition needs to be adaptive to the current state of the vehicle. Extensive testing on multiple missions and vehicles on the Moon and Mars demonstrated that the use of this technology is essential to minimize propellant consumption and reduce the risk of failure during landing.

The second critical element was the creation of an abort guidance sequence during lunar powered descent. To maintain the safety of the crew in all possible scenarios, it is imperative that an abort-ascent solution be available in case the landing on the surface becomes too risky or infeasible. Since the Apollo program, the problem of aborting from powered descent towards an orbit around the Moon had not been addressed. Let alone solving the problem optimally. In this investigation, the first abort guidance approach since the Apollo program was developed using an optimal control ascent guidance approach.

Therefore, the resulting approach is the first abort guidance approach that is completely fuel-optimal in ascent. Moreover, unlike the Apollo days, this novel technique is completely autonomous and does not require any input by the astronauts, thus, guaranteeing that the guidance will always take the astronauts to a safe orbit in case of an emergency at any point during powered descent.

The third contribution in this dissertation is the development of a novel end-to-end EDL trajectory optimization formulation that generates a complete trajectory in real-time. Currently, end-to-end trajectory optimization can only be accomplished offline using optimization software that usually comes at a high computational cost or take extensive processing time, a great limitation for onboard implementation. Few attempts at finding a solution to the complete EDL optimization problem in real-time have been tried, however, many assumptions and simplification are necessary to make it work. In this investigation, a real-time end-to-end EDL optimization is achieved for the first time. This significant result is achieved through the integration of a robust entry guidance algorithm and an optimal powered descent guidance algorithm. The algorithm is formulated as a hybrid optimal control problem and solved with a bi-level optimization technique, where an inner loop optimizes the powered descent phase and an outer loop optimizes the entry trajectory. The robustness of both entry and powered descent guidance algorithms guarantees the convergence of the algorithm if a solution exists. Extensive simulations in Monte Carlo testing showed that this algorithm can reliabley solve the Mars EDL optimization problem fast and without convergence issues. Solving the optimization problem in real-time significantly reduces the amount of time spent generating optimal trajectories that many

times do not consider operational constraints. In this work, the solutions adhere to all the dynamics of a three-degree-of-freedom (3DOF) problem to produce trajectories that are operational. Furthermore, high-fidelity models can be introduced in closed-loop simulation to produce a more accurate prediction without adding a large computational cost. Using this novel technology to generate fast and efficient EDL trajectories in real-time is essential to better predict the best path to land a vehicle on the surface of Mars with the least amount of propellant consumption.

1.5 Dissertation Outline

Since multiple topics in EDL are covered throughout the extent of this investigation, this section describes how the rest of the dissertation will be organized. This way the reader has a clear picture of what will be found in the upcoming pages. The first important observation is that in order to develop an optimized end-to-end guidance solution, each one of the components needed to be investigated separately, sometimes even in different planetary bodies. Chapter 2 gives context and introduces important concepts that will be important to understand before reading through the upcoming chapters. Then, a list of the supporting entry and powered descent guidance algorithms that were used in the development of new technology are described in Chapter 3. The results from this investigation start with a lunar landing demonstration in Chapter 4, where using the recently developed powered descent guidance FP^{2}DG, the technology is demonstrated for the first time in a lunar landing scenario. The importance of the PDI condition selection will play a key role in the rest of this investigation. During the analysis of the lunar landing

problem, the need for an abort guidance strategy in case of an emergency was exposed. In Chapter 5, an abort guidance strategy for lunar landing missions during powered descent is presented. The abort guidance solution resulted in a fascinating discovery on the behavior of the ascent trajectory from a point on the powered descent trajectory. The discovery of multiple optimal solutions with the abort strategy is well documented in Chapter 6. Advancing towards complete EDL trajectory generation, the following Chapters will focus on human-scale landing missions on the surface of Mars. The reason for this change is that, in order to investigate entry guidance, it is necessary to perform the studies in a planet with an atmosphere to obtain the aerodynamic lift and drag necessary to slow down and control the vehicle during entry guidance. Studies on fully integrated entry and powered descent guidance algorithms with performance testing and validation in a high-fidelity simulation environment are the focus of Chapter 7. Finally, Chapter 8 demonstrates that an optimized end-to-end EDL trajectory can be obtained using a bi-level optimization approach in which both entry and powered descent are optimized to obtain a near-optimal propellant consumption solution. A summary of the work accomplished, concluding remarks and recommendations for future work are added in Chapter 9.

Chapter 2

Background

2.1 Introduction

The subject of entry, descent, and landing (EDL) is broad and incorporates multiple research areas. To give a complete background, every component will be addressed separately. Attention will be given to entry guidance, powered descent guidance, and abort guidance; the most significant areas of development in this investigation. Generally, in an EDL mission, only the components of entry and powered descent are considered. To visualize every component of EDL, an overview of a simple mission scenario is shown in Figure 2.1. Entry guidance is shown in green, powered descent is colored yellow, and an optional abort guidance is painted in red. In this chapter, the entry and powered descent will be described in detail. The description of the abort guidance problem and the ascent equations of motion will be presented in Section 5. Furthermore, a brief overview is presented on the direct and indirect methods of optimal control.

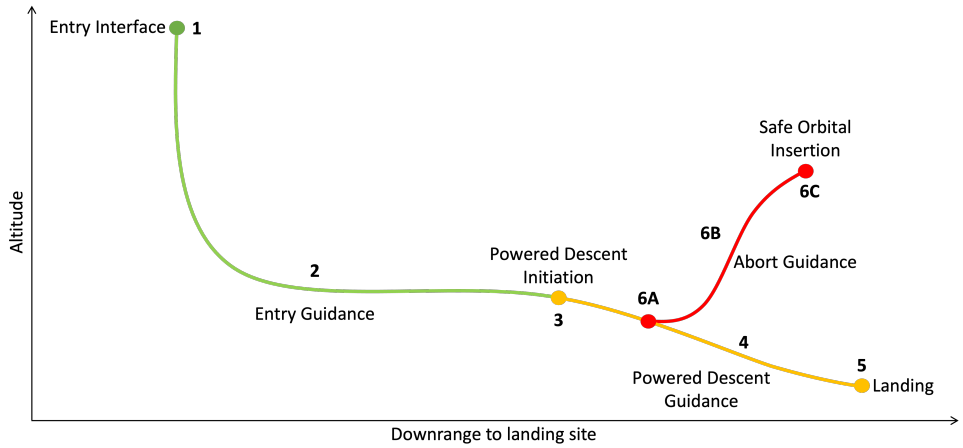

Figure 2.1. Overview of entry, descent, landing and abort mission.

2.2 Overview of Entry, Descent, and Landing

2.2.1 The Entry Guidance Problem

The entry phase of an EDL mission refers to the segment where an hypersonic entry vehicle glides through the atmosphere of a planet using aerodynamic lift as directional control. This phase is only present in a planet with an atmosphere that has sufficient aerodynamic forces to allow guided control. Depending on the mission, the vehicle, and the target planet requirements; an entry phase may or may not be needed. When there is no atmosphere present, the entry phase is non-existent or termed a de-orbit phase. The main goal of the entry phase is to slow down the vehicle as much as possible while keeping it aligned with the landing location. During this phase, a guidance command is produced to control the vehicle through the atmosphere as it achieves a specified final condition. The final condition can consist of a predefined final altitude, velocity, and range-to-go to the landing site. As the spacecraft dives through the atmosphere, aerodynamic forces produce lift and drag that can be utilized to steer the vehicle. Aerodynamic control

surfaces are used to guide the vehicle by directing the lift and drag forces to provide the required control solution. Achieving the final condition at the end of the entry phase is fundamental for the success of the mission as it provides the starting condition for the powered descent guidance. Powered Descent Initiation (PDI) occurs when the control of the vehicle is transferred from the entry guidance algorithm to the powered descent guidance algorithm. Selecting the ideal PDI condition can make an impact on the overall propellant consumed, but more importantly, it can be the difference between the success or failure of the mission.

The highly nonlinear 3-dimensional equations of motion for a gliding vehicle over a spherical rotating planet in non-dimensional form are defined as:

$$\dot{r} = V \sin\gamma \tag{2.1}$$

$$\dot{\theta} = \frac{V \cos\gamma \sin\psi}{r \cos\phi} \tag{2.2}$$

$$\dot{\phi} = \frac{V \cos\gamma \cos\psi}{r} \tag{2.3}$$

$$\dot{V} = -D - \left(\frac{\sin\gamma}{r^2}\right) + \Omega^2 r \cos\phi \left(\sin\gamma \cos\phi - \cos\gamma \sin\phi \cos\psi\right) \tag{2.4}$$

$$\begin{aligned}\dot{\gamma} = \frac{1}{V}\Bigg[L\cos\sigma + \left(V^2 - \frac{1}{r}\right)\left(\frac{\cos\gamma}{r}\right) + 2\Omega V \cos\phi \sin\psi \\ + \Omega^2 r \cos\phi \left(\cos\gamma \cos\phi + \sin\gamma \cos\psi \sin\phi\right)\Bigg]\end{aligned} \tag{2.5}$$

$$\begin{aligned}\dot{\psi} = \frac{1}{V}\Bigg[\frac{L\sin\sigma}{\cos\gamma} + \frac{V^2}{r}\cos\gamma \sin\psi \tan\phi \\ -2\Omega V(\tan\gamma \cos\psi \cos\phi - \sin\phi) + \frac{\Omega^2 r}{\cos\gamma}\sin\psi \sin\phi \cos\phi\Bigg]\end{aligned} \tag{2.6}$$

where r is defined as the radial distance from the planet center to the vehicle; θ and ϕ are the longitude and latitude; V is the planet-relative velocity; γ and ψ are the flight-path-angle and heading angle of the relative velocity vector, with ψ measured clockwise in the local horizontal plane from the north. The bank angle σ is the roll angle of the vehicle about the relative velocity vector, positive to the right. Bank angle and roll angle are different when the angle-of-attack is not zero. The value Ω is the non-dimensional constant that represents the planet self-rotation rate. The initial conditions of entry are the same as the conditions at the entry interface (EI) for the EDL problem:

$$r(t_0) = r_0 \tag{2.7}$$

$$\theta(t_0) = \theta_0 \tag{2.8}$$

$$\phi(t_0) = \phi_0 \tag{2.9}$$

$$V(t_0) = V_0 \tag{2.10}$$

$$\gamma(t_0) = \gamma_0 \tag{2.11}$$

$$\psi(t_0) = \psi_0 \tag{2.12}$$

Final entry constraints are typically set to a point when the trajectory reaches a position at a specified distance s_f (that can be zero) from the target location at a specified final altitude r_f and velocity V_f

$$r(t_f) = r_f \tag{2.13}$$

$$V(t_f) = V_f \tag{2.14}$$

$$s(t_f) = s_f \tag{2.15}$$

Dimensionless aerodynamic lift and drag accelerations in units of g_0 are defined by L and D, respectively and calculated with the following equations:

$$L = \rho(r)V^2 S_{ref} R_0 C_L/(2m_0) \tag{2.16}$$

$$D = \rho(r)V^2 S_{ref} R_0 C_D/(2m_0) \tag{2.17}$$

with ρ as the dimensional altitude-dependent atmospheric density, S_{ref} the dimensional reference area of the entry vehicle, and m_0 the constant mass of the vehicle in kg. C_L and C_D are the nondimensional aerodynamic lift and drag coefficients; both are functions of the vehicle, angle-of-attack α and Mach number. The angle of attack in entry flight for all sections of this work is assumed to be prescribed as a constant or a function of the Mach number.

Generally, bank angle is used as the main guidance control during the entry phase and it is subjected to the following operational constraints

$$\sigma_{min} \leq |\sigma(t)| \leq \sigma_{max} \tag{2.18}$$

In some cases, the rate of bank angle acceleration is also limited to avoid immediate control reaction.

For numerical simulations, is always a good practice to normalize the variables so that their numerical values are on the similar orders of magnitude. In this work, normalization is achieved by scaling lengths by the radius of the planet, $r_{scale} = R_0$; velocities by $V_{scale} = \sqrt{g_0 R_0}$, with g_0 the as the graviational accelration at R_0; and the time by $t_{scale} = \sqrt{R_0/g_0}$.

2.2.2 The Powered Descent Guidance Problem

The main objective of powered descent is to make sure that the vehicle lands gently on the surface and near the landing site. This is accomplished by eliminating the remaining velocity of the vehicle before reaching the landing location using retro-propulsion for a planet without atmosphere or supersonic retro-propulsion (SRP) when there is an atmosphere. If an entry phase is present, the final condition of the entry phase is usually the starting condition of powered descent. Regardless of the actual result after entry guidance, it is important that the powered descent guidance can take the vehicle from its actual state to the final condition on the ground. The guidance achieves this by activating the SRP rockets to produce a thrust force that helps slow down and drive the vehicle. Although it is necessary to use SRP to achieve the desired outcome, it is expected that fuel consumption is kept at a minimum, and the powered descent algorithm is entrusted

to perform this task. The spacecraft steering is also used to reduce the cross-range and downrange distance to the landing site. To accomplish this, the vehicle is controlled from an initial condition to a landing location on the surface of the planet. The powered descent guidance generates the commands for the thrust direction and magnitude necessary to accomplish this goal.

The 3-dimensional equations of motion for powered descent dynamics on a planet or the Moon in a Cartesian coordinate system are represented with:

$$\dot{\boldsymbol{r}} = \boldsymbol{V} \tag{2.19}$$

$$\dot{\boldsymbol{V}} = \boldsymbol{g} + \boldsymbol{a}_T \tag{2.20}$$

$$\dot{m} = -\frac{T}{V_e} \tag{2.21}$$

where $\boldsymbol{r} \in R^3$ and $\boldsymbol{V} \in R^3$ are the position and velocity vectors of the spacecraft. The planetary gravitational acceleration is represented by $\boldsymbol{g}$ and the thrust acceleration vector by $\boldsymbol{a}_T$. A central gravity model is used to make the algorithm applicable for longer duration flights. The aerodynamic forces are generally ignored because an atmosphere does not exist (such as a landing on the Moon), or is thin enough to be ignored by the powered descent guidance solution [22]. However, some aerodynamic forces exist and are not accounted for in the equations of motion for powered descent. The initial state is assumed to be known:

$$\boldsymbol{r}(t_0) = \boldsymbol{r}_0 \tag{2.22}$$

$$\boldsymbol{V}(t_0) = \boldsymbol{V}_0 \tag{2.23}$$

$$m(t_0) = m_0 \tag{2.24}$$

Now, let us introduce a predefined final position, $\boldsymbol{r}_f^*$, velocity, $\boldsymbol{V}_f^*$, and thrust acceleration $\boldsymbol{a}_{T_f}^*$, all specified at a final time, $t_f > 0$. The final position and velocity will define the landing position and velocity vectors as a targeting condition:

$$\boldsymbol{r}(t_f) = \boldsymbol{r}_f^* \tag{2.25}$$

$$\boldsymbol{V}(t_f) = \boldsymbol{V}_f^* \tag{2.26}$$

$$\boldsymbol{a}_T(t_f) = \boldsymbol{a}_{T_f}^* \tag{2.27}$$

Thrust T and thrust direction $\mathbf{1}_T$ are limited by the following constraints

$$T_{min} \leq T(t) \leq T_{max} \tag{2.28}$$

$$||1_T(t)|| = 1 \tag{2.29}$$

where $T_{min} \geq 0$ and $T_{max} \geq T_{min}$ have constant values.

The powered descent is present in all mission cases of this dissertation as it is the last measure to stop the vehicle from directly crashing into the ground before landing.

A New Approach to Entry, Descent, and Landing

Traditionally, both entry and powered descent phases have been developed without taking into account each other in the EDL design and analysis. That is, the entry phase, and descent and landing phases are designed, analysed and evaluated separately. The only connection they have is through a nominal interface condition. Studies have shown that end-to-End optimization of EDL can be achieved and an optimal nominal trajectory can be found for a specific mission scenario [91]. Optimizing the entire EDL trajectory can take a long time and an evaluation of that extend is unlikely to obtain a solution in the amount of time available for flight operations. In this sense, a complete end-to-end optimization is not what is envisioned in this study. Rather, it is the intention of this investigation to apply a fast solution that connects entry and powered descent of two independently developed algorithms through an adaptive PDI condition that benefits the overall performance of EDL. Taking advantage of the PDI logic presented in Lu [61], the development of an optimized set of tools that interact with each other through the proper selection of their interfaces is envisioned. The ultimate goal is to create algorithms that are suitable for on-board implementation without incurring high computational costs. Nonetheless, these algorithms must be reliable in obtaining an accurate and fuel-optimal solution. In addition, using our capability to increase the safety of the mission by providing a solution to an emergency situation is a task that will keep astronauts as the priority.

Taking all aspects in consideration, the following inquires lie around the purpose of this investigation: Can we produce results that are near-optimal with an algorithm like the fractional polynomial guidance? Can a near-optimal entry guidance algorithm be used

to produce a reliable solution to the entry problem without the need for much complexity? Is it possible to abort to a safe orbit during powered descent of a lunar landing mission using a fuel-optimal ascent guidance algorithm? It is intended to deliver an algorithm with onboard capability based on the actual condition and not requiring complex algorithms or functions other than the ones already available for entry and powered descent guidance. Using a new methodology for entry guidance; applying an adaptive PDI formulation; and using a simple, yet powerful, powered descent guidance algorithm can provide a fast and robust solution to the entry, descent, and landing problem.

2.3 Direct and Indirect Methods of Optimal Control

Optimal control methods were utilized in this work to find the solution that minimizes the total propellant consumption in the EDL problem. There are two main options for solving optimal control problems, direct methods and indirect methods of optimal control. The goal in both methods is to find the optimal control inputs to minimize an objective function, subject to certain constraints. In the direct method approach, the optimal control problem is converted into a parameter optimization problem to be solved as a nonlinear programming problem (NLP) [92]. The problem can be transformed into a parameter optimization problem using several methods such as optimal parametric control [93], collocation method [94], differential inclusion [95], and pseudospectral methods [96]. Problems solved with the direct method depend on an initial guess that often needs to be supplied by the user. As a consequence, convergence to the optimal solution is conditional on a proper initial guess. However, direct methods are less vulnerable to

convergence issues if properly configured, even for large problems [94]. A downside is that direct methods can be less accurate in comparison to indirect methods because a solution does not need to satisfy the necessary conditions. However, the direct method is very efficient when solving well-defined large scale problems.

In the direct method of optimal control, the problem is formulated as a mathematical optimization problem or nonlinear programming problem, with the state and control defined as

$$\boldsymbol{x} = [x_1, x_2, \ldots, x_n]^T \in \mathbb{R}^n \tag{2.30}$$

$$\boldsymbol{u} = [u_1, \ldots, u_m]^T \in \mathbb{R}^m \tag{2.31}$$

and the dynamics of the finite-dimensional system are represented by a system of first-order differential equations

$$\dot{\boldsymbol{x}} = \boldsymbol{f}(\boldsymbol{x}, \boldsymbol{u}, t) \tag{2.32}$$

The problem consists in minimizing $f(\boldsymbol{x})$ subject to

$$h(\boldsymbol{x}) = [h_1(\boldsymbol{x}), \ldots, h_m(\boldsymbol{x})]^T = 0, \quad \boldsymbol{h} : \mathbb{R}^n \longrightarrow \mathbb{R}^m \tag{2.33}$$

$$g(\boldsymbol{x}) = [g_1(\boldsymbol{x}), \ldots, g_p(\boldsymbol{x})]^T \leq 0, \quad \boldsymbol{g} : \mathbb{R}^n \longrightarrow \mathbb{R}^p \tag{2.34}$$

where f, $\boldsymbol{h}$, and $\boldsymbol{g}$ are C^1 and $m \leq n$ and $p \geq 0$.

In the indirect method approach, Pontryagin's minimum principle and necessary

conditions are applied to create a two-point boundary-value problem (TPBVP) that is solved numerically to obtain an optimal trajectory [94, 97]. Two of the most accepted methods to solve TPBVPs are approximation [98] and shooting methods [94]. Generally, a guess on the initial value of the adjoint variables is necessary within a certain tolerance. The advantage of the indirect method approach is that a continuous-time solution can be obtained. In problems with nonlinear dynamics such as powered descent, a solution with the indirect method takes advantage of that continuity to produce a trajectory from beginning to end.

To define the problem with the indirect method, the system dynamics are defined by

$$\dot{\boldsymbol{x}} = \boldsymbol{f}(\boldsymbol{x}, \boldsymbol{u}, t) \tag{2.35}$$

with the initial condition at initial time t_0 is

$$\boldsymbol{x}(t_0) = \boldsymbol{x}_0 \in \mathbb{R}^n \tag{2.36}$$

A set of algebraic constraints called *terminal constraints* need to be satisfied at the final time t_f

$$\boldsymbol{g}(\boldsymbol{x}(t_f), t_f) = 0 \tag{2.37}$$

where $\boldsymbol{g}(\cdot, \cdot) : \mathbb{R}^n \times \mathbb{R} \longrightarrow \mathbb{R}^j, (j \leq n)$ is a vector function and t_f can be specified for

a fixed-final time problem or not be specified for a free final-time problem. In a free final-time problem, the final time also needs to be determined as part of the solution.

The control vector that will satisfy the dynamics is defined as $\boldsymbol{u} \in \mathbb{R}^m$ and it is generally a function of time to-be-determined. It is constrained to a set of feasible control values $U \in \mathbb{R}^m$

$$\boldsymbol{u} \in U, \quad \forall t \in [t_0, t_f] \tag{2.38}$$

The performance index is the minimization term of the problem

$$J = \phi(\boldsymbol{x}(t_f)) + \int_{t_0}^{t_f} L(\boldsymbol{x}, \boldsymbol{u}, t)\, dt \tag{2.39}$$

A Hamiltonian function combines the objective function and the system dynamics, and is defined as

$$H = L(\boldsymbol{x}, \boldsymbol{u}, t) + \boldsymbol{p}^T \boldsymbol{f}(\boldsymbol{x}, \boldsymbol{u}, t) \tag{2.40}$$

where L is the Lagrangian of the function defined by

$$L(\boldsymbol{x}, \boldsymbol{\mu}, \boldsymbol{\lambda}) = f(\boldsymbol{x}) + \boldsymbol{\lambda}^T \boldsymbol{h}(\boldsymbol{x}) + \boldsymbol{\mu}^T \boldsymbol{g}(\boldsymbol{x}) \tag{2.41}$$

and $\boldsymbol{p}$ is the co-state vector or the adjoint variables. The co-state equations are derived

from the Hamiltonian function and represent the evolution of the co-state vector over time

$$\dot{\boldsymbol{p}} = -\frac{\partial H}{\partial \boldsymbol{x}} \tag{2.42}$$

The transversality condition consists in satisfying the following equation

$$\boldsymbol{p}_f = \frac{\partial \phi}{\partial \boldsymbol{x}_f} + \frac{\partial \boldsymbol{g}}{\partial \boldsymbol{x}_f}\alpha \tag{2.43}$$

with α a vector multiplier.

In the Pontryagin's Minimum Principle, the optimal state trajectory $\boldsymbol{x}^*$, optimal control $\boldsymbol{u}^*$, and its corresponding Lagrange multiplier vector $\boldsymbol{\lambda}^*$ minimize the Hamiltonian such that

$$H(\boldsymbol{x}^*(t), \boldsymbol{u}^*(t), \boldsymbol{\lambda}(t), t) \leq H(\boldsymbol{x}(t), \boldsymbol{u}(t), \boldsymbol{\lambda}(t), t) \tag{2.44}$$

The necessary condition for an optimal control solution requires that at every point in time, the optimal control $\boldsymbol{u}^*(t)$ and the corresponding co-state vector $\boldsymbol{p}(t)$ must satisfy

$$\frac{\partial H}{\partial \boldsymbol{u}} = 0 \tag{2.45}$$

To solve the optimal control problem the state equations, co-state equations, and the transversality condition need to be solved simultaneously as a two-point boundary value problem (TPBVP), with the initial conditions at the initial time t_0, and the boundary

conditions at t_f.

In this dissertation, both the direct and indirect methods are used to solved the complex entry, optimal powered descent and optimal abort guidance problems. The indirect method of optimal control is utilized to solve the fuel-optimal powered descent guidance problem. Since the indirect method approach is usually faster to solve, the solution can be obtained in real-time. Depending on the complexity of the equations in the problem, the indirect method might not be an option given that it requires advanced mathematical and numerical analysis. For that reason, optimization of entry guidance is difficult to achieve given the highly non-linear equations of motion. Often, complex problems that cannot be solved using the indirect method of optimal control are solved using a direct method approach. Acknowledging that, unless solved analytically to examine if the problem in fact satisfies the necessary conditions, the solution might not be an optimal solution. In the case that an analytical solution cannot be easily found, an understanding of the general solution is necessary to evaluate if the solution obtained is expected. The indirect method is used in this work to validate the discovery of a recently discovered phenomenon in abort guidance that will be discussed further in Section 6 and to create a benchmark solution to the complete EDL optimization problem to compare with the results from the novel EDL optimization approach resulting from this work and that will be discussed in Section 8.

Chapter 3

Supporting Algorithms for Entry and Powered Descent Trajectory Generation

3.1 Introduction

Since multiple guidance algorithms for entry and powered descent will be analyzed, some background on the characteristics of each approach will be given to aid with the understanding of this study. In this section, a group of fast and robust entry and powered descent guidance algorithms will be presented. These algorithms are the state-of-the-art in entry and powered descent guidance and were utilized to obtain many of the results from this work. It is important to point out that the author did not develop these algorithms. The author, however, did contribute in the validation of the algorithms using high-fidelity simulation environments and performance testing in different landing scenarios. This section is included because the algorithms presented here are the building blocks of many of the technology advancements of the original work presented in this dissertation.

3.2 Entry-Guidance Supporting Algorithm

3.2.1 The Fully Numerical Predictor-Corrector Entry Guidance Algorithm

FNPEG is a versatile entry guidance method suitable for a wide range of vehicles with different lift characteristics. The algorithm is capable of inequality constraint enforcement such as heating rate, dynamic pressure, and load factor limits. Altitude rate feedback and inequality constraint enforcement permit diverse orbital and suborbital mission requirements. Bank angle control is employed to steer the vehicle from the end of the deorbit phase until the targeting condition is reached. Altitude and velocity are utilized as the targeting parameters that need to be reached. An initial bank angle is calculated and used to generate a bank-angle magnitude profile. Range-to-go to the final condition is used to define the bank-angle profile. Every iteration, a new initial bank angle magnitude is calculated to ensure that the final condition is met. To maintain performance and reduce crossrange distance towards at the end of the segment, a bank reversal logic is applied to calculate the bank sign of every new bank command calculated. The number of bank reversals performed is selected by the user.

In FNPEG, the bank angle magnitude along the trajectory is parameterized by a linear profile as shown in Figure 3.1. The bank angle profile establishes the longitudinal entry trajectory that will be followed. The independent variable for the entry problem is the energy-like equation e

$$e = \frac{1}{r} - \frac{V^2}{2} \tag{3.1}$$

The importance of this parameter arises from the fact that if higher-terms associated with planet-rotation and J_2 terms are ignored, it can be shown that the derivative $\dot{e}$ is monotonically increasing inside the atmosphere

$$\dot{e} = DV > 0 \tag{3.2}$$

The initial e_0 and final value e_f are specified for given initial and final altitude and velocity values. For predefined values of e_0 and e_f, σ_0 and σ_f define the initial and final bank angle magnitude in the profile curve, these are values of $|\sigma|$ at e_0 and e_f, respectively. The final bank angle must satisfy $\sigma_f > 0$ to provide control margin towards the end of entry flight [99]. The value of the initial bank angle σ_0 is found by a Newton-Raphson method with inexact line search to achieve the specified ground range when the energy target is met, that is, $e = e_f$. If both σ_0 and σ_f satisfy Equation (2.18), then the bank angle constraint will be satisfied throughout the entry flight.

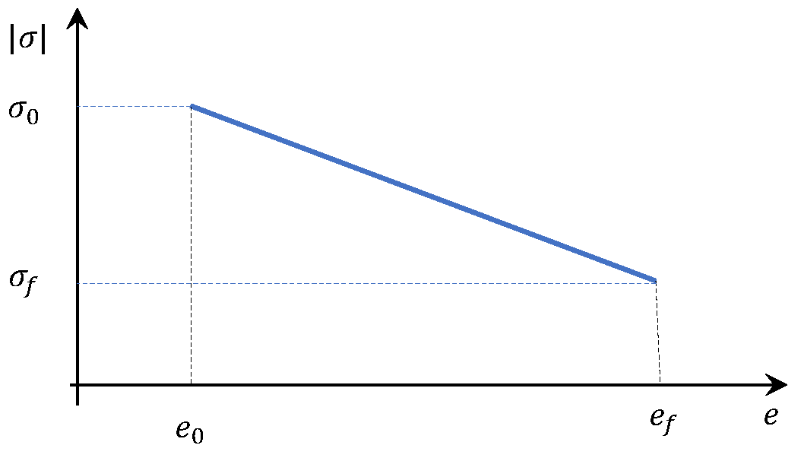

Figure 3.1. Bank angle control parameterization used in the fully numerical predictor-corrector entry guidance.

To reduce large crossrange dispersions, a number of bank reversals are performed by FNPEG during flight. A bank reversal occurs every time the sign of the bank angle is changed instantaneously and the vehicle is banked in the opposite direction of the lift vector. The sign of σ is determined by a numerical predictive lateral control technique [31, 100]. In the lateral control implementation of FNPEG, the user can decide the number of bank reversals to be performed. With the combination of longitudinal and lateral control, a guidance command with the magnitude and sign of σ is produced at any point during the entry trajectory. The command obtained is based on the current condition and the specified target. FNPEG has been highly regarded as the state-of-the-art in entry guidance and has demonstrated to be accurate and highly robust in extensive testing [31].

3.3 Powered Descent Guidance Supporting Algorithms

3.3.1 Fractional-Polynomial Powered Descent Guidance

Building on the legacy of the Apollo Program, FP^{2}DG was born out of the careful analysis of the Apollo Powered Descent Guidance and the E-Guidance Laws. Unlike the guidance laws used in during Apollo, an advantage of this approach is the ability to tune the guidance to meet mission requirements and to increase efficiency. Rather than a single guidance solution, this algorithm is considered a family of solutions that emerge from the selection of user-selected tuning parameters. The guidance parameters selectable by the user are the time-to-go (or total flight time), final altitude, final velocity, final acceleration, and two gains that control the shape of the trajectory. The effect of these parameters on trajectory shaping manifest in the form of engine throttle setting,

pitch angle profile, and powered descent trajectory profile. Multiple solutions under the same guidance approach can be obtained by the careful selection of this tuning gains with advantages on the reduction of propellant consumption and better vehicle positioning by an appropriate trajectory profile selection.

Starting from the 3-dimensional equations of motion for powered descent dynamics on a planet or the Moon in a Cartesian coordinate system defined by Equations 2.19 - 2.21, initial conditions in Equations 2.22 - 2.24, and final conditions from Equations 2.25 - 2.27. Assuming that $\boldsymbol{r}(t)$ and $\boldsymbol{V}(t)$ are known at any point along the trajectory, the guidance problem is to find the appropriate thrust acceleration command $\boldsymbol{a}_T(t)$ at any moment in time to guide the vehicle towards achieving the targeting condition at $t = t_f$.

Recently, a fractional-polynomial powered descent guidance (FP^{2}DG) approach is developed in Lu [64]. A fractional polynomial of a non-negative variable $x \geq 0$ is defined to be

$$p(x) = a_0 + a_1 x^{\gamma_1} + \cdots + a_k x^{\gamma_k} \tag{3.3}$$

where $a_i's$ are real constants, but the exponents $\gamma_1 \geq 0, \cdots, \gamma_k \geq 0$ are not necessarily integers. In FP^{2}DG, consider a reference thrust acceleration profile by

$$\boldsymbol{a}_d(t) = \boldsymbol{a}^*_{T_f} + \boldsymbol{c}_2 t_{go}^{\gamma}, \quad \gamma \geq 0 \tag{3.4}$$

where $\boldsymbol{c}_2 \in R^3$ is a to-be-determined constant vector, and t_{go} is the time-to-go defined by

$$t_{go} = t_f - t \tag{3.5}$$

From the equations of motion 2.19 and 2.20, the corresponding reference profiles for the velocity and position vectors $\boldsymbol{V}_d(t)$ and $\boldsymbol{r}_d(t)$ that also satisfy the terminal conditions 2.25 - 2.27 can be analytically obtained. The commanded thrust acceleration is then generated from the following tracking control law

$$\boldsymbol{a}_T(t) = \boldsymbol{a}_d(t) - \frac{k_V}{t_{go}}\left[\boldsymbol{V}(t) - \boldsymbol{V}_d(t)\right] - \frac{k_r}{t_{go}^2}\left[\boldsymbol{r}(t) - \boldsymbol{r}_d(t)\right] \tag{3.6}$$

where k_V and k_r are two feedback gains. When k_V is chosen to be

$$k_V = \frac{k_r}{(\gamma+2)} + \gamma + 1 \tag{3.7}$$

the resulting guidance command $\boldsymbol{a}_T(t)$ is independent of the to-be-determined coefficient vector $\boldsymbol{c}_2$, and the guidance law becomes what we call FP^{2}DG law that takes the form of

$$\begin{aligned}\boldsymbol{a}_T(t) = {} & \gamma\left[\frac{k_r}{2(\gamma+2)} - 1\right]\boldsymbol{a}_{T_f}^* + \left[\frac{\gamma k_r}{2(\gamma+2} - \gamma - 1\right]\boldsymbol{g} + \frac{\gamma+1}{t_{go}}\left(1 - \frac{k_r}{\gamma+2}\right)\left(\boldsymbol{V}_f^* - \boldsymbol{V}(t)\right) \\ & + \frac{k_r}{t_{go}^2}\left(\boldsymbol{r}_f^* - \boldsymbol{r}(t) - \boldsymbol{V}(t)t_{go}\right)\end{aligned} \tag{3.8}$$

It is revealed in Lu [64] that the FP^{2}DG law is the same as the explicit guidance law derived from the following thrust acceleration profile

$$\boldsymbol{a}_T = \boldsymbol{a}_{T_f}^* + \boldsymbol{c}_1 t_{go}^{\gamma} + \boldsymbol{c}_2 t_{go}^{\gamma_2}, \quad \gamma_2 = \frac{k_r}{\gamma+2} - 2 \tag{3.9}$$

If one integrates the equations of motion with the above thrust profile, use the current

state $[\boldsymbol{r}(t)\ \boldsymbol{V}(t)]$ as the initial condition, and solve the required coefficient vectors $\boldsymbol{c}_1$ and $\boldsymbol{c}_2$ to meet the targeting condition in Equations 2.25 and 2.27, a substitution of the resulting $\boldsymbol{c}_1$ and $\boldsymbol{c}_2$ back into the above a_T profile will produce exactly the FP^{2}DG law. The reader is referred to Lu [64] for much more complete and in-depth derivation and discussion on the guidance method.

There are two parameters in the FP^{2}DG law, $\gamma > 0$ and $k_r \leq 2(\gamma+2)$. The value of k_r, and to a lesser degree, the value of γ, can be adjusted to shape the descent trajectory and the engine throttle characteristics. For instance, a larger value of k_r predictably leads to a steeper trajectory toward the end. Therefore k_r can effectively control the trajectory if there is descent cone constraint at the landing to ensure ground clearance before touchdown. More details on the effects of k_r and *gamma* on the trajectory and propellant usage for a Mars landing mission can be found in Lu [64]. An important class of the FP^{2}DG law family is when $\gamma = 1$. In this case the guidance law becomes the Augmented Apollo Powered Descent Guidance (A^{2}PDG) law first derived in Lu [63]:

$$\boldsymbol{a}_T(t) = (\frac{k_r}{6}-1)\boldsymbol{a}^*_{T_f} + (\frac{k_r}{6}-2)\boldsymbol{g} + \frac{2}{t_{go}}(1-\frac{k_r}{3})(\boldsymbol{V}^*_f - \boldsymbol{V}(t)) + \frac{k_r}{t_{go}}(\boldsymbol{r}^*_f - \boldsymbol{r}(t) - \boldsymbol{V}(t)t_{go}) \quad (3.10)$$

Two very interesting special cases of the A^{2}PDG law (thus special cases of the FP^{2}DG law) are when $k_r = 6$ and $k_r = 12$. At $k_r = 6$, the A^{2}PDG law becomes the Apollo-era E-guidance law developed in Cherry [53]:

$$a_T(t) = -2/t_go[V^*_f - V(t)] + 6/(t_go^2)[r^*_f - r(t) - V(t)t_go] - g(14) \quad (3.11)$$

On the other hand, at $k_r = 12$, the A^{2}PDG law reduces to the Apollo lunar descent guidance law [101, 102, 54]:

$$\boldsymbol{a}_T(t) = \boldsymbol{a}^*_{T_f} - \frac{6}{t_{go}}\left[\boldsymbol{V}^*_f - \boldsymbol{V}(t)\right] + \frac{12}{t^2_{go}}\left[\boldsymbol{r}^*_f - \boldsymbol{r}(t) - \boldsymbol{V}(t)t_{go}\right] \tag{3.12}$$

In this paper the FP^{2}DG law in Equation 3.8 with $\gamma = 1$ and $k_r = 9$ is used as the baseline.

3.3.2 Universal Powered Guidance

The Universal Powered Guidance or UPG is a three dimensional propellant-optimal powered descent guidance algorithm based on the indirect method of optimal control. The algorithm has been developed over the years and applied to ascent, deorbit, and orbital transfers [103, 104, 105, 106]. UPG has been used extensively in Mars landing applications, where the mass of the spacecraft is much heavier than a typical robotic mission and landing precision is a requirement. The problem follows the same dynamics of the powered descent problem described in Section 3.3.2. UPG finds the optimal burn times to activate the spacecraft's SRP and the total flight time to reach the landing site. The formulation of UPG is simpler than algorithms like G-FOLD and it does not require extensive tuning when the mission or vehicle is changed. Different terminal formulations and constraints can be used without affecting the usability of the algorithm. The biggest drawbacks fall on the lack of inequality constraints on glide slope, pointing direction and velocity constraints. Furthermore, the algorithm does not have guaranteed theoretical convergence. Extensive simulations and Monte Carlo testing have shown that the algorithm is very capable of obtaining a solution with the appropriate initial conditions. The algorithm determines the

thrust direction, thrust magnitude and optimal flight time to solve on of the three available powered descent problems in the formulation: pinpoint-landing problem, Bolza-landing problem, and soft-landing problem.

The optimal powered descent problem is to find the thrust magnitude ($T(t)$) and direction ($\mathbf{1}_T(t)$), subject to the constraints in Equations 2.28 and 2.29, to reach a predetermined terminal condition $\boldsymbol{s}\left[\boldsymbol{r}(t_f), \boldsymbol{V}(t_f), t_f\right] = 0$ while minimizing a performance index of the form:

$$J = \kappa\phi(\boldsymbol{r}_f, \boldsymbol{V}_f, t_f) + \varepsilon\left[\int_0^{t_f} \frac{T}{\nu_{ex}}\, dt\right] \tag{3.13}$$

where $\kappa \geq 0$ and $\varepsilon \geq 0$ are constants. Equation 3.13 includes all commonly utilized optimization problems. For instance, if $\phi = 0$, the problem becomes a minimum-propellant problem for any $\varepsilon > 0$. If $\varepsilon = 0$ and $\phi > t_f$, the problem is now a minimum-time problem for any $\kappa > 0$. At last, if $\varepsilon = 0$, $\kappa > 0$, and $\phi = \boldsymbol{V}^T(t_f)\boldsymbol{V}(t_f)$, the problem for the minimum-final-velocity. There are three different optimal powered descent problem solutions for a mission based on the desired targeting conditions. Each case is defined as follows:

Pinpoint-landing Problem

Let us introduce a predefined final position, $\boldsymbol{r}_f^*$,and velocity, $\boldsymbol{V}_f^*$, all specified at a final time, $t_f > 0$. Assuming that $\boldsymbol{r}(t)$ and $\boldsymbol{V}(t)$ are known at any point along the trajectory, the guidance problem is to find the appropriate thrust acceleration command

$\boldsymbol{a}_T(t)$ at any moment in time to guide the vehicle towards achieving the targeting condition at $t = t_f$. The terminal constraints in the pinpoint-landing problem are the following:

$$\boldsymbol{r}(t_f) = \boldsymbol{r}^* \tag{3.14}$$

$$\boldsymbol{V}(t_f) = \boldsymbol{V}^* \tag{3.15}$$

The performance index is the propellant consumption, when $\kappa = 0$ and $\varepsilon = 1$ in Equation 3.13:

$$J = \left[\int_0^{t_f} \frac{T}{\nu_{ex}}\, dt\right] \tag{3.16}$$

In this problem, the vehicle lands exactly at the landing point with the least amount of propellant consumption.

Bolza-landing Problem

In the Bolza-landing problem, the vehicle ends at a specified altitude and velocity. However, the exact location at which the vehicle ends is not specified. The terminal constraints for the Bolza-landing problem are:

$$||\boldsymbol{r}(t_f)|| = ||\boldsymbol{r}^*|| \tag{3.17}$$

$$\boldsymbol{V}(t_f) = \boldsymbol{V}^* \tag{3.18}$$

The use of the Euclidean norm modifies the targeting condition. The final altitude might be defined to be at the surface of the planet, but the landing location might be different than the specified $\boldsymbol{r}^*$. To penalize the landing error $(\boldsymbol{r}(t_f) - \boldsymbol{r}^*$, the performance index is replaced with by:

$$J = \kappa \left[\boldsymbol{r}(tf) - \boldsymbol{r}^*\right]^T \left[\boldsymbol{r}(t_f) - \boldsymbol{r}^*\right] \left[\int_0^{t_f} \frac{T}{\nu_{ex}}\, dt\right] \tag{3.19}$$

with a constant $\kappa > 0$ and constant $\varepsilon = 1$. The penalization of the final position error allows some control over how far the vehicle can land from the target condition. A higher value for κ represents a larger penalization and a landing closer to the target condition. One of the main uses of the Bolza landing problem is to satisfy cases where there no feasible solution exists that satisfy the requirements of the pinpoint-landing problem, either because the divert capability is too low or the dispersions are large to and cannot be achieved by the controls of the vehicle.

Soft-landing Problem

The soft-landing problem is the least constrained of the three powered descent guidance problems. The terminal constraints are the same as in the Bolza problem:

$$||\boldsymbol{r}(t_f)|| = ||\boldsymbol{r}^*|| \tag{3.20}$$

$$\boldsymbol{V}(t_f) = \boldsymbol{V}^* \tag{3.21}$$

Except that in this case, the performance index is only the propellant consumption ($\kappa = 0$):

$$J = \left[\int_0^{t_f} \frac{T}{\nu_{ex}}\, dt\right] \tag{3.22}$$

In this version of the powered descent problem, the goal is to land the vehicle safely and with the least amount of propellant possible. The algorithm is only constrained to reach the ground at a specified velocity and altitude, regardless of its location with respect to the landing site. Hence, this is the most propellant-efficient solution that can be obtained given the problem initial conditions.

The reader is encouraged to look at Lu [22] for more details on the development and formulation of UPG.

3.3.3 Guidance for Propellant-Optimal Landing of a Rocket

The Guidance for Propellant-Optimal Landing of a Rocket, or G-POLAR, is another fuel-optimal powered guidance algorithm based on the indirect-method of optimal control. It solves the optimal control problem reliably given an initial condition. The algorithm is

fast and able to find a solution in under 3 milliseconds on a typical desktop computer. The work on G-POLAR is a continuation of UPG and offers improvements on several fronts such as taking a numerical approach, adding constraints to the thrust pointing direction and solving a solution degradation phenomenon. The solution provides information on the complete 3DOF propellant-optimal powered descent trajectory and is able to predict the final propellant consumption. In the same way as UPG, the software implementation of G-POLAR is relatively simple and requires a small amount of storage space. This is usually common in solutions with the indirect method. Lu [107] provides a complete description and demonstration of G-POLAR.

In GPOLAR, a topocentric Cartesian coordinate frame with origin at the landing site is used. A representation of the topocentric frame is shown in Figure 3.2.

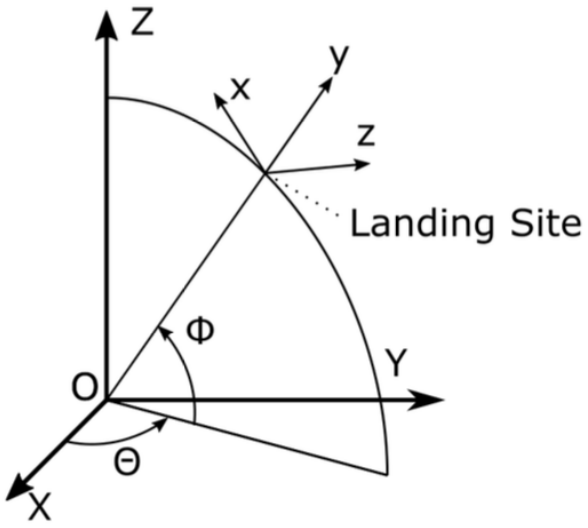

Figure 3.2. Topocentric frame representation with xyz at the landing site (the frame $OXYZ$ is a planet-centered frame).

More information on G-POLAR can be found on Lu [107].

3.3.4 Adaptive Powered Descent Initiation Logic

The powered descent initiation is the moment in which the engine on a spacecraft is activated to start powered descent. In the Apollo program, PDI occurred at the perilune of the descent orbit from the lunar parking orbit. The PDI condition is usually selected as a trigger point, based on pre-planned mission scenarios based on a nominal trajectory. However, a predefined PDI point is not ideal given that uncertainty might drive the state to be far away from the predicted state. For this reason, the determination of the PDI condition is crucial as it defines the diver requirement and stress level that the guidance must endure to control the vehicle towards the target.

Recent developments of work on Mars EDL [22, 63] have demonstrated that an adaptive approach is the best way to predict the ideal PDI condition. When the current state is taken into account, the PDI point can be predicted more accurately. The algorithm is based on the propellant-optimal soft-landing solution to a powered descent guidance problem. Out of the three powered descent landing modes described previously, the soft-landing solution provides the trajectory with the least amount of propellant possible. This is because it is also the least constrained solution. During unpowered flight, the algorithm calculates the total range-to-go to the landing site if the soft-landing powered descent solution were to be activated at that moment. This prediction occurs periodically until the range-to-go reaches zero. At this point, a signal is sent to the algorithm to activate powered descent at that moment. The optimal flight-time is used as the initial guess for the powered descent guidance and the propellant consumption is near-optimal as it is activated at a point that is really close to optimal. The powered descent solution

uses the pinpoint-landing mode to reach the desired target accurately. Figures 3.3 and 3.4 illustrate the working principle of the adaptive PDI logic as it is activated during the entry phase.

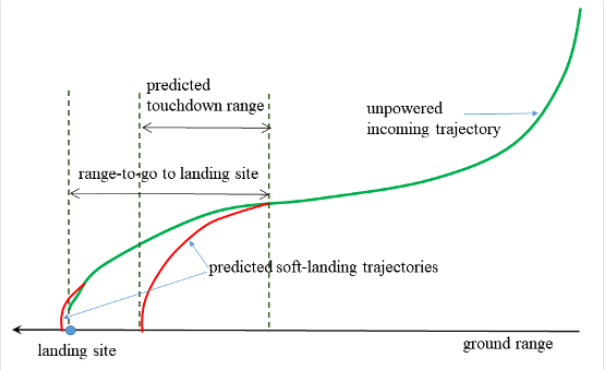

Figure 3.3. Concept of operations of adaptive powered descent initiation logic.

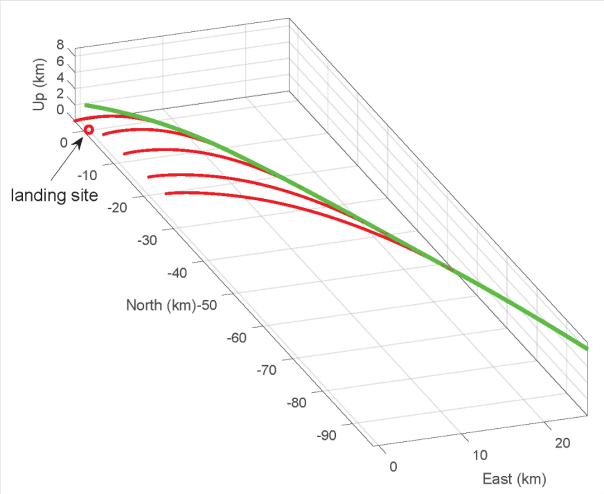

Figure 3.4. Range to landing site measurement in adaptive powered descent initiation logic.

With this method, the PDI condition is not simply a trigger, but an actual point selected by the algorithm to produce a trajectory with optimal propellant consumption. In Section 4 we demonstrate among other aspects that this adaptive PDI logic works very well for lunar landing, dramatically increasing the capability of the vehicle to handle

autonomously dramatic increase of the initial downrange with nearly the same propellant usage and ensured landing accuracy. The PDI logic is deployed at perilune in the simulations in Section 4. But the PDI logic could be activated before perilune as well. In such a case it is expected that the ability of the guidance system to land successfully the vehicle in the presence of more substantial decrease in the initial downrange will be improved.

3.4 Summary

The contents of Chapter 3 describe different supporting algorithms that will be utilized throughout the dissertation. The material provided is not a full reprint, but the author wishes to acknowledge the primary investigators of the sources cited and the contribution of their work on the progress and development of this project. The material on the Fully Numerical Predictor-Corrector Entry Guidance is referenced from Lu, P., "Entry guidance: a unified method," Journal of Guidance, Control, and dynamics, vol. 37, no. 3, pp. 713–728, 2014. The material on the Fractional-Polynomial Powered Descent Guidance is referenced from Lu, P., "Theory of fractional-polynomial powered descent guidance," Journal of Guidance, Control, and Dynamics, vol. 43, no. 3, pp. 398–409, 2020. The material on the Universal Powered Guidance is Lu, P., "Propellant-optimal powered descent guidance," Journal of Guidance, Control, and Dynamics, vol. 41, no. 4, pp. 813–826, 2018. The material on Guidance for Propellant-Optimal Landing of A Rocket is referenced from Lu, P. and Callan, R., "Propellant-optimal powered descent guidance revisited." Journal of Guidance, Control, and Dynamics, vol. 46, no. 2, pp. 215–230, 2023.

Chapter 4

Demonstration of Human-Scale Lunar Landing Mission

4.1 Introduction

In this chapter, a recently developed guidance method named the fractional-polynomial powered descent guidance (FP^{2}DG) is applied for the first time to a crewed lunar landing mission to the South Pole of the Moon. The FP^{2}DG method inherits the maturity and flight-proven legacy of the Apollo lunar descent guidance law, yet, offers much greater flexibility in trajectory shaping and performance trade. For autonomous operation in a diverse range of situations, the FP^{2}DG law is aided by an on-board powered descent initiation algorithm to adaptively determine a best timing for engine ignition based on the actual state of the flight. This guidance approach is reviewed first, then demonstrated in deterministic and Monte Carlo simulations in the lunar landing mission. Nominal and parametric studies show and compare the performance of the guidance law under different gain values. Furthermore, studies on the importance of an appropriate PDI condition are shown and compared to cases in which onboard PDI determination is not active. The robustness, high accuracy and propellant efficiency of FP^{2}DG are supported

by deterministic and Monte Carlo simulations. The guidance approach is shown to be highly robust, accurate, and propellant efficient.

4.2 Vehicle and Mission

The vehicle and mission data used in this demonstration are the same as those presented in Table 4.1. Note that unlike in the Apollo 11 mission, the condition in Table 4.1 is called the perilune condition, not the PDI condition, because the PDI condition will be determined by the adaptive PDI logic in our approach. The adaptive PDI logic is executed from perilune and on until the PDI condition is determined by the logic. Depending on the actual condition (particularly downrange), the PDI condition found can be right at perilune, or at a time after perilune. Together with the PDI point, the initial value of t_{go} is also provided by the fuel-optimal soft-landing solution in the PDI logic. In the nominal case the logic finds the PDI point to be 21 seconds after perilune.

Table 4.1. Initial conditions and vehicle data for lunar landing mission at the South Pole of the Moon.

Perilune Condition	Value
altitude (km)	15.24
longitude (deg)	41.85
latitude (deg)	-71.6
inertial velocity (m/s)	1,698.3
inertial topocentric flight path angle (deg)	0.0
inertial topocentric azimuth angle (deg)	180
downrange (km)	559.41
crossrange (km)	0.48
total vehicle mass (kg)	15,103
total fuel mass (kg)	10,624
vehicle dry mass (kg)	4,479

At PDI, the powered descent commences. The FP^{2}DG law with $\gamma = 1$ and $k_r = 9$

are used. The powered descent phase ends at an altitude of 20 m above the landing with a descent rate of 1 m/s. A terminal descent phase of 20 sec follows and the vehicle touches down at the landing site with a descent rate of 1 m/s. In the terminal descent phase, the vehicle is guided by the FP^{2}DG law with $\gamma = 1$ and $k_r = 6$. These parameters are chosen because they lead to zero total acceleration at the touchdown and the engine throttle is nearly constant in this terminal descent.

Closed-loop simulations are performed in three-degree-of-freedom mode. The guidance cycle time is 0.1 sec (at a rate of 10 Hz). Perfect navigation information is assumed. Therefore, the landing accuracy reported in this paper should be put in the context that it showcases the capability of the powered descent guidance system should other uncertainty and dynamic effects are ignored.

4.3 Nominal Lunar Landing Trajectory using the Fractional-Polynomial Powered Descent Guidance

The nominal descent flight from perilune lasts 701.6 sec, and the powered descent (including the terminal phase descent) takes 680.2 sec. The propellant usage is 7,152 kg, significantly below the allotted fuel mass of 8,248 kg. With perfect navigation and no rotational and engine dynamics considered, the vehicle lands exactly at the South Pole with the required descent rate.

Figure 4.1 shows the altitude versus ground range along the nominal trajectory. The insert in the figure depicts the final portion of the trajectory including the terminal/vertical descent phase. Figure 4.2 gives the nominal engine throttle and thrust acceleration profiles.

The nominal throttle profile has sufficient margins on both the up- and down-side. The effect of sudden reduction in the thrust magnitude caused by switching into the terminal descent phase is evident in the throttle/acceleration profiles.

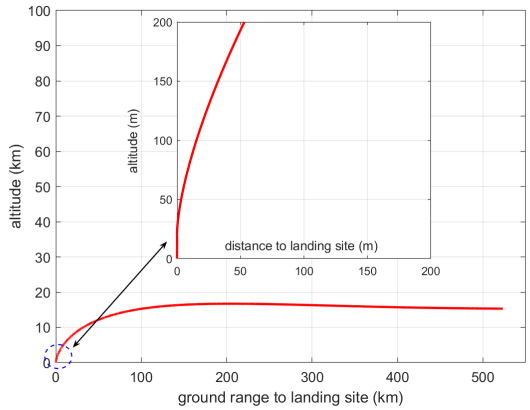

Figure 4.1. Nominal planetodetic altitude in lunar powered descent using the fractional-polynomial powered descent guidance.

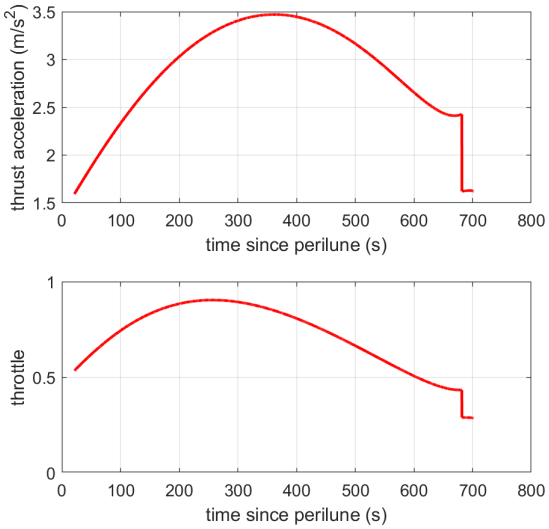

Figure 4.2. Nominal engine throttle and thrust acceleration in lunar powered descent using the fractional-polynomial powered descent guidance.

Assuming that the engine gimbal angle is ignored, the required thrust direction will specify the body orientation of the vehicle. The body pitch and yaw angle of the vehicle

are plotted in Figure 4.3. A final pitch angle of 90 degrees indicates a vertical touchdown as required. The yaw angle is small, a result of nearly perfectly aligned nominal descent trajectory. Figure 4.4 illustrates the variations of the thrust angle, the angle between the thrust vector and the relative velocity vector. A constant 180-deg thrust angle means a pure gravity turn. It is apparent the FP^{2}DG law-guided descent is not a pure gravity turn, except for the terminal descent phase which is practically a vertical descent.

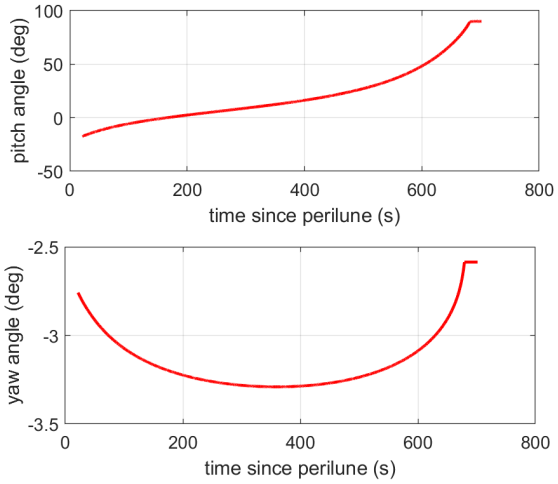

Figure 4.3. Nominal vehicle pitch and yaw angles in lunar powered descent using the fractional-polynomial powered descent guidance.

4.4 Parametric Studies on Thrust Profile and Trajectory Shaping

Studies were performed over the two main parameters of the guidance, k_r and γ. For the parametric studies of k_r , a constant value $\gamma = 1.0$ was used while the value of k_r was varied from 6.0 to 12.0. In Figure 4.5, the trajectories defined by 5 different values of k_r are shown. These trajectories show the uniform pattern created by the selection of different

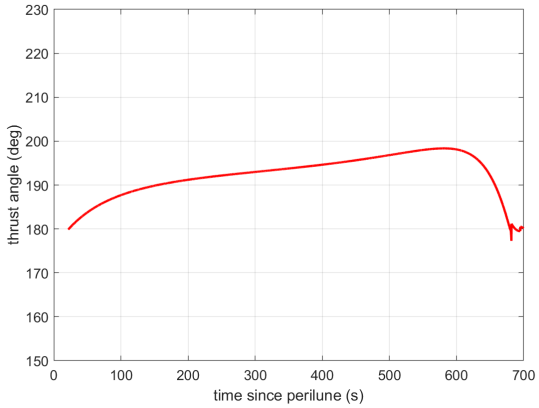

Figure 4.4. Nominal thrust angle profile in lunar powered descent using the fractional-polynomial powered descent guidance.

values of k_r. It was shown in Lu [64] that increasing k_r makes the trajectory shallower for a landing on Mars, the same circumstances apply for a lunar landing. Likewise, the relative velocity in the trajectory pictured in Figure 4.6 follows a pattern that varies uniformly as k_r increases, with greater values of k_r holding slower velocities throughout the trajectory.

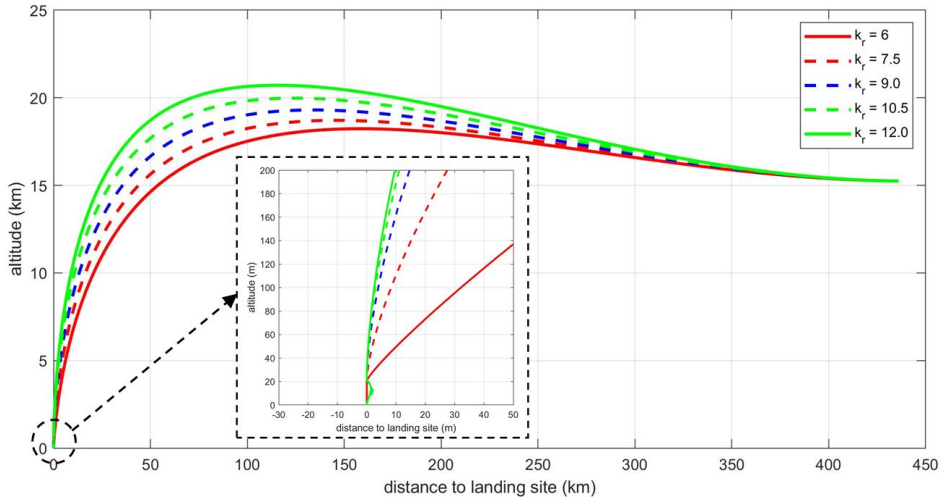

Figure 4.5. Parametric studies on k_r during lunar powered descent, with $\gamma = 1.0$, using fractional-polynomial powered descent guidance: nominal planetodetic altitude vs. distance to landing site.

In terms of thrust acceleration and throttle, three trajectories are presented in

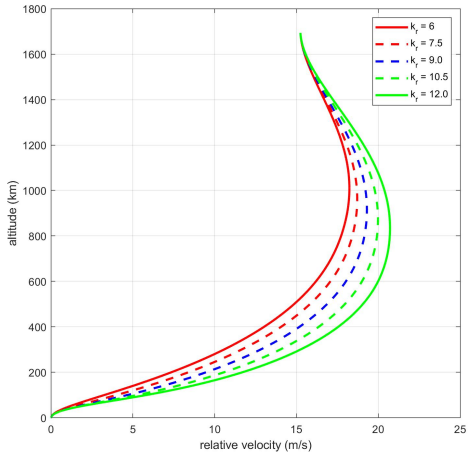

Figure 4.6. Parametric studies on k_r during lunar powered descent, with $\gamma = 1.0$, using fractional-polynomial powered descent guidance: nominal planetodetic altitude vs. relative velocity.

Figure 4.7 for comparison. All three profiles show similar trajectories but depending on the value of k_r the length of the trajectory varies. For bigger values of k_r the total duration of flight gets longer. Notice that the throttle command has a slight jump at the end signaling the change to the vertical descent phase.

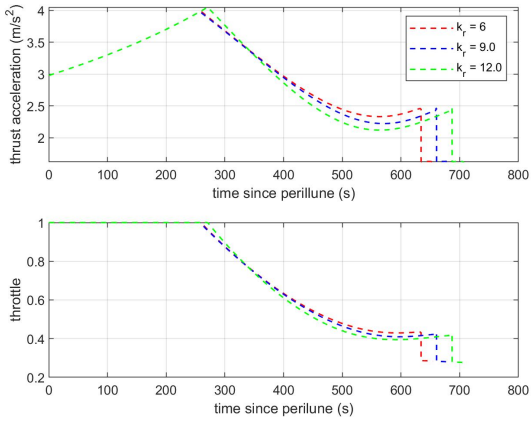

Figure 4.7. Parametric studies on k_r during lunar powered descent, with $\gamma = 1.0$, using fractional-polynomial powered descent guidance: thrust acceleration and engine throttle.

Similarly, the effects of γ on the trajectory can be found by setting a constant value

of k_r and changing the value of γ. For this parametric study, the constant value of k_r = 9.0. The nominal trajectories for different values of γ are shown in Figure 4.8. When γ = 1.0, the trajectory becomes the same as the nominal trajectory. From the plot, it can be gathered that the shape of the trajectory varies but behaves in a way that is easy to predict. The insert shows that the direct implication of increasing γ is that the trajectory becomes shallower towards the end, similar to the effect of decreasing k_r. This goes hand in hand with the results from Figure 4.9, where is shown that the relative velocity remains smaller throughout the trajectory for bigger values of γ. The trajectory shaping capability is clear, having the tuning parameter γ permits to have more flexibility. One thing to note is that the parameter γ is more sensitive than k_r, and the maximum tuning limit depends on the specific scenario in use. In this case, for a lunar landing, the limiting factor was found to be $\gamma = 3.0$.

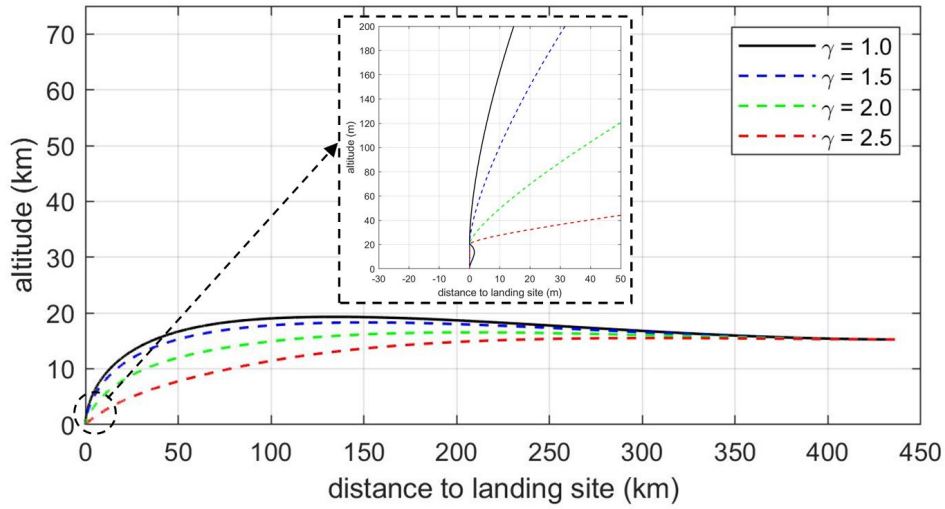

Figure 4.8. Parametric studies on γ during lunar powered descent, with $k_r = 9.0$, using fractional-polynomial powered descent guidance: nominal planetodetic altitude vs. distance to landing site.

Figure 4.10 provides the thrust profile and throttle command that would be issued

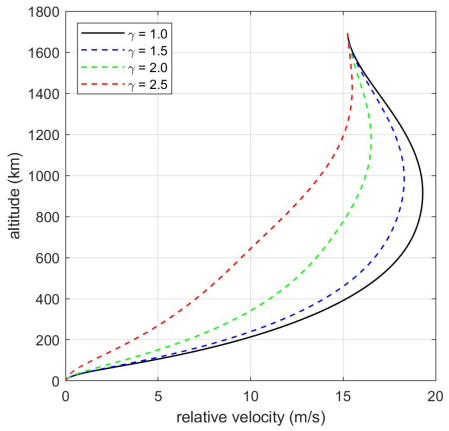

Figure 4.9. Parametric studies on γ during lunar powered descent, with $k_r = 9.0$, using fractional-polynomial powered descent guidance: nominal planetodetic altitude vs. relative velocity.

by the algorithm. The results presented are not uniform, but they follow a specific trend. This shows just how much can be gained from knowing the effects of tuning the guidance.

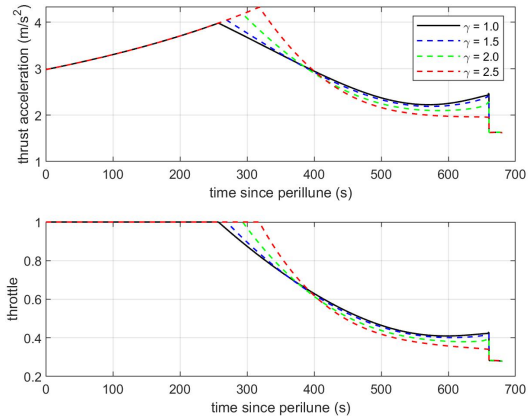

Figure 4.10. Parametric studies on γ during lunar powered descent, with k_r, using fractional-polynomial powered descent guidance: thrust acceleration and engine throttle.

Ultimately, having a tunable guidance capable of solving the landing problem gives the user an opportunity to select a desired trajectory by taking into account the trade-off between trajectory shaping and fuel consumption.

4.5 Onboard Determination of Powered Descent Initiation Condition

While the adaptive PDI logic first presented in Section 3.3.4 is originally developed for Mars EDL where the unpowered phase is entry flight (actively guided or otherwise), nothing in the above described working principle precludes the same algorithm from being applied to lunar landing, even though the unpowered flight before PDI in lunar landing is ballistic (orbital). Perhaps the only consideration is that the ballistic trajectory does not rapid increase in altitude after perilune. This is only precaution (which may not even be necessary for the PDI algorithm to still work safely), and any reasonable descent orbit for a crewed lunar landing mission is likely to be one with a small eccentricity. In this section, it is demonstrated that this adaptive PDI logic works very well for lunar landing, dramatically increasing the capability of the vehicle to handle autonomously dramatic increase of the initial downrange with nearly the same propellant usage and ensured landing accuracy. The PDI logic is deployed at perilune in the simulations, but the PDI logic could be activated before perilune as well. In such a case it is expected that the ability of the guidance system to land successfully the vehicle in the presence of more substantial decrease in the initial downrange will be improved.

Powered descent in all Apollo lunar landing started at perilune. In a significant off-nominal case where perilune occurs much farther from the landing site, PDI at perilune may not be a good, or even a feasible choice. For instance, if for some unforeseen reason the perilune in the preceding mission occurs at the equator instead of at a latitude of -71.6 deg, igniting the engine right away would not even come close to landing vehicle at the

South Pole.

The adaptive PDI logic however would ensure a successful landing by allowing the vehicle to continue on its ballistic trajectory (the ascending part of the 60 nm× 50,000ft descent orbit), until an appropriate time to start the powered descent. In this scenario, the PDI logic will continuously check the condition for PDI while the vehicle is in ballistic flight. At 1,235 seconds after perilune, the PDI logic determines that this is the time for PDI. The vehicle lands at the South Pole accurately 845.7 seconds later, with a propellant usage of 7,375 kg. Figure 4.11 shows the ground track of the trajectory since perilune, with both the ballistic and powered descent phase in blue and red, respectively.

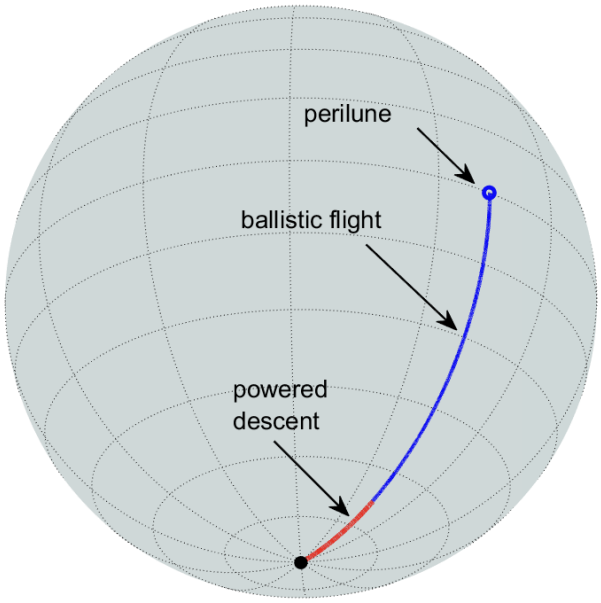

Figure 4.11. Ground track of the powered descent landing trajectory when perilune is at the equator and the adaptive PDI logic is active.

Some results of using the PDI logic under different initial ground ranges is shown in Table 4.2. The case with lowest propellant consumption is shown in green color. For the same vehicle, initial conditions and landing site, it is evident that the PDI logic finds

a particular burn time to be the optimal solution. Increasing the initial ground range just drives the vehicle to coast for a longer period of time until it reaches the optimal PDI condition. This can be seen by taking a look at how the PDI increases as the initial ground increases. On the other hand, decreasing the initial range-to-go makes the PDI logic realize that it should activate immediately but still tries to find an optimal solution. Also, since the PDI logic is trying to find the optimal time PDI, the propellant usage stays close to the value for the nominal trajectory, achieving nearly optimal fuel consumption. After PDI initiation, FP^{2}DG takes over and lands the vehicle safely on the ground. The nominal trajectory is shown for comparison as Test Case 3 in Table 4.2.

Table 4.2. Comparison of nominal lunar powered descent mission at different initial ground ranges when adaptive PDI logic is active.

Test Case	Initial Ground Range (km)	PDI Time (s)	Burn Time (s)	Propellant Usage (kg)
1	1015	293.8	607.9	6945
2	863	202.8	607.7	6941
3	559	21.4	607.4	6935
4	498	0.0	607.4	6970
5	437	0.0	607.4	7087

To show the importance of the PDI logic, a comparison of a lunar landing attempt with different initial ground ranges is summarized in Table 4.3 with Test Case D as the nominal trajectory. The case with lowest propellant consumption is shown in green color and a failed case is shown in red. Notice that all PDI Time is 0 because powered descent starts right away and also the burn time is a fixed 720 seconds. In this test, the PDI logic was not active, instead PDI was activated right away with a fixed initial time-to-go of 720 seconds (the flight time of Apollo 11). It was revealed that beyond 832 km, the algorithm

without PDI logic would fail at landing successfully. This is caused by the vehicle being extremely far and the guidance not being able to reach the landing location. Furthermore, if the ground range is increased or decreased, the fuel consumed starts to increase as well.

Table 4.3. Comparison of nominal lunar powered descent mission at different initial ground ranges when adaptive PDI logic is inactive.

Test Case	Initial Ground Range (km)	PDI Time (s)	Burn Time (s)	Propellant Usage (kg)
A	832	0.0	720.0	Failed
B	711	0.0	720.0	7918
C	620	0.0	720.0	7067
D	559	0.0	720.0	7168
E	498	0.0	720.0	7291
F	437	0.0	720.0	7536

The inclusion of the PDI logic can be the difference between the success or failure of a mission. From Table 4.2, it can be seen that the PDI logic adapts very easily to the conditions and tries to find an optimal solution regardless of the PDI time, with propellant used being nearly optimal. From Table 4.3, it is clear that a time-to-go trigger is not a good metric for PDI and that it only works for a specific set of conditions. Moreover, if the fuel consumption between Tables 4.2 and 4.3 (PDI active/not active) is compared, not having onboard PDI determination always requires a greater amount of fuel for the same conditions. The lower propellant consumption comes from the time-to-go prediction being near-optimal. Dispersed PDI conditions suggest that not a single PDI condition satisfies all possible scenarios.

4.6 Stress Tests on Individual-Parameter Dispersions in Perilune Condition

Here we disperse each initial state variable at the perilune one at a time, to the maximum on both the plus and minus sides, until either (1) the landing condition can no longer be met; or (2) the propellant mass has been depleted. This test helps establish the single-parameter dispersion limits on the perilune state variables and gain an understanding on the performance range of the FP^{2}DG guidance law.

Table 4.4. Monte Carlo dispersions in lunar powered descent: allowable single-parameter ranges.

PDI State	Min Dispersion	Max Dispersion	Notes
Altitude (km)	-14.5	60.0	Limited by landing accuracy
Flight Path Angle (deg)	-6.0	5.0	Limited by landing accuracy or ground clearance
Downrange (km)	-120.0	Not Limited	Adaptive PDI allows the downrange to be increased by any value, given the 100x16 km deorbit ellipse
Crossrange (km)	-240.0	240	Limited by max fuel usage of 8248 kg
Velocity (m/s)	-400.0	180.0	Limited by landing accuracy
Engine thrust magnitude (%)	-7.0%	+50.0%	Limited by landing accuracy

The last row in Table 4.4 reveals that the guidance law is extremely robust with respect to positive thrust dispersions, that is, the actual engine thrust can be 50% higher than the value the guidance solution uses, and the vehicle can still land accurately. Note that thrust dispersions also create mass flow rate dispersions because the mass flow rate

is proportional to the thrust magnitude. The tolerance on negative thrust dispersions (when the actual thrust is lower than the modeled value) is much smaller (yet still at a respectable level of 7%). This finding suggests that, if necessary, the maximum thrust value used in the guidance law may be biased (reduced) from the nominal value. This bias will effectively cause the actual engine thrust level to be positive dispersion to the engine model in the guidance law (unless the actual thrust is much lower than nominal value). This way the guidance would be able to accommodate significant engine dispersions in the minus direction as well.

An elaboration on the "not limited" the maximum dispersion of perilune downrange is in order. As Figure 4.5 vividly illustrates, any increase of initial downrange is simply accommodated by the adaptive PDI logic. Therefore, the upside of initial downrange is not limited by either propellant usage limit or landing accuracy. On the other hand, if PDI must occur at the initial time, the maximum downrange increase is limited by 220 km in this case.

Figure 4.12 demonstrates the ground tracks of 3 different landing trajectories, all starting at the equator (a dispersion of initial downrange of 2,160 km). Two of the trajectories have about the largest initial crossrange dispersions (on both positive and negative sides). The adaptive PDI logic and FP^{2}DG law guide the vehicle for a successful landing at the South Pole in all 3 cases.

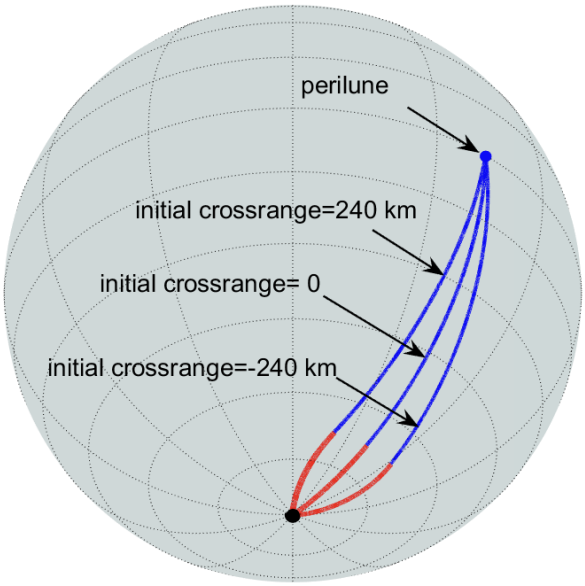

Figure 4.12. Ground tracks of three different powered descent landing trajectories when perilune is at the equator and the adaptive PDI logic is active.

4.7 Robustness Examination using Monte Carlo Simulation

Monte Carlo simulations provide a means to assess the combined effects of the dispersions and modeling uncertainty. Table 4.5 lists the dispersions and uncertainty used in the Monte Carlo simulations reported in this paper. As often employed in Monte Carlo simulations, the notion of the factor of safety (FOS) will be used later where FOS is a positive scaling factor of no smaller than unity that multiplies the nominal dispersions to generate the actual dispersions used in the Monte Carlo simulations. The dispersions in Table 4.5 are for FOS = 1.0. The perilune state dispersions are again known to the guidance system because of the assumption of perfect navigation system. The uncertainty in initial vehicle mass and thrust magnitude however is unknown to the guidance system. It should be pointed out that the sizes of the dispersions and uncertainty in Table 4.5

are very large, with most of them 3 - 10 times the orders of magnitude of the dispersions commonly expected. They are not chosen not to imitate any particular realism, but to stress the guidance system.

Table 4.5. Dispersions and uncertainty values of 3000 lunar powered descent Monte Carlo simulation runs with a factor of safety = 1.0.

Dispersion/Uncertainty	Distribution	3σ-Value
Perilune altitude (m)	Zero-mean Gaussian	1000.0
Perilune longitude (deg)	Zero-mean Gaussian	2.0
Perilune planetodetic latitude (deg)	Zero-mean Gaussian	2.0
Perilune inertial velocity (m/s)	Zero-mean Gaussian	10.0
Perilune inertial flight path angle (deg)	Zero-mean Gaussian	0.5
Perilune inertial azimuth (deg)	Zero-mean Gaussian	10.0
Initial vehicle mass (%)	Zero-mean Gaussian	2.0
Engine thrust (%)	Zero-mean Gaussian	1.0

The results reported in this paper are from a total of 3000 dispersed closed-loop simulations for each value of the FOS. Table 4.6 summarizes the statistics on the touchdown condition and propellant usage for FOS = 1.0. The vehicle lands accurately in all cases with the final velocity very close to the specified velocity of 1.0 m/s. There is no horizontal velocity at touchdown because the flight path angle is practically -90 degree in all cases. With a 90 deg final pitch angle, the vehicle's final attitude is vertical as desired. The maximum propellant usage is 7,690 kg, still significantly below the total propellant mass of 8,248 kg. The adaptive PDI logic determines the powered descent duration (the initial value of t_{go}), and this is why the powered descent durations are not identical. But the variations are within 5 seconds between the shortest and longest duration.

The adaptive PDI logic finds a PDI time for each of the 3000 dispersed trajectories, depending on the actual trajectory state. Figure 4.13 shows the distribution of the PDI

Table 4.6. Statistics of 3000 lunar powered descent Monte Carlo simulation runs with a factor of safety = 1.0.

Parameters	Mean	Standard Deviation	Minimum	Maximum
Touchdown Miss (m)	3.54E-05	1.91E-05	7.65E-06	7.87E-04
Touchdown Velocity (m/s)	9.92E-01	2.36E-02	8.98E-01	1.06E+00
Touchdown Flight Path Angle (deg)	-9.00E+01	1.14E-02	-9.00E+01	-8.96E+01
Touchdown Pitch Angle (deg)	8.99E+01	4.29E-02	8.81E+01	9.00E+01
Propellant usage (kg)	7.18E+03	6.94E+01	7.11E+03	7.69E+03
Duration of Powered Descent (s)	6.80E+02	7.38E-01	6.78E+02	6.83E+02

time since perilune. The best PDI times for the dispersed trajectories were as early as right at the perilune, and as late as 60 seconds after perilune. The ground ranges to the landing site and altitudes at the PDI for the dispersed trajectories are plotted in Figure 4.14. Due to the large dispersions in Table 4.5, the PDI ground ranges and altitudes had also substantial dispersions as the adaptive PDI logic worked on each trajectory. The crossranges at PDI with respect to the landing site can be more than 100 km as seen in Figure 4.15, which indicates that some of the powered descent trajectories were very much 3-dimensional, and the guidance system has the ability to do significant crossrange divert. Finally, the spread of PDI velocities versus altitudes are given in Figure 4.16.

Next, the FOS value is increased to stress further the guidance system to the point where the performance begins to degrade, or the propellant usage exceeds the total propellant mass. A value of FOS = 1.5 (i. e., 50% larger dispersions than those listed in Table 4.5) proved to be the limit. To give a more direct idea on the dispersions for FOS = 1.5, Table 4.7 provides the actual statistics of the dispersions (not the parameters themselves) that happened in the simulations. In particular, it shows that the very

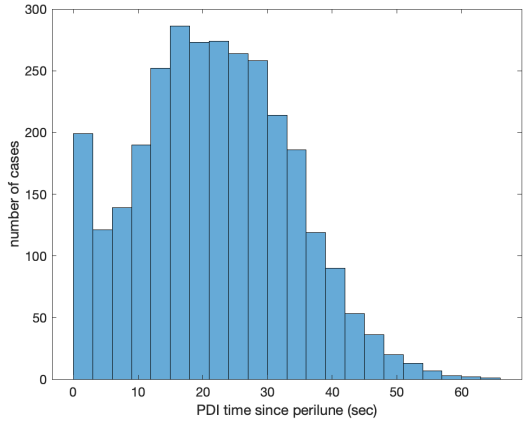

Figure 4.13. Powered descent initiation times of 3000 lunar powered descent Monte Carlo simulation runs with a factor of safety = 1.0.

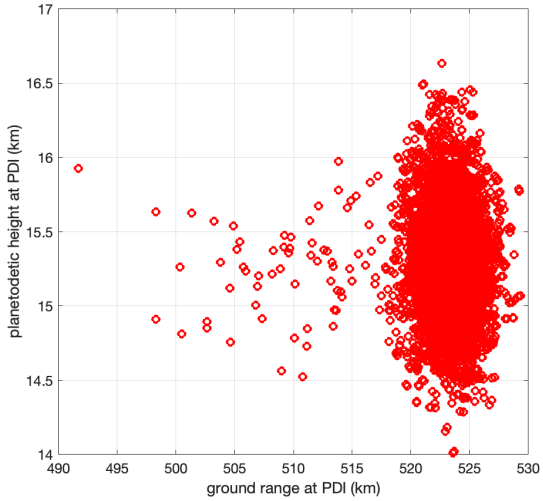

Figure 4.14. Planetodetic height and ground range at powered descent initiation for 3000 lunar powered descent Monte Carlo simulation runs with a factor of safety = 1.0.

significant maximum sizes of the dispersions. These perilune dispersions will necessarily cause PDI condition dispersions. Figures 4.17 and 4.18 show for instance that the PDI ground range and crossrange had even wider spread than in Figures 4.14 and 4.15. The spread of the PDI times since perilune among the 3000 dispersed trajectory is depicted in Figure 4.19. In contrast to Figure 4.13, almost 3 times more cases started the PDI right at

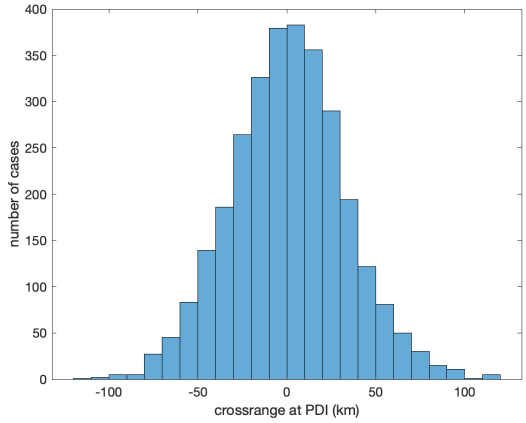

Figure 4.15. Crossrange at powered descent initiation for 3000 lunar powered descent Monte Carlo simulation runs with a factor of safety = 1.0.

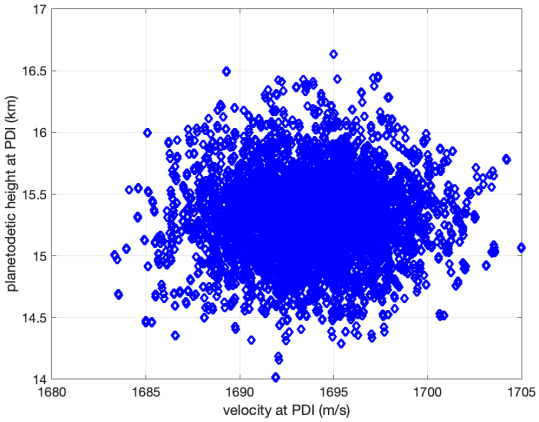

Figure 4.16. Planetodetic height and relative velocity at powered descent initiation for 3000 lunar powered descent Monte Carlo simulation runs with a factor of safety = 1.0.

perilune (where the time since perilune is zero). This is a consequence of the 50% larger dispersions in the perilune ground range in the minus direction (shorter ground ranges) than with FOS = 1.0. As the perilune location moves closer to the landing site, the PDI would have to occur right away in order to still landing at the same designated site.

Table 4.7. Statistics of 3000 lunar powered descent Monte Carlo simulation runs with a factor of safety = 1.5.

Parameters	Mean	Standard Deviation	Minimum	Maximum
Touchdown Miss (m)	4.24E-05	8.57E-05	7.86E-06	1.40E-00
Touchdown Velocity (m/s)	9.92E-01	3.55E-02	8.46E-01	1.10E+00
Touchdown Flight Path Angle (deg)	-9.00E+01	5.98E-02	-9.00E+01	-8.91E+01
Touchdown Pitch Angle (deg)	8.99E+01	2.65E-00	8.59E+01	9.00E+01
Propellant usage (kg)	7.22E+03	1.23E+02	7.10E+03	8.23E+03
Duration of Powered Descent (s)	6.80E+02	1.11E+00	6.77E+02	6.84E+02

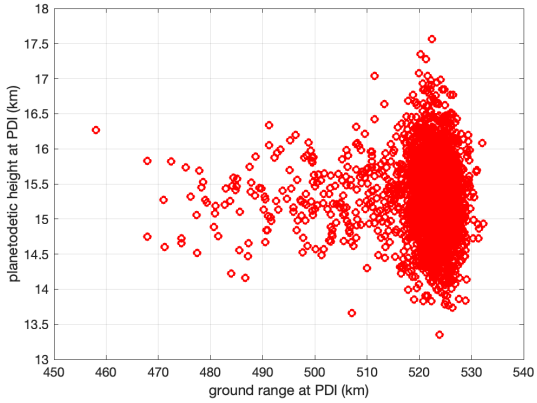

Figure 4.17. Planetodetic height and ground range at powered descent initiation for 3000 lunar powered descent Monte Carlo simulation runs with a factor of safety = 1.5.

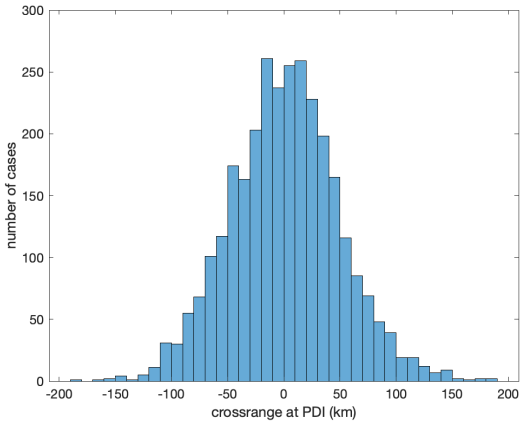

Figure 4.18. Crossrange at powered descent initiation for 3000 lunar powered Descent Monte Carlo Simulation Runs with a Factor of Safety = 1.5.

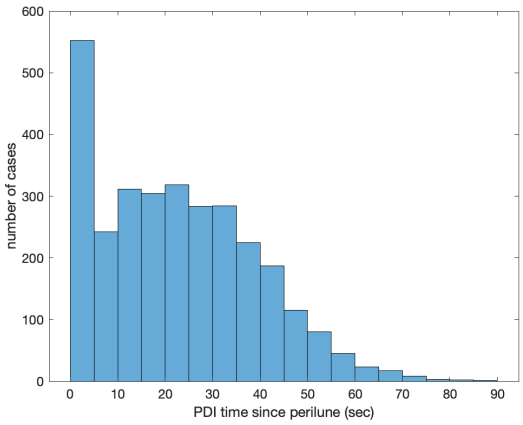

Figure 4.19. Powered descent initiation times of 3000 lunar powered descent Monte Carlo simulation runs with a factor of safety = 1.5.

4.8 Summary

In this section, the powered descent guidance method called FP^{2}DG is applied to a lunar landing mission for the first time, offering a wide range of flexibility in trajectory shaping and fuel consumption. Nominal and parametric studies demonstrate the uniform behavior of the algorithm when different tuning parameters are applied. Through the employment of an adaptive PDI logic developed for Mars missions, it was proven that the logic remains applicable for lunar landing. The inclusion of the PDI logic demonstrates the importance of selecting an appropriate PDI condition in the success of a mission and prove that nearly optimal fuel consumption can be achieved by selecting an appropriate PDI point. Furthermore, unlike APDG or E-Guidance, it was revealed that without additional requirements on trajectory shaping, a single phase for the entire powered descent is sufficient. FP^{2}DG was tested with deterministic and Monte Carlo simulations, demonstrating the high accuracy, robustness, and fuel performance for crewed lunar landing.

Chapter 4, in full, is a reprint of the material as it appears in Powered Descent Guidance for a Crewed Lunar Landing Mission, 2020. Sandoval, Sergio; Lu, Ping. The dissertation author was the primary investigator and author of this paper.

Chapter 5

Abort Guidance during Lunar Powered Descent

5.1 Introduction

In a crewed space mission the ability to abort throughout all the mission phases has been an important requirement since the Apollo program [79]. For a crewed lunar landing mission a particularly challenging phase for abort is in powered descent. In powered descent the abort would be for the lander to stop descent, turn around, and ascend into a pericynthion orbit clear of any mountains on the Moon, and then rendezvous with the rescue spacecraft [79, 80]. It is particularly challenging because abort in this phase necessitates aggressive maneuvers that in most cases must reverse the direction of the vertical motion before the abort, and insertion into the specified orbit must be reliably achieved from a wide range of possible initial conditions that are likely far from a typical initial condition for ascent flight.

In a crewed space mission the ability to abort throughout all the mission phases has been an important requirement since the Apollo program [79]. For a crewed lunar landing mission a particularly challenging phase for abort is in powered descent. In powered

descent the abort would be for the lander to stop descent, turn around, and ascend into a pericynthion orbit clear of any mountains on the Moon, and then rendezvous with the rescue spacecraft [79, 80]. It is particularly challenging because abort in this phase necessitates aggressive maneuvers that in most cases must reverse the direction of the vertical motion before the abort, and insertion into the specified orbit must be reliably achieved from a wide range of possible initial conditions that are likely far from a typical initial condition for ascent flight.

A problem that has not been considered for some years has been uncovered as part of this investigation. The reason for this is that if a completely automatic and reliable guidance is desired, it should encompass every aspect of the mission, including an emergency. In this section, the first fully automatic abort guidance sequence for a lunar landing mission is presented. This approach is not only relevant for being the first fully autonomous guidance sequence, but also obtains a solution that is fuel-optimal from the beginning to the end of powered descent.

5.2 Guidance Problem

In a Cartesian coordinate system with the origin at the center of the Moon, the three-dimensional point-mass equations of motion for a rocket-powered vehicle can be written as:

$$\dot{\boldsymbol{r}} = \boldsymbol{V} \tag{5.1}$$

$$\dot{\boldsymbol{V}} = \boldsymbol{g}(\boldsymbol{r}) + \frac{T}{m(t)}\mathbf{1}_T(t) \tag{5.2}$$

$$\dot{m} = -\frac{T}{v_{ex}} \tag{5.3}$$

$$0 \leq T(t) \leq T_{max} \tag{5.4}$$

The rocket engine thrust has a magnitude T and $\mathbf{1}_T$ is the *unit* vector that defines the thrust direction. The direction of $\mathbf{1}_T$ generally changes with time, and T is allowed to vary as well, subject to the prescribed upper bound limit T_{max}. The effective exhaust velocity of the rocket engine v_{ex} is considered a constant. The vectors $\boldsymbol{r} \in R^3$ and $\boldsymbol{V} \in R^3$ are the position and velocity vector of the vehicle with the current mass m. To capture the effects of the changing direction of the gravitational force in problems with relatively long flight distances, a central gravitational acceleration model $\boldsymbol{g} = -\mu\boldsymbol{r}/R_0^3$ is used where μ is the gravitational parameter of the Moon, and R_0 is the equatorial radius of the Moon. Clearly this is an approximation to the Newtonian gravity $\boldsymbol{g} = -\mu\boldsymbol{r}/\|\boldsymbol{r}\|^3$. The powered guidance problem is to determine $\mathbf{1}_T$, T and the burn time to meet the required targeting condition and optimized a performance index when applicable.

5.3 Nominal Crewed Lunar Landing Mission

In an abort scenario, the first instinct is to start the ascent towards a safe orbit immediately, regardless of the current state of the vehicle. This belief stems from the

idea that an instantaneous evacuation of the vehicle is necessary to keep astronauts safe. However, it is important to recognize that the conditions of the vehicle during powered descent can render starting the abort ascent immediately a potentially risky proposition, especially late in descent, where the danger of colliding with the ground exists. we will demonstrate such possibilities through investigation in this paper.

To ensure safe and fuel-efficient abort, an automated two-phase powered-descent-abort guidance strategy is developed in this work [90]. The first phase is a pull-up phase where the vehicle maneuvers to stop descending and achieve a initial favorable state for ascent that assures ground clearance during ascent. The second phase is fuel-optimal ascent into the specified orbit. This guidance strategy and the target pericynthion orbit remain the same for abort throughout the entire powered descent trajectory, greatly simplifying the implementation and guidance logic. Figure 5.1 illustrates the concept of operations for this powered-descent-abort strategy.

The fuel-optimal guidance is performed by the algorithm in Lu [103], dubbed Universal Powered Guidance for Ascent (UPG+A). It is an indirect-method based algorithm that solves the 3-dimensional fuel-optimal ascent problem quickly and reliably. To allow flexibility in the orbital insertion point of the abort ascent, depending on the condition of abort along the powered descent trajectory, the deployed orbital insertion constraints only specify the shape, size and orientation of the pericynthion orbit, but not the actual insertion point into the orbit (sometimes known as "free-attachment-point"). This freedom however produces a phenomenon that there may be two local optimal solutions for the fuel-optimal ascent problem [108]. In this work this issue is carefully investigated to

provide a clear understanding that the abort ascent trajectory by the proposed guidance strategy is always safe and satisfies accurately the orbital insertion requirements.

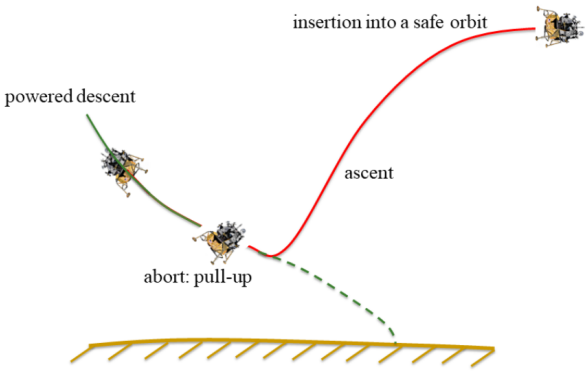

Figure 5.1. Concept of operations for two-phase abort strategy during lunar powered descent.

In the rest of this investigation, the abort guidance problem during powered descent is formulated; the two-phase abort guidance strategy is supported by the development of fuel-efficient pull-up guidance laws, and introduction of the fuel-optimal ascent guidance algorithm. The fuel-optimal ascent solution is carefully analyzed to gain a full understanding, and its validity is verified by an independent direct-method. End-to-end Monte Carlo simulations for abort throughout the powered descent trajectory for a lunar landing mission at the South Pole of the Moon are provided to demonstrate the robustness and effectiveness of the guidance approach.

The vehicle and mission are the same as described in Section 4. For this section, the descent propulsion system (DPS) is assumed to be healthy and available for an abort. The guidance abort approach described in this paper however is also applicable to an abort with only the ascent stage as well. The combined fuel in the descent and ascent stages is assumed to be available for abort in assessing abort feasibility. The descent stage engine of

the LM has a maximum thrust of 45,000 N and a specific impulse of 311 sec. The descent condition starts at the perilune of a 60 nm x 50,000 ft descent orbit [78]. The complete set of initial conditions are given in Table 4.1 [109]. All the 3DOF simulation results in this section are obtained by closed-loop simulations where the guidance commands are updated at a rate of 2 Hz. The Moon is modeled as an ellipsoid and self-rotation of the Moon is considered. Perfect navigation information is assumed. Figure 5.2 shows the ground track of the landing trajectory from the perilune of the descent orbit to touchdown at the South Pole.

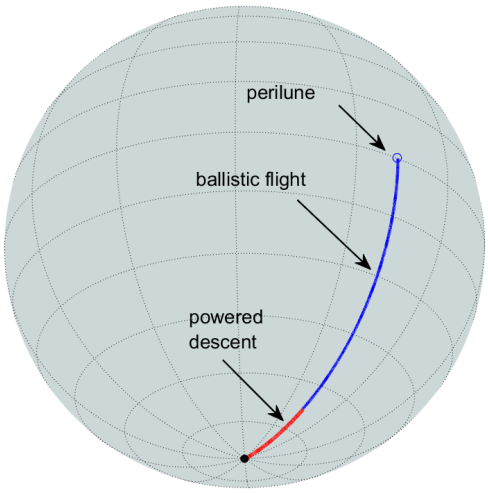

Figure 5.2. Nominal ground track for landing at the south pole of the Moon.

$$\bar{\boldsymbol{r}}' = \bar{\boldsymbol{V}} \tag{5.5}$$

$$\bar{\boldsymbol{V}}' = -\frac{1}{\|\bar{\boldsymbol{r}}\|^3}\bar{\boldsymbol{r}} + \frac{T}{m(t)g_0}\mathbf{1}_T(t) \tag{5.6}$$

where the prime represents the differentiation with respect to the dimensionless

time $\tau = t/t_{scale}$, $\bar{\boldsymbol{r}} = \boldsymbol{r}/r_{scale}$ and $\bar{\boldsymbol{V}} = \boldsymbol{V}/V_{scale}$.

5.4 Direct-Abort Guidance Approach

When it becomes necessarily to abort the landing mission, the lander is to fly into a 10 km $\times$ 150 km pericynthion orbit at an inclination of 90 deg. The perilune altitude of 10 km of this orbit will clear off any mountains on the Moon [80]. The apolune altitude and inclination may be determined by the phasing and rendezvous considerations with respect to the Command Module after the abort. In an abort scenario, the thrust magnitude T is always at full throttle, $T(t) = T_{max}$. Hence, the only control available is the thrust direction vector $\mathbf{1}_T(t)$, changing with time. In this section we briefly investigate the viability of the strategy of immediately commanding ascent to the target pericynthion orbit from the powered descent trajectory by an optimal guidance algorithm, as soon as abort is commenced.

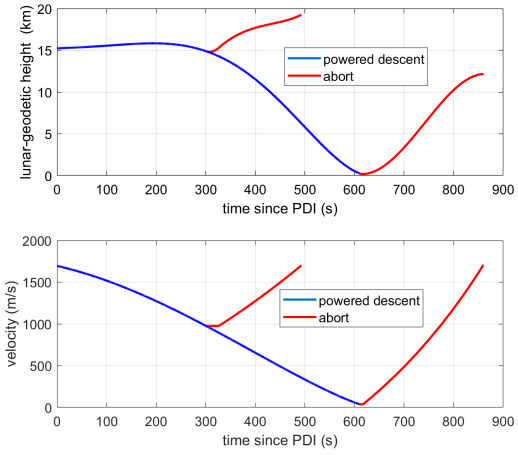

Figure 5.3. Two abort cases along the lunar powered descent trajectory: abort at 300 seconds since powered descent initiation (PDI), and 610 sec since PDI.

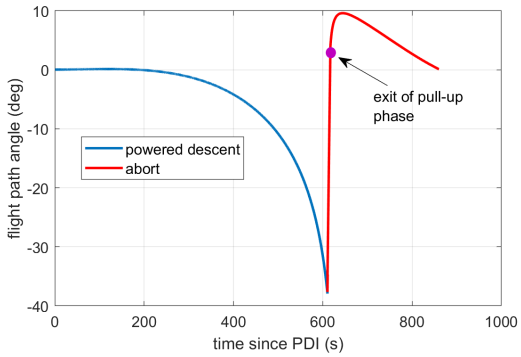

Figure 5.4. Flight path angle along a complete lunar descent trajectory that initiated abort at 610 seconds since powered descent initiation.

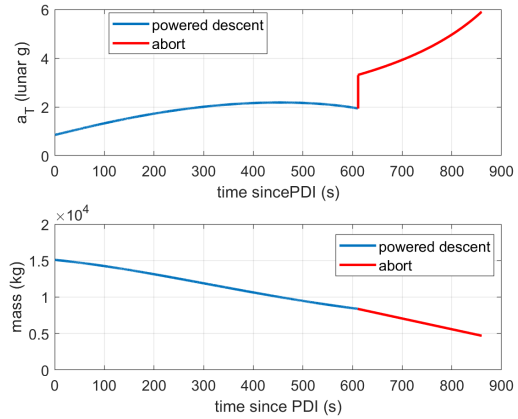

Figure 5.5. Thrust acceleration a_T and mass along a complete lunar descent trajectory that initiated abort at 610 seconds since powered descent initiation.

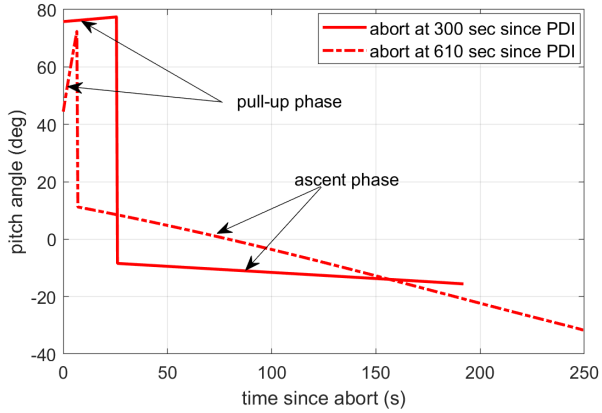

Figure 5.6. Pitch angle along two ascent trajectories from lunar abort at 300 and 610 seconds since powered descent initiation.

5.5 Abort Guidance Problem

The abort guidance problem is separated in two phases: a pull-up maneuver and an optimal ascent guidance phase. The pull-up maneuver is necessary to position the vehicle in a suitable direction to start optimal ascent. This is accomplished by the rapid change of a negative descent flight path angle towards a positive flight path angle ready for ascent. The fastest way to achieve these changes is by pointing the thrust vector in a direction perpendicular to the velocity vector of the vehicle. Three different guidance laws were developed in to complete this maneuver. The complete derivation of the pull-up maneuver can be found on Lu [90]. In this paper, a general ascent guidance problem is solved. The three-dimensional equations of motion for a vehicle with rocket propulsion defined as a point-mass system in a Cartesian coordinate system are defined as follows:

$$\dot{\boldsymbol{r}} = \boldsymbol{V} \tag{5.7}$$

$$\dot{\boldsymbol{V}} = \boldsymbol{g}(r) + \frac{T}{m(t)}\mathbf{1}_T \tag{5.8}$$

$$\dot{m} = -\frac{T}{g_0 I_{sp}} = -\frac{T}{v_{ex}} \tag{5.9}$$

The origin of the equations is at the center of the Moon. The equations describe the dynamics of the rocket as it moves around the Moon with $\boldsymbol{r} \in R^3$ and $\boldsymbol{V} \in R^3$ specifying the position and velocity, respectively.

In an abort scenario, the thrust magnitude T is always at full throttle, $T(t) = T_{max}$. Hence, the only control variable available is the thrust direction $\mathbf{1}_T(t)$, changing with time. For a small variation of the radius, as it is the case in the ascent problem, the following formulation for the gravitational acceleration of g can be applied [110]:

$$\boldsymbol{g}(r) = -\frac{\mu}{r^3}\boldsymbol{r} \tag{5.10}$$

The performance index is selected to minimize the propellant consumption of the vehicle at full throttle:

$$J = \int_{t_0}^{t_f} -\frac{T_{max}}{v_{ex}} dt = m(t_f) - m(t_0) \tag{5.11}$$

Where T_{max} is the constant maximum thrust of the rocket required to escape as fast as possible during an emergency and v_{ex} is the escape velocity of the rocket on Earth. This is equivalent to minimizing the propellant consumption during ascent.

A total of 7 algebraic equations are solved simultaneously by UPG+A to solve the ascent guidance problem. These equations represent the orbital insertion conditions for the final orbit and the corresponding reduced transversality conditions [111]. The following 3 equations specify the semi-major axis, eccentricity, and orbital inclination at the engine cut-off time t_f (which is free):

$$(\boldsymbol{r}_f \times \boldsymbol{V}_f)^T(\boldsymbol{r}_f \times \boldsymbol{V}_f) - \mu a^*(1 - e^{*2}) = 0 \tag{5.12}$$

$$\frac{\boldsymbol{V}_f^2}{2} - \frac{\mu}{\boldsymbol{r}_f} + \frac{\mu}{2a^*} = 0 \tag{5.13}$$

$$\mathbf{1}_z^T(\boldsymbol{r}_f \times \boldsymbol{V}_f) - |\boldsymbol{r}_f \times \boldsymbol{V}_f| \cos i^* = 0 \tag{5.14}$$

The final altitude and velocity vectors to be found by the optimization algorithm are represented by r_f and V_f, with their norms $\boldsymbol{r}_f = ||\boldsymbol{r}_f||$ and $\boldsymbol{V}_f = ||\boldsymbol{V}_f||$, respectively. The prescribed values of semi-major axis, eccentricity, and inclination for the final orbit are defined by a^*, $e^* \neq 0$, and $i^* \neq 0$. The vector 1_z is unit vector parallel to the polar axis of the Moon pointing towards the North. The orbital conditions selected correspond to a free-attachment-point case, where the final position and velocity of the spacecraft is not specified. It is the duty of the algorithm to find the best position and velocity for orbital insertion.

The 3 transversality conditions required to solve the indirect-method problem are related to the 3 free orbital elements of the problem that are argument of perilune, longitude of the ascending node and true anomaly at the insertion point [111]:

$$(\boldsymbol{p}_{r_f} \times \boldsymbol{r}_f + \boldsymbol{p}_{V_f} \times \boldsymbol{V}_f)^T(\boldsymbol{r}_f \times \boldsymbol{V}_f) = 0 \tag{5.15}$$

$$(\boldsymbol{p}_{r_f} \times \boldsymbol{r}_f + \boldsymbol{p}_{V_f} \times \boldsymbol{V}_f)^T\mathbf{1}_z = 0 \tag{5.16}$$

$$\boldsymbol{p}_{r_f}^T \boldsymbol{V}_f - \frac{\mu}{r_f^3} \boldsymbol{p}_{V_f}^T \boldsymbol{r}_f = 0 \tag{5.17}$$

In these equations, the costate vectors for radius and velocity at the final time t_f in the optimal ascent problem are $\boldsymbol{p}_{r_f}$ and $\boldsymbol{p}_{V_f}$. A final transversality condition at t_f related to the Hamiltonian for free-time optimal control problems completes the set of 7 algebraic equations that UPG+A needs to solve [111]:

$$\boldsymbol{p}_{r_f}^T \boldsymbol{V}_f - \mu \boldsymbol{p}_{V_f}^T \boldsymbol{r}_f + T_{max} \frac{||\boldsymbol{p}_{V_f}||}{m(t_f)} - 1 = 0 \tag{5.18}$$

The complete set of equations to solve the optimal ascent problem with the indirect-method of optimal control are (5.12) - (5.18). Solving the problem with the direct-method of optimal control only requires the orbital insertion conditions given by equations (5.12)-(5.14).

It is important to recognize that the equations shown above are in dimensional form. In numerical optimization, scaling optimization variables appropriately contributes to the efficiency of the algorithm [112]. Variables with similar orders of magnitude result in faster convergence. In this investigation, scaling played an important role in the implementation the ascent problem using the direct-method of optimal control, where the algorithm takes longer to converge. Besides longer simulation time, incorrect scaling also caused convergence issues in some cases. One way to accomplish this is by nondimensionalizing the equations required to solve the optimal ascent problem. A common approach is to normalize the distance by the equatorial radius of the planet, velocity by $\sqrt{g_0 R_{eq}}$, and

time with $\sqrt{R_{eq}/g_0}$ [103]. The complete set of normalized equations can be found on Lu [103].

5.5.1 Optimal Ascent Guidance

Ascent guidance in this paper is accomplished by the the UPG+A algorithm [103]. In this subsection UPG+A is briefly reviewed. The reader is referred to Lu [103] and Lu [22] for algorithmic details. UPG+A solves the optimal control problem subject to the dynamics in Equations (5.1)–(5.3) and with a performance index of minimizing the propellant consumption

$$J = \int_{t_0}^{t_f} [-T(t)/v_{ex}]\, dt = m(t_f) - m(t_0) \tag{5.19}$$

where t_0 is the time when the ascent phase starts, and t_f is free. Since the thrust T is fixed at the maximum value, the propellant-optimal problem is the same as the time-optimal problem. While UPG+A allows any combinations of orbital insertion conditions, the final constraints for the optimal abort-ascent problem are the orbital insertion conditions into the target abort orbit specified by the given semi-major axis a^*, eccentricity $e^* \neq 0$, and orbital inclination $i^* \neq 0$. In terms of the final radius and velocity vectors $\boldsymbol{r}_f = \boldsymbol{r}(t_f)$ and $\boldsymbol{V}_f = \boldsymbol{V}(t_f)$ at the engine cut-off time t_f, these terminal constraints may be expressed in the following form:

$$(\boldsymbol{r}_f \times \boldsymbol{V}_f)^T(\boldsymbol{r}_f \times \boldsymbol{V}_f) - \mu a^*(1 - e^{*2}) = 0 \tag{5.20}$$

$$V_f^2/2 - \mu/r_f + \mu/2a^* = 0 \tag{5.21}$$

$$\mathbf{1}_z^T(\boldsymbol{r}_f \times \boldsymbol{V}_f) - \|\boldsymbol{r}_f \times \boldsymbol{V}_f\| \cos i^* = 0 \tag{5.22}$$

where $r_f = \|\boldsymbol{r}_f\|$, $V_f = \|\boldsymbol{V}_f\|$, and $\mathbf{1}_z$ is a unit vector parallel to the polar axis of the Moon (pointing to the North). Note that the insertion point into the specified orbit is not specified (not at a particular point of the orbit, e.g., the perilune), but is left for the guidance algorithm to optimize. This is a so-called free-attachment point case. Not limiting the orbital insertion to occur at a particular point leaves much welcomed flexibility for the ascent trajectory in the already highly stressful situation in a powered-descent-abort. Depending on when abort happens during powered descent, the freedom to insert into the specified orbit at a most suitable point for the case is important, as will be seen later.

Among the 6 classical orbital elements, the 3 that are free in this case are the argument of perilune, longitude of the ascending node, and true anomaly at insertion. The corresponding *reduced transversality conditions* are then [113]:

$$(\boldsymbol{p}_{r_f} \times \boldsymbol{r}_f + \boldsymbol{p}_{V_f} \times \boldsymbol{V}_f)^T(\boldsymbol{r}_f \times \boldsymbol{V}_f) = 0 \tag{5.23}$$

$$(\boldsymbol{p}_{r_f} \times \boldsymbol{r}_f + \boldsymbol{p}_{V_f} \times \boldsymbol{V}_f)^T\mathbf{1}_z = 0 \tag{5.24}$$

$$\boldsymbol{p}_{r_f}^T\boldsymbol{V}_f - \frac{\mu}{r_f^3}\boldsymbol{p}_{V_f}^T\boldsymbol{r}_f = 0 \tag{5.25}$$

where $\boldsymbol{p}_{V_f}$ and $\boldsymbol{p}_{r_f}$ are the velocity and radius costate vectors at the final time t_f in the optimal ascent problem [22]. The last condition is from the transversality condition on the Hamiltonian at t_f for free-time optimal control problems [103]:

$$\boldsymbol{p}_{r_f}^T \boldsymbol{V}_f - \mu \boldsymbol{p}_{V_f}^T \boldsymbol{r}_f + T_{max} \|\boldsymbol{p}_{V_f}\| / m(t_f) - 1 = 0 \tag{5.26}$$

In UPG+A, the costate vectors $\boldsymbol{p}_r(t)$ and $\boldsymbol{p}_V(t)$ have closed-form solutions as functions of time t and the initial costate $\boldsymbol{p}_{r_0}$ and $\boldsymbol{p}_{V_0}$. With given initial state at t_0 and a piecewise-constant thrust profile (in this case it is all constant) the solution to the state equations can also be approximated by numerical quadratures in closed form as the functions of $\boldsymbol{p}_{r_0}$ and $\boldsymbol{p}_{V_0}$. See References [103] and [22] for detail. The solution to the optimal ascent problem is then determined by the 7 unknowns $\boldsymbol{p}_{r_0}$, $\boldsymbol{p}_{V_0}$ and t_f. Equations (5.20)–(5.26) constitute the 7 constraints that must be satisfied by the 7 unknowns. UPG+A solves this zero-finding problem problem quickly and reliably. The solution provides the optimal command for $\mathbf{1}_T(t)$ at the current time t as

$$\mathbf{1}_T(t) = \boldsymbol{p}_V(t) / \|\boldsymbol{p}_V(t)\| \tag{5.27}$$

In the next guidance cycle, the problem is resolved with the actual trajectory state at the time as the initial condition, and the updated command for $\mathbf{1}_T$ and the time-to-insertion are obtained. In this way, closed-loop ascent guidance is effectively

achieved by UPG+A. The orbital insertion conditions are typically attained with high accuracy by the guidance (thus there is no need for targeting error budget for guidance).

It should be noted that even though UPG+A is used for descent-abort guidance in this paper, the same algorithm/software is well suited for nominal lunar ascent. Hence no added cost or software complexity would incur associated with using the same software for abort guidance if it is already implemented for lunar ascent. Furthermore, since the algorithm is model based, the same software/program would be used regardless of whether the abort is performed with the descent-stage engine or ascent stage engine.

5.5.2 Direct-Abort Solutions

During the powered descent, at any particular instant when abort is commenced, UPG+A is deployed immediately to guide the lander to ascent to the target orbit. In Figure 5.7 a number of closed-loop guided ascent trajectories are plotted that correspond to abort at different times after PDI which signifies the start of the powered descent. These abort instants are at a 100-sec increment after PDI until 600 sec after PDI. Notice that the ascent trajectories until around 300 seconds after PDI insert into the target orbit at a higher altitude than the perilune altitude (about 12 km in geodetic altitude). This is a manifestation of the fact that UPG+A finds the optimal insertion altitude to take advantage of free-attachment-point in the orbital insertion conditions. After 300 sec since PDI, the abort ascent trajectories all enter the target orbit at the perilune, again optimal in these cases.

To show the validity of the solutions by UPG+A, the optimal ascent trajectories from the closed-loop simulations guided by UPG+A are verified by an independent software

named OpenMDAO [114]. OpenMDAO is an open-source optimization framework and a platform to building new analysis tools for faster, more stable design optimization with tight integration of high-fidelity analyses into system level models. A functionality of OpenMDAO is to solve the trajectory optimization problem by the direct-method.

The same abort-ascent problems at different times since PDI are also solved by OpenMDAO to minimize the fuel consumption (or equivalently, the flight time). Plotted in Figure 5.7 in green dashed line are also the ascent trajectories obtained by OpenMDAO. In all but one case the trajectories are practically the same in the scale of the figure. The only case where some relative small differences are visible is the case of abort at 600 sec since PDI. This is the latest abort among all the cases (and the most challenging one). Still, considering that the UPG+A trajectory is the result of closed-loop simulation, and the solution by OpenMDAO is an open-loop trajectory, the differences are quite reasonable. Table 5.1 compares the propellant consumption between the two groups of the trajectories. The differences are in the range of $0.1\% - 1.7\%$. Again, these small discrepancies can be attributed predominantly to the differences between the closed-loop simulated trajectories under UPG+A and open-loop solutions from OpenMDAO.

Table 5.1. Propellant consumption comparison between UPG+A closed-loop solutions and OpenMDAO open-loop solutions.

Abort Time since PDI (sec)	Propellant Consumption (kg)	
	UPG+A guided	OpenMDAO
100	808.58	823.21
200	1709.74	1723.94
300	2546.47	2556.99
400	3224.36	3234.16
500	3619.76	3623.54
600	3665.82	3681.30

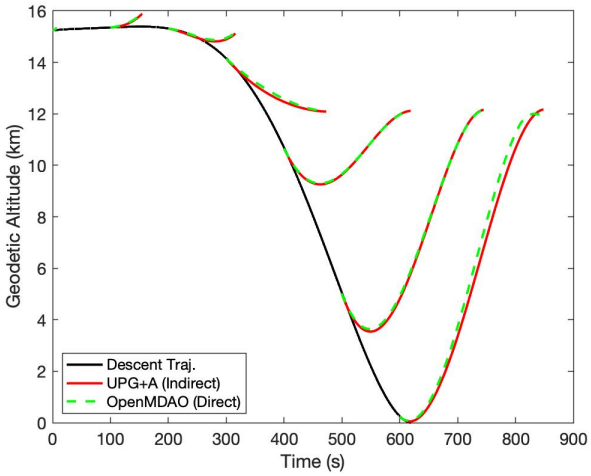

Figure 5.7. Abort trajectories during lunar powered descent from closed-loop simulations guided by UPG+A and open-loop solutions from OpenMDAO.

So far the tests seem to suggest that direct-abort is viable. But a closer examination of the ascent trajectories in late abort cases reveals a critical issue: the ascent trajectories in some late abort cases risk to collide with the lunar surface before ascending to the orbit. This problem can get significantly worse if abort takes place further late into the powered descent. Figure 5.9 zooms in the final portion of the powered descent phase and illustrates several direct-abort trajectories from 580 sec to 620 sec since PDI. It can be seen that some of the abort-ascent trajectories indeed intersect the ground.

To eliminate the risk of colliding with the lunar surface in abort, a ground clearance constraint may be imposed in UPG+A. But this will significantly complicates the algorithm and adversely affect the robustness of the algorithm. A simpler, fail safe, and propellant-efficient strategy is necessary to pull the lander out of descent and enable fuel-optimal ascent into the target orbit. Such a necessity motivates the two-phase guidance strategy developed in the next section.

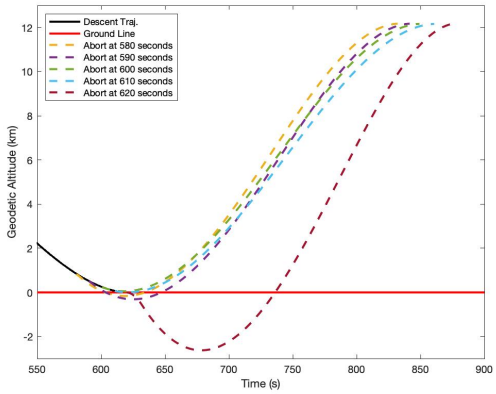

Figure 5.8. Late Abort Solutions using direct abort.

Figure 5.9. Single-phase (direct) abort solutions for late abort cases during lunar powered descent.

5.6 Two-Phase Abort Guidance Strategy

To ensure a safe and propellant efficient abort trajectory once abort is commanded during lunar powered descent, a two-phase abort strategy is proposed. The abort problem is separated in two phases: a pull-up maneuver and an optimal ascent guidance phase. The pull-up maneuver is an additional segment of abort used to rotate the initial velocity vector and position the vehicle in a suitable direction to start optimal ascent. This is accomplished by the rapid change of a negative descent flight path angle towards a positive flight path angle ready for ascent. After the completion of the pull-up maneuver, the optimal ascent guidance (UPG+A) steers the vehicle from the end condition of the pull-up phase to the insertion into the abort orbit.

5.6.1 Pull-Up Guidance Laws

The pull-up maneuver is intended to turn around the velocity vector of the vehicle quickly during powered descent in preparation for ascent into a safe pericynthion orbit.

Thus the pull up is characterized by the change of the flight path angle from a negative value during descent to a positive targeted value at the end of the pull-up phase. The guidance strategy for this phase should focus on changing the direction of the velocity vector from a negative flight path angle during descent to a positive targeted value without significantly changing the velocity magnitude. The requirement on not causing large changes in the velocity magnitude is important because a way to change (increase) the flight path angle quickly is to reduce the velocity, which makes changing the direction of the velocity vector easier. But a lower velocity after the pull-up means more propellant is needed to increase the velocity for orbital insertion. On the other hand the velocity magnitude should not be increased significantly either in the pull up phase because the direction of a velocity vector with a larger magnitude is more difficult to change. Therefore, objectives of the pull-up guidance are

1. Increase the flight path angle quickly from its initial (likely negative) value to a specified positive value in getting ready for ascent into the orbit

2. Cause little or no change in the magnitude of the velocity

The derivations of the following guidance laws are motivated by these two objectives. The engine thrust is always at full throttle for all the cases. The guidance laws will then determine the direction of the thrust vector.

Pull-Up Guidance Law I

In this case the direction of the thrust vector is pointed upward in the vertical plane (the plane formed by the position vector $\boldsymbol{r}$ and velocity vector $\boldsymbol{V}$) and is perpendicularly

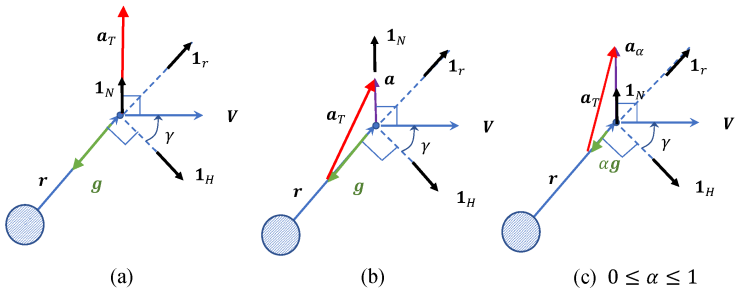

Figure 5.10. Determination of the thrust acceleration vector $\boldsymbol{a}_T$ for pull-up maneuver: (a) $\boldsymbol{a}_T$ is perpendicular to the velocity vector $\boldsymbol{V}$.; (b) $\boldsymbol{a} = \boldsymbol{g} + \boldsymbol{a}_T$ is perpendicular to $\boldsymbol{V}$.; (c) $\boldsymbol{a}_\alpha = \alpha \boldsymbol{g} + \boldsymbol{a}_T$ is perpendicular to $\boldsymbol{V}$.

to $\boldsymbol{V}$. See Figure 5.10(a). In this case where the full thrust vector is applied to change the direction of $\boldsymbol{V}$.

Define the unit vectors

$$\mathbf{1}_r = \boldsymbol{r}/\|\boldsymbol{r}\|, \ \mathbf{1}_h = \boldsymbol{r} \times \boldsymbol{V}/\|\boldsymbol{r} \times \boldsymbol{V}\|, \ \mathbf{1}_H = \mathbf{1}_h \times \mathbf{1}_r \tag{5.28}$$

where $\mathbf{1}_H$ is the unit vector that defines the local horizontal direction in the vertical plane (see Figure 5.10). Let γ be the flight path angle. Then the unit vector perpendicular to $\boldsymbol{V}$ and pointing upward is (cf. Figure 5.10)

$$\mathbf{1}_N = \cos\gamma \mathbf{1}_r - \sin\gamma \mathbf{1}_H \tag{5.29}$$

The unit vector that defines the direction of the commanded thrust acceleration vector $\boldsymbol{a}_T$ then is given by the guidance law

$$\mathbf{1}_T = \mathbf{1}_N = \cos\gamma \mathbf{1}_r - \sin\gamma \mathbf{1}_H \tag{5.30}$$

The magnitude of $\boldsymbol{a}_T$ is $T_{max}/m(t)$ at the current time t.

Pull-Up Guidance Law II

The direction of $\boldsymbol{a}_T$ is chosen so that the *total* acceleration vector $\boldsymbol{a} = \boldsymbol{g} + \boldsymbol{a}_T$, where $\boldsymbol{a}_T = (T_{max}/m)\mathbf{1}_T$, is perpendicular to $\boldsymbol{V}$ and pointing upward, as illustrated by Figure 5.10(b). The application of the law of cosines to the triangle formed by the acceleration vectors $\boldsymbol{a}$, $\boldsymbol{g}$, and $\boldsymbol{a}_T$ in Figure 5.10(b) leads to

$$a^2 + (2g\cos\gamma)a + g^2 - a_T^2 = 0 \tag{5.31}$$

where $a = \|\boldsymbol{a}\|$, $g = \|\boldsymbol{g}\|$, and $a_T = \|\boldsymbol{a}_T\| = T_{max}/m(t)$. For $a_T > g$ (and $|\gamma| \leq \pi/2$) this quadratic equation in a always has just one positive real root which is given by

$$a = -g\cos\gamma + \sqrt{g^2\cos^2\gamma + a_T^2 - g^2} \tag{5.32}$$

Clearly in this case

$$\boldsymbol{a} = a\mathbf{1}_N \tag{5.33}$$

Thus, the commanded direction of the thrust acceleration vector is

$$\boldsymbol{a}_T = a_T\mathbf{1}_T = \boldsymbol{a} - \boldsymbol{g} \tag{5.34}$$

By using $\boldsymbol{g} = -g\mathbf{1}_r$, we have the guidance law for the thrust vector direction

$$\mathbf{1}_T = (g/a_T)\mathbf{1}_r + (a/a_T)\mathbf{1}_N \tag{5.35}$$

Because the total acceleration vector $\boldsymbol{a}$ is perpendicular to $\boldsymbol{V}$, the magnitude of the velocity vector will remain constant during the pull-up maneuver, as can be seen from the fact that

$$d\|\boldsymbol{V}\|/dt = \boldsymbol{V}^T\dot{\boldsymbol{V}}/\|\boldsymbol{V}\| = \boldsymbol{V}^T\boldsymbol{a}/\|\boldsymbol{V}\| = 0 \tag{5.36}$$

Pull-Up Guidance Law III

Here we develop a guidance law that is a more general form that includes both guidance laws I and II as special cases. For a specified constant α define an acceleration $\boldsymbol{a}_\alpha$

$$\boldsymbol{a}_\alpha = \alpha\boldsymbol{g} + \boldsymbol{a}_T, \quad 0 \leq \alpha \leq 1.0 \tag{5.37}$$

Again, $\|\boldsymbol{a}_T\| = a_T = T_{max}/m(t)$. The direction of $\boldsymbol{a}_T$ is chosen so that the direction of $\boldsymbol{a}_\alpha$ is in the direction of $\mathbf{1}_N$. See Fig. 5.10(c). Similar to the derivation in guidance law II, the law of cosines gives

$$a_\alpha = -\alpha g\cos\gamma + \sqrt{\alpha^2 g^2\cos^2\gamma + a_T^2 - \alpha^2 g^2} \tag{5.38}$$

where $a_\alpha = \|\boldsymbol{a}_\alpha\|$. The guidance law then is

$$\mathbf{1}_T = (\alpha g/a_T)\mathbf{1}_r + (a_\alpha/a_T)\mathbf{1}_N, \quad 0 \leq \alpha \leq 1.0 \tag{5.39}$$

Evidently, when $\alpha = 0$, Guidance Law III in (5.39) is the same as Guidance Law I in Equation (5.30); when $\alpha = 1.0$, Guidance Law III becomes Guidance Law II in Equation (5.35). Hence Guidance Law III may be regarded as a nonlinear interpolation of Guidance Laws I and II over α. The presence of α offers a flexibility to adjust the guidance law for different vehicles and missions. For the vehicle model used in this paper (that of Apollo 11 Lunar Module), there is little difference for any $\alpha \in [0, 1]$, α may have more pronounced influence in other cases (especially when the thrust-to-weight ratio is low). Note that guidance laws in Equations (5.30), (5.35), and (5.39) are closed-loop guidance laws because $\mathbf{1}_r$, $\mathbf{1}_N$, a and a_α are functions of the current state.

From Equations (5.29) and (5.39), it is clear that the pull-up guidance laws developed here (with any $\alpha \in [0, 1]$) do not command a vertical rise – the thrust direction always has a horizontal component in the $\mathbf{1}_H$ direction unless $\gamma = 0$. If the powered descent trajectory is steep, commanding a vertical rise would kill much of the velocity of the vehicle before re-building the velocity for ascent. An extreme scenario is where the powered descent is nearly vertical. The propellant penalty of commanding a vertical rise at the beginning of abort in such a case can be non-trivial in comparison to turning the velocity vector around by the pull-up guidance law in Equation (5.39) without reducing its magnitude.

Under the guidance law (5.39), the flight path angle of vehicle will start to increase, while the velocity changes little. The pull-up phase is terminated as soon as the flight path

angle reaches a prescribed targeting value of $\gamma_{end} > 0$. The attainment of the targeting condition by this simple guidance approach is guaranteed for any starting condition (that a powered descent trajectory can possibly have) and any γ_{end}, provided that the vehicle has a thrust-to-weight ratio greater than 1, a condition met by any lander. If the flight path angle is already greater or equal to γ_{end} at the start of pull-up, the pull-up phase is skipped, and the abort guidance directly enters the ascent phase. With the fuel optimal ascent guidance and the set of orbital insertion conditions for the subsequent ascent trajectory in Section 5.5.1, it is found that the combined propellant usage in pull-up and ascent phases is always close to the minimum when γ_{end} has a small value, regardless where in powered descent abort is initiated. Therefore, a positive constant γ_{end} may be used. It will be shown in Section 5.6.3 that γ_{end} has a noticeable effect in overall propellant consumption in early aborts.

5.6.2 Two-Phase Abort Solutions

The two-phase abort guidance resulted in successful abort trajectories along the entire powered descent trajectory. A set of abort cases throughout powered descent are plotted in blue solid line in Figure 5.11. The value of $\gamma_{end} = 3$ deg is used in the simulations. Also shown in Figure 5.11 are the abort trajectories in the same cases with direct-abort. Consistent with the results in direct-abort cases, the two-phase guidance still results in the spacecraft inserting into the target orbit at the perilune in late abort cases. However, as a result of the pull-up maneuver, in aborts between 0 and 400 seconds after PDI, the two-phase guidance strategy inserts the spacecraft into the orbit at an altitude higher than the perilune altitude, and also higher than the insertion altitudes of the direct-abort

trajectories, even though the spacecraft enters the same pericynthion orbit.

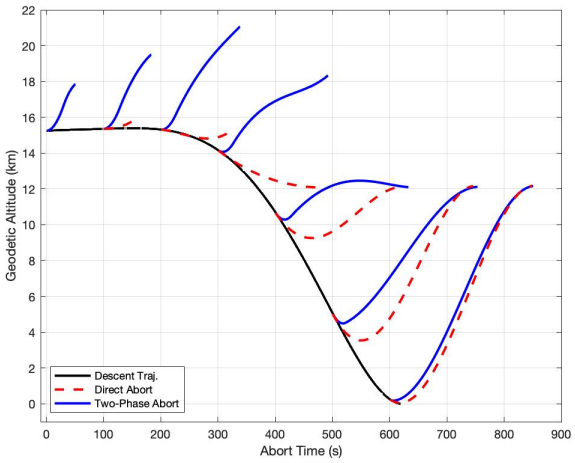

Figure 5.11. Altitude comparison between direct- and two-phase lunar abort solutions.

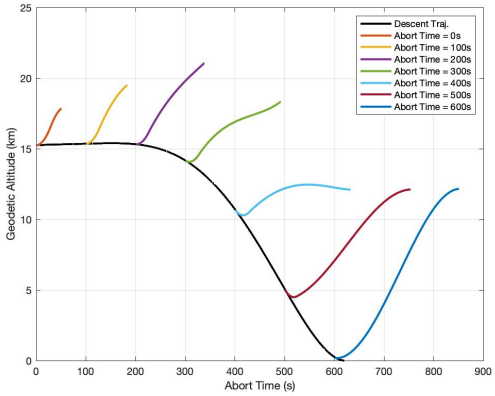

Figure 5.12. Two-phase abort solutions along powered descent trajectory.

The effectiveness of the pull-up maneuver in ensuring safety during late aborts are shown in Figure 5.13, where the same abort cases in Figure 5.9 are now guided by the two-phase strategy. All cases clear the ground, in a sharp contrast with direct-abort.

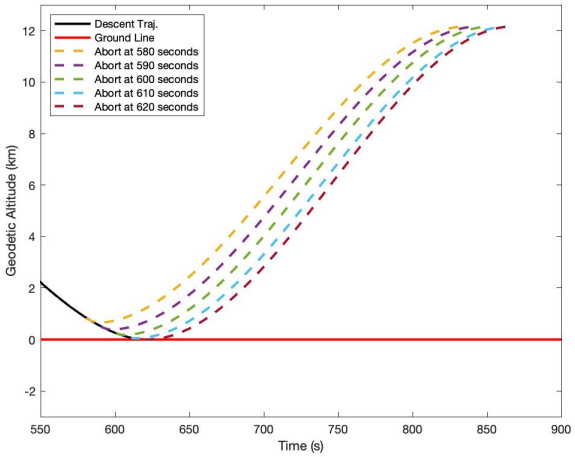

Figure 5.13. Two-phase abort solutions for late abort cases during lunar powered descent.

5.6.3 Comparing Propellant Consumption

Direct-abort under UPG+A is propellant optimal. The two-phase guidance is propellant optimal from the exit of pull-up to orbital insertion. But how does the total fuel consumption from both phases of the abort compare to the optimal value? The answer depends on the value of γ_{end}, the target flight path angle that defines the end of the pull-up maneuver. Table 5.2 summaries the propellant consumption for several abort cases taking place at points from early in powered descent to near touchdown with direct-abort and two-phase abort. Two different values of γ_{end} are used in the closed-loop simulations, 3.0 deg and 0.1 deg, respectively. For $\gamma_{end} = 3.0$ deg, the propellant usage by the two-phase guidance approach is noticeably higher than that by direct-abort for early aborts. But the difference shrinks as abort occurs later in powered descent, to the point of practically nonexistent toward the end.

On the other hand, if $\gamma_{end} = 0.1$ deg is used, late abort trajectories still clear the

Table 5.2. Propellant consumption comparison between single- (direct) and two-phase abort solutions

Abort Time (s)	Total Propellant Consumption (kg)		
	Direct-Abort	Two-Phase Abort ($\gamma_{end} = 3$ deg)	Two-Phase Abort ($\gamma_{end} = 0.1$ deg)
100	808.58	1209.95	820.76
200	1709.74	2021.44	1738.65
300	2546.47	2821.90	2632.29
400	3224.36	3420.66	3332.84
500	3619.76	3730.45	3703.49
600	3665.82	3687.72	3685.21

ground, and the propellant consumption by the two-phase abort guidance approach comes very close to the overall optimal values (by direct-abort) throughout the powered descent phase, as can be seen in Table 5.2. This is not a surprise though. Recall that the pull-up guidance law is developed with the realization that using the thrust vector to only change the direction of the velocity vector in pull-up phase should be fuel efficient. Here we have demonstrated that with an appropriate choice of γ_{end} (likely a small positive value), the overall propellant consumption of the two-phase guidance strategy is near optimal. Hence, the proposed two-phase guidance approach not only effectively addresses the ground clearance concerns, but also can be made achieve practically minimum propellant usage.

Figure 5.14 depicts the abort trajectories with $\gamma_{end} = 0.1$ deg and $\gamma_{end} = 3$ deg starting from the same conditions at a several points along the powered descent trajectory. In early aborts, and larger γ_{end} results in a higher orbital insertion altitude. But for late aborts, the effects of different values of γ_{end} gradually diminish, eventually to a negligible level. If necessary, a predefined table of γ_{end} as a function of the abort time since PDI may be loaded into the guidance system to provide a means for shaping the abort trajectory.

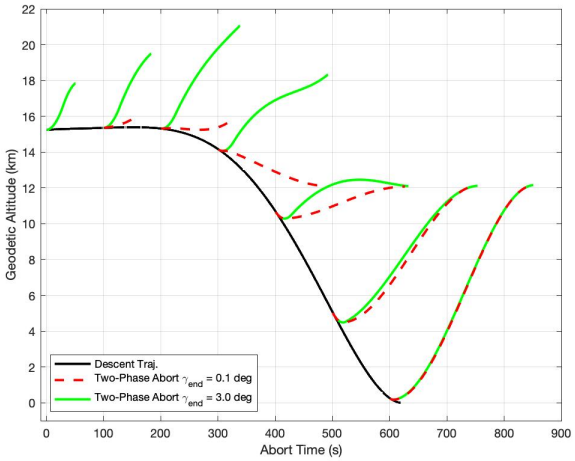

Figure 5.14. Ascent trajectory comparison for two-phase lunar abort with two different flight-path-angle settings γ_{end} in pull-up maneuver.

5.7 Monte Carlo Testing of Two-Phase Guidance

To gain a better assessment of the performance and reliability of the two-phase abort guidance method, Monte Carlo closed-loop simulations are performed. The initial condition of the powered descent trajectory is dispersed randomly, resulting different powered descent trajectory in each case. Furthermore, the initial mass of the vehicle and the actual engine thrust are also dispersed, and the actual values are not known to the guidance system system. The abort time is randomly chosen between 0 and 610 sec since PDI in each Monte Carlo simulation, signifying the fact that abort can happen at any moment throughout the powered descent. Table 5.3 shows the distributions and 3-sigma/min-max values of the dispersions. These values represent "nominal dispersions", and they correspond to a factor of safety (FOS) of 1.0. The FOS is essentially a scaling factor. At FOS of 2.0, all the 3-sigma values in Table 5.3 will be doubled (the range of variations of the abort time is not affected by FOS), FOS of 5.0 leads to 5 times as large

dispersions, and so on and so forth. Therefore a larger value of FOS stresses the guidance system more. All the dispersions except for the abort time are Gaussian with a zero mean. The abort time is dispersed as a uniform distribution to simulate the fact that abort can happen at any time during the powered descent.

Table 5.3. Dispersions and uncertainty values of 3000 Monte Carlo simulation runs of lunar abort guidance with a factor of safety = 1.0.

parameter	distribution	3-sigma (or [min, max])
PDI altitude (m)	zero-mean, Gaussian	100
PDI longitude (deg)	zero-mean, Gaussian	0.25
PDI latitude (deg)	zero-mean, Gaussian	0.25
PDI velocity (m/s)	zero-mean, Gaussian	3.3
PDI flight path angle (deg)	zero-mean, Gaussian	0.1
PDI azimuth angle (deg)	zero-mean, Gaussian	0.17
PDI mass (kg)	zero-mean, Gaussian	49.84
engine thrust (N)	zero-mean, Gaussian	450.0
abort time (s)	Uniform	$[0, 610]$

With the dispersions in Table 5.3, 3000 dispersed at runs at FOS = 1.0 were made under the proposed two-phase abort guidance method. Figure 5.15 shows the 3000 abort trajectories during powered descent. Table 5.4 lists statistics in the orbital insertion conditions, propellant usages, and ascent times of the 3000 trajectories. Note that the specified orbital insertion conditions are the eccentricity (0.0385), semi-major axis (1818.1 km) and inclination (90 deg) of the final orbit. Table 5.3 indicates that the specified final orbit was accurately achieved in all cases. On the other hand, the insertion altitude, velocity, and flight path angle are not specified and they are depend on where the ascent trajectory enters the target orbit (therefore the data in Table 5.3 on these quantities do not reflect any measure of accuracy). The statistics on propellant usage (or on the insertion mass), as compared to the propellant mass in Table 5.2 suggest that there was still propellant left at the orbital insertion, even in the worst case. Therefore, the vehicle

can successfully and safely abort throughout the powered descent.

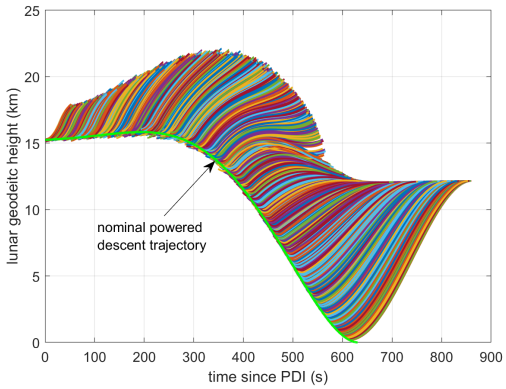

Figure 5.15. Abort trajectories for 3000 Monte Carlo simulation runs of lunar abort guidance with a factor of safety = 1.0.

Figure 5.16 shows the spread of the true anomalies at the orbital insertion along the 3000 trajectories. It can be seen that earlier aborts entered the target orbits after the perilune, with true anomaly as large as 30 deg; late aborts entered the target orbit pre-perilune with negative true anomalies. When the aborts occurred after 500 sec since PDI, the abort trajectories inserted right at perilune with a zero true anomaly. There are a few cases for abort at about 210 sec that appear to have out-of-pattern true anomalies. These cases will be investigated later in detail.

Table 5.4. Statistics of orbital insertion conditions in 3000 Monte Carlo simulation runs of lunar abort guidance with a factor of safety = 1.0.

parameter	mean	standard deviation	max	min
ascent time (s)	1.5283E+02	7.2254E+01	2.4315E+02	2.0748E+01
altitude (km)	1.4431E+01	3.9175E+00	2.0029E+01	1.0003E+01
velocity (m/s)	1.7020E+03	3.6722E+00	1.7062E+03	1.6967E+03
flight path angle(deg)	5.5749E-01	5.2055E-01	1.1383E+00	-8.9695E-01
eccentricity	3.8500E-02	1.9880E-06	3.8586E-02	3.8436E-02
semi-major axis (km)	1.8181E+03	3.7472E-03	1.8183E+03	1.8180E+03
inclination (deg)	9.0000E+01	0.0000E+00	9.0000E+01	9.0000E+01
propellant usage (kg)	2.2549E+03	1.0661E+03	3.5876E+03	3.0613E+02
insertion mass (kg)	9.1603E+03	3.0610E+03	1.4386E+04	4.6981E+03
abort time (s)	3.0698E+02	1.7438E+02	6.0987E+02	2.0829E-01

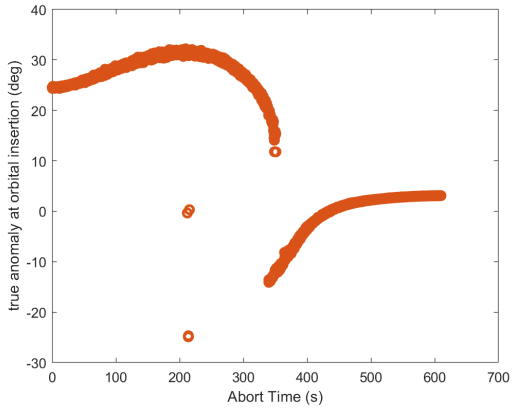

Figure 5.16. True anomaly at orbital insertion for 3000 Monte Carlo simulation runs of lunar abort guidance with a factor of safety = 1.0.

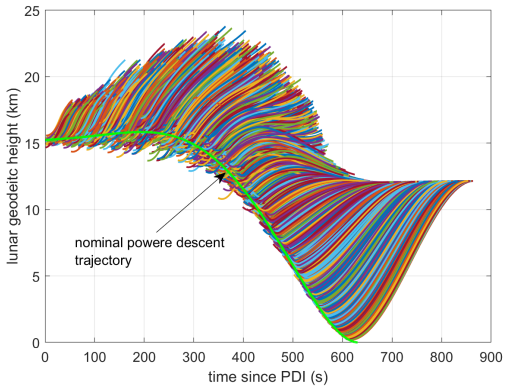

Figure 5.17. Abort trajectories for 3000 Monte Carlo simulation runs of lunar abort guidance with a factor of safety = 5.0.

Next, to really stress the abort guidance, 3000 Monte Carlo simulations were performed at FOS = 5.0, that is, with 5 times the dispersions in Table 5.3. Figure 5.17 shows the 3000 dispersed abort trajectories. The effects of significantly larger dispersions are clearly visible as compared to Fig. 5.15. The fact that many of the abort trajectories in Figure 5.17 started noticeably away from the nominal powered descent trajectory is because the actually dispersed powered descent trajectories (where the aborts started) were significantly off from the nominal powered descent trajectory at FOS of 5.0. In contrast to

Figure 5.15, Figure 5.17 also points to large spread of orbital insertion conditions due to the dispersions of 5 times compared at FOS = 1.0.

Table 5.5. Statistics of orbital insertion conditions in 3000 Monte Carlo simulation runs of lunar abort guidance with a factor of safety = 5.0.

parameter	mean	standard deviation	max	min
ascent time (s)	1.5288E+02	7.2334E+01	2.4839E+02	2.0850E+01
altitude (km)	1.4409E+01	3.9265E+00	2.1700E+01	1.0003E+01
velocity (m/s)	1.7020E+03	3.6807E+00	1.7066E+03	1.6952E+03
flight path angle(deg)	5.4801E-01	5.2773E-01	1.2216E+00	-9.5137E-01
eccentricity	3.8501E-02	1.0953E-05	3.9099E-02	3.8499E-02
semi-major axis (km)	1.8181E+03	2.0722E-02	1.8192E+03	1.8181E+03
inclination (deg)	9.0000E+01	0.0000E+00	9.0000E+01	9.0000E+01
propellant usage (kg)	2.2557E+03	1.0673E+03	3.6649E+03	3.0764E+02
insertion mass (kg)	9.1586E+03	3.0642E+03	1.4481E+04	4.5200E+03
abort time (s)	3.0698E+02	1.7438E+02	6.0987E+02	2.0829E-01

Table 5.5 contains the statistics of the orbital insertion conditions in these cases. It is evident from the table that the orbital insertion conditions on eccentricity, semi-major axis, and inclination were still accurately attained. The orbital insertion altitude (which is not constrained) has a significantly large spread as compared to the cases with FOS = 1.0. Figure 5.18 confirms this observation with the plot of the orbital insertion altitudes versus abort time for both FOS = 1.0 and FOS = 5.0. The much larger spread for FOS = 5.0 is unmistakable. A manifestation of significantly larger dispersions is wider variations of propellant usage as evidenced in Figure 5.19. In the worst case the propellant mass used was about the same as the total propellant mass in Table 5.2, meaning that there was no propellant margin left at FOS of 5.0. Nonetheless, the abort guidance held up really well even in the presence of very large dispersions at FOS of 5.0, guiding every single abort trajectory successfully into the specified target orbit.

Figures 5.20 and 5.21 illustrate the histograms of the instants when aborts happened during the powered descent along the 3000 trajectories, and the times of flight for ascent

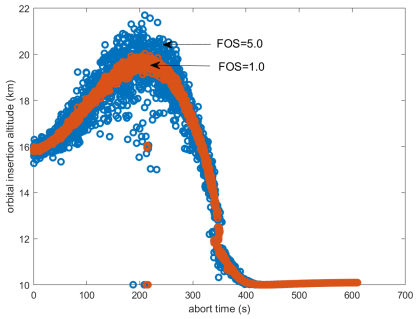

Figure 5.18. Planetocentric altitude comparison at orbital insertion for 3000 Monte Carlo simulation runs of lunar abort guidance with factors of safety = 1.0 and 5.0.

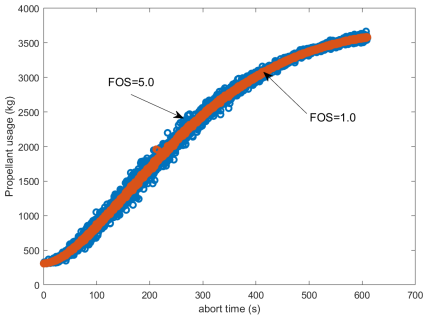

Figure 5.19. Propellant consumption at orbital insertion for 3000 Monte Carlo simulation runs of lunar abort guidance with factors of safety = 1.0 and 5.0.

into the target orbit. As expected, the abort times were distributed uniformly throughout the powered descent as they were so implemented in the Monte Carlo simulations. The ascent times in more cases appear to cluster around the high end of 240 sec than other values, perhaps a reflection of a nonlinear correlation between the abort times and ascent times.

5.8 Summary

This work represents a first focused effort in public domain since the Apollo program on developing guidance strategy for abort during powered descent of a crewed lunar mission. A novel guidance technique was developed to solve the problem of aborting into a safe

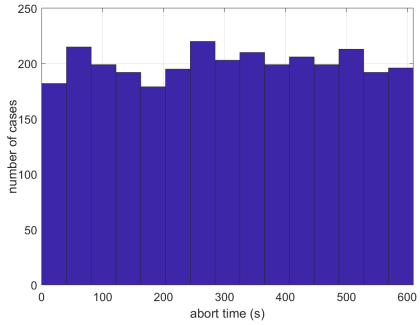

Figure 5.20. Uniform distribution of abort trigger times along lunar powered descent used in Monte Carlo simulation.

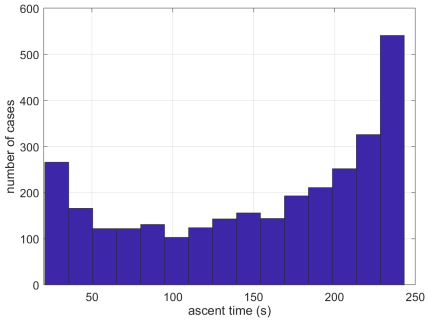

Figure 5.21. Total abort flight time of 3000 lunar powered descent Monte Carlo simulation runs with a factor of safety = 1.0.

orbit directly from powered descent. Using a fuel-optimal ascent guidance based on the indirect-method of optimal control, it was demonstrated that the problem can be solved with a single-phase abort maneuver. However, this method fails to provide a solution with enough ground clearance when an abort is called late in the descent. The introduction of a pull-up maneuver to improve the initial conditions used by the fuel-optimal ascent guidance results in a two-phase abort maneuver that solves the problem of ground clearance effectively. Uniform and well-conditioned trajectories towards a safe orbit were achieved by the two-phase abort maneuver throughout the powered descent trajectory. Monte Carlo simulations were used to demonstrate the effectiveness of the abort solution in dispersed

cases. Parametric studies on the target flight-path-angle at the end of the pull-up maneuver showed that the total propellant consumption achieved by the two phase maneuver can be similar to the fuel-optimal solution. The solutions obtained by the fuel optimal ascent guidance were validated using the direct-method of optimal control. Finally, the discovery of multiple optima during ascent from powered descent provided a new insight into the behavior of an abort solution on the Moon that can aid contingency planning in case of an emergency.

Chapter 5 is currently under review for publication as Abort Guidance during Lunar Powered Descent at the Journal of Guidance, Control, and Dynamics. Sandoval, Sergio; Lu, Ping; Hwang, John. The dissertation author was the primary investigator and author of this material.

Chapter 6

Multiple Optima in Abort-Ascent

6.1 Introduction

During the powered descent of a human mission on the Moon, terminating the descent and ascending to a safe lunar orbit must be part of the abort strategy for contingency. A recently developed abort guidance approach based on the indirect method of optimal control has shown that a fuel-optimal ascent solution to this complex problem can be found along the descent trajectory. A deeper examination of the abort guidance solution identified a previously unknown phenomenon that caused some trajectories to converge to lower altitudes than their neighboring solutions. The discovery of the existence of multiple solutions in the optimal abort-ascent problem gives an explanation to this phenomenon and is the focus of this work. The complete formulation of the problem and method of solution are shown. The findings are pertinent to any optimal abort to orbit during powered descent and it becomes an important topic for discussion regarding mission planning and astronaut training. Validation and verification of the algorithm and its results has been achieved with an implementation of the problem with the direct method of optimal control.

Despite the exiting results obtained, an unexplained phenomenon lingered among the solutions. Almost all the trajectories obtained followed an altitude pattern that ended at an orbit radius similar to its neighboring solutions. Yet amid the solutions, some of the trajectories separated from the final altitude pattern and successfully converged to a lower altitude where all the orbital insertion conditions were still met accurately. Figure 6.1 shows the resulting trajectories of 3000 abort cases along the powered descent trajectory in a mission to land a spacecraft on the Moon. The figure demonstrates that some of the abort cases appear to be inconsistent with the rest. At first sight, it appears that these cases failed to meet the terminal conditions successfully, but a closer look shows that each of the abort trajectories successfully delivers the vehicle to the specified final orbit. Given that the safety of the crew is the most important part of the mission, gaining an understanding of the potential outcomes during an abort is of vital importance. This is particularly relevant during to astronaut training since a large portion of it involves exercises to prepare for unexpected circumstances. Through careful exploration of the solution, these inconsistent cases were analyzed to find the cause of the sudden discontinuity in orbital insertion altitude. Analyzing the elements of the final orbit such as eccentricity, semi-major axis, and inclination, demonstrated that the discrepant cases were indeed inserted into the correct orbit. Furthermore, sampling some of these cases at different true anomalies and recording the propellant consumption revealed that multiple optimal solutions exist for most of the abort scenarios during powered descent. An inspection of the true anomaly across the different cases uncovered that some of these cases end up at local minimum rather than the global minimum of the ascent problem. It is the goal of

this paper to demonstrate the rationale behind this phenomenon and to provide validation and verification of this discovery using the direct and indirect methods of optimal control.

6.2 Abort Guidance Solution with Direct- and Indirect-Methods of Optimal Control

As described in Section 2.3, an optimal control problem can be solved via direct or indirect method. Since the abort guidance solution with UPG+A obtained in Chapter 5 is based on the indirect method of optimal control, the direct method of optimal control will be used to demonstrate that multiple optima exist regardless of the algorithm being used.

To solve numerically an optimal control problem, the numerical algorithm is based on either the indirect or direct method. The indirect method works to solve the two-point-boundary-value problem arising from the application of the necessary conditions for the optimal control problem (aka Pontryagin's Minimum Principle) [115]. There is no direct minimization of the performance index (hence the "indirect" method). In the direct method, the problem is transcribed into a nonlinear programming problem (NLP) by discretization of the state and control functions [116]. The problem is solved using an NLP algorithm to (directly) minimize the cost function subject to all imposed constraints. The following are two examples of algorithms that implement the indirect and direct methods. These algorithms were employed for the results of this paper.

6.2.1 Implementation of the Indirect-Method with the Universal Powered Guidance (UPG)

The Universal Powered Guidance (UPG) is a three-dimensional optimal powered guidance formulated on the indirect method of optimal control [22]. It is a multipurpose optimal control algorithm that has been applied to various scenarios such as descent, ascent, deorbit, and orbital transfers [104, 105, 106]. The ascent version of the algorithm is labelled UPG+A, but it will simply be referred as UPG for the remainder of this paper.

Based on Pontryagin's Maximum Principle, this method follows the necessary conditions of optimal control. The dynamics and performance index of the problem are as defined by equations (5.7)-(5.11). Seven nonlinear algebraic equations on the orbital insertion conditions, transversality conditions and Hamiltonian for a final free-time problem are specified in equations (5.12)-(5.18). Given some initial conditions and a final targeting condition, the problem is formulated as a two-point boundary value problem (TPBVP). The 7 nonlinear algebraic equations are solved simultaneously as a root-finding problem in closed-form using the Powell's dogleg optimization method. The optimization method requires an initial guess to solve the problem. The optimal solution finds the control and trajectory that satisfies all seven nonlinear algebraic equations. The thrust direction is found as the optimal solution that minimizes the performance index.

6.2.2 Implementation of Direct-Method with OpenMDAO

OpenMDAO is a Multidisciplinary Design Optimization (MDO) framework used to solve large-scale optimization problems efficiently [117]. It was initially developed to solve large-scale design problems with coupled numerical models. The need to implement

modern algorithms with better efficiency resulted in a new problem structure that improved performance by taking advantage of hierarchical strategies, distributed-memory parallelism, and high-performance computing [117]. Although OpenMDAO was initially developed for large-scale design optimization problems, its efficiency and simplicity facilitate the use in multiple applications [117].

In this study, OpenMDAO was used to verify and validate the results obtained previously with UPG in Lu [90] and new discoveries developed in this paper. A version of the fuel-optimal ascent problem based on the direct method was implemented in OpenMDAO. The problem was transcribed as an NLP and solved with gradient-based optimization using Newton-type algorithms. Since transversality conditions and the Hamiltonian are not required, only equations (5.7)-(5.14) are considered. The system dynamics are defined as ordinary differential equations (ODEs). Time steps are vectorized by a parallel time integration algorithm, while a framework of linear methods is used for numerical integration [118]. In the implementation, an Explicit Midpoint method was utilized to solve the problem without sacrificing too much computational efficiency.

6.3 Nominal Powered Descent Abort Mission

The lunar landing trajectory obtained in Chapter 5 is employed as the descent trajectory from which abort will occur. The Apollo Lunar Module (LM) was used as the vehicle in the simulations of this study [119]. The LM propulsion system is divided in a descent propulsion system (DPS) and an abort guidance system (AGS) [80]. The descent propulsion system (DPS) is used in both powered descent and abort guidance solutions to

emulate a sudden emergency scenario. A total of 45,000 N of thrust are available with the DPS. The specific impulse of the engine is of 311 sec. All the remaining fuel in the vehicle at the time of abort is assumed to be available. The nominal powered descent part of the mission was conducted by the Fractional Polynomial Powered Descent Guidance (FP^2DG) for lunar landing mission [109]. The landing location is at the South Pole of the Moon. The initial conditions of the mission are the same as those in Lu [90] and listed in Table 4.1. The pull-up maneuver was solved by the Universal Powered Guidance (UPG+A). The fuel-optimal ascent guidance is the only part of the mission that is relevant to the results of this paper. The powered descent and pull-up maneuver are necessary to obtain the initial conditions for the fuel-optimal ascent guidance, but their terminal conditions do not affect the discovery of this investigation. The target orbit for all abort scenarios is a 10 km x 150 km pericynthion orbit around the Moon. The orbit has a 90 deg inclination and a perilune altitude of 10 km. Simulations were performed in 3 degrees-of-freedom (3DOF) with a guidance update rate of 2 Hz and a perfect navigation. UPG + A was used to solve the fuel-optimal ascent guidance.

6.4 Discovery of Multiple Optima in Fuel-Optimal Ascent Guidance

The novel abort guidance developed in Lu [90] has shown that a solution to the complex problem of inserting a spacecraft safely into a specified final lunar orbit can be found online. This can be achieved during the entire powered descent trajectory using the indirect method of optimal control. The method utilizes an advanced propellant-optimal guidance algorithm called UPG 3.3.2. In this methodology, the abort guidance problem is

implemented as a two-phase maneuver: a pull-up phase and a fuel-optimal ascent guidance. In both abort phases, thrust is kept at its maximum level to ensure a fast transition to the final orbit. In the first phase, the pull-up maneuver is responsible of changing the velocity vector of the vehicle from its current state towards a more favorable direction to begin ascent. It does this by increasing the initial flight path angle from a negative initial value to a positive value. In the second phase, the optimal ascent guidance UPG+A takes over starting from the final state of the pull-up maneuver and guides the spacecraft towards a safe pericynthion orbit around the Moon.

A set of "free-attachment" orbital insertion conditions are used to allow maximum flexibility to achieve the specified orbit. The true anomaly at the orbital insertion point is kept free for the guidance to find. This allowed the algorithm to select the optimal final position and velocity regardless of where the actual insertion occurs in the orbit. The advantage of the free-attachment point is that the algorithm is free to choose the best orbital insertion condition in every abort scenario. Within UPG, a system of 7 nonlinear algebraic equations is solved as a root-finding problem to find the thrust direction vector and time-to-go ($t_{go} = t_f - t_0$) to reach the abort orbit [22]. Depending on the selection of the targeting conditions, the 7 algebraic equations are a combination of orbital insertion conditions and their corresponding transversality conditions [111]. The Powell's trust-region method is used to effectively solve the system of equations. Simulations revealed that UPG can achieve the desired orbit from anywhere along the powered descent trajectory wherever it is physically feasible [90].

Despite the successful results obtained by the abort guidance algorithm, an unex-

pected phenomenon appeared among the solutions without a clear explanation. In each of the abort cases tested, the algorithm reached the orbital insertion conditions successfully. In most cases, the altitude corresponding to the orbital insertion conditions followed a consistent pattern, see Figure 6.1 from 0 to 200 seconds and 300 to 600 seconds. However, a cluster of cases between 200 and 250 seconds converged successfully to a lower altitude than the rest of the solutions. See the cluster in Figure 6.1 between 200 and 250 seconds. A closer examination of the final conditions confirmed that the spacecraft ended in the correct orbit in these "out-of-family" cases. Figure 6.2 shows the propellant consumption of every abort case along the powered descent. In all cases, propellant increases as the abort cases start later in the descent.

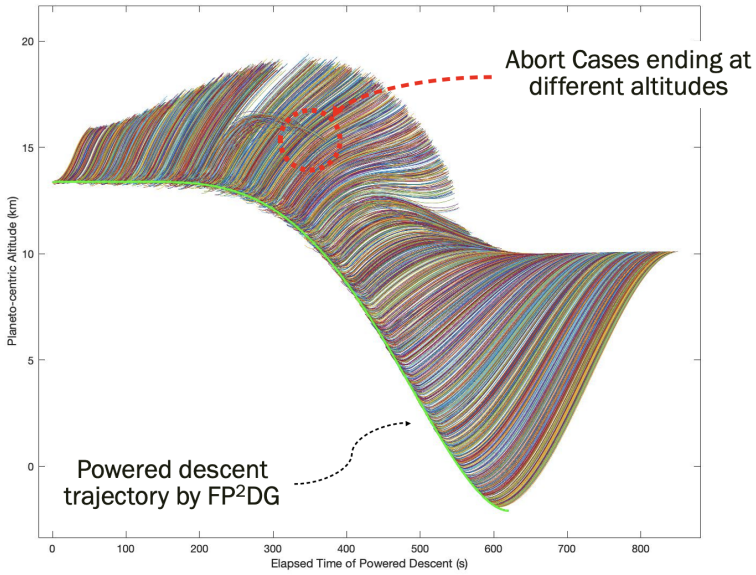

Figure 6.1. Abnormal cases in abort trajectories for 3000 Monte Carlo simulation runs of lunar abort guidance with a factor of safety = 1.0.

The latest abort guidance approach solved the problem of a contingency during descent; however, it left one question unanswered: Why are some of the solutions ending at

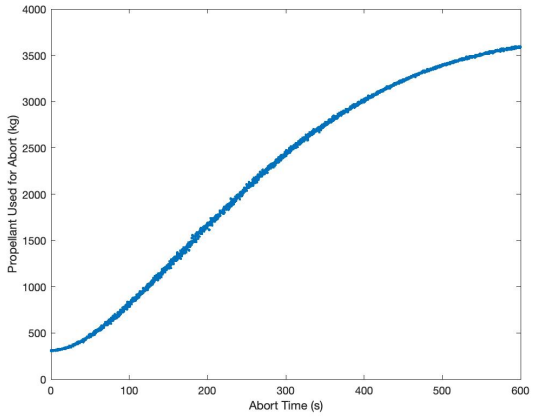

Figure 6.2. Propellant consumption in abort trajectories for 3000 Monte Carlo simulation runs of lunar abort guidance with a factor of safety = 1.0 with abnormal cases.

different altitudes? Looking at the results, it was evident that all trajectories successfully converged to a correct solution. This was confirmed by the agreement found by the fuel consumption comparison among neighboring solutions. In all cases, fuel consumption increased as expected without any jumps or discontinuities. The abort cases converging to a lower altitude followed the system dynamics and ended at a feasible solution. The fact that the algorithm implemented a free attachment point raised some questions about the way in which these points were being chosen by the algorithm. The first encounter of a difference in orbital insertion conditions was found in the true anomaly at the time of orbit insertion. Figure 6.3 shows the true anomaly at insertion for each of the abort cases studied.

This figure reveals two curves that encompass all the potential final true anomaly angles for the abort cases in this study. An upper curve for cases that started an abort between 0 and 340 seconds and a lower curve that includes cases for aborts from 340 to 600 seconds. The cases in the higher curve insert the vehicle at a true anomaly angle

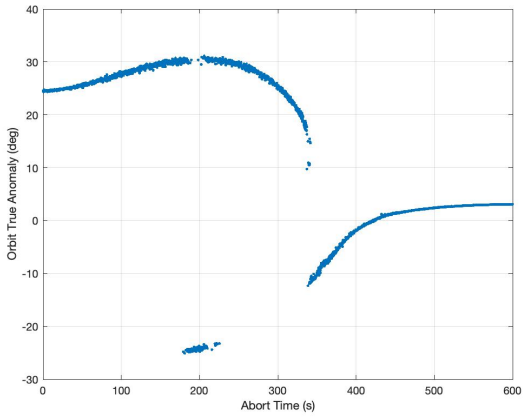

Figure 6.3. True anomaly in abort trajectories for 3000 Monte Carlo simulation runs of lunar abort guidance with a factor of safety = 1.0 with abnormal cases.

between 10 and 30 degrees, while the lower curve inserts vehicles at true anomaly angles between -25 and 3 degrees. Unexpectedly, some of the cases that were predicted to fall under the upper curve ended in the lower curve. These cases were the same that formed part of the out-of-family cluster found before!

The plot of true anomaly at insertion point gave an insight into one of the possible reasons to the existence of a discontinuity. To understand the cause of the mismatch, a new approach was developed to investigate this phenomenon. A fixed orbital insertion point was selected instead of the free attachment point used previously. This allowed the exact angle of insertion into the orbit to be chosen by the user. The new strategy consisted in solving the ascent guidance problem at different true anomaly angles on the same final orbit. The final orbit was defined by the known semi-major axis, eccentricity, and inclination. These orbital insertion parameters along with the user-selected true anomaly were used to calculate the final position, velocity, and flight path angle required to insert the spacecraft into the abort orbit. Unlike the free-attachment solution that optimized for

the orbit insertion point, in the fixed-point solution it is required to specify the position, velocity, inclination and flight path angle of the desired final condition. Thus, leaving the arguments of periapsis and ascending node as free parameters.

Abort cases activated at every 100 seconds along the powered descent trajectories were selected and their initial conditions recorded. Using the initial conditions for each case, a true anomaly scan between -100 deg to 100 deg was performed to investigate changes in propellant consumption as the spacecraft entered the orbit at different points. Each angle in this range was solved to generate a total of 201 solution points and optimal fuel consumption at each true anomaly angle was recorded. This range was selected to compare the behavior of the algorithm before and after perilune. Cases at different abort times during powered descent were selected for testing. Figure 6.4 displays the propellant consumption of the spacecraft at different insertion points along the final orbit caused by changes in true anomaly.

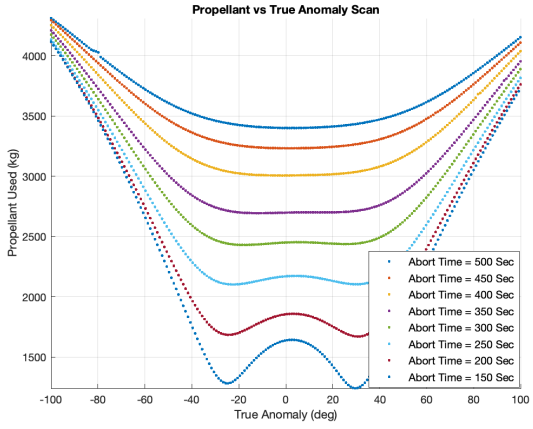

Figure 6.4. Propellant consumption during lunar abort at different orbital insertion points (true anomaly variation). Each curve represents a different abort start time during Lunar Powered Descent starting from 150 seconds at the bottom to 500 seconds at the top.

Each curve in Fig. 6.4 represents the propellant consumption for an abort guidance with the same initial conditions. The different points along the curve represent a different orbital insertion true anomaly. The bottom curve represents an abort case activated at 150 seconds from PDI, while the case at the top represents an abort case activated at 500 seconds from PDI. As we move along the powered descent trajectory, contingencies arise at later times and the optimal solution changes. The true anomaly scan shows the evolution of the propellant curve as abort guidance is initiated at different times. Early on, the curves are more pronounced and characterized by two minima, but they transform into a global minimum as the abort guidance is activated afterwards. The fact that the solution changes from two minima to a single global minimum can be explained by the fact that early on the algorithm has more space and flexibility to decide which way to go. That is, for some time, the flight time from the initial conditions to the two local minima is roughly the same and the difference in propellant consumption is negligible. This surprising result shows that more than one local minimum exists for the same abort cases at different orbital insertion conditions. Figure 6.5 is a representation of the two guidance solutions available for abort cases early in the descent.

Notice that both solutions end at the same orbit despite entering at a different true anomaly angle. In each curve, one of the solutions is a local minimum and the other is a global minimum. The global minimum appears to favor a positive true anomaly after perilune. Further analysis showed that the global minima is always associated with the solution at the highest altitude, but that the propellant consumption differs by a very small amount. The fact that in some cases the solution ends at a different altitude means

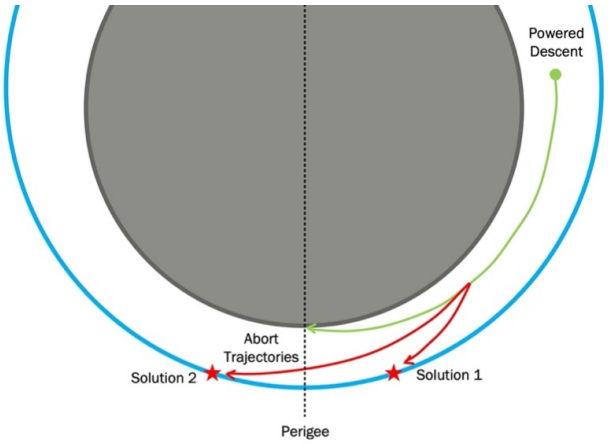

Figure 6.5. Representation of multiple optimal ascent solutions in abort scenario at the Moon.

that the algorithm found the local solution instead of the global solution. It is evident that the previously unanswered phenomenon is a result of this property. The altitude pattern that most abort trajectories follow corresponds to the global minimum from the propellant consumption curve. However, there are some cases that end up trapped in the sphere of influence of the other local minimum that has a similar propellant consumption.

Furthermore, as the descent progresses, aborting from a lower altitude becomes more challenging and the algorithm starts to lose some leeway. Eventually, there is only one clear optimal solution, and the algorithm must choose that orbital insertion point. The orbit perilune, defined as 10 km for this problem, is the closest point from the orbit to the Moon. The latest cases start abort at an altitude below perilune, therefore the only possible solution is to abort to perilune. Only abort cases that begin after 400 seconds are guaranteed to find a unique global minimum. These cases begin ascent at an altitude below perilune, and the only possible solution is to target perilune. It should be recognized that perilune is not fixed to a specific point relative to the Moon and can be changed

by the guidance solution. Given that abort is such an important safeguard of a landing mission, exploring the solution and getting answers to all the unknown behavior is the focus of this work. The implications of this discovery are important to understand any potential drawbacks or unexpected situations that might arise from abort maneuvers. In addition, future missions to the Moon can take advantage of this discovery for mission planning or astronaut training. Since the possibility to abort into the same orbit at a different altitude is present for a big part of the descent, it is important to be aware that such a situation might emerge. Should there be any question about the expected ending conditions during a particular mission to the Moon, the information revealed here has the potential to influence the selection of the best decision given a particular scenario.

6.5 Verification of Multiple Optima in Lunar-Abort Solution using Direct-Method of Optimal Control

Validation and verification (V&V) of the algorithm was performed to establish confidence in the results. The solution to the abort guidance problem was obtained by UPG, an optimal control guidance algorithm based on the indirect method of optimal control. Considering that a spacecraft landing on the Moon would require onboard computation to perform all the maneuvers, the indirect method finds a fast and reliable solution to the abort problem. However, replicating these results with a different method would confirm the accuracy and validity of the solution.

To corroborate these results, we resorted to the direct method of optimal control in which the problem is solved as a nonlinear programming problem. The goal is to

provide a comparison with a clear agreement between the direct and indirect method solutions. For the direct method approach, the abort guidance problem was solved using an open-source software named OpenMDAO. Solving with both methods would allow us to trust that the algorithm is finding the correct solution. Since both methods solve the problem differently, matching the solutions would signify that we can trust both algorithms with great confidence.

In testing, the free-attachment problem was implemented to allow the algorithm to optimize the orbital insertion condition. The formulation with the direct method consisted in implementing the equations (5.7)-(5.14) in the abort guidance problem. The transversality conditions and the Hamiltonian are not required to solve the problem with the direct method of optimal control. OpenMDAO was able to successfully obtain a solution to all the abort scenarios analyzed, thus giving confidence that the formulation with both methods was appropriate and that the solution is trustworthy. Furthermore, it was shown that most abort scenarios converged to the same solution and followed the same trajectory in both methods. The outcomes of the analysis demonstrated the effectiveness of UPG to find an optimal solution. Notwithstanding, an unexpected revelation showed that some of the abort scenarios analyzed with OpenMDAO converged successfully to different final conditions than those from UPG. This was surprising since this behavior was only evident in selected abort cases solved with UPG. In Fig. 6.1, this outcome is shown for two cases that initiated abort at 200 and 250 seconds after PDI.

In Fig. 6.6, the solution with UPG inserts the vehicle at an altitude of 19 km, while the solution with OpenMDAO does the same but ends at an altitude of close to

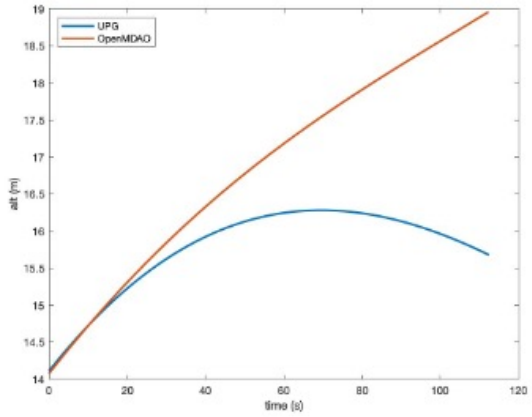

Figure 6.6. Optimal ascent trajectory for an abort start time of 200 seconds after powered descent initiation.

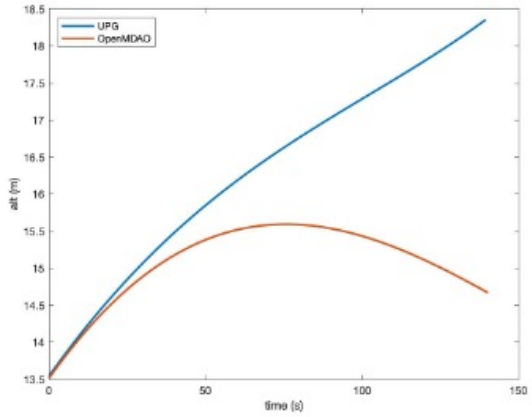

Figure 6.7. Optimal ascent trajectory for an abort start time of 250 seconds after powered descent initiation.

15.5 km. The difference between both solutions is of more than 3 km. Similarly, in Fig. 6.7, the solution obtained by UPG enters orbit at close to 18.4km, while OpenMDAO ends at 14.6 km. In this case, the difference is of almost 4 km. Note that in both cases, even though the solution ends at different altitudes, the total flight time is essentially the same. Since thrust is always at full throttle, this means that the propellant consumption is indistinguishable in both trajectories. The reason this result is surprising is because

the solution that gives the highest altitude in both cases alternates between UPG and OpenMDAO. Before this comparison, the multiple optima were noticed in the solution with UPG. Since each one of these methods converged to a viable solution, detecting multiple solutions with the direct and indirect methods implies that this behavior is not dependent on the implementation, or the method used. Effectively, any method that finds an optimal solution to the abort guidance problem will encounter this phenomenon. This reiterates the belief that this discovery is an important tool for contingency planning in preparation for future missions to the Moon.

Motivated by this new discovery and certain that the results found with the indirect method could be replicated with the direct method. A new true anomaly scan was performed using the direct method of optimal control to examine the propellant consumption obtained with this method. The propellant curve for varying true anomalies is presented in Fig. 6.8.

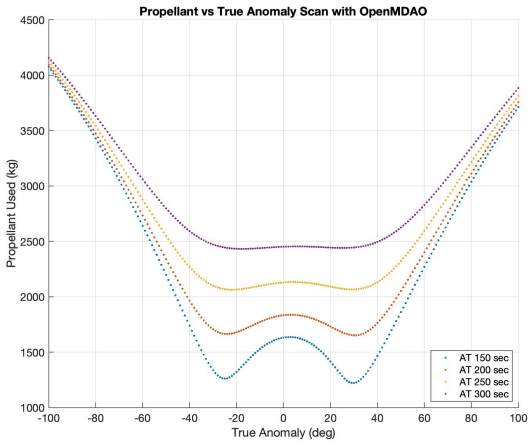

Figure 6.8. Propellant consumption during lunar abort at different orbital insertion points (true anomaly variation) using OpenMDAO. Each curve represents a different abort start time during lunar powered descent starting from 150 seconds at the bottom to 300 seconds at the top.

The resulting propellant consumption at different orbital insertion points exhibited the same behavior with OpenMDAO. Albeit more computationally expensive, a closer look revealed that the propellant curve matched exactly the curves obtained with UPG. The existence of multiple optima is evident in both cases and confirms the results obtained previously. In Fig. 6.9, a glance at the abort solutions for cases throughout the descent exposes their ascent trajectories.

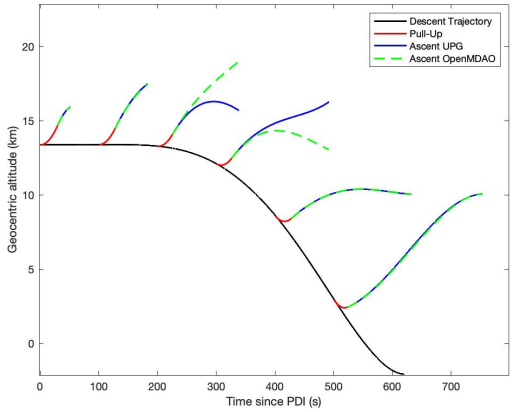

Figure 6.9. Comparison of abort solution between UPG and OpenMDAO at different abort start times along the lunar powered descent trajectory.

Starting from a powered descent trajectory generated by FP2DG, abort can begin at any time during the descent. The complete abort solution presented in Lu [90] performs a pull-up maneuver to align the vehicle and a fuel-optimal ascent guidance to determine the best orbital insertion condition. The black line represents the powered descent guidance without any abort and the red portion is the pull-up maneuver. The fuel-optimal ascent guidance is differentiated by a continuous blue line for UPG and a dashed green line for OpenMDAO. In this paper, only the fuel-optimal ascent guidance is involved in the multiple optimal solution.

Abort cases initiated at the first or final portion of the descent converge to the same solution. At the beginning, the initial conditions and initial guess of the optimization algorithm favor the global minimum. Although the propellant curve reveals a more pronounced minima for earlier cases, it seems that the position of the vehicle and the direction of the ascent trajectory benefit an insertion into the orbit before perilune. On the other hand, cases closer to the end of the descent are bound to only one solution at perilune. The middle portion of the trajectory contains all the cases that exemplify the subject of having multiple solutions to the same problem. Cases in the middle are more complex, as they depend on the initial conditions of the problem, the initial guess and the type of optimization method used. Using the final ascent conditions, the true anomaly at insertion can be calculated for each case. Figure 6.10 combines the true anomaly calculated with the propellant curve for 3 different abort cases and unveils important information about the orbital insertion altitude as a function of true anomaly.

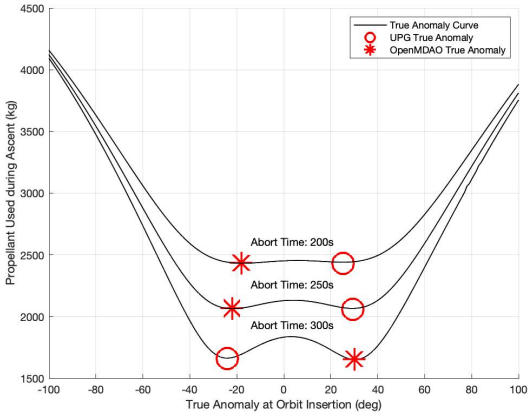

Figure 6.10. Comparison of true anomaly at orbital insertion point between UPG and OpenMDAO at different abort start times along the lunar powered descent trajectory.

Propellant curves for abort cases starting at 200, 250 and 300 seconds are plotted.

These cases were selected because they are part of the cluster cases for both UPG and OpenMDAO. Each of these cases clearly shows the two local minima. Adding the true anomaly resulting from the orbital insertion conditions for these cases demonstrates that the difference in altitude is related to the true anomaly at insertion point, with a higher altitude entering at a negative true anomaly, while the lower altitude enters orbit at a positive true anomaly. The uncovering of multiple solutions gives reassurance on the nature of this phenomenon. Every abort scenario has at most two solutions and neither of them are arbitrary. Understanding the solution helps predict the outcome of an emergency before it happens. Furthermore, knowing that both solutions are near fuel-optimal allows the manipulation of the solution to be forced to enter the orbit at a specific location.

The last component of this investigation involved a more detailed inspection on the nature of the cluster cases in the middle. A comparison of the results obtained by OpenMDAO and UPG would give an insight on the similarities and differences among these cases. A comparison of the ascent trajectories for some abort cases between 200 and 300 seconds after PDI is shown in Fig. 6.11.

In the case of OpenMDAO, it appears that the cluster of cases ending at a lower altitude starts a little bit later. The ascent solution by UPG converges to a lower solution in cases that started abort at 200 and 225 seconds, while OpenMDAO converges a higher altitude in the same cases. On cases that started abort at 250, 275 and 300 seconds, OpenMDAO converges to a lower altitude, while UPG enters orbit at a higher altitude. Due to the computational time expense of the direct method, 3000 Monte Carlo simulations were not performed with this method. But a small experiment with UPG revealed that

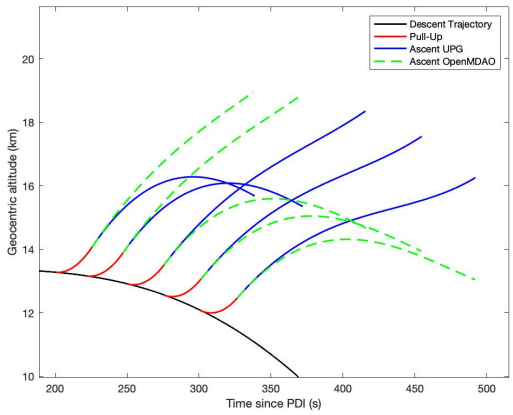

Figure 6.11. Comparison of abort trajectories in cases converging to a different altitude using UPG and OpenMDAO.

changing the initial guess of the optimization method influences the range of the cluster cases. For instance, the nominal ascent guess time for UPG is of 200 seconds. Reducing the ascent guess time caused the cluster cases to shift to the left, while increasing the guess time caused them to move to the right. Changing the initial guess time did not eliminate the cluster. Although OpenMDAO utilizes a vector of normalized times rather than an initial guess, it is possible that the mechanism used to solve the solution acts similar than the initial guess implemented in UPG. This would explain the different ranges found for each method. This is merely an observation that goes beyond the scope of this paper.

Additionally, velocity profiles for each abort case revealed similar patterns among all solutions. Figure 6.12 shows a velocity profile comparison for the cluster cases tested. This demonstrated that the velocity is the same using both methods, regardless of the final altitude achieved. The implication of this result means that the propellant consumption should be very close among solution to the same case using different methods. The fact that the velocity profiles were identical, implied that the total ascent time must be similar since

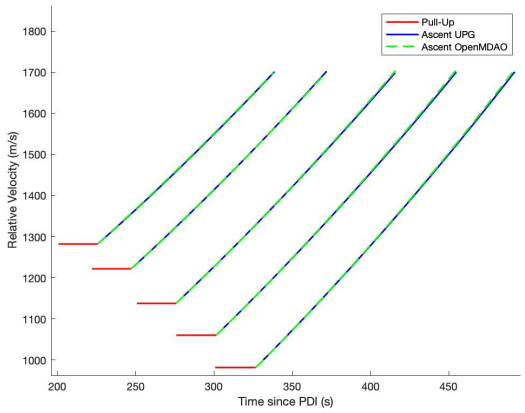

Figure 6.12. Comparison of relative velocity in cases converging to a different altitude using UPG and OpenMDAO.

both implementations are running at full throttle. This was confirmed by the propellant comparison in Fig. 6.13.

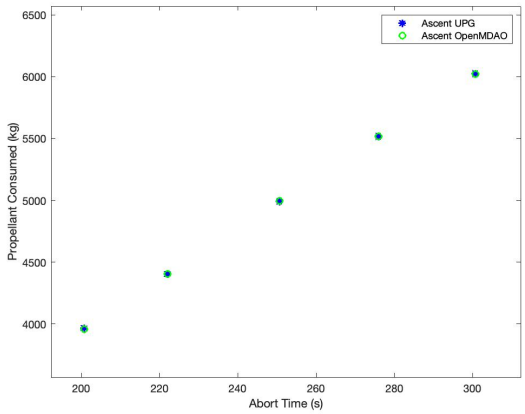

Figure 6.13. Comparison of propellant consumption in cases converging to a different altitude using UPG and OpenMDAO.

Propellant consumption increases as the abort occurs later in the descent. Since the vehicle gets closer to the ground as it moves through the descent trajectory, it requires more propellant to ascend into the final orbit. The propellant consumption among the cluster cases tested is indistinguishable between the two methods. This means that both solutions

are near-optimal despite entering the final orbit at a different altitude. Knowing that either solution is near-optimal, there is no impact in propellant efficiency by the selection of a specific final altitude. The discovery of the two minima in the propellant curve indicates that at every point before 400 seconds, multiple fuel-optimal ascent solutions exist. This is an important discovery for crewed lunar landing missions on the grounds that in case of a contingency, the crew and support team should be prepared to encounter this type of behavior. The only concern is to be able to predict the altitude that the algorithm will choose at any given time. This could be predicted by testing different initial conditions in Monte Carlo simulations.

Although a spacecraft insertion to a lower altitude is also a safe solution to the abort ascent problem, it is not ideal to deviate from the rest of the solutions. This is especially concerning if the propellant consumption is the same and there is no added benefit to take a different route. Furthermore, being unaware of the expected result is an idea that goes opposite to the principle of contingency. Perhaps a better solution is to require the guidance to end above a specific altitude in case of abort. This can be accomplished by forcing the solution to insert the vehicle at a negative true anomaly. Multiple methods can be implemented to ensure that the guidance selects a particular solution. The important takeaway is that knowledge of the two possible solutions enables multiple approaches to influence the result. The fact that the final condition can now be predicted is the greatest advantage of this discovery.

6.6 Summary

In any human mission, the priority is the safety of the crew. A great deal of attention is spent on the guidance, navigation and control systems to reduce the risks involved in space missions. One such component of is the abort capability that the spacecraft possess to take a spacecraft from an emergency situation during lunar powered descent into a safe orbit around the Moon. The problem of abort guidance during lunar powered descent was resolved with an innovative approach that updated abort guidance methods that were in place since the Apollo missions. Among the set of solutions obtained from this new algorithm, an unexplained phenomenon arose where some of the abort trajectories converge to a different altitude than anticipated. In this paper, an analysis of the abort solutions provide the answer to the unsolved mystery. A new fixed-point formulation allowed the discovery of multiple optima on many of the abort guidance solutions. This realization gives a better understanding of the characteristics of an abort trajectory and allows future missions to plan in advance for this phenomenon. The results found in this study are not unique to this implementation and will emerge in similar optimal control approaches. The implications of this finding pertain the contingency planning in future missions to the Moon. Validation and verification of the algorithm is performed to demonstrate the efficacy of the algorithm and the reliability of the solution.

Chapter 6 is currently under review for publication as Abort Guidance during Lunar Powered Descent at the Journal of Guidance, Control, and Dynamics. Sandoval, Sergio; Lu, Ping; Hwang, John. The dissertation author was the primary investigator and

author of this material.

Chapter 7

Integration of Entry and Powered Descent for Human-Scale Mars Landing Mission

7.1 Introduction

The entry and powered descent guidance algorithms can be integrated to produce an end-to-end simulation from the moment the spacecraft enters the atmosphere and all the way to the landing point. Large uncertainty in atmospheric conditions at Mars make entry, descent, and landing a challenging task for human-scale missions that require safe and precise landing. Since the knowledge of the actual conditions is limited by the navigation system of the vehicle, guidance algorithms capable of accommodating these types of dispersions are critical to develop future human missions to Mars. This paper focuses on the performance comparison of two state-of-the-art numerical predictor-corrector (NPC) entry guidance algorithms and guidance approaches: one uses direct-force control and the other the conventional bank-angle control. The algorithms are applied to a reference human-scale Mars mission. Both algorithms are implemented in the Program to Optimize Simulated Trajectories II (POST2) at the Langley Research Center. Three

degree-of-freedom end-to-end simulations of the low lift-to-drag ratio NASA reference entry vehicle are used to compare the performance of both algorithms. Monte Carlo simulations enable performance comparison by introducing dispersions that the guidance algorithms must accommodate. The results from this study provide a comparative assessment of the current EDL guidance capability for human-scale Mars Mission.

7.2 Description of Entry and Powered Descent Guidance Algorithms

7.3 Entry Guidance Algorithms

The entry guidance algorithms that will be tested in this study are of the numerical predictor-corrector (NPC) type. The NPC process consists of predicting a vehicle trajectory to generate a control command to target a final constraint from the current state or initial constraint. Using this prediction, the algorithm compares the resulting trajectory to the final constraint and calculates the error in the prediction. Finally, a correction is issued by updating the control command to minimize the error.

To obtain a measurement of performance by the supporting entry and powered descent algorithms used in this investigation, a comparison with a state-of-the-art entry and powered descent algorithm was performed. This resulted in two entry and powered descent guidance combinations that can be better visualized in Table 7.1. The first combination uses FNPEG as entry guidance (described in more detail in Section 3.2.1) and FP^{2}DG as the powered descent guidance (described in Section 3.3.1). For the second combination, an algorithm named the Numerical Predictor-Corrector Entry Guidance (NPCG) offers both

an entry guidance solution and a powered descent solution via an augmented gravity turn.

NPCG is a generalized NPC algorithm designed to permit the user wide flexibility in designing and implementing guidance laws for a variety of mission segments such as aerocapture, entry, and powered descent. Generally, it is up to the user to define the vehicle, environment, and steering algorithms in the NPCG framework. The NPCG prediction phase then consists of integrating the 3-DOF translational equations of motion from an initial navigated state towards the predefined targeting condition using an initial control vector. For the correction phase, a gradient-based targeting algorithm is used to select a control vector that meets the final conditions with the least amount of error. A command generated by the control solution found is issued at every guidance call and updated as necessary to minimize targeting errors. For this vehicle, the NPCG drives the vehicle using Direct Force Control (DFC) by maneuvering the angle of attack and angle of sideslip. Usually, this is accomplished by control surfaces on the vehicle. Along the trajectory, multiple segments with distinct targeting conditions can be defined and the guidance satisfies the final constraint in each segment before moving on to the next one.

For HIAD powered descent, the NPCG is programmed to use an Augmented Gravity Turn. Nominally, a pure gravity turn consists of pointing the thrust vector in the opposite direction of the velocity vector. Thrust forces acting on the vehicle reduce the total velocity over time. Aided by the gravity of the planet, the vehicle rotates as the velocity diminishes in the horizontal direction. Eventually, only velocity in the upward direction remains and the vehicle is naturally aligned at -90 degrees. A gravity turn is useful because it is not complex and constructs a clean solution to the soft-landing

problem. Improvements, or augmentations, of the gravity turn are changes to the simple method described above to produce a more capable solution. The Augmented Gravity Turn applied to this study is able to target a specific landing location. NPCG is a complete EDL guidance algorithm that has entry and powered descent capability. An Augmented Gravity Turn works in conjunction with the entry phase in NPCG to solve the EDL problem as one single algorithm. This cooperation improves the efficiency of the powered descent by presenting an adequate PDI condition.

7.4 Integration of Entry and Powered Descent

Entry and powered descent guidance can be independent algorithms that produce a solution based on the current navigated state and the corresponding target condition at every phase. However, it is known that powered descent can achieve better performance given a proper PDI condition [61, 22]. When entry and powered descent guidance are constructed to collaborate by targeting an appropriate PDI point during entry, improved success rate and propellant consumption can be attained. For instance, in this study, NPCG is the only algorithm that was optimized to produce an optimal propellant solution and an appropriate PDI condition.

7.5 Nominal End-to-End Mars-Landing Trade Studies

From a polar orbit of 33793 km apoapsis altitude by 250 km periapsis altitude, a deorbit burn is commanded on the spacecraft at apoapsis to coast until the beginning of the atmospheric entry interface at an altitude of 125 km and a velocity of 2650 m/s. The

landing site selected is located at 25.25 deg latitude and 5.04 deg longitude. During the entry phase, the atmospheric and aerodynamic models are activated to give the vehicle maneuverability with its the control surfaces. The entry algorithms require certain level of force to be able to operate, therefore they are activated at specific values of sensed acceleration or dynamic pressure, NPCG activates at a sensed acceleration of 0.15 g's while FNPEG activates when a dynamic pressure of 15 Pa is reached. Once entry guidance is activated, commands for angle of attack and angle of sideslip, in the case of NPCG, or bank angle, in the case of FNPEG, are generated throughout the entry phase to control the vehicle until the start of powered descent. These guidance commands give authority to the vehicle's control surfaces to direct the vehicle towards a specific target while reducing the downrange and crossrange error. A PDI condition is selected to start powered descent, and it is usually the same as the target condition for entry. When powered descent is initiated, supersonic retropropulsion rockets with differential throttling are used to slow down the vehicle rather than the atmosphere alone. During powered descent, atmosphere and aerodynamic models are deactivated because it is assumed that the supersonic retropropulsion forces outweigh the aerodynamic forces. The goal of the powered descent is to guide the vehicle towards the landing site and reach an altitude of 12.5 m and with a velocity of 2.5 m/s. The terminal phase of powered descent consists of a 5 second vertical descent at a constant 2.5 m/s. The vehicle touches the ground at the end of the vertical descent and the EDL portion of the mission is completed.

The HIAD vehicle, one of the candidate vehicles in development under EDLAS, was selected to perform this investigation. The vehicle is a low L/D ratio inflatable capsule

with a diameter of 16m and a height of 4.3 m. The ballistic coefficient and L/D ratio of the vehicle are 155 kg/m2 and 0.15, respectively. The total weight is approximately 57 t at launch and 49 t at the entry interface. It possesses a set of aerodynamic flaps necessary during entry to control angle of attack, angle of sideslip or bank angle. Eight engines producing a total of 800,000 N of force are grouped in the middle portion of the heat shield in a doublet formation. The thrust generated is sufficient to slow down the vehicle throughout the powered descent phase. Figure 1 illustrates the complete EDL mission concept of operations with HIAD. Figure 7.1 illustrates the complete EDL mission concept of operations with HIAD obtained from Cianciolo [120].

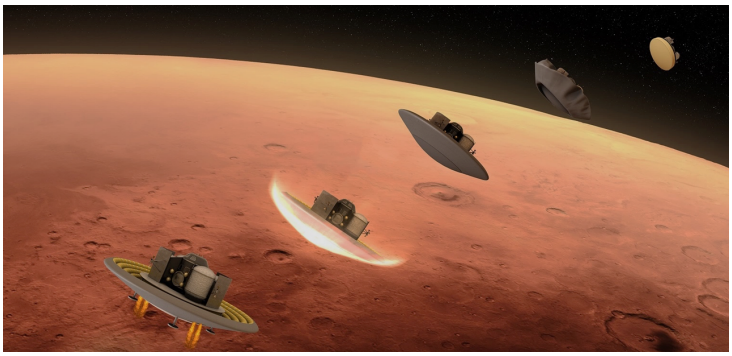

Figure 7.1. Entry, descent, and landing concept of operations using the hypersonic inflatable aerodynamic decelerator entry vehicle.

The nominal EDL trajectory consists of two segments: entry and powered descent. The entry guidance algorithm controls the vehicle from the end of the deorbit phase until it reaches a predetermined targeting condition suitable to start Powered Descent. Aerodynamic forces are used to control the vehicle during entry to reach the final conditions. In powered descent, the guidance algorithm produces a thrust vector command composed of thrust magnitude and direction. Utilizing the algorithms described in the “Background”

section, the two trade studies on Table 7.1 were proposed to test the performance of the vehicle using different approaches for the same mission.

Table 7.1. Entry, descent, and landing guidance trade studies for a human-scale Mars mission.

Trade Study	Entry Guidance	Powered Descent Guidance
1	NPCG	NPCG
2	FNPEG	FP^{2}DG

Each trade study represents a combination of entry and powered descent guidance approaches. The first trade study consists of the NPCG approach for entry and powered descent. The NPCG suite has been largely tested at LaRC for EDL missions to Mars, and more information on the performance of this method is reported in Lu [64]. The second trade study brings together FNPEG and FP^{2}DG for entry and powered descent, respectively. Both guidance algorithms have been tested extensively in other studies, an example of an application of FNPEG and FP^{2}DG to a crewed Mars mission can be found on Cianciolo [26]. Although these trade studies have been examined in the past, this is the first time that these comparisons have been realized under the same conditions and simulation environment. Thus, this gives a first look into the performance of these algorithms using the same settings as they complete the mission.

A critical component of this study was the selection of an appropriate PDI condition to satisfy both trade studies. An optimal PDI condition for NPCG had already been found by optimizing the simulation of a 3-DOF Mars mission in POST2. Since the goal is to provide a comparison under similar conditions, the optimal PDI condition for NPCG was selected to activate powered descent in all trade studies. This decision was made on the

basis that the optimization of NPCG sets Trade Study 1 as the performance benchmark. Table 7.2 lists the PDI condition selected to start powered descent in all trade studies.

Table 7.2. Nominal powered descent initiation conditions in entry, descent, and landing guidance trade studies for a human-scale Mars mission.

Geodetic Altitude Target (m)	5000.0
Relative Velocity Target (m/s)	550.0
Range-To-Go Target (m)	11500.0

FP^{2}DG is called twice, the first time during a braking phase that starts at the PDI condition and a second time during an approach phase as the spacecraft gets closer to the landing site. The braking phase is the longest part of powered descent, it is the section that slows down the vehicle the most before reaching the approach phase and landing. The purpose of the approach phase is to serve as a vehicle alignment phase in the case that onboard instrumentation needs to be pointed in a certain direction before touchdown. Additionally, a vertical descent phase was added at the end of all powered descent trajectories to guarantee that the vehicle's velocity vector is perpendicular to the ground and to avoid any involuntary horizontal velocity towards the end caused by the improper alignment of the lander.

7.6 Simulation of Nominal Trade Studies

Complete end-to-end, 3DOF simulations were performed in POST2, a simulation tool at NASA's Langley Research Center. Perfect navigation is assumed with an update rate of 1 Hz for entry and 10 Hz for powered descent. The update rate on the Augmented Gravity Turn was set to 1 Hz. The nominal results show the complete trajectories of the trade studies formulated for this investigation. Plots comparing similarities and differences

among different guidance approaches allow the clear observation of trajectory shape, control command and propellant performance.

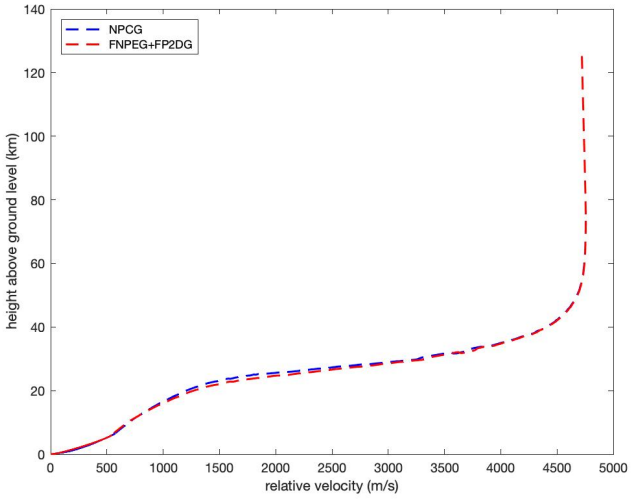

Figure 7.2. Comparison of end-to-end trajectories in entry, descent, and landing guidance trade studies for a human-scale Mars mission.

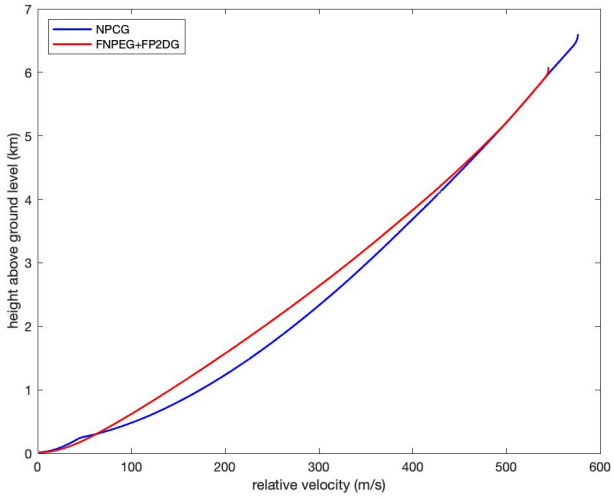

Figure 7.3. Comparison of powered descent trajectories in entry, descent, and landing guidance trade studies for a human-scale Mars mission.

Nominal EDL trajectories for each trade study are illustrated in Figures 7.2 and 7.3. The complete end-to-end trajectory is presented in Figure 7.2, where entry is represented by

a dotted line and powered descent by a solid line. The plot shows the actual height above the ground and the relative velocity experienced by the spacecraft. From this perspective, it is clear that the entry phase represents a bigger portion of the entire EDL trajectory. By comparison, the entry portion of EDL lasts up to 400 seconds, while powered descent is between 50 - 70 seconds. Also, it is interesting to note that although two different entry guidance approaches are used, the trajectories are close together in velocity-altitude space as the vehicle slows down through the atmosphere. At higher altitudes, aerodynamic forces are smaller, and the velocity reduction is smaller in comparison to the rest of the entry phase. A considerable reduction in speed occurs at when maximum aerodynamic acceleration reaches 30 m/s^2 around 3000 m/s. Figure 7.3 gives a closer look at the powered descent trajectories of each case. The first thing to notice is that the PDI conditioned achieved by both entry guidance algorithms is different, this happens because although NPCG and FNPEG are targeting the same starting point for powered descent, the way the achieve it is different. For instance, NPCG activates once this target has been achieved, while FNPEG targets an energy-like equation containing the target parameters. The difference in PDI condition between these two approaches is related to the formulation of each guidance and not an error in the targeting condition.

Both approaches reach a reasonable condition to start PDI. Figure 7.4 shows the PDI starting conditions achieved by each method. Trade Study 1 uses NPCG and starts PDI at a Mach number of 2.47, while FNPEG starts at a slightly lower Mach number of 1.34. Another important aspect of this plot is the fact that the FP^2DG guidance flies at a higher altitude than the NPCG powered descent approach. Depending on the selection

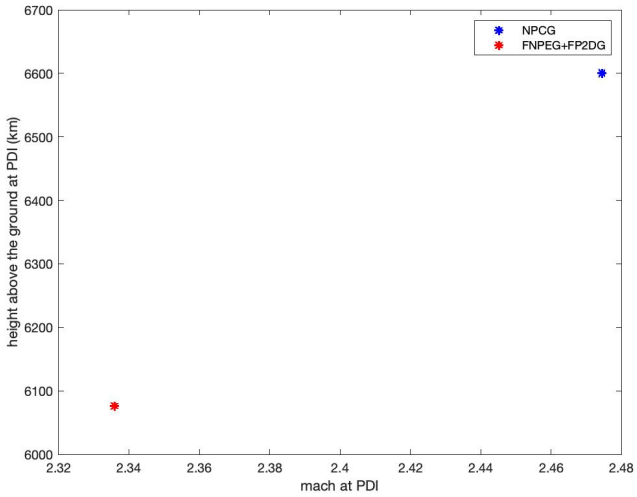

Figure 7.4. Comparison of powered descent initiation conditions in entry, descent, and landing guidance trade studies for a human-scale Mars mission

of the tuning parameters on FP^{2}DG, different propellant consumption and trajectories can be obtained. Trajectory shaping has important applications for instrument alignment, propellant consumption, and limits imposed for the safety of the crew. The nominal parameters selected for FP^{2}DG in this study are listed in Table 7.3.

Table 7.3. Nominal FP^{2}DG parameter selection for entry, descent, and landing guidance trade studies on a human-scale Mars mission.

Time-To-Go (s)	55.0
γ Tuning Parameter	1.5
k_r Tuning Parameter	12

These parameters were selected to provide a powered guidance solution that achieved the final conditions successfully with the PDI condition given. These parameters can also be tuned for performance and trajectory shaping. For the nominal case, the goal is to provide a comprehensive comparison of these three approaches without jumping into any guidance tuning. A section on FP2DG's guidance tuning and trajectory shaping is

included later in this paper.

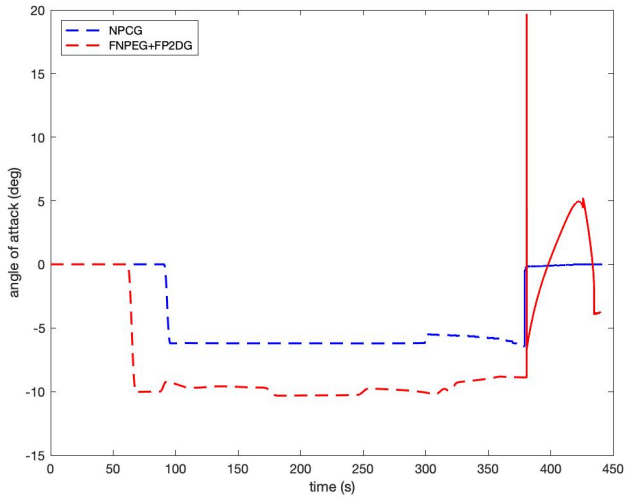

Figure 7.5. Comparison of entry guidance angle of attack in entry, descent, and landing guidance trade studies for a human-scale Mars mission.

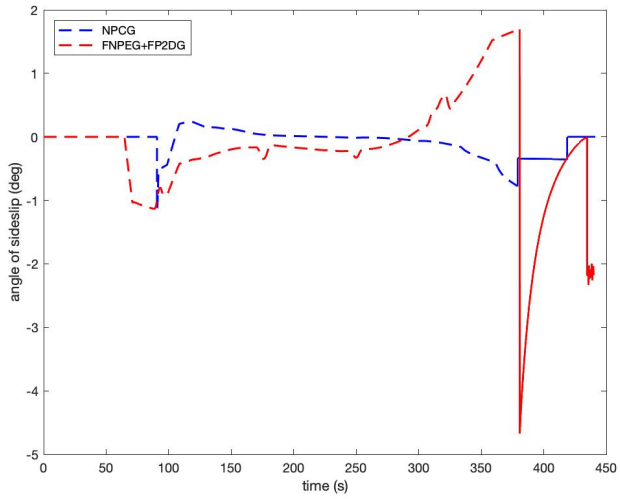

Figure 7.6. Comparison of entry guidance angle of sideslip in entry, descent, and landing guidance trade studies for a human-scale Mars mission.

The two control methods used in entry guidance are DFC of angle of attack and angle of sideslip, and bank angle control. The NPCG approach uses DFC to guide the vehicle, while FNPEG uses bank angle control. Figures 7.5, 7.6, and 7.7 show a comparison

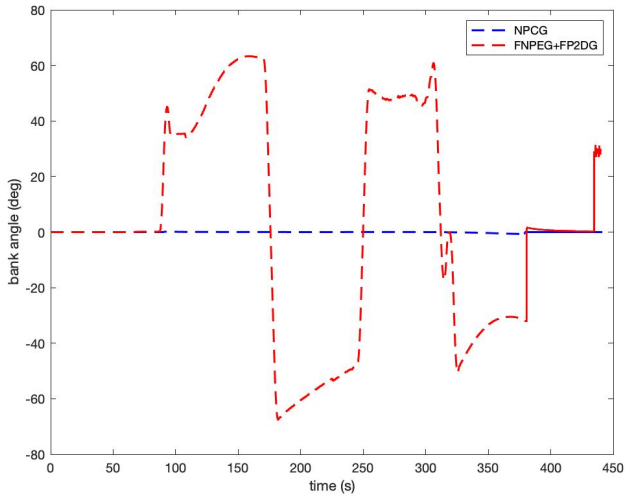

Figure 7.7. Comparison of entry guidance bank angle in entry, descent, and landing guidance trade studies for a human-scale Mars mission.

of angle of attack, angle of sideslip and bank angle during entry and powered descent.

The control angles used during the entry phase are represented by dotted line segments. Figures 7.5 and 7.6 show a comparison of the planet relative angle of attack and angle of sideslip, the control angles used for the NPCG entry guidance approach. Although these angles are not used as controls by FNPEG, they still vary with the dynamics of the vehicle as it moves relative to the atmosphere. A trim angle of attack of -10 deg was chosen for FNPEG to produce a suitable combination of lift and drag, and to maintain a constant vehicle direction as it maneuvers with bank angle control. Albeit it appears that the angle of attack is constant in both entry guidance algorithms, NPCG is doing active angle of attack modulation in Trade Study 1 and is predicting the vehicle dynamics well in the nominal sense, resulting in an essentially constant angle of attack. The angle of attack commanded by NPCG is smaller than the trim angle of attack selected for FNPEG. An important observation is that the angle of sideslip shown Figure 7.6 is in the

planet-relative frame, while the commands are sent in the wind relative frame. Hence, the angle of sideslip shown for FNPEG deviates from being zero throughout entry guidance. Again, since FNPEG is not commanding angle of sideslip, this angle is just following the natural motion of the vehicle as it maneuvers using bank angle control. The bank angle control used by FNPEG is visible in Figure 7.7, where the guidance algorithm performs the 4 predefined bank reversals while NPCG stays at 0 deg. One advantage of using bank angle control is that the same results can be obtained by using only one control angle. This comes at a cost as bank angle control generates greater crossrange errors. An important discussion point is the fact that during the entry maneuvers, the Reaction Control System (RCS) is constantly working to maintain the correct roll/bank attitude of the vehicle. The work on this paper focuses on 3DOF simulations, where RCS control is not modeled. Other studies have shown that accounting for RCS control for DFC can increase propellant consumption up to 1 ton [40]. A greater crossrange with bank angle control suggests that more propellant consumption might be required with RCS thrusters to maintain the bank attitude of the vehicle. However, a complete 6-DOF simulation is necessary to provide accurate estimates of propellant consumption with bank angle control.

Even though the atmosphere starts to make an impact at high altitudes, it is not until a specific threshold is reached that the guidance system is commanded to react. This is clear in Figure 4a where the angle of attack for all the trade studies reacts sometime after entry has commenced. As mentioned before, entry guidance starts generating a control command when a sensed acceleration of 0.15 g's for NPCG and a dynamic pressure of 15 Pa for FNPEG are achieved.

Variation in angle of attack during powered descent occurs because the thrust direction is changing constantly to mitigate crossrange and downrange errors as it approaches the landing site. In the AGT, the thrust vector is pointed directly opposite to the velocity vector and the angle of attack is kept near 0 deg. When using FP^{2}DG, the thrust vector is in a different direction than the negative of the velocity vector and the angle of attack of the vehicle changes as this happens. This is not an issue in 3-DOF simulation, but it needs to be considered in 6DOF as it would require additional propellant consumption to point the vehicle in the correct direction using RCS and differential throttle. Bank angle affects the position of the vehicle with respect to the landing site, especially if horizontal velocity has not been mitigated completely close to the landing. The rockets on the HIAD are fixed to the vehicle, therefore bank angle during powered descent is controlled by the RCS.

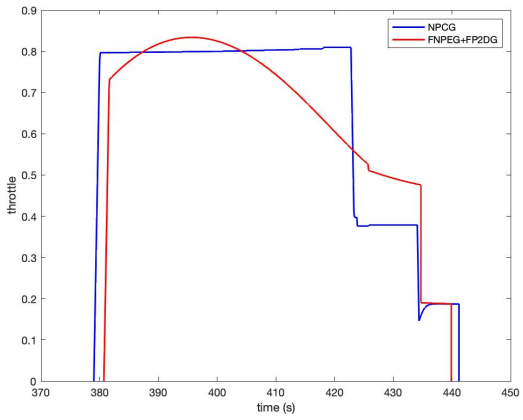

Figure 7.8. Comparison of powered descent thrust profile in entry, descent, and landing guidance trade studies for a human-scale Mars mission.

The thrust profiles of each trade study are shown in Figure 7.8. A slight difference in PDI is caused by the distinct targeting approach used by each entry guidance algorithm.

The target entry condition for all trade studies is the same given in Table 7.2. This difference is not concerning as each guidance algorithm found an appropriate solution to start PDI. FP^{2}DG used a slightly higher maximum thrust for a couple of seconds but quickly lowered thrust for the remaining of its engine burn. Even though there are clear differences between each method used, the area under the profile for each trade study is alike. FP^{2}DG is based on the polynomial curve of the Apollo Powered Descent Guidance, hence the curved shape of the thrust profile. The gravity turn approach uses a constant thrust while keeping zero angles of attack and sideslip. Both approaches include a vertical descent phase that can be found in the last 5 seconds of the thrust profile. The vertical descent phase maintains a constant velocity of 2.5 m/s to take the vehicle from an initial altitude of 12.5 m to the ground.

Thrust saturation occurs when the engine throttle is at the maximum level allowed by the engine. To prevent saturation, the augmented gravity turn approach in Trade Studies 1 is designed to nominally use 80% thrust throughout powered descent. This is noticed in the near constant throttle in Figure 7.8. On the other hand, FP^{2}DG's absence of a thrust limit allows the possibility for saturation and could cause problems if the guidance needs to command a higher thrust to accommodate for dispersions. Additionally, if there is a need for differential throttling to change the direction of the vehicle with thrust alone, there would be no margin to perform that maneuver if saturation is present. To avoid this, it is possible to reduce the thrust limit that the guidance perceives to be less than the actual thrust limit, this would make the guidance work with a lower thrust limit value and compensate for that with a longer burn time.

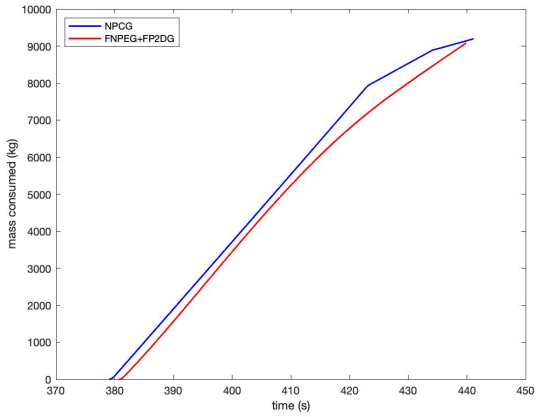

Figure 7.9. Comparison of powered descent propellant consumption in entry, descent, and landing guidance trade studies for a human-scale Mars mission.

Even though each trade study has a different thrust profile and burn time, the propellant consumption for each method is similar. A comparison of the propellant consumed by each trade study is pictured in Figure 7.9. A total of 8867.32 kg of propellant were used by FNPEG and FP^{2}DG in Trade Study 2 making it the EDL approach with the least propellant consumed in the nominal case. It was followed by NPCG in Trade Study 1, using 8983.78 kg of propellant. The difference is approximately 117 kg. As a reminder, the total propellant consumed for this 3-DOF study does not account for the RCS propellant consumed during entry maneuvering, which would increase the propellent used by FNPEG given that the bank angle maneuvers require more vehicle attitude control. It is worth noting that Trade Study 1 is the only optimized guidance combination and that both trajectory and PDI condition were optimal for this mission scenario.

7.6.1 Monte Carlo Simulations of Nominal Trade Studies

In addition to the nominal cases, Monte Carlo simulations were performed to test the algorithms under more stringent situations. Each trade study was subject to a set of

random dispersions in initial conditions, mass, atmosphere, aerodynamics, and propulsion. The purpose of these uncertainties is to try to replicate random atmospheric conditions that might occur during a mission and to evaluate how each algorithm will react with these off-nominal parameters. From these simulations, statistics for each trade study are generated that help investigate advantages and disadvantages of each method. The list of dispersion parameters for this study is presented in Table 7.4.

The main segments of interest are the conditions at the start of PDI and at touchdown. The start of PDI is a critical factor for the success of the mission, an appropriate condition allows the powered descent phase to perform the landing in a safe and efficient form. For this problem, PDI condition is composed of altitude, relative velocity and range-to-go to the landing site. Generally, these values are predetermined from the optimization of the algorithm using a program like POST2. This could be useful for a nominal case, but a static PDI condition may result in reduced performance in dispersed trajectories. Lu [22] presents an adaptive PDI logic that predicts a near-optimal PDI condition to start powered descent and explains the importance of this selection in Mars EDL mission. The crossrange and downrange are important metrics that reveal the alignment of the vehicle with respect to the landing site at the end of entry. A comparison of the Monte Carlo statistics at PDI is shown in Figures 7.10, 7.11, 7.12, and 7.13.

The success criteria in Table 7.5 were applied to the results from the Monte Carlo simulation to define when the mission was accomplished effectively. In both Trade Studies, the success rate was 100%, indicating that both guidance implementations and tuning parameters were effective in achieving a safe landing.

Table 7.4. Dispersions and uncertainty values of 8000 Monte Carlo simulation runs of a human-scale Mars landing mission with a factor of safety = 1.0.

Category	Parameter	Dispersion	Distribution
Initial Conditions	Inclination	0.01 deg (1σ)	Normal
	Longitude of the Ascending Node	0.01 deg (1σ)	Normal
	Periapsis Altitude	0.01 km (1σ)	Normal
	Apoapsis Altitude	0.01 km (1σ)	Normal
	True Anomaly	0.01 deg (1σ)	Normal
	Argument of Periapsis	0.01 deg (1σ)	Normal
	Deorbit Burn Bias	0.135 m/s (3σ)	Normal
Mass	Dry Mass	500 kg (3σ)	Normal
	X_{cg} Offset	0.05 m (3σ)	Normal
	Y_{cg} Offset	0.05 m (3σ)	Normal
	Z_{cg} Offset	0.05 m (3σ)	Normal
	I_{xx} Multiplier	0.05 kg-m^2 (3σ)	Normal
	I_{yy} Multiplier	0.05 kg-m^2 (3σ)	Normal
	I_{zz} Multiplier	0.05 kg-m^2 (3σ)	Normal
Atmosphere	Density	MarsGRAM	–
	Winds	MarsGRAM	–
	Dusttau	0.1 : 0.9	Uniform
Aerodynamics	Aerodynamic database uses coefficient multipliers and adders for different aerodynamic regimes based on CFD, wind tunnel tests, and flight data from similar shapes		
Propulsion	Peak Thrust	Scale Factor: 1% (3σ)	Normal
	Peak I_{sp}	Scale Factor: 1% (3σ)	Normal
	Oxidizer Flow Rate	Scale Factor: 1% (3σ)	Normal
	Startup Rate	Scale Factor: 1% (3σ)	Normal
	Main Phase Rate	Scale Factor: 1% (3σ)	Normal
	Shutdown Rate	Scale Factor: 1% (3σ)	Normal
	Start Time	0.0 : 0.2s	Uniform

Table 7.5. Success criteria for trade studies in Monte Carlo simulations for a human-scale Mars landing mission with a factor of safety = 1.0.

Total Range at PDI Start	$<$	1.0E7 km
Relative Velocity at Vertical Descent	$\leq$	3.0 m/s
Height Above the Ground at Vertical Descent Start	$>$	-1.0 m
Horizontal Velocity at Touchdown	$\leq$	3 m/s
Pitch at Touchdown	$\leq$	-87.0 deg

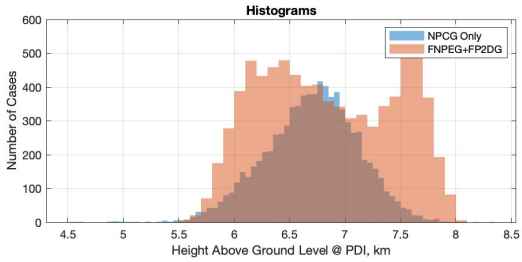

	NPCG Only	FNPEG+FP2DG
Nominal	6.47	5.94
Mean	6.7	6.84
3-sigma	1.25	1.8
1.00 %-tile	5.68	5.78
99.00 %-tile	7.59	7.91
Max Value	8.34	8.08
Min Value	4.54	5.53
Success	8000	8000
Percent	100	100

Figure 7.10. Height above ground at start of PDI for 8000 Monte Carlo cases in a human-scale Mars landing mission with a factor of safety = 1.0.

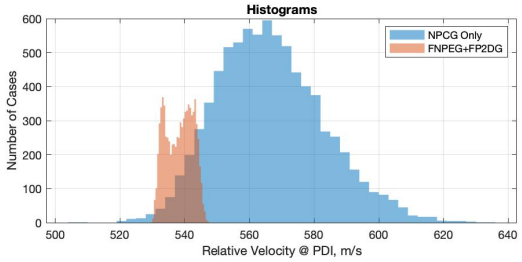

	NPCG Only	FNPEG+FP2DG
Nominal	575.85	544.57
Mean	566.4	538.37
3-sigma	49.81	12.37
1.00 %-tile	533.23	531
99.00 %-tile	608.87	545.66
Max Value	635.59	547.3
Min Value	506.94	529.84
Success	8000	8000
Percent	100	100

Figure 7.11. Relative velocity at start of PDI for 8000 Monte Carlo cases in a human-scale Mars landing mission with a factor of safety = 1.0.

Figures 7.10, 7.11, 7.12, and 7.13 show statistics on the dispersions at the start of PDI conditions. On Figure 7.10, the altitude above the ground for all cases is displayed. The mean altitude of all cases is of 6.8 km, with a difference of 140 meters between the

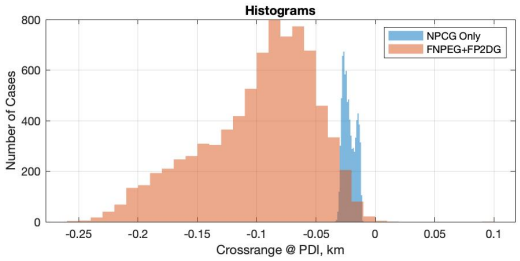

	NPCG Only	FNPEG+FP2DG
Nominal	-0.03	-0.21
Mean	-0.02	-0.1
3-sigma	0.02	0.14
1.00 %-tile	-0.03	-0.22
99.00 %-tile	-0.01	-0.02
Max Value	-0.01	0.09
Min Value	-0.03	-0.26
Success	8000	8000
Percent	100	100

Figure 7.12. Crossrange at start of PDI for 8000 Monte Carlo cases in a human-scale Mars landing mission with a factor of safety = 1.0.

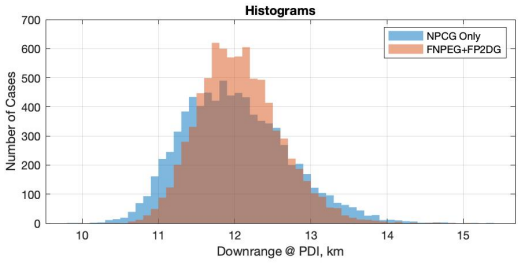

	NPCG Only	FNPEG+FP2DG
Nominal	12.48	11.48
Mean	12.01	12.06
3-sigma	2.07	1.61
1.00 %-tile	10.69	10.97
99.00 %-tile	13.84	13.47
Max Value	15.35	15.06
Min Value	9.89	10.37
Success	8000	8000
Percent	100	100

Figure 7.13. Downrange at start of PDI for 8000 Monte Carlo cases in a human-scale Mars landing mission with a factor of safety = 1.0.

highest and lowest mean starting point. This relation is maintained when looking at the lower and maximum altitude values achieved in all cases. A lower relative velocity at PDI facilitates the effort exerted by the powered descent guidance to slow down the vehicle

before landing. The relative velocities achieved by NPCG and FNPEG are 566.4 m/s and 538.37 m/s, respectively, as displayed on Figure 7.11. The difference in velocity is not as significant, but the spread of the velocity with FNPEG is reduced to a smaller area.

The shape of the altitude and velocity spreads by FNPEG can be explained by the targeting technique used by this method. FNPEG targets an energy-like equation that is a function of final altitude and velocity. The algorithm tries to achieve the final conditions by satisfying this equation with slightly higher or lower values of altitude and velocity. Although relative velocity at the start of PDI carries a bigger weight on powered descent, its impact increases when it is in a good combination with the altitude at PDI. This explains that the distribution of altitude and velocity appears to be less uniform. In this equation, the final velocity has a bigger weight than the altitude, therefore altitude varies the most to favor the velocity target.

Measurements of crossrange and downrange at the start of PDI measure the distance from the vehicle to the landing site. The downrange measures the arc length from the current latitude and longitude to that of the landing site. Interestingly, both entry guidance algorithms activate PDI around a 12km downrange. Crossrange indicates the distance perpendicular to the direction of flight pointing towards the landing site. In the case of Trade Study 1, the use of DFC for entry control has a minimal effect on crossrange, a mere 30 meters to the side of the landing site. Trade Study 2 shows a maximum crossrange distance of 260 meters with the use of bank angle control. The bigger crossrange in the second case needs to be mitigated by the powered descent guidance, and FP^{2}DG is shown to manage crossrange dispersions well.

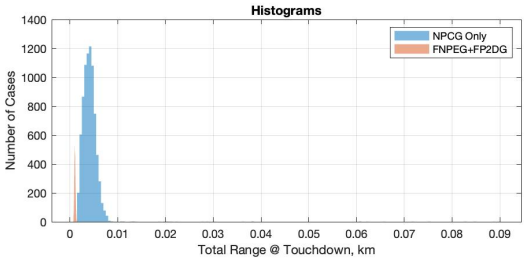

	NPCG Only	FNPEG+FP2DG
Nominal	0	0
Mean	0	0
3-sigma	0.01	0
1.00 %-tile	0	0
99.00 %-tile	0.01	0
Max Value	0.09	0
Min Value	0	0
Success	8000	8000
Percent	100	100

Figure 7.14. Total range at touchdown for 8000 Monte Carlo cases in a human-scale Mars landing mission with a factor of safety = 1.0.

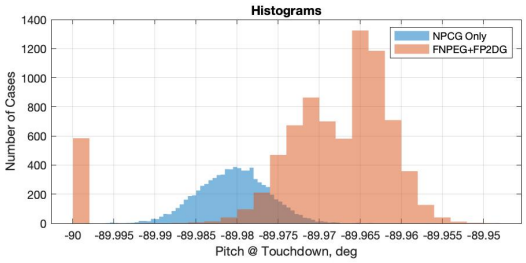

	NPCG Only	FNPEG+FP2DG
Nominal	-89.98	-89.97
Mean	-89.98	-89.97
3-sigma	0.01	0.03
1.00 %-tile	-89.99	-90
99.00 %-tile	-89.97	-89.96
Max Value	-89.96	-89.95
Min Value	-90	-90
Success	8000	8000
Percent	100	100

Figure 7.15. Pitch at touchdown for 8000 Monte Carlo cases in a human-scale Mars landing mission with a factor of safety = 1.0.

The touchdown conditions in Figures 7.14, 7.15, and 7.16 show the overall performance of the guidance combinations at the end of the mission. All successful cases reached the landing site inside 90 meters. Trade Study 2 reached the landing site within 1

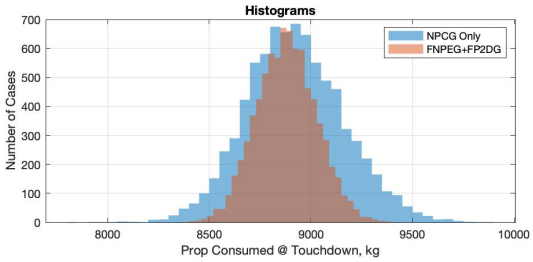

	NPCG Only	FNPEG+FP2DG
Nominal	8983.8	8867.3
Mean	8920.8	8880.2
3-sigma	719.86	440.93
1.00 %-tile	8377.8	8544.6
99.00 %-tile	9510.8	9225.2
Max Value	9868.6	9423.6
Min Value	7843.9	8359.5
Success	8000	8000
Percent	100	100

Figure 7.16. Propellant consumed at touchdown for 8000 Monte Carlo cases in a human-scale Mars landing mission with a factor of safety = 1.0.

meter, with a negligible 3-sigma variation. Trade Study 1 maintained a 3-sigma variation of 10 meters. The zeros in the statistics indicate that the value is below three decimal numbers, and the numbers are rounded to zero. At touchdown, horizontal velocity must be mitigated with the vehicle needs to be pointing in a vertical direction for safe landing. A pitch of -90 deg represents the vertical direction of the vehicle with the engines pointing down towards the ground. The pitch at touchdown for both cases is close to the desired target of -90 deg. In Trade Study 1 , the gravity turn aligns the vehicle as it finds a solution during powered descent. The thrust is pointed in the opposite direction of the velocity vector and naturally ends up in the vertical direction. An instantaneous pitch control of -90 deg was designed for Trade Study 2 to guarantee a pitch of -90 deg during the vertical descent. In a 6-DOF simulation, the vertical attitude of Trade Study 2 might change once pitch rate limits and RCS control are applied to the vehicle.

The smallest propellant consumption was obtained using the configuration in Trade Study 2, where FNPEG and FP^{2}DG take control of the vehicle. The mean propellant consumption by this approach was of 8880.19 kg with a 3-sigma variation of 440.93 kg. Trade Study 1 used an average of 8920.83 kg, just 40 kg below Trade Study 2, with a 3-sigma variation of 719.86 kg. Recall, however, that these simulations do not account for RCS propellant consumption, and Trade Study 2 will likely require more propellant consumption to execute bank reversals that are not required for DFC used in Trade Study 1. Although there is not a set propellant limit to this vehicle yet, it is desired that the propellant consumption does not exceed 10 tons. Propellant loads larger than 10 tons would require a vehicle redesign.

Both DFC and bank angle control provide the powered descent guidance with an appropriate PDI condition to complete a successful landing. The powered descent guidance approaches supplied by NPCG and FP^{2}DG could bring the vehicle to the landing location safely. FP^{2}DG's success was not affected by the larger crossrange values, a convenient advantage when large uncertainty might deviate from a small crossrange.

7.7 Fractional-Polynomial Powered Descent Guidance Tuning and Trade Studies

Additional trade studies on FNPEG + FP^{2}DG were performed under different setup conditions to illustrate trajectory shaping and propellant performance. These studies were performed on the same mission as the nominal trade studies. On the nominal cases, Trade Study 2 was implemented without any kind of optimization. This left some room for improvement considering that FP^{2}DG is readily available for parameter tuning to

cause an effect in trajectory shaping and propellant consumption. The ability to adjust to unexpected circumstances is a desired characteristic of any powered descent guidance and FP^{2}DG demonstrated that this is possible without many adjustments. Another reason for further investigation of FP^{2}DG is that with some changes in trajectory shape and better PDI conditioning, propellant consumption improvements can be achieved.

The main tuning parameters in FP2DG are the time-to-go from the start of PDI to the landing site, and two parameters, γ and k_r, that affect trajectory shaping. In addition, changing the PDI condition might benefit the efficiency of the algorithm by providing a better starting condition. A set of modifications were applied to PDI condition and the tuning parameters in FP^{2}DG to reach lower levels of propellant consumption. Two new test cases were created to compare the results, with their details presented in Table 7.6.

Table 7.6. PDI conditions and tuning parameters in FNPEG + FP^{2}DG trade studies for a human-scale Mars landing mission.

Case Study	Targeting PDI Conditions	Tuning Parameters
FNPEG + FP^{2}DG Nominal	Geodetic Altitude = 5000.0 m Relative Velocity = 550 m/s Range-To-Go = 11.5 km	Time-To-Go = 55 s $\gamma = 1.5$ $k_r = 12.0$
FNPEG + FP^{2}DG Trade 1	Geodetic Altitude = 3000.0 m Relative Velocity = 350 m/s Range-To-Go = 9.5 km	Time-To-Go = 64 s $\gamma = 1.0$ $k_r = 12.0$
FNPEG + FP^{2}DG Trade 2	Geodetic Altitude = 3000.0 m Relative Velocity = 550.0 m/s Range-To-Go = 0.0 km	Time-To-Go = 50 s $\gamma = 1.0$ $k_r = 12.0$

FNPEG + FP^{2}DG Nominal is the same as Trade Study 2 in the previous section, this was used as the new baseline for this comparison. In FNPEG + FP^{2}DG Trade 1, the PDI condition was lowered to start closer to the landing site and at a lower velocity.

Table 7.7. Actual PDI condition at entry hand-off in FP^{2}DG trade studies on a human-scale Mars landing mission

Case Study	Targeting PDI Conditions	Tuning Parameters
FNPEG + FP^{2}DG Nominal	Geodetic Altitude	5000.0 m
	Relative Velocity	550 m/s
	Range-To-Go	11.5 km
FNPEG + FP^{2}DG Trade 1	Geodetic Altitude	3000.0 m
	Relative Velocity	350 m/s
	Range-To-Go	9.5 km
FNPEG + FP^{2}DG Trade 2	Geodetic Altitude	3133.3 m
	Relative Velocity	439.92 m/s
	Range-To-Go	7.5 km

Altitude was also reduced to achieve the desired lower velocity. FNPEG + FP^{2}DG Trade 2 was created to push the algorithm to the limit. This was achieved by reducing the speed and altitude at PDI as much as possible. In this case, FNPEG is configured to fly a low trajectory that ends above the landing site. Not that a target relative velocity of 250 m/s with entry alone is not attainable, but because FNPEG will always try to get as close to the target condition as possible, it will find the smallest velocity achievable. This guarantees that there will always be a solution, even if it is not exactly the targeting condition. As a reminder, this is only for the purpose of testing the guidance to the limit, FNPEG can reach targeting conditions that are more reasonable, just as it was shown in the nominal trade study. In previous cases, PDI activates when FNPEG reaches an energy value related to the targeting conditions. In this case, although a lower trajectory is flown, a different targeting condition to start PDI at a near-optimal condition. This was accomplished by using a PDI Logic based on a propellant-optimal powered descent guidance called the Universal Powered Guidance (UPG) [61, 22]. With the aid of this

algorithm, a better PDI starting condition was selected. In this sense, FNPEG flies a trajectory that is independent of the PDI condition. The PDI condition activates at a point along the trajectory even though the trajectory target has not been reached. This has been tested previously in the literature, where it has been shown that PDI plays an important part in the efficiency of powered descent guidance. The actual trajectory flown by FNPEG + FP^{2}DG Trade 2 is based on the "Entry Trajectory PDI Target" values on Table 7.6 and the "Actual PDI Condition" on Table 7.7 defines the point along the entry trajectory when powered descent is initiated [61, 22].

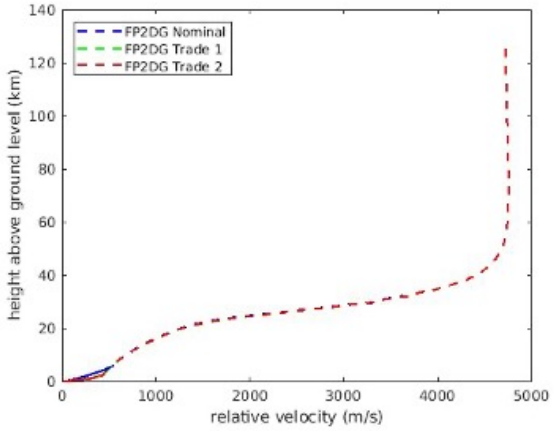

Figure 7.17. Complete end-to-end EDL trajectories in FP^{2}DG trade studies for a human-scale Mars landing mission.

The nominal trajectories for the FNPEG + FP^{2}DG trade studies are shown in Figures 7.17 and 7.18. In Figure 7.17, the complete end-to-end trajectory shows a similar profile for all three cases. The only difference appears towards the end, where PDI conditions change. Figure 7.18 shows the powered descent trajectories of these 3 cases, where the different PDI conditions can be noticed. The trajectories in Trades 1 and 2 start PDI at lower values than the nominal by more than 3 km in geodetic altitude and

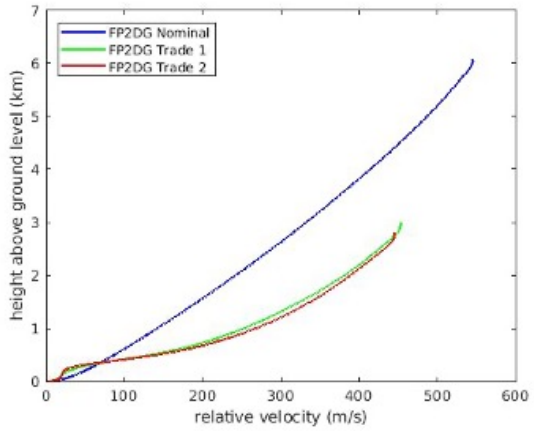

Figure 7.18. Powered descent trajectories in FP^{2}DG trade studies for a human-scale Mars landing mission.

by almost 100 m/s in relative velocity. An interesting observation is that the difference in PDI condition between Trades 1 and 2 is minimal, this is because the optimal PDI condition is very close in both cases.

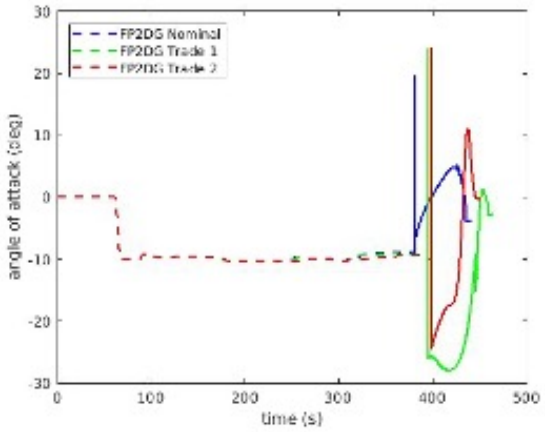

Figure 7.19. Comparison of angle of attack for FP^{2}DG trade studies for a human-scale Mars landing mission.

Figures 7.19, 7.20, and 7.21 show the angle of attack, angle of sideslip, and bank angle during entry and powered descent. The figures show similar behavior than the nominal cases. The only control used by FNPEG is bank angle, with a trim angle of

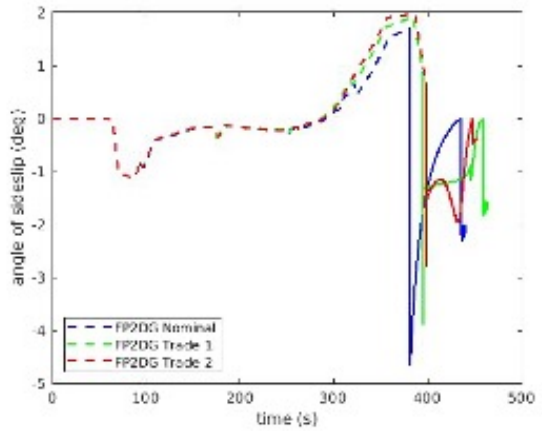

Figure 7.20. Comparison of angle of sideslip for FP^{2}DG trade studies for a human-scale Mars landing mission.

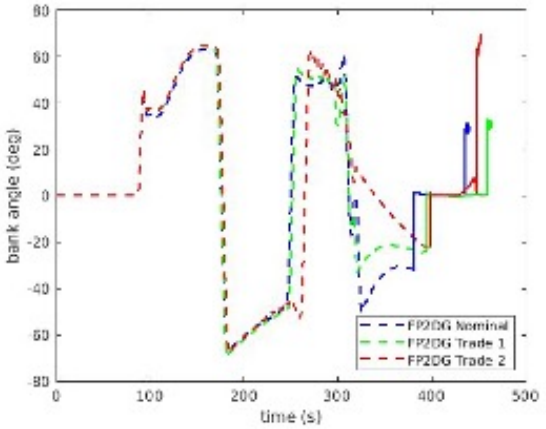

Figure 7.21. Comparison of bank angle for FP^{2}DG trade studies for a human-scale Mars landing mission.

attack of -10 deg. Changes in angle of sideslip result from the angle commands sent on the wind-relative frame in POST2, this causes a small variation in the planet-relative angles. Figure 7.21 shows the bank angle profile of the three trade cases and how FNPEG adapts to fly different trajectories. Relatively small changes in bank angle make a significant difference in the trajectory flown and the conditions achieved.

In Figure 7.22, the final conditions attained by each trade study are compared.

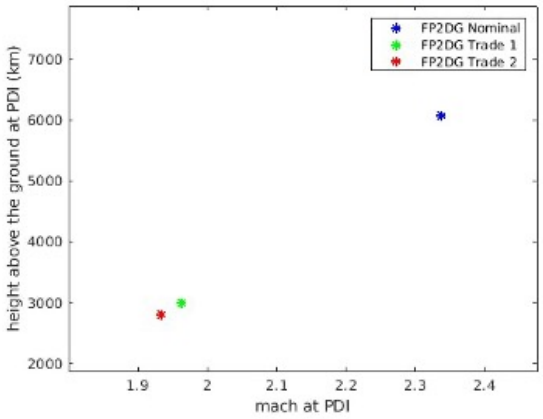

Figure 7.22. Comparison of PDI starting conditions in FP^{2}DG studies for a human-scale Mars landing mission.

The nominal case starts PDI at an altitude close to 6 km and a Mach number of 2.34. The FNPEG + FP^{2}DG Trade 1 PDI condition started at 3 km, while Trade 2 started at 2.8 km. Regarding relative velocity, Trade 1 started at a Mach number of 1.96, against a Mach number of 1.93 for Trade 2. Trades 1 and 2 offer a significant improvement in velocity reduction versus the nominal case. The goal of lowering the PDI conditions and trajectory targets in Trade 1 and Trade 2 was to slow down the vehicle as much as possible to improve propellant efficiency. A PDI with lower velocity requires less propellant because the powered descent guidance will run for a shorter time.

A comparison of the throttle profile generated by these trade studies is presented in Figure 7.23. As a reminder, the maximum thrust capacity of the HIAD is of 800,000 N. The total powered descent run time of the nominal case is of 55 seconds, a total of 64 seconds for Trade 1 and 50 seconds for Trade 2. Notice that Trade 1 consumes less propellant than the nominal case despite having a longer flight time, this highlights the importance of an appropriate PDI condition.

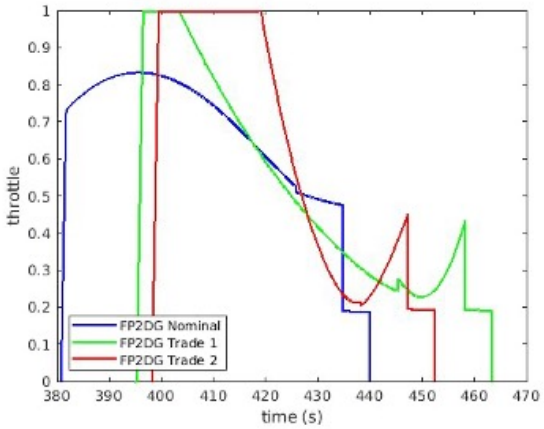

Figure 7.23. Throttle profile comparison in FP^{2}DG trade studies for a human-scale Mars landing mission.

In terms of total throttle, the nominal case operates significantly below 90% of the maximum thrust allowed, while the trade studies suffer from saturation in the early part of powered descent. It is desirable to avoid any saturation to maintain full control of the spacecraft since maneuvering is performed using differential throttling. However, having some saturation is expected for this scenario since we are pushing the guidance to the very limit of what is physically possible to attain. The propellant-optimal powered descent solution produces a bang-bang profile [22]. A bang-bang profile consists of three segments: a first segment at the maximum allowable thrust, a middle segment at the minimum allowable thrust, and a final segment at the maximum allowable thrust again. By doing this, the flight time is the smallest possible and the velocity reduction is increased using the maximum thrust. In the case of FP^{2}DG, optimization is not playing a part, but the saturation at the beginning involves the same principle. To reduce velocity to achieve a safe landing, some portion of powered descent needs to perform at maximum thrust. In this study, no thrust limit was added to FP^{2}DG. It is possible that adding

a limit at 90% thrust would eliminate saturation, but at the cost of more propellant consumption. Additionally, it is important to consider that although throttle control is a very important mechanism for the control of the vehicle, the thrust direction vector also plays an important part in the efficiency and control of the spacecraft.

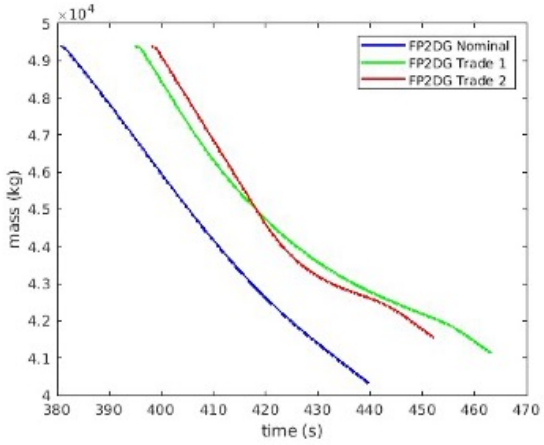

Figure 7.24. Mass consumption in FP^{2}DG trade studies for a human-scale Mars landing mission.

The resulting mass from the nominal runs is shown in Figure 7.24. It is clear that there is a significant propellant reduction in Trades 1 and 2 that results in a higher final mass. The nominal propellant consumption by the nominal case is of 8867.3 kg, with Trade 1 and 2 using 8051.2 kg and 7665.6 kg, respectively. The difference in propellant consumption between the nominal case and Trade 1 is of 816.1 kg, a difference of almost 1 metric ton. Furthermore, a difference of 1201.7 kg was attained by Trade 2 against the nominal case, a difference of 1.2 metric tons. A considerable decrease in propellant spending can be achieved by changing the PDI condition and tuning some of the powered descent guidance parameters.

7.7.1 Monte Carlo Simulations for Fractional-Polynomial Powered Descent Guidance Trade Studies.

In the same way as the previous study, 8000 Monte Carlo runs were performed on the FNPEG + FP^{2}DG study to give a better idea of the performance of the algorithm with different configurations. The dispersions applied to these simulations are the same provided in Table 7.4. Because targeting conditions were different for FNPEG in Trades 1 and 2, some variation in the PDI conditions was expected. The final values reached by the entry guidance in the 3000 cases of the Monte Carlo simulation can be seen in Figures 7.25, 7.26, 7.27, and 7.28.

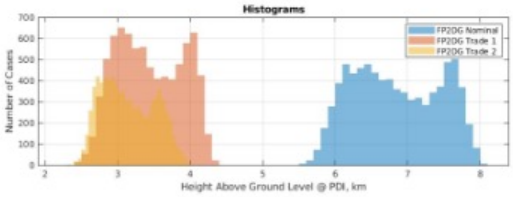

	FP2DG Nominal	FP2DG Trade 1	FP2DG Trade 2
Nominal	5.94	2.87	2.68
Mean	6.84	3.44	3.14
3-sigma	1.8	1.36	1.09
1.00 %-tile	5.78	2.61	2.52
99.00 %-tile	7.91	4.24	3.88
Max Value	8.08	4.39	4.08
Min Value	5.53	2.37	2.25
Success	8000	8000	8000
Percent	100	100	100

Figure 7.25. Height above ground at start of PDI for 8000 Monte Carlo cases in a human-scale Mars landing mission with a factor of safety = 1.0.

The first thing to notice is that all three cases obtained a 100% success rate regardless of the entry trajectory flown or the powered descent configuration. Satisfying the stringent conditions in Table 7.5 demonstrates the robustness of the algorithm even when flying a more aggressive trajectory. Figure 7.25 shows the geodetic altitude at the start of PDI. The mean altitude at PDI for both Trades 1 and 2 is close to 3 km, while

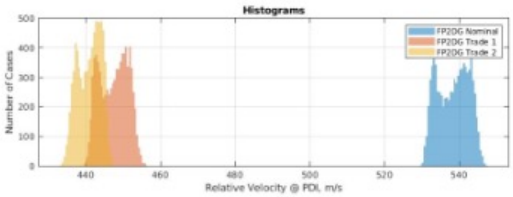

	FP2DG Nominal	FP2DG Trade 1	FP2DG Trade 2
Nominal	544.57	452.24	444.91
Mean	538.37	447.5	441
3-sigma	12.37	11.25	9.2
1.00 %-tile	531	440.83	434.75
99.00 %-tile	545.66	454.31	446.2
Max Value	547.3	456.25	448.49
Min Value	529.84	439.6	433.06
Success	8000	8000	8000
Percent	100	100	100

Figure 7.26. Relative velocity at start of PDI for 8000 Monte Carlo cases in a human-scale Mars landing mission with a factor of safety = 1.0.

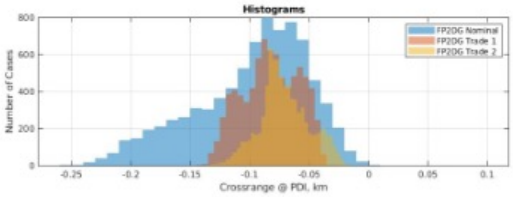

	FP2DG Nominal	FP2DG Trade 1	FP2DG Trade 2
Nominal	-0.21	-0.12	-0.09
Mean	-0.1	-0.08	-0.07
3-sigma	0.14	0.07	0.06
1.00 %-tile	-0.22	-0.13	-0.12
99.00 %-tile	-0.02	-0.04	-0.03
Max Value	0.09	-0.03	-0.01
Min Value	-0.26	-0.14	-0.14
Success	8000	8000	8000
Percent	100	100	100

Figure 7.27. Crossrange at start of PDI for 8000 Monte Carlo cases in a human-scale Mars landing mission with a factor of safety = 1.0.

the nominal case starts PDI at 6.84 km. The relative velocity comparison in Figure 14b displays the greater speed reduction obtained from using lower entry guidance targets. At PDI, relative velocity in Trades 1 and 2 are 90.87 m/s and 97.37 m/s slower than the nominal case, respectively. Even though this appears to be a small reduction in comparison to the initial relative velocity of 2650 m/s, it causes an significant difference in propellant consumption. The difference in downrange among the three cases can be observed in Figure 7.28. The mean downrange for the nominal case is of 12.06 km, Trade

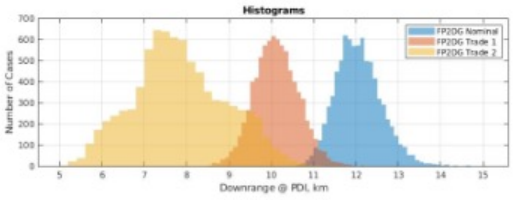

	FP2DG Nominal	FP2DG Trade 1	FP2DG Trade 2
Nominal	11.48	9.34	7.02
Mean	12.06	10.12	7.85
3-sigma	1.61	1.57	3.27
1.00 %-tile	10.97	8.94	5.65
99.00 %-tile	13.47	11.41	10.28
Max Value	15.06	12.9	11.69
Min Value	10.37	8.16	5.04
Success	8000	8000	8000
Percent	100	100	100

Figure 7.28. Downrange at start of PDI for 8000 Monte Carlo cases in a human-scale Mars landing mission with a factor of safety = 1.0.

2 reaches a downrange of 10.12 km and Trade 2 a downrange of 7.85 km. From this image, a discrepancy between the target range-to-go in Trade 2 and the actual downrange achieved can be perceived. The target range-to-go was selected to be at the landing site, while Trade 2 is 7.85 km from the landing site in downrange. Although FNPEG targets altitude, velocity and range-to-go, PDI occurs before reaching the targeting conditions. The target altitude and velocity are used as the trigger to start PDI, while range-to-go is targeted by the bank angle parametrization. This means that PDI can be triggered by altitude and velocity alone. This mechanism is useful because altitude and velocity usually contribute more to a better PDI condition. The reduction in relative velocity goes alongside a reduction in altitude. The difference in relative velocity at PDI between the nominal case and Trades 1 and 2 is a significant reduction caused by the need to fly for a longer period. To obtain the desired velocity reduction, the vehicle needs to fly longer. Similarly, range-to-go needs to be reduced to accommodate this additional flight time during entry. Interestingly, flying a longer entry trajectory also results in a reduction in

crossrange error at PDI. The bank reversal logic of FNPEG calculates when to perform a bank reversal to reach the predefined number of bank reversals selected by the user. As the vehicle advances through the entry phase, FNPEG minimizes the crossrange error with each bank reversal. The additional flight time allows FNPEG to reduce the crossrange error as it approaches the lower targeting conditions.

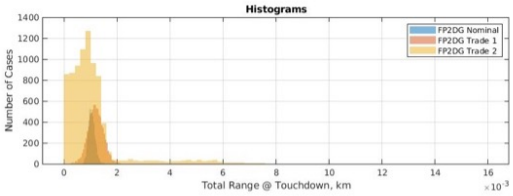

	FP2DG Nominal	FP2DG Trade 1	FP2DG Trade 2
Nominal	0	0	0
Mean	0	0	0
3-sigma	0	0	0
1.00 %-tile	0	0	0
99.00 %-tile	0	0	0.01
Max Value	0	0	0.02
Min Value	0	0	0
Success	8000	8000	8000
Percent	100	100	100

Figure 7.29. Total range at touchdown for 8000 Monte Carlo cases in a human-scale Mars landing mission with a factor of safety = 1.0.

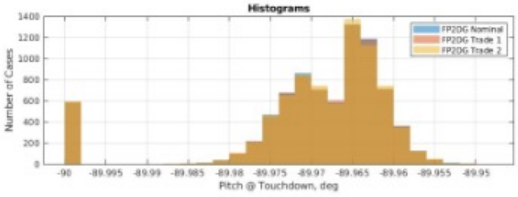

	FP2DG Nominal	FP2DG Trade 1	FP2DG Trade 2
Nominal	-89.97	-89.97	-89.97
Mean	-89.97	-89.97	-89.97
3-sigma	0.03	0.03	0.03
1.00 %-tile	-90	-90	-90
99.00 %-tile	-89.96	-89.96	-89.96
Max Value	-89.95	-89.95	-89.95
Min Value	-90	-90	-90
Success	8000	8000	8000
Percent	100	100	100

Figure 7.30. Pitch at touchdown for 8000 Monte Carlo cases in a human-scale Mars landing mission with a factor of safety = 1.0.

Figures 7.29, 7.30, and 7.31 show the Monte Carlo statistics when the vehicle arrives on the ground. A measure of the total range to the landing site is gathered in

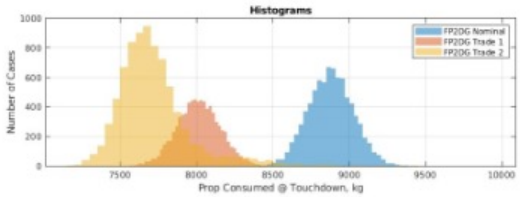

	FP2DG Nominal	FP2DG Trade 1	FP2DG Trade 2
Nominal	8867.3	8051.2	7665.6
Mean	8880.2	8013.3	7720.7
3-sigma	440.93	426.09	737.61
1.00 %-tile	8544.6	7680.3	7320.7
99.00 %-tile	9225.2	8344.5	8582.3
Max Value	9423.6	8515.8	9926
Min Value	8359.5	7521.7	7173.8
Success	8000	8000	8000
Percent	100	100	100

Figure 7.31. Propellant consumed at touchdown for 8000 Monte Carlo cases in a human-scale Mars landing mission with a factor of safety = 1.0.

Figure 7.29. The total range evaluates the distance from the vehicle to the landing site. At touchdown, all three cases achieve total ranges that are in the order of $10^{-}3$. The total range values appear as zero because the statistics shown in the plot only allow up to 2 decimal places. In Trade 2, the maximum value is of 20 meters away from the landing site. This is expected since Trade 2 is flying a very low trajectory with more restricted control. Even in these situations, the total range is so small that it is not a cause for concern. During vertical descent and at touchdown, it is necessary to point the vehicle in the correct direction to avoid any horizontal velocity. A -90.0 degree pitch corresponds to the correct position to start vertical descent. Figure 7.30 shows the resulting pitch at touchdown in this Monte Carlo test. All three cases were able to achieve a vertical descent with a pitch near -90.0 deg. The mean pitch angle in all cases deviates from -90.0 deg by 0.03 degrees, which is essentially a straight vertical descent. Finally, propellant consumption using FNPEG and FP^{2}DG with different configurations is compared in Figure 7.31. In this figure, the effect of PDI condition and tuning parameters on propellant consumption can

be appreciated. The propellant consumed by all three cases followed a similar trend than what was observed in the nominal cases. The smallest mean propellant consumed was of 7720.7 kg by Trade 2, while the greatest propellant consumed was a total of 8880.2 kg by the nominal case. Trade 1 obtained a propellant consumption of 8013.3 kg, a considerably lower propellant consumption against the nominal case given that the only difference was a reduction in entry target conditions. Trade 2 also holds a more conservative propellant spread with a 426.09 kg 3-sigma variation. Trade 3 spent a little more fuel in some cases, bringing the variation to 737.61 kg. Again, this is attributed to the fact that the guidance is flying a more limiting trajectory.

The importance of these trade studies is to show the ability of FNPEG + FP^{2}DG to accommodate rigorous dispersions. Additionally, tuning the entry and powered descent guidance offers a reduction in propellant consumption that bring the total mass of the vehicle down by up to 1.1 tons. Naturally, this comes at the cost of rigorous flying conditions that might need to be revised to make sure it meets the requirements of a crewed mission. The important takeaway is that this test allows the discovery of the maximum performance that can be attained by the algorithm before other constraints are included. Using the full potential of the entry guidance algorithm to target a better PDI condition is fundamental for the acquisition of these results. A better PDI condition reduces the amount of flight time and thrust setting, resulting in a smaller amount of propellant needed to accomplish the mission successfully.

7.8 Summary

Trade studies on entry and powered descent guidance using the HIAD vehicle on a crewed mission to Mars were completed successfully. Despite all the effort to develop new guidance algorithms, it is not often that multiple of these algorithms are tested and compared under similar conditions. Different simulation environments, atmospheric models, computational power, and other factors affect the reproduction of the results under the same circumstances. A comprehensive evaluation of two entry guidance algorithms and two powered descent guidance algorithms has been realized to assess the performance of modern EDL control methods. Three trade studies were generated by a combination of these algorithms and the result of this analysis provides some feedback about the current capability available when tested under similar conditions. The studies performed demonstrate that both direct force and bank angle control during entry can supply a proper PDI condition to allow a successful landing by the powered descent guidance. The effectiveness of the NPCG and FP^{2}DG powered descent approaches was demonstrated under randomized uncertainty in Monte Carlo simulations. All guidance approaches exhibited similar propellant consumption characteristics in 3-DOF simulation. Furthermore, updates on the PDI condition and tuning parameters of the FP^{2}DG approach produced an overall reduction of propellant reduction in 3-DOF and Monte Carlo simulations. The outcome of this study provides a better understanding of the characteristics given by each approach and encourages further development on parameter tuning and optimization to extract better performance.

Most importantly, the ability to integrate a robust entry guidance algorithm with a propellant-optimal powered descent guidance algorithm successfully leads to a strong foundation required for the complete EDL optimization achieved in Chapter 8. Particularly, the FP^{2}DG studies in Section 7.7 reveal that the hand-off point between entry and powered descent can lead to a worse propellant consumption if not properly selected, even when using a propellant-optimal powered descent guidance. This is the motivation for the fully optimized EDL trajectory in the following chapter.

Chapter 7, in full, is a reprint of the material as it appears in Simulation Comparison of Entry and Powered Descent Guidance Algorithms for a Human-Scale Mars Mission, 2022. Sandoval, Sergio; Lugo, Rafael; Lu, Ping; Cianciolo, Alicia. The dissertation author was the primary investigator and author of this paper.

Chapter 8

Optimization of End-to-End Human-Scale Mars Landing Mission

8.1 Introduction

In Section 7, the demonstration of a human-scale Mars landing mission was shown. Integration of the entry and powered descent guidance algorithms resulted in a complete EDL trajectory that successfully delivered a vehicle from the entry condition to the landing location on the ground. To satisfy the safety and accuracy requirements, the guidance algorithms were exposed to the most stringent conditions. One of the main goals of Section 7 was to evaluate the performance and strengths of each algorithm and validate that a complete EDL trajectory can be achieved with the integration of both algorithms. The use of a PDI logic, described in Section 3.3.4, helped identify the near-optimal powered descent starting condition to minimize the propellant-consumption during powered descent subject to the entry trajectory produced by the entry guidance. However, the EDL trajectory falls short of being optimal given the lack of optimization during the entry phase. Using the PDI logic propellant consumption can be improved, but it does not mean that the complete EDL solution is optimal in any sense.

In this chapter, a new approach is presented for the end-to-end optimization of an EDL problem. By taking advantage of the strong foundation that the entry and powered descent algorithms implemented, and transforming the problem into a hybrid-optimal-control problem, it is possible to obtain an EDL solution with near-optimality. The development of this approach, all the assumptions to guarantee convergence and extensive demonstrations of robustness will be shown in the following sections.

8.2 End-to-End Fuel-Optimal Entry and Powered-Descent Problem

8.2.1 Entry-Flight Dynamics for a Gliding Vehicle About an Oblate Planet

In general, the equations of motion for entry flight are of the same form as Equations 2.1-2.6. However, the terms for velocity, flight-path-angle, and heading angle rates do not take into account the oblateness of the planet. To increase model fidelity, the 3-dimensional equations of motion for a gliding vehicle on a rotating, oblate planet, using non-dimensional variables, are as follows:

$$\dot{r} = V \sin\gamma \tag{8.1}$$

$$\dot{\theta} = \frac{V \cos\gamma \sin\psi}{r \cos\phi} \tag{8.2}$$

$$\dot{\phi} = \frac{V \cos\gamma \cos\psi}{r} \tag{8.3}$$

$$\dot{V} = -D - g_r \sin\gamma - g_\phi \cos\gamma \cos\psi + \Omega^2 r \cos\phi \left(\sin\gamma \cos\phi - \cos\gamma \sin\phi \cos\psi\right) \tag{8.4}$$

$$\dot{\gamma} = \frac{1}{V}\left[L\cos\sigma + \left(V^2/r - g_r\right)\cos\gamma + g_\phi \sin\gamma \cos\psi + 2\Omega V \cos\phi \sin\psi \right.$$
$$\left. + \Omega^2 r \cos\phi \left(\cos\gamma \cos\phi + \sin\gamma \cos\psi \sin\phi\right)\right] \tag{8.5}$$

$$\dot{\psi} = \frac{1}{V}\left[\frac{L\sin\sigma}{\cos\gamma} + \frac{V^2}{r}\cos\gamma \sin\psi \tan\phi + g_\phi \frac{\sin\psi}{\cos\gamma}\right.$$
$$\left. -2\Omega V(\tan\gamma \cos\psi \cos\phi - \sin\phi) + \frac{\Omega^2 r}{\cos\gamma}\sin\psi \sin\phi \cos\phi\right] \tag{8.6}$$

with the same variable definitions and nondimensionalization technique as described in Section 2.2.1. The only additional terms are g_r and g_ϕ described in the following way:

$$g_r = \frac{1}{r^2}\left[1 + J_2\left(\frac{1}{r}\right)^2\left(1.5 - 4.5\sin^2\phi\right)\right] \tag{8.7}$$

$$g_\phi = \frac{1}{r^2}\left[J_2\left(\frac{1}{r}\right)^2\left(3\sin\phi\cos\phi\right)\right] \tag{8.8}$$

In equations 8.7 and 8.8, J_2 is defined as the planet zonal gravitational coefficient. The value of J_2 varies depending on the planet under investigation, for Mars $J_2 = 1.96045 \times 10^{-3}$ while for Earth $J_2 = 1.08263 \times 10^{-3}$.

The high nonlinearity of the entry guidance problem has been previously mentioned, and the addition of the gravitational components in Equations 8.7-8.8 do not make the problem any simpler. However, it will be shown that for an entry guidance such as FNPEG, the addition of these terms do not jeopardize its fast convergence and reliability. Therefore, the additional fidelity helps create a more accurate simulation environment.

Given the entry dynamics defined in Equations 8.1-8.6, the entry state will be defined as follows:

$$\boldsymbol{x}_e = (r, \theta, \phi, V, \gamma, \psi) \in \mathbb{R}^6 \tag{8.9}$$

The initial condition $\boldsymbol{x}_e(0)$ is assumed to be given. The entry guidance problem consists in obtaining the bank angle control $\sigma(t)$ on the time interval $t \in [t_0, t_{PDI}]$. The initial time t_0 starts at the entry interface, while t_{PDI} is the to-be-determined time at the end of entry. The bank angle control is subject to the constraint in Equation 2.18. Other path constraints on the trajectory such as heat rate, dynamic rate, or load limit can be included as exemplified in Lu [21]. The application of this control should result in a trajectory with a final state $\boldsymbol{x}_e(t_{PDI})$ that permits the safe and successful landing of the vehicle using a propellant-optimal powered descent guidance.

The entry guidance algorithm used to generate the entry trajectory will be FNPEG, described in more detail in Section 3.2.1. The variable e is used as the independent variable in the formulation of FNPEG and in this work.

8.2.2 Powered Descent Guidance Equations of Motion

In the powered descent guidance problem, the three-dimensional equations of motion in a Cartesian coordinate frame over a flat planet surface when the aerodynamic forces are ignored are represented by Equations 2.19 - 2.21 defined in Section 2.2.2. The initial conditions for the powered descent problem are given by:

$$\boldsymbol{r}(t_{PDI}) = \boldsymbol{r}_{PDI} \tag{8.10}$$

$$\boldsymbol{V}(t_{PDI}) = \boldsymbol{V}_{PDI} \tag{8.11}$$

$$m(t_{PDI}) = m_{PDI} \tag{8.12}$$

The variables $\boldsymbol{r}$, $\boldsymbol{V}$, and $\boldsymbol{g}$ are the position, velocity, and gravitation acceleration vectors in the topocentric reference frame. The gravitational acceleration vector is defined as a constant with magnitude g_0. t_{PDI} is the time when the powered descent phase starts, the PDI condition that needs to be determined and that corresponds to the final condition of entry phase. At PDI, a smooth transition between entry and powered descent must occur. The rocket jet engine thrust, T, is constrained by the following upper and lower bounds:

$$T_{min} \leq T \leq T_{max} \tag{8.13}$$

Operationally, it is difficult to turn back on an engine during the powered descent

phase and it should only be allowed to change throttle within a specified range. To avoid the complete shut down of the engine during the short duration of powered descent, $T_{min} > 0$. The rocket exhaust velocity is defined as a constant and must adhere to the constraint $V_e > 0$. The last remaining constraint for powered descent is on throttle direction:

$$\mathbf{1}_T^T \mathbf{1}_T = 1 \tag{8.14}$$

Where $\mathbf{1}_T \in \mathbb{R}^3$ is the unit vector that defines the thrust direction. Te state and control vectors for the powered descent phase will be denoted by:

$$\boldsymbol{x}_p = (\boldsymbol{r}^T, \boldsymbol{V}^T, m)^T \in \mathbb{R}^7 \tag{8.15}$$

$$\boldsymbol{u}_p = (T, \mathbf{1}_T^T)^T \in \mathbb{R}^4 \tag{8.16}$$

A topocentric frame with the origin at the landing location will be used for powered descent. Figure 3.2 is an illustration of the topocentric coordinate system. The targeting conditions in powered descent are those of the "pinpoint landing" defined on Section 2.2.2. With Equations 3.14 and 3.15 defining the terminal position and velocity conditions at the landing site. In the topocentric frame, a final position of $\boldsymbol{r}_f^* = 0$ indicates a landing at the predefined landing location. The time $t_f > t_{PDI}$ is the final time to be determined.

8.3 Hybrid-Optimal-Control Problem

To design the complete EDL optimization problem it is necessary to understand that entry and powered descent have different states, constraints and final conditions. Solving the end-to-end trajectory optimization problem requires that each guidance problem be treated separately while solving the same minimization problem together. In order to smoothly transition from one guidance algorithm to the other, it is necessary to design the problem in such a way that current state is transmitted between the two phases. When this transition point is added, the problem becomes an Hybrid-Optimal-Control (HOC) Problem. The HOC problem allows both phases to be considered in the overall problem description while keeping their individual dynamics and constraints separated during the optimization process. In this formulation, the entry dynamics will be denoted by Equations 8.1 - 8.6 and the following entry trajectory constraints:

$$\dot{\boldsymbol{x}}_e = \boldsymbol{f}_e(\boldsymbol{x}_e, \sigma), \quad \boldsymbol{x}_e(0) = \boldsymbol{x}_{EI} \tag{8.17}$$

$$\boldsymbol{h}_e(\boldsymbol{x}_e(t), \sigma(t)) \leq 0, \quad t \in [0, t_{PDI}] \tag{8.18}$$

where $\boldsymbol{x}_{EI}$ defines the known state at entry interface (EI) or at a point after EI; and $t_{PDI} > 0$ is the to-be-determined time for powered descent initiation (PDI), when powered descent begins. The constraints in the entry phase consist of Equation (2.18) and any other trajectory constrained imposed for safety, operational or mission dependent considerations. Examples of possible constraints are aerodynamic load, heat rate, and dynamic pressure

limits. Lu [21] describes how these constraints are implemented in FNPEG.

For powered descent, a similar approach is taken to define the system dynamics and constraints. In this case, the initial point begins at PDI after the entry phase is complete. In mathematical terms, this would be defined during the time interval $[t_{PDI}, t_f]$, where $t_f > t_{PDI}$ is the final time to be determined. The following equations define the system during powered descent:

$$\dot{\boldsymbol{x}}_p = \boldsymbol{f}_p(\boldsymbol{x}_p, \boldsymbol{u}_p) \tag{8.19}$$

$$\boldsymbol{h}_p\left(\boldsymbol{x}_p(t), \boldsymbol{u}_p(t)\right) \leq 0, \quad t \in [t_{PDI}, t_f] \tag{8.20}$$

$$\boldsymbol{s}\left(\boldsymbol{x}_p(t_f)\right) = 0 \tag{8.21}$$

in which the state equations are defined by Equations 2.19 - 2.21 and the initial conditions by Equations 8.10 - 8.12. The inequality constraints include Equations 8.13 and 8.14. Equation 8.14 can be included using the fact that equality constraints of the form $f(x) = 0$ can be separated into two inequality constraints of the form $f(x) \leq 0$ and $-f(x) \leq 0$. An additional inequality constraint on the thrust pointing direction can be added for further attitude control. Lu [107] provides details on the implementation of such a constraint. The "pinpoint landing" constraints in Equations 3.14 and 3.15 represent the terminal constraints at t_f.

At the transition point between entry and powered descent, the state in both phases must be equal. The initial condition for $\boldsymbol{x}_p$, also known as the PDI condition, is defined as:

$$\boldsymbol{x}_p(t_{PDI}) = \boldsymbol{q}(\boldsymbol{x}_e(t_{PDI})) := \boldsymbol{x}_{PDI} \tag{8.22}$$

The term $\boldsymbol{q}(\cdot) : \mathbb{R}^6 \rightarrow \mathbb{R}^7$ is a nonlinear coordinate transformation or mapping from $\boldsymbol{x}_e$ to $\boldsymbol{x}_p$. This transformation is necessary to convert the state variables in the entry system to the variables that will be used in powered descent. Since mass was constant during entry, the term $q_7(\cdot)$ was added as $m(t_{PDI}) = m_{PDI} = m_0$ for powered descent. In this case, there was no jettison of an aeroshell or any mass depletion before powered descent. If jettison of any spacecraft structure is planned, then $m_{PDI} < m_0$.

Hybrid-Optimal-Control Problem Definition

The solution to the hybrid-optimal-control problem consists in finding: the transition time t_{PDI}, the final time t_f where $t_f > t_{PDI}$, a piecewise continuous $\sigma(t)$ for $t \in [0, t_{PDI}]$, and a piecewise continuous $\boldsymbol{u}_p(t)$ for $t \in [t_{PDI}, t_f]$, such that the trajectory constructed by the entry system in Equations 8.17 - 8.18 in $[0, t_{PDI}]$, and then by the powered descent system in Equations 8.19 - 8.21 with the initial condition in Equation 8.22, minimizes the propellant consumption in the powered descent phase during $[t_{PDI}, t_f]$ and represented by the performance index

$$J = m_0 - m(t_f) \tag{8.23}$$

8.4 Solution via Bi-Level Optimization Approach

8.4.1 Bi-Level Optimization Problem and Algorithm

The entry dynamics in Equations (8.1) - (8.6) are complex and highly nonlinear. Adding a powered descent phase to produce a complete EDL problem is more challenging, but possible, as shown in Section 7. To solve an entry trajectory optimization problem is a difficult operation that requires many assumptions and problem manipulation. However, uniting entry and powered descent in a complete EDL trajectory optimization problem is a very ambitious objective that has hardly ever produced any results in the literature. The reason is that transforming the equations of the problem into any optimization systems requires the introduction of a large number of new variables and an immense amount of algebraic manipulation. Wan [121] is an example of the transformation of the EDL problem into a quadratic-polynomial system. If the problem is able to be transformed into a QCQP problem, it will be a large-scale problem with a long convergence time. Furthermore, the problem is highly simplified demonstration of a 2-dimensional solution and not a trajectory that can be readily flown by a real vehicle. It exposes the difficulty of finding the optimal solution of the EDL problem. Another method of optimization is to use an entry and powered descent guidance in a high-fidelity simulation environment to calculate thousands of trajectories and recording the propellant consumption in each trajectory. The propellant consumption is compared and the trajectory that produces the least amount of propellant is selected as the optimized trajectory. Multiple parameters in the entry and powered descent guidance can be changed as the optimization is occurring to provide better trajectory shaping and propellant consumption. The argument against this

method is that it is an arduous undertaking as it requires a lot of computational power and it can only predict one optimized trajectory. During flight, any changes in initial or atmospheric conditions have the potential of making the trajectory unattainable.

The options to solve a problem of this magnitude are limited. A different approach offers a fast and robust solution to the EDL optimization problem. Rather than optimizing the entry algorithm itself, it is possible to leverage the strengths of a highly reliable entry guidance algorithm to produce a better trajectory to start powered descent. The high dependency of powered descent on the initial condition point towards the final entry condition as the most important aspect of optimization. However, as important as the PDI condition is to start powered descent, the trajectory flown by the vehicle also affects its position and velocity, making it crucial in the propellant-minimization process. The method developed in this work is a bi-level optimization approach that uses FNPEG, an entry guidance algorithm demonstrated to be accurate and highly robust [31] and G-POLAR, a propellant-optimal powered descent guidance [107] to produce an optimized end-to-end EDL solution rapidly and efficiently.

Given a PDI condition $\boldsymbol{x}_p(t_{PDI})$ produced by the entry guidance, the fuel-optimal powered descent guidance algorithm finds a solution to the problem posed in Equations (8.19) - (8.21) that minimizes the performance index in Equation (8.23). The solution to the hybrid-optimal-control problem defined in the previous section is found by determining the best PDI condition $\boldsymbol{x}_p(t_{PDI})$ to start powered descent. In other words, the solution consists in finding the final entry phase state $\boldsymbol{x}_e(t_{PDI})$ that leads to the overall minimum propellant consumption in the powered descent phase. The propellant-optimal powered

descent guidance already find the minimum propellant consumption possible during powered descent using GPOLAR. However, there is no optimization of the entry guidance trajectory computed by FNPEG. To optimize the entry trajectory, and subsequently the complete EDL trajectory, the problem is formulated as a bi-level optimization problem. In the bi-level optimization approach, an inner optimization loop in obtains the powered descent trajectory with the least fuel consumption given a PDI condition $\boldsymbol{x}_p(t_{PDI})$, while an outer loop optimizes the entry trajectory to provide a terminal state $\boldsymbol{x}_e(t_{PDI})$ of the system defined by Equations (8.17) - (8.18) such that the corresponding $\boldsymbol{x}_p(t_{PDI})$ from Equation 8.22 results in the smallest propellant consumption by the inner loop optimization.

In order to select the entry trajectory that minimizes the propellant consumption during powered descent, multiple trajectories need to be produced and compared. There are two ways to accomplish this using FNPEG. The first option is to change the target altitude and velocity, consequently changing the final energy e_f at which the target range is achieved. The second, and less obvious option, is to modify the final bank angle target σ_f to alter the linear bank angle profile. This is a simple parameter that is usually selected as a constant, but that can influence the entry trajectory enormously. In this work, it was discovered that changing the final bank angle target results in a greater propellant consumption reduction and was used for the demonstration of results in the following sections. In addition, Section 8.9 provides evidence showing that changing the final altitude and velocity targets achieves minimal changes in propellant consumption if the adaptive PDI logic is active.

In the bi-level optimization approach, the parameter σ_f is determined by the outer

loop optimization. The outer optimization is an unconstrained univariate minimization problem on $sigma_f$ to minimize the cost function J. FNPEG is run in a closed-loop simulation to find σ_0 and determine the guidance command σ for entry flight. The dynamics and constraints in the entry system are satisfied by the closed-loop simulation. The optimization is an iterative process to determine for which value of σ_f the trajectory produced will yield the lowest propellant consumption. Each cost evaluation in the outer loop corresponds to a different value of $sigma_f$. To successfully achieve the desired result, appropriate bounds on the entry control σ_f of the form $\sigma_{min} \geq \sigma_{f_{min}}$ and $\sigma_{f_{max}} \leq \sigma_{max}$ need to be added such that the bank angle limit in Equation 2.18 is satisfied.

During entry-flight, changes in initial and atmospheric conditions affect the course of the trajectory. Therefore, it is unrealistic to assume that the nominal trajectory will be flown. Multiple studies have shown that the PDI condition depends significantly on the entry trajectory flown. Consequently, the starting condition for powered descent determines how much propellant can be saved. To account for these changes, an adaptive PDI logic is implemented. As the trajectory flies towards the designated entry final condition in the closed-loop simulation, the adaptive PDI logic examines the current state to decide the best PDI condition to start powered descent. When an appropriate PDI condition is found, a signal is sent to handover the vehicle from the entry guidance to the powered descent guidance immediately. Besides making a difference between success and failure of the mission, the predicted time-to-go for optimal soft-landing solution powered descent is calculated by the PDI logic, providing the best starting point to initiate powered descent [109]. Notice that by adding the PDI logic, the transition time t_{PDI} is not found

explicitly by the optimization loop. The adaptive PDI logic is a more effective way of transitioning between entry and powered descent, with the added benefit of providing a custom PDI condition during every mission scenario. More details on the working principle of the adaptive PDI logic can be found on Section 3.3.4.

Once the PDI logic has identified an appropriate PDI condition, the entry phase terminates and the powered descent takes over. Thus, the inner loop optimization begins. In the inner loop, optimization of the powered descent guidance is performed to obtain the optimal propellant consumption. In this work, the G-POLAR algorithm is used to calculate the fuel-optimal powered descent solution from the PDI condition. The dynamics and constraints for powered descent are satisfied by G-POLAR. The minimum propellant consumption is obtained given the initial conditions provided by the entry guidance trajectory and the PDI logic. More details on how the inner optimization loop is performed can be found on Sections 3.3.2 and 3.3.3. The cost function J is assigned the value of the optimal propellant consumption. The outer optimization is solved by the Golden-Section search method [122] in the interval $[\sigma_{f_{min}}, \sigma_{f_{max}}]$.

Once a complete iteration from entry to powered descent is completed, a cost function evaluation with respect to the optimization variable σ_f in the outer loop is completed. Subsequent evaluations calculate the optimal propellant consumption for multiple values of σ_f according to the process of the outer optimization algorithm. At some point, the optimal value of σ_f that yields the lowest value of J by G-POLAR will be found. A *near-optimal* solution to the HOC problem has been found once the outer loop optimization converges. For better visualization, an optimization step using the bi-level

optimization approach developed in this work can be seen in Figure 8.1

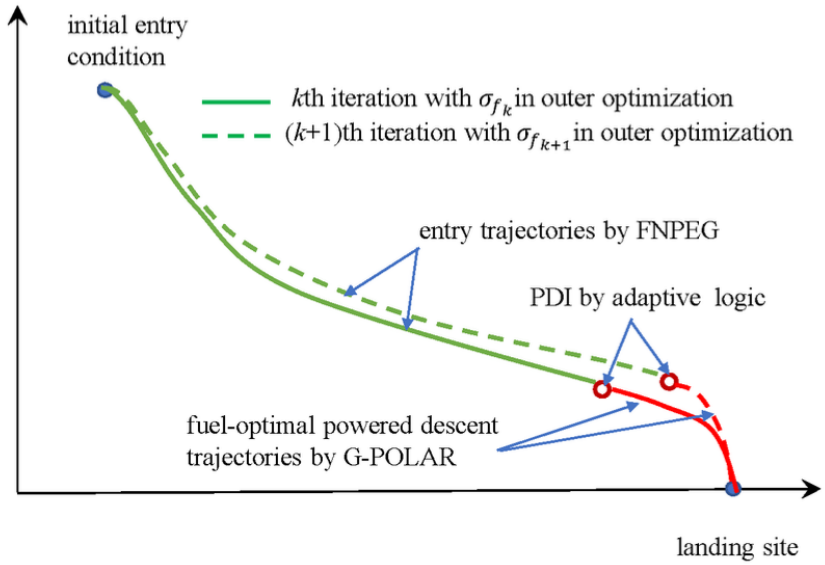

Figure 8.1. Flowchart of EDL trajectory generation in bi-level optimization approach iterations.

The solution of the bi-level optimization approach is *near-optimal*, rather than strictly optimal. To understand the reasoning behind this assumption it is important to analyze two important factors in the development of this problem and its solution:

- The low-dimension of the univariate parameterization of the bank angle magnitude profile
- The determination of a near-optimal PDI point by the adaptive PDI logic

Both of these factors provide approximations that facilitate the solution of the problem and are justified by the following logic. The low dimensionality of the univariate parameterization arises from the fact that in entry-flight the bank angle is executed by the attitude control system of the vehicle. Higher-order representations of the bank angle

profile can have rapid and large variations that might make it harder to control the vehicle precisely. Therefore, a monotonic and slow-varying bank angle magnitude profile provides is preferred. The simplest form of a bank angle profile with those characteristics is a linear profile such as the one in Figure 3.1. There is no substantial loss of performance by the selection of the linear profile, instead it is more operationally desirable. The other factor concerns the use of the adaptive PDI logic to find the transition point at t_{PDI}. As mentioned before, the PDI condition found by this technique is a result of the propellant-optimal soft-landing powered descent solution. The propellant consumption in the soft-landing problem is the lowest possible propellant consumption among the three different landing problems stated in Section 3.3.2. The approximated time-to-go and PDI condition predicted by the soft-landing solution is a close as possible to the optimal time-to-go in the pinpoint landing solution. Because the time-to-go is not exactly the same in these two problems, it can only be inferred that the solution is near-optimal. The algorithmic description of the complete bi-level optimization process is shown in Figure 8.2.

Since both FNPEG and G-POLAR have been successful in extensive testing, the strengths of these algorithms are immediately transferred to this method. An advantage of the proposed method is that no major changes in the algorithms and software are necessary for on-board implementation. The capability of optimizing an end-to-end EDL trajectory is readily available with the same algorithms that might be already resting in the guidance system on-board the vehicle.

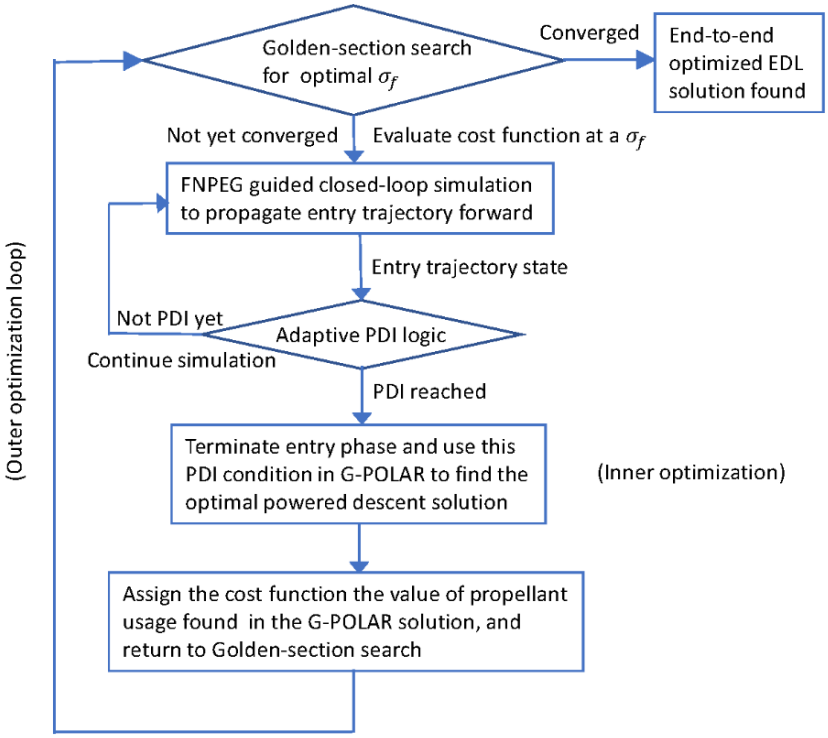

Figure 8.2. Bi-level optimization algorithm description.

8.4.2 Guaranteed Convergence in Bi-Level Optimization Algorithm

A critical consideration of this algorithm is its reliability to convergence. In such a sensitive environment such as space exploration, it is necessary to have an assurance that a solution will be found that meets the minimum requirements for a safe and successful mission. To provide such a guarantee, the following assumptions need to be taken into consideration:

Assumptions

1. For the given initial condition on the entry phase and vehicle models:

   $\exists\,[\sigma_{f_{min}}, \sigma_{f_{max}}] \subset [\sigma_{min}, \sigma_{max}] \quad s.t. \quad \forall \sigma_f \in [\sigma_{f_{min}}, \sigma_{f_{max}}]$, there is an end-to-end

entry and (fuel-optimal) powered descent trajectory, found by FNPEG and G-POLAR, as described in the outer optimization loop of Figure 8.2.

2. The models for the atmosphere, aerodynamic coefficients, and any other parameters used to find the FNPEG guidance solution and closed-loop simulation are C^1 (i.e., they have continuous first-order partial derivatives with respect to the trajectory state variables).

3. Any numerical integration errors in the closed-loop simulation are sufficiently small and can be ignored for analysis purposes.

Analysis

Assumption 1 implies not only that FNPEG will generate a feasible entry trajectory for every $\sigma_f \in [\sigma_{f_{min}}, \sigma_{f_{max}}]$, but also that the adaptive PDI logic will produce along this entry trajectory a PDI condition that allows G-POLAR to successfully find a pinpoint-landing solution. The first part of this implication is very reasonable, both from the hysics of the entry problem and the proven capability of FNPEG. The second part is supported by the extensive emprical evidence of tens of thousands of Monte Carlo closed-loop simulations in Lu [107], Sandoval [62], and Lu [61], where the PDI logic has been demonstrated to produce successful PDI conditions in all of those dispersed entry trajectories.

Assumption 2 is already the normal setting in a well prepared entry trajectory optimization problem.

Assumption 3 allows us to focus on the central tenet of generating the entry trajectory without being buged down on non-essential factors.

Proposition

Under the previous assumptions, a conclusion on the existence of the minimum of the bi-level optimization problem and the convergence of the bi-level optimization algorithm is presented as follows:

> There exists a minimum for the bi-level optimization problem at some $\sigma_f^* \in [\sigma_{f_{min}}, \sigma_{f_max}]$ with the guaranteed convergence of the algorithm proposed in Figure 8.2.

Proof

The reasoning behind *Assumption 1* has been already analysed in the previous section, where a feasible entry trajectory can be generated for every $\sigma_f \in [\sigma_{f_{min}}, \sigma_{f_{max}}]$. From the physics of the entry problem, this is a reasonable assumption that can be accomplished with the linear bank angle magnitude profile from Figure 3.1. The proven capability of FNPEG in exhaustive testing testifies that such an assumption is guaranteed. Similarly, extensive testing of the powered descent guidance on thousands of dispersed closed-loop simulations defend this assumption when an adequate PDI condition is provided. The adaptive PDI logic ensures that an appropriate PDI condition is always selected. Thus, making it possible to generate a complete end-to-end trajectory successfully.

Assumption 2 indicates that the right-hand sides of the entry dynamics equations (8.1) - (8.6) are continuously differentiable with respect to the state vector $\boldsymbol{x}_e$ for $\boldsymbol{x}_e \in S \in \mathbb{R}^6$, where S is a set that includes all reasonably possible values of $\boldsymbol{x}_e$ along the entry trajectory, that is, nothing close to $r = 0$, $V = 0$, $\gamma = \pm\pi/2$, or similar. Furthermore, the right-hand sides of Equations (8.5) and (8.6) are continuously differentiable with respect

to σ represented in FNPEG by:

$$|\sigma| = \sigma_0 + \frac{e - e_0}{e_f - e_0}(\sigma_f - \sigma_0) \tag{8.24}$$

If the bank reversals in entry-flight are ignored and only the absolute value of σ is considered in Equation 8.24, then the right-hand sides of the entry dynamic equations are also continuously differentiable with respect to σ_f. By the theory of continuous dependence of solutions of ordinary differential equations (ODEs) on parameters [123], the entry trajectory generated by FNPEG is continuously dependent on σ_f. That is, the state $\boldsymbol{x}_e(t)$ at any point on the entry trajectory is a continuous function of σ_f.

Given that the models and initial condition for the closed-loop simulation and FNPEG are the same for the entry phase, *Assumption 3* implies that the FNPEG solution can be used directly to represent the entry trajectory.

In G-POLAR, the optimal thrust magnitude T^* is represented by a continuously differentiable function that closely approximates the bang-bang optimal thrust magnitude [107]. The optimal thrust direction $\mathbf{1}_T^*$ is also a continuously differentiable vector function [107]. Both T^* and 1_T^* are C^1 functions of certain solution parameters that depend on the initial condition $\boldsymbol{x}_{PDI}$ of the powered descent phase in a continuously differentiable fashion. Therefore, the right-hand sides of the powered descent dynamic equations are continuously differentiable with respect to the state vector $\boldsymbol{x}_p$ and those solution parameters. By repeated use of the theory of continuous dependence of solutions of ODEs on initial condition and parameters [123], we conclude that the final state of the G-POLAR solution $\boldsymbol{x}_p(t_f)$, in particular the final mass $m(t_f)$, is a continuous function of

the PDI condition $\boldsymbol{x}_p(t_{PDI}$.

The adaptive PDI logic in Figure 3.3 uses the final ground-range traveled in the soft-landing solution from G-POLAR starting from a point on the entry trajectory. By combining the continuous dependence of the final state of the soft-landing trajectory on the initial condition, and the continuous dependence of the state at any point along the entry trajectory on σ_f, we have that the state $\boldsymbol{x}_e(t_{PDI}$ on the entry trajectory where the PDI logic declares PDI is a continuous function of σ_f. The nonlinear coordinate transformation $\boldsymbol{q}(\cdot)$ in Equation 8.22 is continuous, hence the PDI condition $\boldsymbol{x}_{PDI} = \boldsymbol{x}_p(t_{PDI})$ is a continuous function of σ_f.

Using the standard result in calculus that a composite function formed by two continuous functions is also continuous with respect to the independent variable, we conclude that the cost function of the outer optimization in Equation 8.23 is a continuous function of σ_f. By the Weierstrass Theorem [124], J has a minimum with respect to σ_f in the closed interval $[\sigma_{f_{min}}, \sigma_{f_{max}}]$. The second part of the *Proposition*, the convergence of the outer optimization loop, follows the fact that just like the bi-section search, the Golden-Section search in the outer optimization is guaranteed to converge to an extreme of a continuous univariate function in a closed interval.

To complete the argument, let us consider the effects of the bank reversals in FNPEG. With the instantaneous bank reversals, the right-hand sides of Equations 8.5 and 8.6 are piecewise continuously differentiable with respect to σ_f, and the state $\boldsymbol{x}_e(t)$ is continuous at the instants of bank reversals. Therefore, by applying the continuous dependence arguments along each continuously differentiable segment sequentially on the

entry trajectory, we can still arrive at the conclusion that the state $\boldsymbol{x}_e(t)$ is continuously dependent on σ_f at any point along the entry trajectory, thus the claims in the *Proposition* can be proved in the same way.

■

The *Proposition* does not assert that the solution the Golden-Section search converges to is necessary the solution that results in the (global) minimum of J in $[\sigma_{f_{min}}, \sigma_{f_{max}}]$. This is because if J has multiple local minima in $[\sigma_{f_{min}}, \sigma_{f_{max}}]$, the Golden-Section search can potentially converge to a local minimum of J. On the other hand, if J is uni-modal (in minimum) in $[\sigma_{f_{min}}, \sigma_{f_{max}}]$ (which will be true if $(\sigma_{f_{max}} - \sigma_{f_{min}})$ is sufficiently small, or the interval $[\sigma_{f_{min}}, \sigma_{f_{max}}]$ happens just to bracket only the minimum), the Golden-Section search will be guaranteed to converge to the minimum of J in $[\sigma_{f_{min}}, \sigma_{f_{max}}]$.

Corollary

In addition to the three assumptions highlighted above, if the cost function of the outer optimization loop in the bi-level optimization algorithm is uni-modal in minimum with respect to $\sigma_f \in [\sigma_{f_{min}}, \sigma_{f_{max}}]$, the bi-level optimization algorithm is guaranteed to converge to the minimum of the cost function in $[\sigma_{f_{min}}, \sigma_{f_{max}}]$.

8.5 End-to-End Trajectory Simulation Strategy

The FNPEG algorithm will guide the vehicle during the entry phase. For powered descent, G-POLAR will calculate the thrust and thrust direction to reach the landing location. Each algorithm is able to produce a feasible trajectory internally given the initial

condition, in this sense, FNPEG and G-POLAR are independent components that are integrated together for a complete EDL optimization process.

One benefit of using FNPEG in closed-loop simulation is that the adaptive PDI logic can be readily applied as the vehicle flies the entry trajectory. For our purposes, it is important to determine the PDI condition appropriately for the optimization to work. The PDI logic is an important component of the bi-level optimization approach as it dictates the near-optimal transition point between entry and powered descent. However, since FNPEG generates a complete 3-DOF feasible entry trajectory in the solution process, it is possible to apply the PDI logic to the stored entry trajectory without using closed-loop simulation. The true advantage emerges when a higher-fidelity simulation environment is desired.

To generate a trajectory rapidly, as is it would be required for on-board generation of trajectories, the optimization time inside the guidance algorithms needs to be significantly reduced. Usually, models inside the entry and powered descent guidance algorithms are simplified to improve efficiency. However, reducing the fidelity of the models might diverge from a realistic recreation of the environment. In the description of the bi-level optimization approach, it was mentioned that to generate the entry trajectory, a closed-loop simulation was utilized. While it is possible to generate a complete 3-DOF feasible entry trajectory without closed-loop simulation, implementing a closed-loop simulation during entry offers multiple advantages that were exploited in this investigation.

For a realistic aerospace system, higher fidelity models such as those for aerodynamic coefficients, atmospheric parameters, or propulsion subsystems, result in more accurate

predictions. Simpler models usually converge faster, but this may come at the cost of lower fidelity and trajectories that are far from realistic. If the trajectory produced by simpler models is far from a realistic model, the trajectory may even lack sufficient fidelity to ensure full feasibility, capture important physical characteristics, or inform accurately on the performance. One of the main advantages of using closed-loop simulation is to capitalize on the use of high-fidelity models for trajectory optimization. When higher-fidelity models are used, there is greater confidence in the solution. However, a drawback of high-fidelity models is that they can be data and computationally intensive, and possibly complex to the point of being algorithms on their own [125]. Implementing these models inside the algorithm becomes computationally prohibitive as these models need to be called repeatedly in the optimization process. This problem is similar to one that arises in Multidisciplinary Design Optimization when high-fidelity models are part of the optimization [126, 127].

FNPEG is an iterative process that requires numerical integration of multiple trajectories to find the final guidance solution. When simple low-fidelity models for environment and systems parameters are used, for example, those for atmospheric density and aerodynamic coefficients, the guidance solution is found quickly. If higher-fidelity models are introduced, it is not necessary to add them internally as part of the algorithm, they can simply be added as part of the closed-loop simulation and called every step of the way. The bi-level optimization algorithm presented in Figure 8.2 benefits from this approach as higher-fidelity models for aerodynamic coefficients and atmospheric environments may be used. An outstanding example is to use the Mars Global Reference Atmosphere Model

(Mars GRAM) [128]. Mars GRAM is a large software that containts an engineering-level atmospheric model of Mars. It is used for many diverse applications including mission simulations, systems design, performance analysis, and traejctory planning for EDL, aerobraking, and aerocapture missions [128]. If Mars GRAM was included as part of FNPEG, every iteration on the inside would need to call this big software and the computation time would increase. Instead, a simple aerodynamic model is used internally and Mars GRAM is added as part of the closed-loop simulation. Thus, the complex subsystem and environment models are only integrated once at every closed-loop iteration step along the entry trajectory, rather than multiple times in multiple trajectories. This approach is taken to effectively generate a high-fidelity entry trajectory without suffering from the computational cost from multiple calls to the high-fidelity models.

An additional benefit of running the simulation in closed-loop is that the solution to the optimized end-to-end EDL trajectory and its performance are similar to what can be expected in actual flight if the same guidance algorithm is used. In this case, since FNPEG is designed as an entry guidance algorithm, the trajectory it generates is free of unrealistic flight features such as getting too close to the ground or allowing phugoid oscillations. On the other hand, solutions from an optimal control software can include undesirable and/or unrealistic trajectories in search of all the allowable performance. If not properly managed, the optimal entry guidance problem might produce an unsafe trajectory or one that does not have any control margin left. Basically, most trajectories that extract the most performance try to reach the control limits. Trajectories of this sort are not of practical interest since they cannot be used in actual flight.

The aforementioned advantages on closed-loop simulation can be applied to the powered descent phase to produce a trajectory guided by G-POLAR. The needs during powered descent are different than those seen in entry. A look into the dynamics exhibits how many of these differences depend on the behavior of flight. For instance, a high-fidelity atmospheric model during entry makes a considerable difference in the resulting trajectory. Generally, aerodynamic forces are ignored in the process of solving the powered descent solution. From an optimal control point of view, solving the powered descent dynamics with aerodynamic forces makes the problem too complex to solve or generate a solution reliably. Instead, the optimal powered descent problem can be solved using the indirect method of optimal control and a larger and/or more complex model can be called regularly in a closed-loop simulation. This simple trade-off between internal or external calling of a higher-fidelity model results in a slightly larger computational time with the advantage of a more accurate prediction of the trajectory and the total propellant consumption. Allowing G-POLAR to maintain its simplicity results in fast and reliable convergence of the solution. Similarly, other more complex models can also be used, for instance, a model for the SRP to include the transient response of the engine thrust to the throttle command or more sophisticated modeling of the specific impulse I_sp. Realizing that some performance might be lost for the benefit of a more realistic trajectory is such an important discovery because it allows us to steer away from believing that extracting the most performance is always the best outcome. Realistic models and practical solutions supersede unrealistic solutions with superior performance. Extensive demonstrations of the concepts discussed in this sections will be presented in Sections 8.10 and 8.11.

8.6 EDL Optimization Mission and Vehicle

The simulation of a human-scale Mars EDL mission was selected for the demonstration of the bi-level optimization algorithm. The challenging entry and powered descent conditions of Mars offer valuable information on the capability of the algorithm. End-to-end simulations in a 3DOF simulation environment are performed from EI at an altitude of 125 km to touchdown at the landing location. The vehicle's inertial velocity at EI is 4700 m/s, while the downrange to the landing site is 1200 km. Perfect navigation is assumed with an update rate of 1 Hz for entry and 10 Hz for powered descent. The entry flight starts from the South and heads towards the North. A slender-body aeroshell called the Mid lift-to-drag ratio Rigid Vehicle (MRV) is the model used for the three-dimensional simulations. MRV has a total mass of 61,838 kg at EI. The MRV is equipped with an SRP system with 8 engines producing a total of 800,000 N of thrust and a specific impulse of 360 s. The minimum throttle allowed is 20% and the maximum is 100%. The vehicle model used represents one of the proposed concepts for a human-scale Mars landing mission [129] and it is one of many updated iterations of a previous ellipsled concept for a human-scale Mars mission [3]. The hypersonic lift-to-drag ratio of the MRV is 0.54, and it lands horizontally. In this configuration, the MRV does not require jettison of a structural component, hence, keeping the mass constant between entry and powered descent. The ballistic coefficient of the vehicle is 379 kg/m^2. An illustration of the vehicle can be observed in Figure 8.3 during entry and powered descent. More details on vehicle data and characteristics can be found in Cerimele [129], Johnson [130], and Johnson [131].

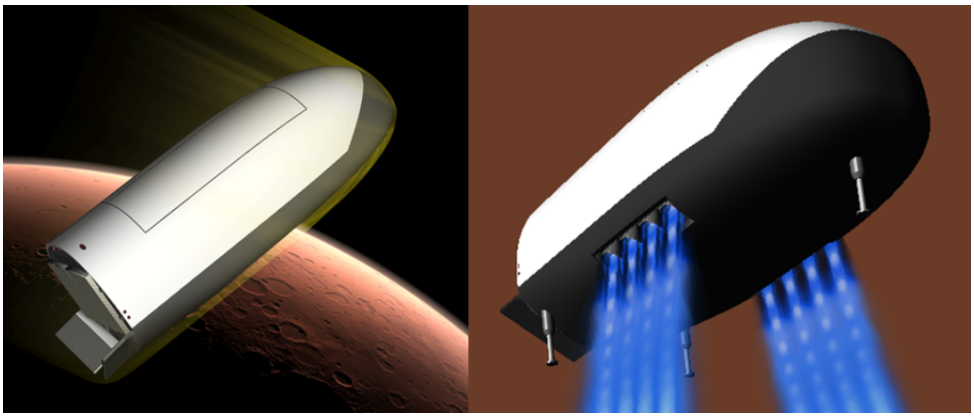

Figure 8.3. Artist representation of the Mid Lift-to-Drag Rigid Vehicle used for human-scale landing missions on Mars.

8.7 Independent Benchmark Solution

With the aim of creating a benchmark solution with the minimum propellant consumption possible for a mission of this category, the human-scale Mars EDL landing mission was solved using a state-of-the-art pseudospectral optimal control software [132]. The knotting techniques developed in Ross [133] where used to adhere to the hybrid control problem defined above. Results from this independent method served as a benchmark for comparison and verification of the solution obtained by the bi-level optimization approach.

One aspect that makes solutions with the direct method not adequate for rapid generation of trajectories is the time limitation. On a desktop computer with a 3.8GHz 8-Cor Intel Core i7 processor, the CPU time needed to obtain a solution ranges from one thousand to nine thousand seconds. This range is dependent on minor variations in the parameter settings of the software. In some cases, small changes in apparently inconsequential settings, such as bounds on variables that are not close to the solution, would result in the software not finding a solution altogether or affecting severely the

computational time. This is a testament to the difficulty of the problem and how even a state-of-the-art software might struggle to find a feasible solution.

Given enough time, the pseudospectral method will obtain a solution with the lowest propellant consumption possible with the given conditions. As such, the algorithm with do any maneuver available within the legality of the dynamics of the problem and the constraints added. In an EDL trajectory optimization problem, the best solution is the one that reduces the speed the most without using any propellant consumption. Therefore, if velocity is reduced as much as possible during entry, then powered descent flight time will be reduced accordingly. Generally, the higher density levels in the atmosphere are at lower altitudes, making the aerodynamic drag is higher. As a result, the entry trajectory gets as low to the ground as possible as it tries to slow down the vehicle. Furthermore, to reduce the velocity even more, the trajectory might make use of phugoid oscillations to increase the drag reduction during entry. Even though the propellant reduction is greater by this approach, flying a vehicle close to the ground at high speeds and in a phugoid oscillatory pattern is risky and posses a threat to the structural stability of the vehicle due to the high load and heat rate limits.

To eliminate the risk of flying the vehicle too close to the ground, a *regularization* term in the performance index (Equation 5.19). This technique is very effective in shaping the trajectory to reduce altitude monotonically. The modified performance index becomes:

$$\tilde{J} = J + k \int_0^{t_{PDI}} \left(\dot{r}^2\right)\, dt = m_0 - m(t_f) + k \int_0^{t_{PDI}} \left(\dot{r}^2\right)\, dt \tag{8.25}$$

where $k > 0$ is a penalty coefficient and the integration portion of the equation is

only using during the entry phase. In contrast, the bi-level optimization problem does not include a regularization term during entry because FNPEG is equipped with a mechanism to prevent phugoid oscillations from happening [21].

In addition, it is necessary to change the formulation of the entry-flight problem to generate an operational trajectory. This mainly pertains the control authority of the vehicle to produce a bank angle profile that can be realized by the flight control system of an entry vehicle. To overcome this, the following first-order dynamics are introduced to the entry guidance problem:

$$\dot{\sigma} = -\frac{1}{\tau}(\sigma - u) \tag{8.26}$$

where $\tau > 0$ is a chosen time constant and u is the bank angle command to be optimized. In this work and the numerical results obtained, $\tau = 10$ was selected. Moreover, a bank angle rate-limit was added to avoid immediate changes in the control command. A typical bank angle rate for an entry vehicle must not exceed 5 deg/s. The following inequality constraint was added to the magnitude of the bank angle dynamics in Equation 8.26:

$$|\dot{\sigma}| = \frac{1}{\tau}|\sigma - u| \leq \dot{\sigma}_{max} \tag{8.27}$$

The optimal end-to-end EDL control problem was solved with and without the regularization terms in Equation 8.25. In both cases, the following constraint to the lower altitude limit is added as a safeguard against finding a solution that goes below the ground

($h_{min} = 0$):

$$h_{min} - h(t) \leq 0, \quad t \in [0, t_{PDI}] \tag{8.28}$$

A comparison of the altitude profiles for the problem solved with and without regularization is shown in Figure 8.4. The entry trajectory exhibits a clear phugoid oscillation pattern and flies considerably close to the ground for a relatively large period of time. At one point, the vehicle appears to be grazing the ground, a maneuver that cannot be flown in any realistic scenario. This behavior is expected, as it depletes a significant portion of the velocity when flying close to the surface. PDI starts at a low velocity close to 370 m/s and a very low altitude of 1.2 km. The PDI condition can be seen in more detail in the insert of Figure 8.4.

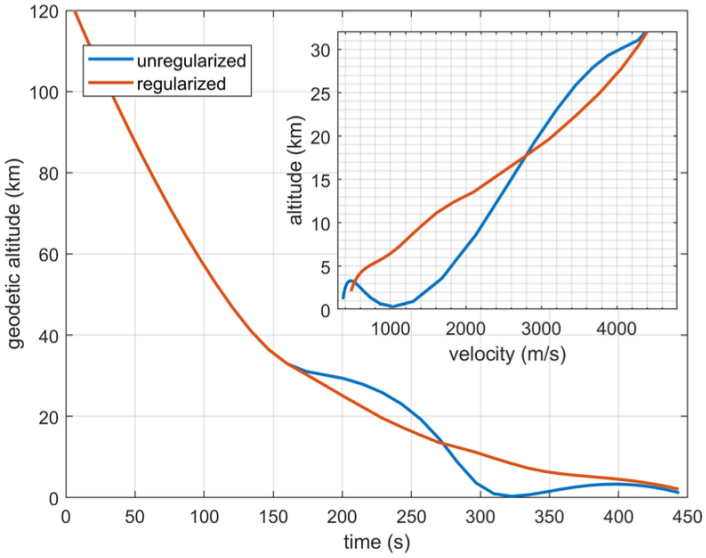

Figure 8.4. Entry trajectories in the end-to-end fuel-optimal EDL solutions using a pseudospectral optimization software with and without the regularization term in Equation 8.25.

The resulting propellant consumption from the powered descent phase given these

initial conditions is of 6,825 kg for the unregularized solution. However, this trajectory is operationally unacceptable considering the collision risks and safety concerns on aero-thermal and aerodynamic loads caused by flying near the ground at hypersonic speeds. This corroborates the idea that not all "optimal" solutions may produce a readily applicable solution. Undesirable trajectory behavior needs to be accounted for and dealt with caution. Nonetheless, the solution to the unregularized problem is still important for academic purposes as it provides a limit on what can be "physically" achieved if risk was not taken into consideration. It is always good practice to calculate the best case scenario and then move forward to more realistic cases. In this case, moving from such a dangerous maneuver is required for operational applicability. It is tempting to believe that simply raising the altitude limit from a non-zero value ($h_{min} > 0$) in the constraint of Equation 8.28 would eliminate the problem. However, increasing the value of h_{min} simply raises the entry trajectory above the ground, overlooking the existing phugoid oscillations near h_{min}. Constraining h_{min} also impacts the choice of PDI condition and the propellant performance. Since the altitude is now limited, the guidance needs to find a new trajectory at a higher altitude and possible higher velocity to start PDI. In fact, the propellant consumption calculated with the regularization term is of 8,462 kg, a difference of 1,637 kg from the unregularized solution. The considerably higher propellant is expected given the nature of the new trajectory. In the new solution, the vehicle flies a more realistic trajectory than the unregularized solution.

When the regularization term k in Equation 8.25 is sufficiently large ($k > 0$), it effectively damps out the phugoid oscillations utilized by the unregularized trajectory to

slow down the vehicle. The optimal end-to-end solution results in a significantly more benign entry trajectory with the expected behavior from typical entry-flight. Besides removing the phugoid oscillations, the trajectory ends at a PDI condition with an altitude of 2.1 km and a velocity of 477 m/s. The slighly higher velocity is a result of flying at higher altitudes and consequently results in the higher propellant consumption by the regularized trajectory. The computational times for these two solutions are about 2,000 and 4,700 seconds, respectively.

Even tough the regularization tries to approximate the optimal solution to a realistic solution, it is still much simpler than a guidance solution like the one provided by FNPEG. For instance, the implementation in the pseudospectral control software omits inequality constraints on heat rate, load limits and dynamic pressure limits that might be necessary for operational purposes. Despite this shortfal, it is still a good comparison for the bi-level optimization approach. The regularized solution is the chosen benchmark solution for comparison.

The bank control found by the direct method approach with unregularized and regularized terms can be devised on Figure 8.5. It is clear that the regularization has an effect on the bank angle control. In the unregularized control, there is only one change from zero to around 125 degrees and then back to zero. On the other hand, the regularized control has a total of three bank reversals with opposite signs. It is interesting that in both cases, the final entry bank angle is zero. This indicates that the guidance control happens between 100 and 400 seconds. Then, it tries to fly with full lift-up ($\sigma = 0deg$) all the way to the end. Again, this is the best possible scenario in which the vehicle flies

the optimal solution. To take advantage of every bit of control, the optimization software decides to eliminate any last second control. However, this behavior is undesirable because the vehicle is left with no control margin to eliminate any dispersion near the end. A non-zero final bank angle is a better choice for entry-flight as it allows some additional control in off-nominal cases [99]. In a more realistic scenario, it is good to assume that there will be some kind of dispersion toward the end.

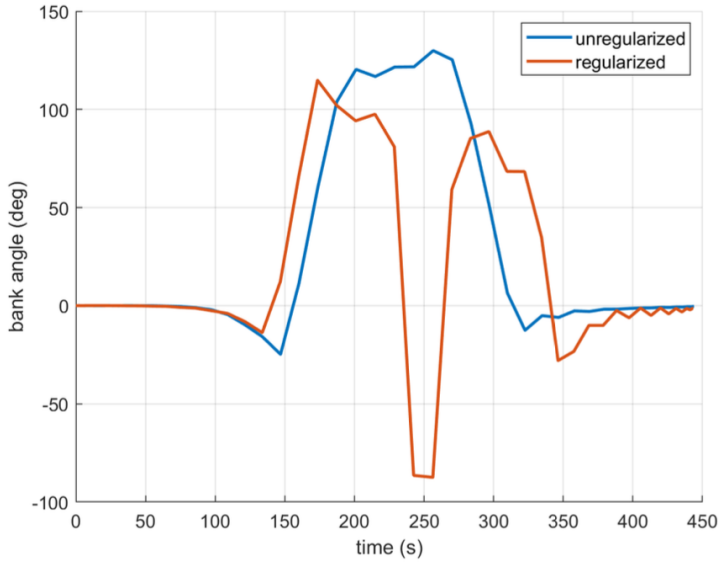

Figure 8.5. Bank angle control for entry in the end-to-end fuel-optimal EDL solutions using a pseudospectral optimization software with and without the regularization term in Equation 8.25.

8.8 Demonstration of Bi-Level Optimization Algorithm

8.8.1 Solution from Bi-Level Optimization

The bi-level optimization algorithm described in Section 8.4 is applied to the same EDL mission to land a spacecraft on the surface of Mars. In this approach, the algorithm takes about 12 seconds to find a solution on the same computer. This is 1/400 of the time

required by the general-purpose optimization software used to calculate the regularized benchmark solution. Additionally, the computational time remains similar despite changes in problem settings, such as adding dispersions to the EI condition. In contrast, the general-purpose trajectory optimization software had widely varying computational times depending on the problem settings. To present the results, the optimized trajectory generated by the bi-level optimization approach will be compared to a solution with a fixed $\sigma_f = 40$ deg in FNPEG. The powered descent phase is still fuel optimal as it is obtained by G-POLAR. This comparison will establish the impact of the bi-level algorithm.

In Figure 8.6, the bank angle profiles for the fixed and optimized sigma are shown. The bi-level optimized solution yields a $\sigma_f^* = 23.5$ deg, as opposed to the 40 deg in the fixed final bank angle. The different σ_f^* values is evident towards the end of the bank profile, were both trajectories end at different bank angle values. In both cases, the solution prodduced by FNPEG results in a nonzero bank angle towards the end of the profile. This is in agreement with the design of FNPEG to leave control margin towards the end [21, 99].

The number of bank reversals is predefined in FNPEG, this contributes to the similarities in both profiles. However, the time at which reversals occur and the magnitude of the bank angle explain the bigger differences in the entry trajectory. The entry trajectories for both of these cases are in Figure 8.7. The flight time of the bi-level optimized trajectory is slightly higher than the flight time of the regularized benchmark solution in Figure 8.4. The solid line represents the entry-flight, while the dotted line is the powered descent phase. It is clear from Figure 8.4 that the powered descent phase is significantly shorter than the entry-flight.

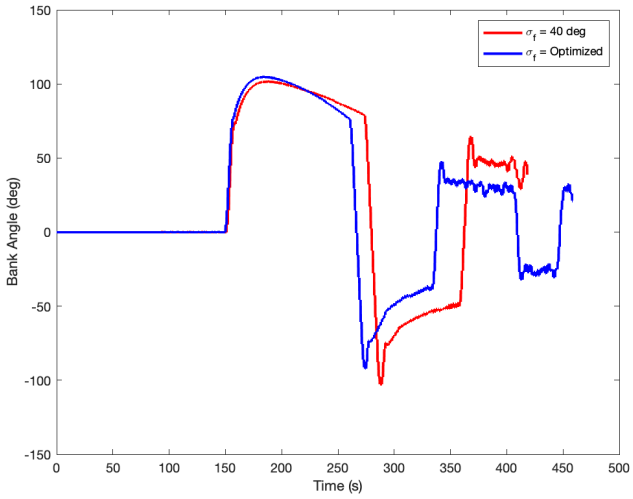

Figure 8.6. Comparison of bank angle profile during the entry phase of a human-scale Mars landing mission using the bi-level optimization approach and a fixed final bank angle $\sigma_f = 40$ deg.

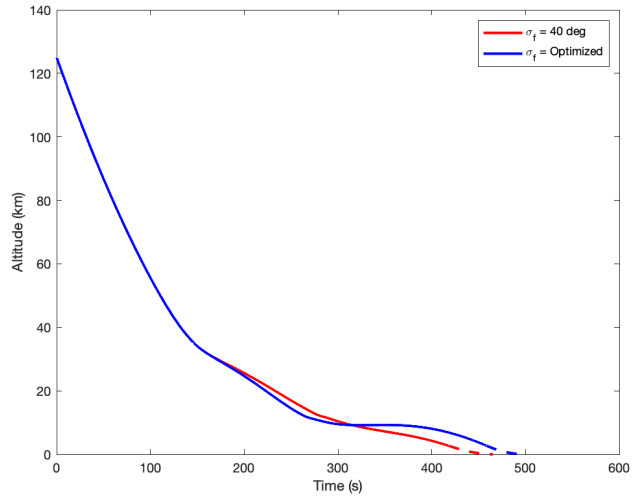

Figure 8.7. Comparison of entry trajectories on a human-scale Mars landing mission using the bi-level optimization approach and a fixed final bank angle $\sigma_f = 40$ deg.

An advantage of using FNPEG is that the algorithm is designed to generate a safe and gentle trajectory that takes care of possible harmful features such as phugoid oscillations or flying at a low altitude. No additional tuning is necessary for its implementation in the bi-level optimization algorithm. Despite damping phugoid oscillations, the optimized

solution results in a longer entry trajectory that allows the vehicle to reduce its speed even further. Figure 8.8 is a closeup image of the final entry condition before starting powered descent. It is clear that the additional seconds of flight and difference in bank profile yields a PDI velocity of 578 m/s for the fixed trajectory as opposed to 496 m/s for the optimized trajectory. The PDI altitude is essentially the same for both cases. For the same mission, the propellant consumption found by the bi-level optimized solution is of 8,899 kg. Conversely, the propellant consumption for the fixed σ_f solution is of 10,132 kg. This represents a difference in propellant of 1,233 kg when compared to the optimized solution, a 13.9% reduction led by the outer optimization on the entry phase. The main contributor to the difference in propellant consumption is the lower velocity at PDI that resulted from flying the optimized entry trajectory.

On the other hand, this result is slightly higher than the regularized benchmark solution by 437 kg, a difference of only about 5% from the benchmark solution, but without the significantly costlier computation of two or more orders of magnitude. A difference this small accounts for less than 1% from the total weight of the vehicle. Being that the result from the bi-level optimization approach is so close to the regularized optimal solution, the optimized solution can be considered to be "near-optimal." On top of that, with the bi-level optimization method, finding a solution is predictable and reliable, and the trajectory obtained is what is expected of a guided trajectory without the need of any additional complex or large software.

In Braun [14], it is approximated that the mass fraction requirement for an entry vehicle such as the MRV for a Mars EDL mission is of 28%. The resulting propellant

consumption of the bi-level optimization approach is equivalent to a mass fraction of only 14.5%, a reduction of nearly 50% from the non-optimized estimate that far exceeds the expected propellant-mass ratio of a Mars vehicle. The simplicity of the approach emerges from the robustness of the entry and powered descent algorithms that sit at the core of the optimization mechanism.

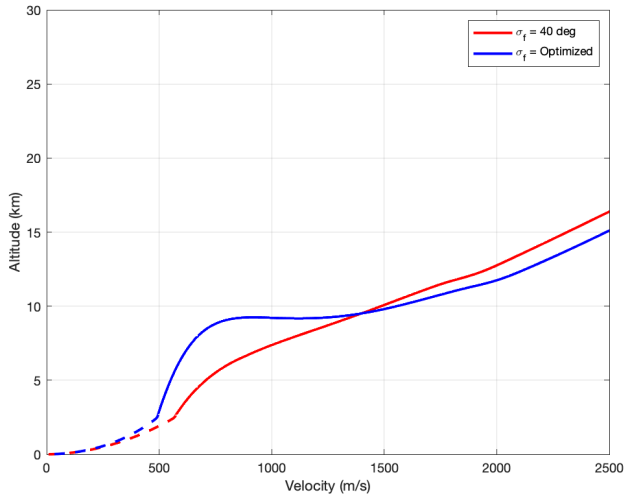

Figure 8.8. Comparison of altitude-versus-velocity profile during the entry phase of a human-scale Mars landing mission using the bi-level optimization approach and a fixed final bank angle $\sigma_f = 40$ deg.

From the PDI point and onward, G-POLAR delivers the vehicle safely to the landing location. A fuel-optimal powered descent solution is obtained as part of the inner optimization loop of the algorithm. In Figure 8.9, the three-dimensional powered descent guidance in the topocentric frame can be appreciated. The landing location is at the coordinates $(0, 0, 0)$.

The throttle and planet-relative velocity along the powered descent trajectory are shown in Figure 8.10. The smooth transition of the throttle between the lower-bound and

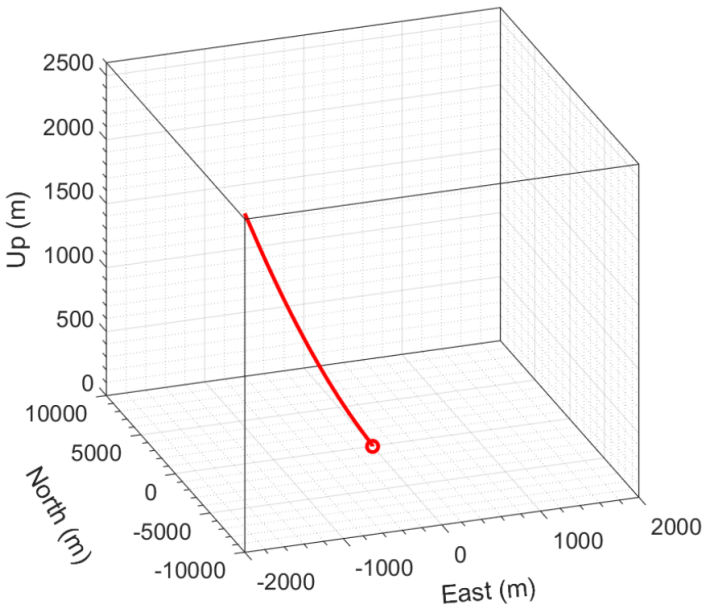

Figure 8.9. Powered descent trajectory in the end-to-end bi-level optimization EDL solution in the topocentric coordinate frame of Figure 3.2.

upper-bound is a characteristic of the fuel-optimal powered descent solution produced by G-POLAR. The optimal powered descent solution results in a bang-bang thrust profile that instantaneously shifts between the lower-bound and upper-bound. In a typical fuel-optimized end-to-end EDL trajectory, the PDI condition is driven as close as possible to the landing location. A consequence of this is that the optimal throttle in the powered descent phase is not exactly the bang-off-bang structure exhibited in Lu [22]. Instead, the optimal throttle stays at the maximum, when the only remaining flight time is at the last arc of the bang-off-bang structure; or, almost at the moment of the second switch as seen in Figure 8.10. In G-POLAR, a new method of solution makes this transition more realistic to how an actual engine operates [107]. With the throttle setting at close to 100%, velocity decreases from 496 m/s to 2.5 m/s in 42 seconds of powered descent flight.

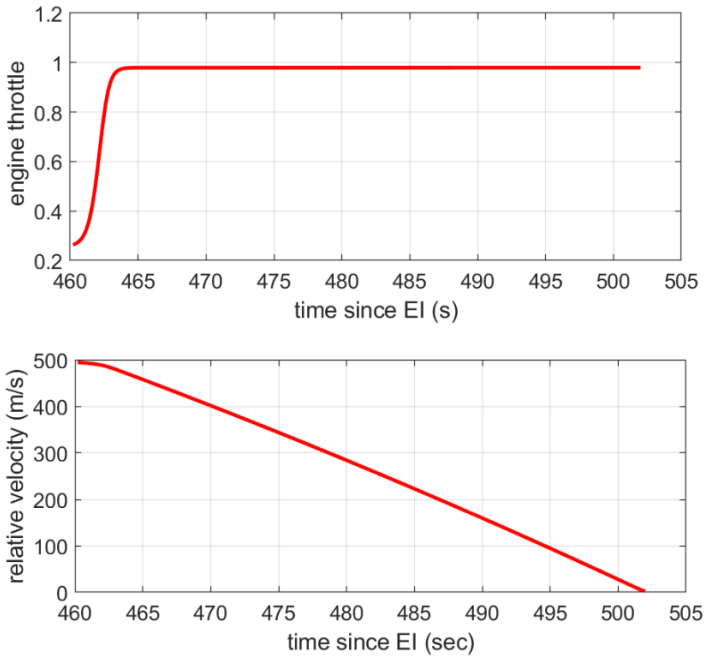

Figure 8.10. Engine throttle and relative velocity profiles in the powered descent phase of the end-to-end bi-level optimization EDL solution.

8.8.2 Robustness Demonstration of Bi-Level Optimization Algorithm using Monte Carlo Dispersions

The Monte Carlo simulation demonstrates the the bi-level algorithm is effective at finding an overall optimized solution to the minimum-fuel problem even under dispersed EI conditions. The results from the previous section are promising as they establish that the bi-level approach is effective in finding an optimized solution to the minimum-fuel problem. However, to demonstrate that the method is capable of solving the problem reliably in any feasible cases, a complete optimization was performed on 3000 cases with randomly dispersed initial conditions at the start of entry. Table 8.1 lists the dispersion parameters for the Monte Carlo simulation [107]. For the complete EDL optimization, only the EI conditions are dispersed since these alone cause significant variation throughout

the trajectory, including the PDI condition for powered descent. Therefore, each one of the dispersed cases is entirely different than the rest.

Table 8.1. Dispersions and uncertainty values of 3000 Monte Carlo simulation runs of the bi-level optimization of a human-scale Mars landing mission with a factor of safety = 1.0.

Parameter	Distribution	3-Sigma Min	3-Sigma Max
EI planetodetic altitude (m)	Gaussian	-300.0	300.0
EI longitude (deg)	Gaussian	-0.75	0.75
EI planetodetic latitude (deg)	Gaussian	-0.75	0.75
EI inertial velocity (m/s)	Gaussian	-10.0	10.0
EI inertial flight-path-angle (deg)	Gaussian	-0.3	0.3
EI inertial azimuth (deg)	Gaussian	-0.5	0.5
EI vehicle mass (percentage)	Gaussian	-1.0%	1.0%
C_L (percentage)	Uniform	-10.0%	10.0%
C_D (percentage)	Uniform	-10.0%	10.0%
Atmospheric density	Mars GRAM 2010	Mars GRAM 2010	Mars GRAM 2010
Mars GRAM 2010 *dusttau*	Uniform	0.1	0.9
Total SRP max thrust (percentage)	Gaussian	-1.0%	1.0%

A total of 3000 dispersed cases were successfully optimized with the bi-level optimization method. The successful convergence of all cases is a testament to the robustness of the algorithm. The statistics on propellant consumption, the optimized values for the final bank angle target σ_f, and computational times on the same desktop computer are summarized in Table 8.2.

Table 8.2. Statistics on the performance of 3000 Monte Carlo end-to-end bi-level optimization runs of a human-scale Mars landing mission with a factor of safety = 1.0.

	Mean	Standard Deviation	Max	Min
Propellant Consumption (kg)	8,881.61	122.34	9,249.25	8,408.42
Optimized σ_f^* (deg)	20.25	3.0	28.89	11.80
CPU Time (s) (on a desktop)	13.88	1.25	28.73	10.58

Remarkably, the mean propellant consumption of 8,881 kg in the table accounts for a propellant mass fraction of only 14.4% for the MRV, a substantially lower value than the estimated 30% in Braun [14]. On the study, however, optimization for the class

of vehicles like the MRV were not considered. Taking advantage of the tools available for EDL guidance and optimization if the biggest contribution of this work. It is worthy to highlight that a complete EDL optimization that can reliably produced an optimized solution in a matter of seconds is a groundbreaking achievement.

Surprisingly, the optimization approach works extremely well by changing just one parameter in FNPEG. Despite that, it is necessary to go through the optimization process to find the correct σ_f^* for each specific case. Figure 8.11 shows the spread of the optimized values for σ_f^* in the 3000 dispersed cases. As seen from the figure, the optimized σ_f^* is dependent on the actual EI condition and varies between 12 and 29 degrees. There is no single value of $sigma_f^*$ to optimize all 3000 cases. A similar phenomenon is found in the distribution of PDI conditions across all cases, where not a single time-to-go (total powered descent flight time) resulted in a good PDI condition or even a successful case. Section 4 covers more on the importance of the PDI condition even when there is no atmosphere.

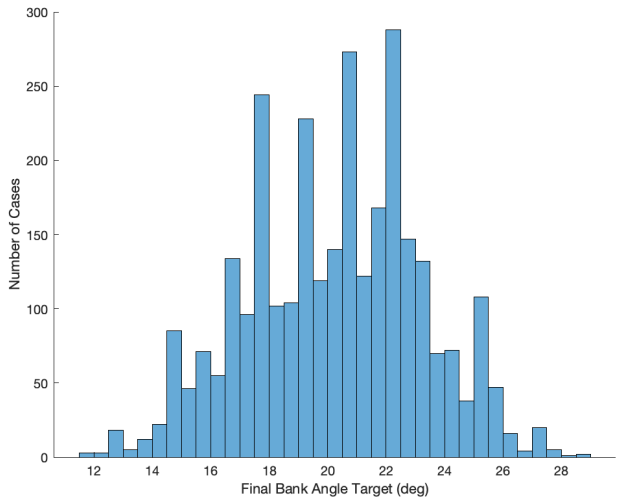

Figure 8.11. Value distribution of 3000 optimized σ_f solutions from the bi-level optimization approach on a human-scale Mars landing mission.

For comparison, if the bi-level optimization approach is not used and the same 3000 cases are run with a fixed $\sigma_f = 40$ deg in entry, the mean propellant consumption without entry optimization is 9,999.6 kg, over one metric ton more than the mean propellant consumption that the bi-level algorithm is able to achieve. Note that G-POLAR still calculates the optimal powered descent solution given the non-optimized entry trajectory. This highlights the fact that even with an optimal powered descent guidance, the trajectory flown during entry impacts the result greatly.

The bank angle profiles during the entry phase for 100 of the 3000 optimized cases are shown in Figure 8.12. Only 100 cases are shown for visibility. The profiles that are shown, demonstrate that in this optimization approach, with a different σ_f^* value for each case, FNPEG still generates a typical bank angle profile flown by an operational entry vehicle, rather than an unrealistic or undesirable solution from a generic trajectory optimization tool. For instance, Figure 8.13 shows the resemblance to the typical Space Shuttle bank angle profile taken from Harpold [36]. The concept of the bank reversal has been used throughout the years as a dependable technique to reduce crossrange dispersions towards the end. Equally important is the non-zero bank angle leading to the end of entry-flight to leave some control capability.

Figure 8.14 shows the altitude versus velocity variations in the entry phase. The repercussions of varying the EI condition are displayed in this figure. An example of the changes that can occur is in the difference in altitudes at the same velocity among different entry trajectories. At some point, this difference reaches up to 5-6 km at a velocity of 1000-1500 m/s (Mach 4-6).

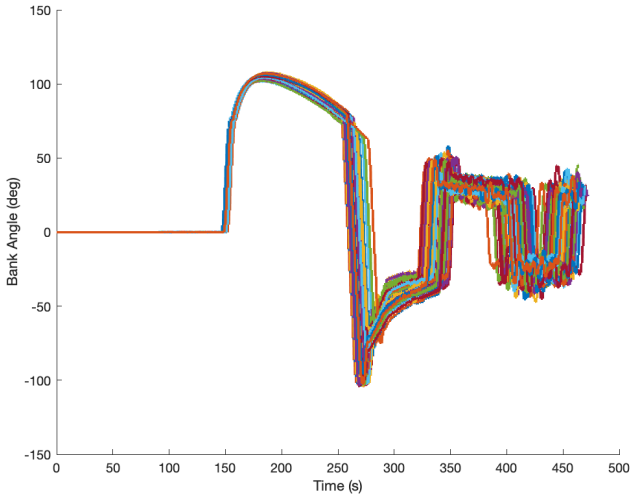

Figure 8.12. Optimized bank angle profile solutions from bi-level optimization approach to a human-scale Mars landing mission (only 100 entry trajectories shown for better visibility).

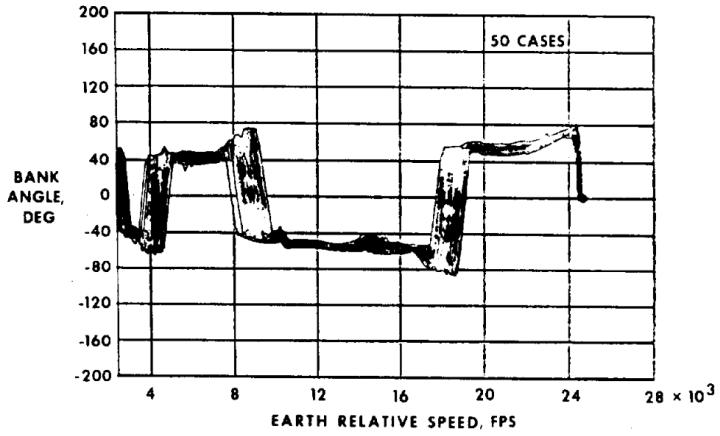

Figure 8.13. Space shuttle bank angle profile from Monte Carlo analysis.

The complete altitude profiles from entry through powered descent are plotted in Figure 8.15 and the altitude versus velocity profiles are plotted in Figure 8.16. The PDI velocities range from 460 to 530 m/s, while the PDI altitudes are between 2.2 and 3.4 km. The variation on EI conditions propagates throughout entry, resulting in a different PDI condition for each trajectory. Despite using the PDI logic to calculate the best PDI point,

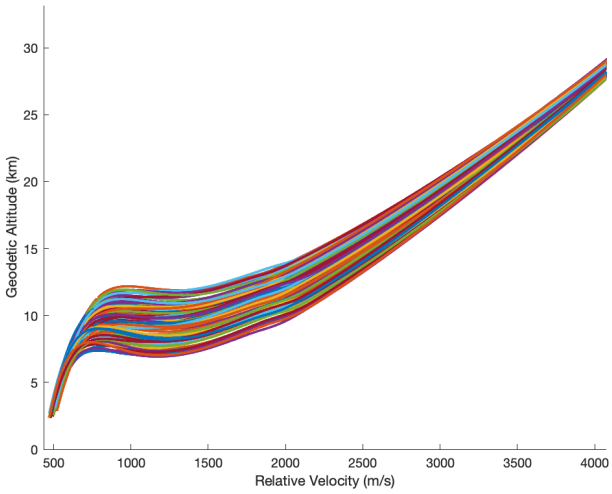

Figure 8.14. Altitude versus velocity profiles in entry phase along 100 optimized end-to-end trajectories (the portion at higher altitude is cut off for better view of the trajectories).

it is clear that even with an optimization setup such as the bi-level optimization approach, the PDI condition depends on the trajectory itself and it cannot be a single point for all cases.

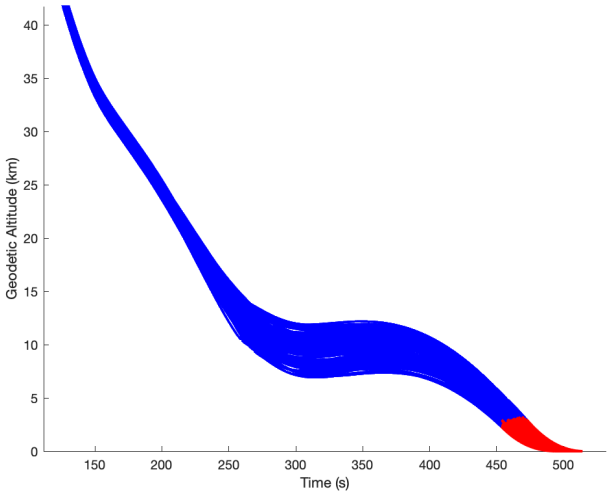

Figure 8.15. Altitude profiles along 100 optimized end-to-end trajectories (the portion at higher altitude is cut off for better view of the trajectories).

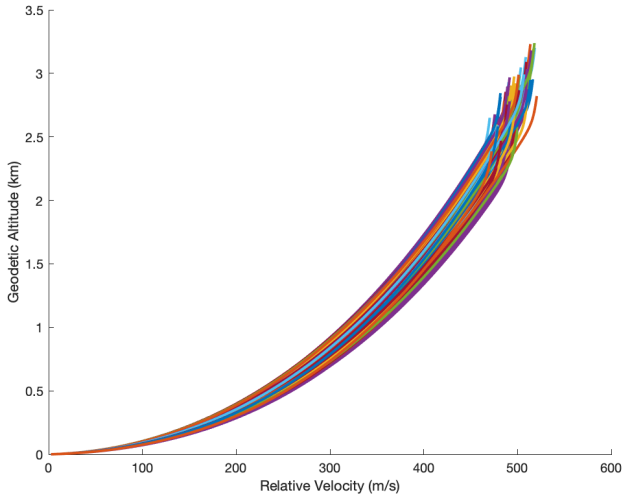

Figure 8.16. Altitude versus velocity profiles in powered descent phase along 100 optimized end-to-end trajectories.

The powered descent trajectory is noticeably different as well, mainly because the starting condition is different in all cases. The same powered descent trajectories in a three-dimensional view in the topocentric coordinate frame (Figure 3.2) are displayed in Figure 8.17. All of the trajectories in the 3000 dispersed cases successfully reached the predefined landing location.

Finally, Figure 8.18 shows the throttle variations for the optimized powered descent trajectories. The throttle profile is similar to the nominal case shown in Figure 8.10. However, in this case, the PDI start time is different in each case and can vary as much as 20 seconds.

Under Monte Carlo dispersions of the entry conditions, the bi-level optimization algorithm cleary demonstrates its robustness and its advantage over a conventional nominal trajectory. The algorithm successfully finds a solution to all the dispersed cases of the extensive testing. Furthermore, it cannot be ignored that the computational cost of finding

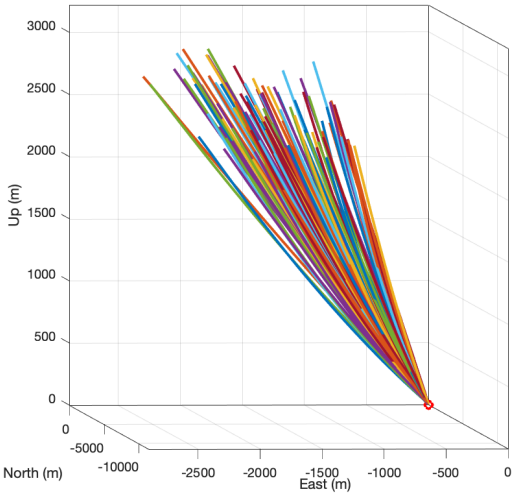

Figure 8.17. Three-dimensional powered descent trajectories along 100 optimized end-to-end EDL trajectories in the topocentric coordinate frame in Figure 3.2.

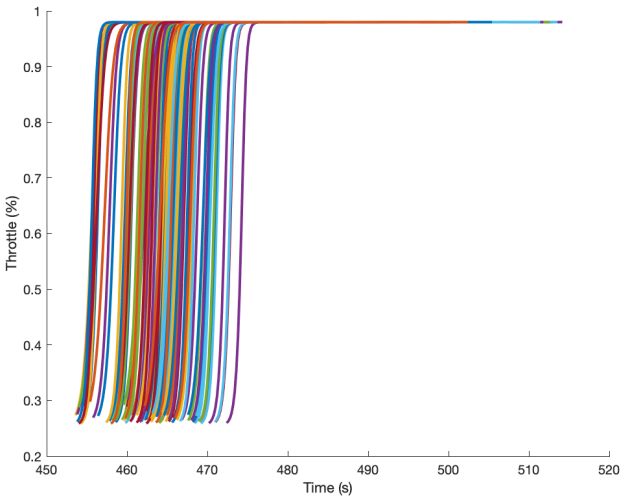

Figure 8.18. Engine throttle profiles in powered descent phase along 100 optimized end-to-end trajectories.

one solution is just a fraction of a generic optimization tool. In fact, a 3000 Monte Carlo demonstration would be impossible with current computational power. This demonstration clearly solves a very important problem in EDL. The bi-level optimization approach is an effective tool for solving teh EDL optimization problem fast and reliably.

8.9 Selection of σ_f as the optimization variable

One of the characteristics that makes the bi-level optimization approach successful is that the entry guidance algorithm is left untouched. This guarantees that fast convergence and robustness in FNPEG are maintained and that a smooth trajectory will be generated. To achieve this, the optimization of the entry guidance was implemented as an outside loop that only required changing one targeting parameter. As a user, the initial and final conditions can be specified, as well as the constraints that will be utilized. The initial conditions are set by the problem and cannot be modified. The constraints in heat rate, load rate, and dynamic pressure rate are also defined by the limits imposed for astronaut or spacecraft protection. The only remaining tuning parameter is the targeting condition. The usual entry targeting conditions are on the final altitude, velocity, and range to the landing site. Additionally, it is possible to modify the final bank angle target in the control parameterization profile of FNPEG shown in Figure 3.1.

To select the value to be used for optimization, a couple of tests were done in individual simulations with each potential variable. In FNPEG, the terminal conditions for altitude and velocity are combined through the energy equation used as the independent variable in Equation 3.1. This means, that multiple combinations of altitude and velocity can produce the same energy value. For that reason, one parameter can be left constant while the other is allowed to vary. Since the dominant term in Equation 3.1 is the velocity term, final altitude was left constant while velocity was the variable. Interestingly, the propellant consumption did not experience big effects on propellant consumption as a

consequence of the variation in velocity. The reason is that with the adaptive PDI logic active during the entry trajectory, a proper PDI was selected at a point in the trajectory with a similar propellant consumption. Utilizing the range to the landing site is more complicated since it is the variable used in FNPEG as the stopping parameter to reach the final energy level by design. However, selecting the range-to-go would experience the same effect than the altitude or velocity parameters because of the active adaptive PDI logic.

Interestingly, the selection of different final bank angle made a more substantial difference in the entry trajectory and the propellant consumption during powered descent, even when the adaptive PDI logic is active. Initially, $\sigma_f = 40.0$ deg was selected to run all the complete EDL simulations and a propellant consumption of 10,047 kg. For comparison, running the simulation with $\sigma_f = 30.0$ deg resulted in a propellant consumption of 9,137 kg, already a considerable reduction. Compared to the other parameter options, σ_f has the biggest effect on the trajectory and the propellant consumption during powered descent. Therefore, the final bank angle target for the linear bank angle parameterization in FNPEG was chosen as the optimization variable in the bi-level method. The results from optimizing the complete EDL trajectory have been demonstrated in Sections 8.8.1 and 8.8.2.

To corroborate that the selection of σ_f was appropriate. A series of simulations using the bi-level optimization approach were conducted on the 3000 cases simulated for the Monte Carlo test in Section 8.8.2. In each simulation, a different velocity target would be selected while the altitude was kept constant at 2km. The range-to-the landing site is zero, with the objective of ending the entry trajectory at the landing site. The selection of the zero range-to-go is by design, since it is known that the adaptive PDI logic will select

a point along the trajectory before the landing site is reached. The range for the velocity target was between 200 and 450 m/s, to show a wide range of solutions. In Figure 8.19, the comparison of the average propellant consumption for the optimized cases at different velocities is shown. Between 200 and 400 m/s, the propellant consumption remains close to 9000 kg. Only after 400 m/s, the propellant consumption starts to go up, victim of a higher PDI velocity, altitude and range, as it can be seen from Figure 8.20. The associated values that result from the bi-level optimization can be found in Table 8.3

Table 8.3. Statistics on 100 optimized results from bi-level optimization approach for different final entry velocity targets

Target Velocity (m/s)	200.0	250.0	300.0	350.0	400.0	450.0
Optimized Bank Target (deg)	19.89	19.20	22.38	22.38	19.87	34.88
Optimized Propellant (kg)	9026.8	9008.3	9011.9	8996.5	9004.7	9718.8
Total Optimization Time (s)	18.66	18.98	18.60	18.53	19.35	11.57
PDI Velocity (m/s)	496.21	494.82	496.76	495.78	493.69	550.30
PDI Altitude (km)	2.79	2.78	2.70	2.69	2.75	3.09
PDI Range (km)	10.87	10.80	10.88	10.83	10.79	12.78
PDI Crossrange (m)	146.20	26.81	-53.79	-67.35	126.24	-123.06
PD Flight Time (s)	42.1	41.97	42.03	41.93	41.94	45.26

A closer look at the results between 400 and 450 m/s details the moment changing the velocity starts to increase propellant consumption, Taking a look at Table 8.4, after Vf = 420 m/s a change in propellant consumption, pdi velocity, pdi altitude, and pdi range starts to occur. At this point, the beginning of powered descent starts to happen farther and farther from the landing location. This stresses the powered descent because now the flight time needs to be longer, causing the propellant consumption to increase. However, the optimization is still trying to find the final bank angle that will minimize this propellant consumption. A large change in bank angle also occurs at around Vf = 420

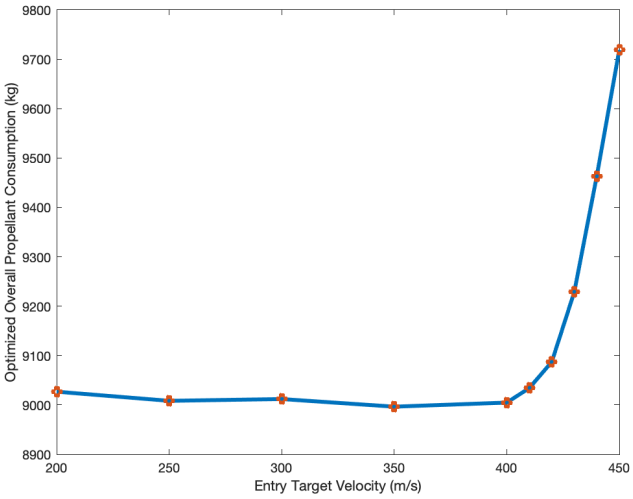

Figure 8.19. Propellant consumption when final velocity target is varied in bi-level optimization approach.

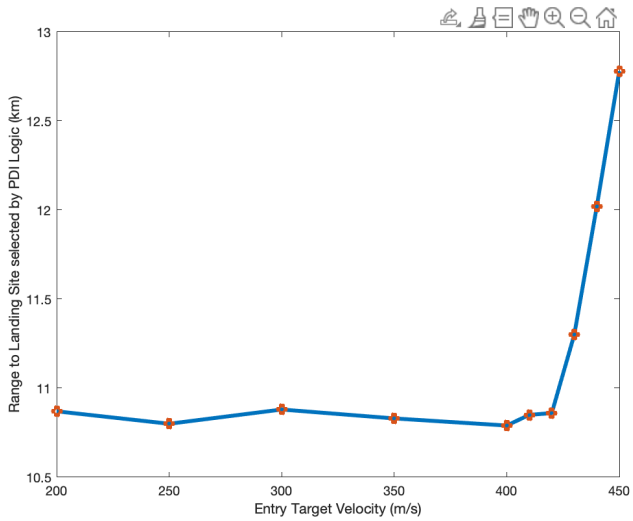

Figure 8.20. PDI range to landing site when final velocity target is varied in bi-level optimization approach.

m/s, at that point the optimization is doing its best at keeping propellant consumption low.

The resulting optimized final bank angle targets can be seen on Figure 8.22. Unlike the rest of the plots, the bank angle changes constantly to adapt the trajectory to the

Table 8.4. Statistics on results from bi-level optimization approach for different final entry velocity targets from 400 to 450 m/s

Target Velocity (m/s)	410.0	420.0	430.0	440.0	450.0
Optimized Bank Target (deg)	17.64	17.64	26.39	31.75	34.88
Optimized Propellant (kg)	9034.1	9087.1	9228.6	9463.3	9718.8
Total Optimization Time (s)	20.62	20.46	17.11	14.21	11.57
PDI Velocity (m/s)	494.75	500.36	513.73	531.83	550.30
PDI Altitude (km)	2.86	3.16	3.16	3.10	3.09
PDI Range (km)	10.85	10.86	11.30	12.02	12.78
PDI Crossrange (m)	99.22	133.70	90.50	1.81	-123.06
PD Flight Time (s)	42.14	42.38	43.09	44.14	45.26

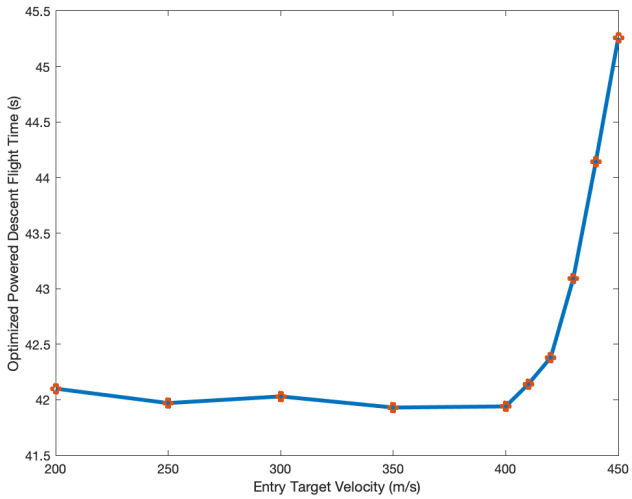

Figure 8.21. Powered descent flight time when final velocity target is varied in bi-level optimization approach.

needs of powered descent.

The results from these studies determined that the selection of the final bank angle target was appropriate to solve the complete EDL optimization problem. It would seem that changes to the final altitude, velocity or range would cause a bigger effect on the propellant consumtion, however, since an adaptive PDI logic is implemented in the bi-level optimization approach, it is inevitable that the PDI condition will be chosen before the

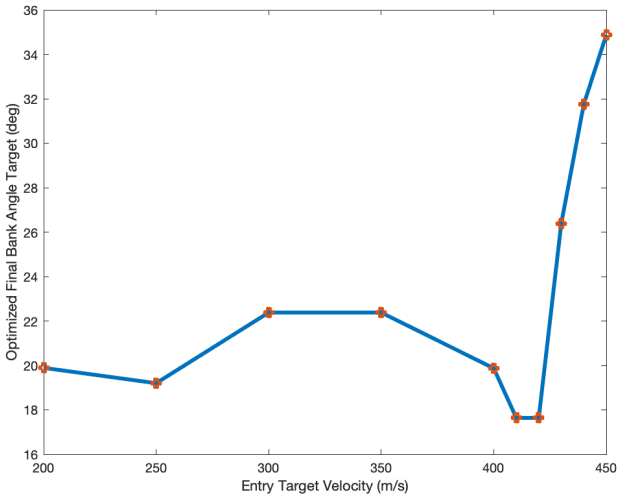

Figure 8.22. Optimized final bank angle when final velocity target is varied in bi-level optimization approach.

final condition is reached. The PDI condition selected is usually similar in propellant consumption, given that G-POLAR finds the optimal solution to the soft-landing problem, which is very similar since no targeting condition is imposed. Furthermore, the linear bank parameterization profile allows this simple option. A more complicated parameterization would require the optimization of multiple parameters.

8.10 Inclusion of High-Fidelity Atmospheric Model in the Entry Phase

In entry-flight, simple deterministic models were used for the atmospheric density and speed of sound at Mars as a function of altitude. The optimized end-to-end trajectories obtained in Section 8.8.2 successfully found a feasible trajectory with these simplified models. Usually, entry guidance is fitted with such simplistic models to be able to rapidly generate a trajectory. However, some of the important details of a complete

atmospheric model are missing and might cause simple models to deviate from reality. More complex models for the Mars atmosphere can better and more accurately capture the complex variations of Mars atmospheric parameters, albeit at a higher computational cost. Such a tool is the Mars Global Reference Atmospheric Model (Mars GRAM), an engineering-oriented atmospheric model developed over the years to estimate mean values and statistical variations of atmospheric properties for Mars [128]. The software itself is a large FORTRAN program that needs to be called as a subroutine. The user is able to give specific altitude, location, date and time of day, dust level, and other variables and receive the value of the atmospheric density and speed of sound as an output. It can also produce dispersed atmospheric parameters based on a collection of measured data on the actual atmosphere of Mars. It is desired to incorporate a high-fidelity tool such as Mars GRAM as part of the entry guidance. However, including the complete atmospheric model into the simulation is not as simple and the high computational cost that might be counterproductive to the purpose of finding a trajectory promptly. Any attempt at interrogating the large program in every iteration of an entry guidance such as FNPEG will result in a more intensive and far longer computational time.

In this section, a different approach is taken at the implementation of a high-fidelity model. Instead of directly implementing the model as part of the entry guidance iterations, the high-fidelity model will be used in the closed-loop simulation to generate the trajectory as shown in the bi-level optimization algorithm on Figure 8.2. The difference in this approach is is that a call is made to Mars GRAM a single time each simulation step. Nevertheless, the entry trajectory generated from the closed-loop simulation carries

the full fidelity of Mars GRAM. This is because in each simulation step, the guidance command generated by FNPEG using a simple model gets transmitted to the integration in closed-loop simulation where the high-fidelity model is used.

Another Monte Carlo simulation was setup in which Mars GRAM and Mars GRAM dispersions are active in the closed-loop simulations of the entry phase. Everything else on the bi-level optimization approach is unchanged. Table 8.5 shows the statistics of the resulting propellant consumption, optimized σ_f^*, and computation time on the same desktop computer.

Table 8.5. Statistics of 3000 Monte Carlo end-to-end optimized EDL trajectories using Mars GRAM in entry phase.

	mean	standard deviation	max	min
Propellant Consumption (kg)	9,067.12	281.46	9,898.09	8,080.51
Optimized σ_f^* (deg)	13.43	2.87	25.29	10.03
CPU Time (s) (on a desktop)	22.23	4.04	42.87	12.22

The most visible change from Table 8.2 is the difference on the mean σ_f^* value. When the effects of Mars GRAM are present, the mean value of $\sigma_f = 13.43$ deg instead of 20.25 deg without Mars GRAM. The propellant consumption increased by a mere 185 kg. The similar average propellant consumption is attributed to the outer loop optimization of $sigma_f$, even though the atmospheric density by Mars GRAM is very different from the model used in the previous section. Another observation on the propellant consumption is that the spread between the minimum and maximum values is larger. Even though the increase is minimal, it can be accounted to the higher-fidelity of the atmospheric model. By adding Mars GRAM, accuracy during entry-flight increases. The slight increase in propellant consumption is a small price to pay in comparison to the benefit of flying a

trajectory that closely assimilates true flight conditions. All the previous observations point to the importance of carrying out a repeated optimization of the entry phase based on the current condition. The trajectory planning and guidance will take care of the uncertainty as the vehicle flies the entry trajectory, adapting as needed to produce a performance similar to the nominal one.

In the bi-level optimization approach proposed, it is possible to increase the fidelity of the atmospheric model without increasing the computational time an unreasonable amount. The average computational time with Mars GRAM in closed-loop simulation is less than double. It is important to remember that Mars GRAM is a program itself composed of multiple subroutines. Being able to obtain a solution in under 23 seconds is already an enormous undertaking when compared to the 4,700 seconds that it can take with the direct method approach. Similarly, if Mars GRAM was directly used in the iterations of trajectory optimization rather than closed-loop simulations, the computational time for finding the solution would have been easily one to two orders of magnitude longer. For onboard purposes, the bi-level approach can be called multiple times during an actual flight to find a new optimized trajectory based on the current conditions.

8.11 Inclusion of Aerodynamic Forces in Powered Descent

Flying at supersonic speeds on Mars has significant effect on the aerodynamic forces of the vehicle. The flow field around the vehicle that results from the initiation of the SRP and the chemical reaction while it is active presents complex dynamics that often are hard to determine and are different from those seen on a "clean" vehicle [27]. The interactions

among propulsion and aerodynamic forces increase uncertainty, causing important changes on flight control and trajectory [65]. Even though the powered descent starts at supersonic speed in a high-mass EDL Mars mission, the aerodynamic effects are usually ignored in the dynamics of powered descent to simplify the problem. When aerodynamic forces are present, the dynamic equation for velocity in the powered descent problem (Equation 2.20 becomes:

$$\dot{\boldsymbol{V}} = \frac{T}{m}\mathbf{1}_T + \boldsymbol{g} - D\mathbf{1}_V + L\mathbf{1}_L \tag{8.29}$$

where $\mathbf{1}_V = \boldsymbol{V}/||\boldsymbol{V}||$, $\mathbf{1}_L$ is a unit vector defining the direction of the aerodynamic lift force, and L and D are the aerodynamic lift and drag accelerations. Since the MRV vehicle lands horizontally, the thrust direction $\mathbf{1}_T$ will be assumed to be perpendicular to the body longitudinal axis and in the direction of the negative body z-axis. The symmetric plane of the vehicle is formed by $\mathbf{1}_T$ and $\mathbf{1}_V$ to suggest that the vehicle is in a coordinated turn with a zero sideslip angle. Then, the body y-axis may be defined by the following equation:

$$\mathbf{1}_y = \mathbf{1}_V \times \mathbf{1}_T \tag{8.30}$$

Lastly, the direction of the lift force is:

$$\mathbf{1}_L = \mathbf{1}_y \times \mathbf{1}_V \tag{8.31}$$

Adding aerodynamic forces increases the nonlinearity in the dynamics of the problem, making it more difficult to solve. To find the optimal powered descent solution with the indirect method, it is necessary to use the general simplified dynamics to be able to solve the problem with the minimum principle, otherwise it can be challenging to reach convergence of the solution. However, it is possible to use closed-loop simulation to generate a near-optimal trajectory that incorporates more complex dynamics to solve the bi-level optimization problem. The powered descent phase in the bi-level optimization algorithm is now run in closed-loop simulation. The G-POLAR algorithm remains unchanged and is used to calculate the optimal control solution. The closed-loop solution dynamics are updated to include aerodynamic forces in a process similar to the one described in Section 8.10. The solution from G-POLAR is optimal to the problem without aerodynamic forces. The control obtained from G-POLAR is then used to integrate the dynamics with aerodynamic forces. Since the optimal control is for a different problem, the solution is not theoretically fuel optimal because the solution to G-POLAR does not include the aerodynamic effects. Nonetheless, a comparison of a G-POLAR guided trajectory with an open-loop solution that includes the aerodynamic forces by the general-purpose optimization tool in Ross [132] revealed that the fuel consumption increase by the G-POLAR guided trajectory is less than 300kg. The loss of performance is below 3.5% for

the same conditions. Even though the solution cannot be considered theoretically optimal anymore, the propellant consumption is very close to the actual optimal value. The total propellant consumption in the bi-level optimization when the aerodynamic forces are included is of 8,129 kg.

The inclusion of aerodynamic forces results in a reduction in propellant consumption of 8.6% or 770 kg. The propellant reductions arises from the effect of some aerodynamic forces actually producing lift and drag that reduced the velocity of the vehicle before touchdown. This is confirmed by the throttle difference between the vacuum solution and the solution with aerodynamic forces in Figure 8.23. The lower throttle through most of powered descent exhibits the areas where aerodynamic forces help reduce the velocity. Even though the solution from G-POLAR is based on the vacuum model, the nature of the closed-loop guidance is to incorporate all the constraints of the problem with aerodynamic forces. The final constraints on the trajectory are met exactly using this method.

Additionally, the same 3000 dispersed cases run in previous sections were optimized with the bi-level approach and added aerodynamic forces in the powered descent closed-loop solution. All the trajectories land successfully in the designated are within a fraction of a meter and at the desired final velocity. A summary of the statistics on propellant consumption and optimized σ_f^* is presented in Table 8.6.

Table 8.6. Statistics of 3000 Monte Carlo end-to-end optimized EDL trajectories with aerodynamic forces included in powered descent.

	mean	standard deviation	max	min
Propellant Consumption (kg)	8,119.20	165.42	8,600.62	7,558.08
Optimized σ_f^* (deg)	20.39	3.19	30.00	11.69

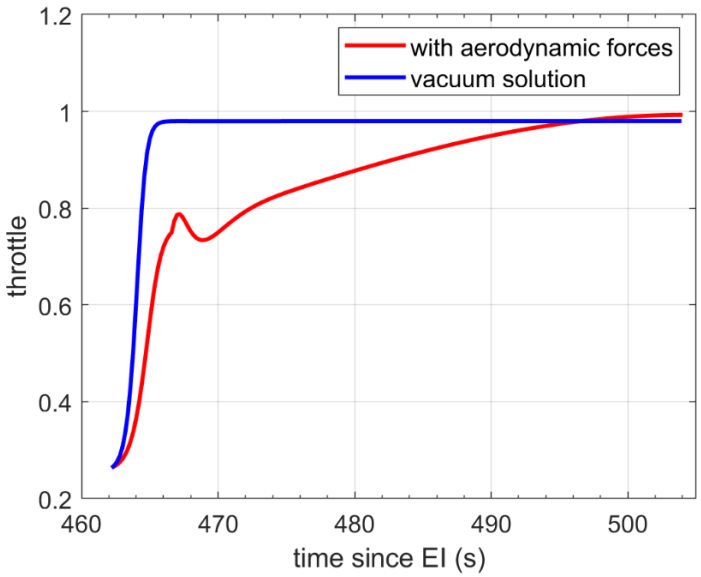

Figure 8.23. Engine throttles in powered descent by G-POLAR when aerodynamic forces are included in closed-loop simulation and when the flight is assumed to be in vacuum.

The introduction of aerodynamic forces has a positive effect in propellant consumption, reducing it by 762kg when compared to the results in Table 8.2. The value of σ_f^* has a negligible change. In Section 8.10, the change in σ_f^* was more significant since the addition of Mars GRAM directly affected entry guidance. In the case of the aerodynamic effects in powered descent, the entry trajectory does not need to change much. Figure 8.24 shows the histogram comparison of the propellant consumption when aerodynamic forces are present against the vacuum solution. A similar comparison on the distribution of σ_f^* among all 3000 cases is shown in Figure 8.25.

Including aerodynamic forces in powered descent increments the accuracy of the powered descent solution by adding more realistic dynamics to the problem. No major changes to the main optimal powered descent algorithm are necessary owing to the fact that only the dynamics on the closed-loop simulation are changed. The accuracy of the

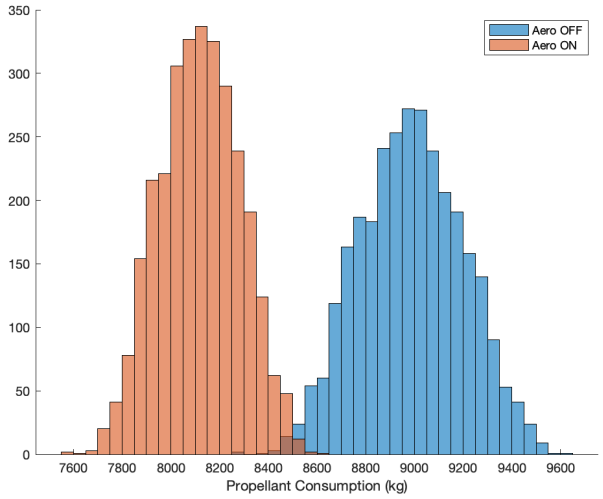

Figure 8.24. Comparison of propellant consumption in the same 3000 cases with and without consideration of aerodynamic forces in powered descent.

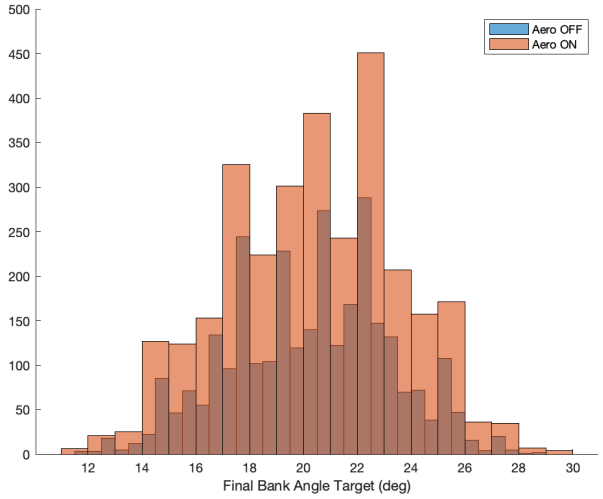

Figure 8.25. Comparison of optimized σ_f^* in the same 3000 cases with and without consideration of aerodynamic forces.

problem is not affected since the terminal conditions are still met. Moreover, even though the solution is not theoretically optimal, there is a reduction in propellant consumption caused by the effects of the aerodynamic forces reducing the velocity of the vehicle during powered descent. The Monte Carlo simulations demonstrated that the solution is robust

when solved with the bi-level optimization approach.

8.12 Summary

The overall success of the algorithm emerges from two very reliable entry and powered descent algorithms. The rapid generation of trajectories is a result of the combination of the robust entry guidance algorithm FNPEG and the optimal control solution of G-POLAR with the indirect method of optimal control. The end-to-end EDL problem is defined as a hybrid optimal control problem that minimized the total propellant consumption. The problem is solved using a bi-level optimization approach that consists in an inner optimization of powered descent guidance to obtain the lowest propellant consumption possible given the initial conditions, and an outer optimization on the entry guidance algorithm to modify the trajectory to produce a better PDI condition. The algorithm was tested in Monte Carlo dispersions with a 100% success rate and a near-optimal solution was found in under 30 seconds. Furthermore, high-fidelity models can be added in closed-loop simulation to produce solutions based on more realistic atmospheric parameters or aerodynamics.

Chapter 8 is based on the paper coauthored with Lu, Ping and Davami, Christopher and under review for publication as Fast and Robust Optimization of Full Trajectory From Entry Through Powered Descent at the Journal of Guidance, Control, and Dynamics. The dissertation author was the primary author of this chapter.

Chapter 9

Concluding Remarks

9.1 Objective and Approach

The goal of this investigation was to produce an optimized end-to-end EDL trajectory capable of safely landing a spacecraft on the surface of another planetary body, particularly the Moon and Mars, with the least amount of propellant possible. To this end, the investigation was divided in multiple segments to test each one of the EDL components individually, then add them together to produce a complete EDL algorithm, and finally take advantage of the robustness of the developed algorithms to lead to an optmization technique to obtain a fast and optimized trajectory.

To build the foundation of the completely optimized EDL algorithm. The fast and robust entry guidance approach FNPEG was rigorously tested in multiple settings, including as an integrated component with a propellant-optimal powered descent guidance named UPG. Multiple scenarios on the Moon and Mars where set up to point out the minimum required tuning of the parameter and vehicle settings on the algorithm, making it ideal for their simplicity. Furthermore, a completely integrated EDL mission was integrated in a high-fidelity simulation environment to show the effectiveness at completing all the

mission requirements and to demonstrate the importance of the powered descent initiation condition as a key element in the reduction of overall mission propellant consumption. The results demonstrated the capability of these algorithms and their convergence effectiveness to find a solution. Integration of entry and powered descent using an optimal powered descent guidance solution offered the opportunity of improving the propellant consumption during powered descent.

Lastly, the culmination of this work is the complete optimization of an EDL trajectory taking advantage of both entry and powered descent guidance. Combining a state-of-the-art entry guidance algorithm to provide the entry trajectory and an optimal powered descent guidance algorithm to land the vehicle safely on the ground using supersonic retropropulsion it is possible to generate a complete EDL trajectory. In addition, taking advantage of the optimal solution to the soft-landing powered descent guidance problem it is possible to calculate the approximate time to start powered descent. A bi-level approach is introduced by using a lower level optimization loop during powered descent and an upper-level optimization loop on a key parameter on the entry guidance. Combining these two techniques with a newly developed bi-level optimization approach, it is possible to obtain near-optimal propellant consumption.

9.2 Conclusions

The results obtained from this research have implications in the design of guidance, navigation, and control (GNC) systems for spacecraft in future exploration missions. These results will help identify solutions to propellant efficiency problems during EDL. It is very

important that missions take advantage of resources intelligently. By exploring different scenarios and discovering the most efficient ones for propellant usage, resources can be allocated efficiently and mission cost can be reduced. Furthermore, creating new guidance solutions to known problems encourages the comparison of the best methods available. In doing this, it will be possible to demonstrate that more powerful and efficient guidance algorithms can be created with the help of optimization that can help reduce the cost of space exploration for longer and more complex missions. The presentation of this suite of algorithms will benefit the guidance community by creating new and innovative space technologies to explore and understand our solar system. By improving current capabilities, focus on newer technologies that will expand our knowledge of the solar system are encouraged. The fundamental discoveries and developments of this work are summarized as follows:

Appropriate PDI condition is required for Optimal Propellant Performance

The importance of a proper PDI condition to start powered descent is stressed in multiple occasions throughout this work. Utilizing a mechanism to predict the optimal PDI condition for the powered descent soft-landing solution, a near-optimal powered descent pinpoint landing solution can be obtain on the Moon and Mars. The PDI adaptive logic has been demonstrated to produce near-optimal solutions even for powered descent algorithms that are not optimized in any sense. Furthermore, the selection of a proper PDI condition can be the difference between the success and failure of a mission, as shown in Section 4. The adaptive PDI logic serves as an excellent transition between entry and

powered descent, and it is later used as the mechanism that makes the complete EDL optimization possible.

Optimal Abort Guidance during Lunar Powered Descent

To truly implement an abort guidance during an emergency, the system must be completely automated. The reaction time during an emergency is many times faster than the speed at which a human can operate. To this end, a new guidance approach was developed as a safety mission for future human landings on the Moon. The approach consists in using an optimal abort guidance solution during lunar powered descent to insert the vehicle into a safe orbit away from any obstacles. To safely keep astronauts away from the ground, a pull-up maneuver is implemented in which the velocity vector is quickly turned towards the safe orbit, avoiding the lower altitude that can sometimes appear as part of the optimal solution. The resulting algorithm provides the only means available to safely and accurately guide a vehicle from any point during powered descent towards a safe orbit. Moreover, the resulting trajectory is truly autonomous and optimal in fuel consumption.

Complete EDL Optimization can be achieved with a Bi-Level Optimization Approach

One of the main goals of this work was to produce an optimized entry, descent, and landing trajectory using the reliable tools that are available today. The aim was to produce a completely optimized end-to-end solution that produced an EDL trajectory with the least amount of propellant possible and in a short amount of time. Usually, optimal or

optimized solutions are obtained using optimization software that not necessarily produce an operational trajectory. Even so, obtaining a solution might take an extended period of time or have convergence issues. In this work, novel approach was developed to produce complete optimized EDL trajectory. The method is a bi-level optimization approach in which an inner-loop obtains an optimal powered descent solution and an outer loop optimizes the entry guidance to deliver the ideal PDI condition. The Adaptive PDI logic is implemented as the transition point that predicts the best PDI condition given the entry trajectory flown. Furthermore, studies demonstrated that high-fidelity models can be implemented in the closed-loop simulation without suffering from high computational cost, allowing for more accurate trajectory predictions. The approach was tested extensively and demonstrated that a fast and reliable EDL solution with near-propellant consumption can be obtained with this method.

9.3 Recommendations for Future Work

- The abort scenario investigated in this work was to a safe orbit around the Moon. In future missions to the Moon that will rely on a Gateway station, it will be important to plan sending the spacecraft to a different orbit during an abort. The algorithm is able to calculate the thrust, thrust direction, and flight time required to reach an orbit that is defined by the orbital parameters. Further studies on the limits of the algorithm need to be studied.

- Investigation into potential abort scenarios on the surface of Mars to find out what would be necessary for the vehicle to be able to safely remove astronauts from a

dangerous situation. The atmosphere and the weight of the vehicle make an abort mission to Mars more complicated. Taking a look at the problem and understanding the minimum requirements for an abort-ascent solution during an EDL mission on Mars is worth the effort.

- An area of research with potential for uncovering interesting results is in Multi-disciplinary Design Optimization. An investigation into the combination of EDL and vehicle optimization using large-scale design optimization might offer appealing results that reveal unique results about an optimal EDL vehicle and its corresponding trajectory.

- This investigation was purely in 3DOF, thus no attitude control consideration. The resulting trajectories assume that the landing vehicle is a point mass, thus, the propellant consumption does not include the propellant that should be accounted for a Reaction Control System (RCS) taking care of the attitude of the vehicle.

- The current simulation setup assumes perfect navigation in 3DOF simulations. This provides an advantage to the guidance as it is always receiving accurate information about the current state of the vehicle even under dispersed initial conditions. In future work, it is recommended that simulations take into account some level of navigation uncertainty to produce a more realistic solution.

Bibliography

[1] E. M. Emme, "Historical persepectives on apollo," *Journal of Spacecraft and Rockets*, vol. 5, no. 4, pp. 369–382, 1968.

[2] D. Comstock and D. Lockney, *NASA's Legacy of Technology Transfer and Prospects for Future Benefits*.

[3] M. K. Lockwood, "Introduction: Mars science laboratory: The next generation of mars landers," *Journal of Spacecraft and Rockets*, vol. 43, no. 2, pp. 257–257, 2006.

[4] *Ingenuity: Design of the Mars Helicopter*, ch. Chapter 4, pp. 73–86.

[5] M. Vozoff and J. Couluris, *SpaceX Products-Advancing the Use of Space*.

[6] J. G. Cook, *Challenges of building the International Space Station*.

[7] *Human Spaceflight Operations: Lessons Learned from 60 Years in Space*, pp. i–xvi. 2021.

[8] T. Adamski, *Command and control of the Voyager spacecraft*.

[9] R. Polidan, *Hubble Space Telescope overview*. 1991.

[10] J. Mather, *James Webb Space Telescope*. 2004.

[11] B. Cassenti, *Human Mars Exploration*. 2007.

[12] E. Lineberry and J. Soldner, *Mission profiles for human Mars missions*. 1990.

[13] M. K. B. M, S. Ayyappan, A. Thomas, R. K. V, and N. B. Das, *A Baseline Strategy for Human Mars Exploration*. 2021.

[14] R. Braun and R. Manning, "Mars exploration entry, descent, and landing challenges," *Journal of Spacecraft and Rockets*, vol. 44, no. 2, pp. 310–323, 2007.

[15] A. Chen, M. Greco, T. Martin-Mur, B. Portock, and A. Steltzner, "Approach and entry, descent, and landing operations for mars science laboratory," *Journal of Spacecraft and Rockets*, vol. 51, no. 4, pp. 1004–1013, 2014.

[16] D. A. Spencer, R. C. Blanchard, R. D. Braun, P. H. Kallemeyn, and S. W. Thurman, "Mars pathfinder entry, descent, and landing reconstruction," *Journal of Spacecraft and Rockets*, vol. 36, no. 3, pp. 357–366, 1999.

[17] D. Baird, T. McElrath, B. Portock, E. Graat, G. Wawrzyniak, P. Knocke, L. D'Amario, M. Watkins, L. Craig, and J. Guinn, *Mars Exploration Rovers Entry, Descent, and Landing Navigation*.

[18] R. W. Maddock, A. M. D. Cianciolo, A. M. Korzun, D. K. Litton, C. H. Zumwalt, and C. D. Karlgaard, "Insight entry, descent, and landing postflight performance assessment," *Journal of Spacecraft and Rockets*, vol. 58, no. 5, pp. 1530–1537, 2021.

[19] G. Mendeck and L. Craig, *Entry Guidance for the 2011 Mars Science Laboratory Mission*.

[20] R. P. Kornfeld, R. Prakash, A. S. Devereaux, M. E. Greco, C. C. Harmon, and D. M. Kipp, "Verification and validation of the mars science laboratory/curiosity rover entry, descent, and landing system," *Journal of Spacecraft and Rockets*, vol. 51, no. 4, pp. 1251–1269, 2014.

[21] P. Lu, "Entry guidance: a unified method," *Journal of Guidance, Control, and dynamics*, vol. 37, no. 3, pp. 713–728, 2014.

[22] P. Lu, "Propellant-optimal powered descent guidance," *Journal of Guidance, Control, and Dynamics*, vol. 41, no. 4, pp. 813–826, 2018.

[23] J. Davis, A. D. Cianciolo, R. Powell, J. Shidner, and E. Garcia-Llama, *Guidance and Control Algorithms for the Mars Entry, Descent and Landing Systems Analysis*.

[24] A. M. Dwyer-Cianciolo and T. Polsgrove, "Human mars entry, descent and landing architecture study overview," in *SPACE and Astronautics Forum and Exposition*, AIAA, 2016.

[25] A. M. Dwyer-Cianciolo and T. Polsgrove, "Human mars entry, descent, and landing architecture study: Phase 2 summary," in *SPACE and Astronautics Forum and Exposition*, AIAA, 2018.

[26] A. M. Dwyer-Cianciolo, T. Polsgrove, R. R. Sostaric, K. T. Edquist, A. M. Korzun, and J. A. Garcia, "Human mars entry, descent, and landing architecture study: Phase 3 summary," in *Scitech Forum and Exposition*, AIAA, 2020.

[27] A. Korzun, F. Canabal, C. Tang, R. Childs, J. Van Norman, J. Tynis, and K. Bibb, "Computational investigation of powered descent for human-scale mars landers," in *AIAA Scitech 2020 Forum and Exposition*, AIAA Paper 2020-2299, 2020.

[28] T. Kelly, "A review of the apollo lunar module program and its lessons for future space missions," Space Programs and Technologies Conference, 1990.

[29] S. Potter, "Nasa selects first commercial moon landing services for artemis," May 2019.

[30] A. B. Acikmese and S. Ploen, *A Powered Descent Guidance Algorithm for Mars Pinpoint Landing*.

[31] P. Lu, C. Brunner, S. Stachowiak, M. Tigges, and C. Cerimele, "Verification of a fully numerical entry guidance algorithm," *Journal of Guidance, Control, and Dynamics*, vol. 40, no. 2, pp. 230–247, 2017.

[32] P. E. Moseley, "The apollo entry guidance: A review of the mathematical development and its operational characteristics," Technical Note 69-FMT-791, TRW, Houston, TX, December 1969.

[33] C. A. Graves and J. C. Harpold, "Apollo experience report: Mission planning for apollo entry," Technical Note D-6725, NASA, March 1972.

[34] G. F. Mendeck and L. Craig McGrew, "Entry guidance design and postflight performance for 2011 mars science laboratory mission," *Journal of Spacecraft and Rockets*, vol. 51, no. 4, pp. 1094–1105, 2014.

[35] J. Rea and Z. Putnam, *A Comparison of Two Orion Skip Entry Guidance Algorithms*.

[36] J. C. Harpold and A. Graves, "Shuttle entry guidance," *The Journal of the Astronautical Sciences*, vol. 27, no. 3, pp. 239–268, 1979.

[37] J. C. Harpold and D. E. Gavert, "Space shuttle entry guidance performance results," *Journal of Guidance, Control, and Dynamics*, vol. 6, no. 6, pp. 442–447, 1983.

[38] K. J. Murphy, R. J. Nowak, R. A. Thompson, B. R. Hollis, and R. Prabhu, "X-33 hypersonic aerodynamic characteristics," *Journal of Spacecraft and Rockets*, vol. 38, no. 5, pp. 670–683, 2001.

[39] R. Machin, J. Stein, and J. Muratore, *An overview of the X-38 prototype crew return vehicle development and test program*.

[40] R. A. Lugo, R. Powell, and A. M. Dwyer-Cianciolo, "Overview of a generalized numerical predictor-corrector targeting guidance with application to human-scale mars entry, descent, and landing," in *AIAA Scitech 2020 Forum and Exposition*, AIAA Paper 2021-0505, 2020.

[41] W. E. Giberson, *Surveyor Project Status*, pp. 877–904. 1962.

[42] R. Cheng and D. Conrad, *Design considerations for Surveyor guidance*.

[43] S. W. Thurman, *Surveyor Program Automatic Landing System*.

[44] J. J. Ribarich, "Surveyor spacecraft landing accuracy," *Journal of Spacecraft and Rockets*, vol. 5, no. 7, pp. 768–773, 1968.

[45] G. A. Soffen and C. W. Snyder, "The first viking mission to mars," *Science*, vol. 193, no. 4255, pp. 759–766, 1976.

[46] R. N. Ingoldby, "Guidanec and control system design of the viking planetary lander," *Journal of Guidance, Control, and Dynamics*, vol. 1, no. 3, pp. 189–196.

[47] R. Braun, D. Spencer, P. Kallemeyn, R. Vaughan, R. Braun, D. Spencer, P. Kallemeyn, and R. Vaughan, *Mars Pathfinder atmospheric entry navigation operations.*

[48] J. K. Erickson, R. Manning, and M. Adler, *MARS EXPLORATION ROVER: Launch, Cruise, Entry, Descent, and Landing.*

[49] M. Grover, P. Desai, and B. Cichy, *Overview of the Phoenix Entry, Descent and Landing System Architecture.*

[50] C. D. Karlgaard, A. M. Korzun, M. Schoenenberger, E. Bonfiglio, D. Kass, and M. R. Grover, *Mars InSight Entry, Descent, and Landing Trajectory and Atmosphere Reconstruction.*

[51] D. A. Spencer, D. S. Adams, E. Bonfiglio, M. Golombek, R. Arvidson, and K. Seelos, "Phoenix landing site hazard assessment and selection," *Journal of Spacecraft and Rockets*, vol. 46, no. 6, pp. 1196–1201, 2009.

[52] P. N. Desai, J. L. Prince, E. M. Queen, M. M. Schoenenberger, J. R. Cruz, and M. R. Grover, "Entry, descent, and landing performance of the mars phoenix lander," *Journal of Spacecraft and Rockets*, vol. 48, no. 5, pp. 798–808, 2011.

[53] G. Cherry, "A general, explicit, optimizing guidance law for rocket-propelled spaceflight," in *Astrodynamics Guidance and Control Conference*, AIAA, 1964.

[54] A. R. Klumpp, "Apollo lunar descent guidance," *Automatica*, vol. 10, p. 133–146, mar 1974.

[55] C. S. D'Souza, "An optimal guidance law for planetary landing," AIAA Guidance, Navigation, and Control Conference, 1997. AIAA Paper 1997-3709.

[56] D. Ives, D. Geller, and G. Carman, *Apollo-derived Mars precision lander guidance.*

[57] E. C. Wong, G. Singh, and J. P. Masciarelli, "Guidance and control design for hazard avoidance and safe landing on mars," *Journal of Spacecraft and Rockets*, vol. 43, no. 2, pp. 378–384, 2006.

[58] R. Sostaric and J. Rea, *Powered Descent Guidance Methods For The Moon and Mars.*

[59] B. A. Steinfeldt, M. J. Grant, D. A. Matz, R. D. Braun, and G. H. Barton, "Guidance, navigation, and control system performance trades for mars pinpoint landing," *Journal of Spacecraft and Rockets*, vol. 47, no. 1, pp. 188–198, 2010.

[60] I. Gerth and E. Mooij, *Guidance for Autonomous Precision Landing on Atmosphereless Bodies*.

[61] P. Lu, R. R. Sostaric, and G. F. Mendeck, "Adaptive powered descent initiation and fuel-optimal guidance for mars applications," in *Guidance, Navigation, and Control Conference*, AIAA, 2018.

[62] S. A. Sandoval, R. A. Lugo, P. Lu, and A. D. Cianciolo, "Simulation comparison of entry and powered descent guidance algorithms for a human-scale mars mission," in *AAS Guidance, Navigation, and Control Conference*, AAS 22-042, 2022.

[63] P. Lu, "Augmented apollo powered descent guidance," *Journal of Guidance, Control, and Dynamics*, vol. 42, no. 3, pp. 447–457, 2019.

[64] P. Lu, "Theory of fractional-polynomial powered descent guidance," *Journal of Guidance, Control, and Dynamics*, vol. 43, no. 3, pp. 398–409, 2020.

[65] B. J. Johnson, P. Lu, and R. R. Sostaric, *Mid Lift-to-Drag Rigid Vehicle 6-DoF Performance for Human Mars Entry, Descent, and Landing: A Fractional Polynomial Powered Descent Guidance Approach*.

[66] S. Ploen, B. Acikmese, and A. Wolf, *A Comparison of Powered Descent Guidance Laws for Mars Pinpoint Landing*.

[67] B. Acikmese and S. R. Ploen, "Convex programming approach to powered descent guidance for mars landing," *Journal of Guidance, Control, and Dynamics*, vol. 30, no. 5, pp. 1353–1366, 2007.

[68] B. Acikmese, D. Scharf, L. Blackmore, and A. Wolf, *Enhancements on the Convex Programming Based Powered Descent Guidance Algorithm for Mars Landing*.

[69] D. Malyuta, T. Reynolds, M. Szmuk, M. Mesbahi, B. Acikmese, and J. M. Carson, *Discretization Performance and Accuracy Analysis for the Rocket Powered Descent Guidance Problem*.

[70] U. Lee and M. Mesbahi, *Optimal Power Descent Guidance with 6-DoF Line of Sight Constraints via Unit Dual Quaternions*.

[71] D. P. Scharf, B. Acikmese, D. Dueri, J. Benito, and J. Casoliva, "Implementation and experimental demonstration of onboard powered-descent guidance," *Journal of Guidance, Control, and Dynamics*, vol. 40, no. 2, pp. 213–229, 2017.

[72] T. P. Reynolds and M. Mesbahi, "Optimal planar powered descent with independent thrust and torque," *Journal of Guidance, Control, and Dynamics*, vol. 43, no. 7, pp. 1225–1231, 2020.

[73] J. Rea and R. Bishop, *Analytical Dimensional Reduction of a Fuel Optimal Powered Descent Subproblem*.

[74] L. Blackmore, B. Acikmese, and D. P. Scharf, "Minimum-landing-error powered-descent guidance for mars landing using convex optimization," *Journal of Guidance, Control, and Dynamics*, vol. 33, no. 4, pp. 1161–1171, 2010.

[75] M. Szmuk, U. Eren, and B. Acikmese, *Successive Convexification for Mars 6-DoF Powered Descent Landing Guidance.*

[76] M. Szmuk, T. P. Reynolds, and B. Acikmese, "Successive convexification for real-time six-degree-of-freedom powered descent guidance with state-triggered constraints," *Journal of Guidance, Control, and Dynamics*, vol. 43, no. 8, pp. 1399–1413, 2020.

[77] P. Lysandrou and R. D. Braun, *A 6-DoF Successive Convexification Powered Descent Guidance Implementation using Modified Rodrigues Parameters.*

[78] F. V. Bennett, "Apollo experience report - mission planning for lunar module descent and ascent," Technical Note D-6846, NASA, Manned Spacecraft Center, Houston, Texas 77058, June 1972.

[79] C. T. Hyle, C. E.Foggatt, and B. D. Weber, "Apollo experience report - abort planning," Technical Note D-6847, NASA, 1972.

[80] P. M. Kurten, "Apollo experience report-guidance and control systems: Lunar module abort system," Technical Note D-7990, NASA, 1975.

[81] J. L. Goodman, "Powered guidance development for apollo and the space shuttle," in *AAS*, Paper 16-093, 2016.

[82] H. N. Scofield, "A simplified explicit guidance scheme for orbital injection," *Journal of Spacecraft and Rockets*, vol. 5, no. 11, pp. 1309–1311, 1968.

[83] V. Kenny, S. G. Hendrix, S. You, R. Dai, and J. R. Rea, *Feature-based Learning for Optimal Abort Guidance.*

[84] Z. Wang and M. J. Grant, *Near-Optimal Entry Guidance for Reference Trajectory Tracking via Convex Optimization.*

[85] Z. Wang and M. J. Grant, "Autonomous entry guidance for hypersonic vehicles by convex optimization," *Journal of Spacecraft and Rockets*, vol. 55, no. 4, pp. 993–1006, 2018.

[86] Y. Lee and D. Y. Lee, *Optimal Trajectory Generation for Mars Atmospheric Entry Guidance using Parameter Optimization.*

[87] S. You, C. Wan, R. Dai, P. Lu, and J. R. Rea, *Learning-based Optimal Control for Planetary Entry, Powered Descent and Landing Guidance.*

[88] C. Wan, G. Jing, R. Dai, and J. R. Rea, *Fuel-Optimal Guidance for End-to-End Human-Mars Entry, Powered-Descent, and Landing Mission.*

[89] W. R. Johnson, P. Lu, and S. Stachowiak, *Automated Re-entry System using FNPEG*.

[90] P. Lu and S. A. Sandoval, "Abort guidance during powered descent for crewed lunar missions," in *SciTech Forum and Exposition*, AIAA, Paper 2021-0505, 2021.

[91] C. Wan, G. Jing, R. Dai, and J. R. Rea, *Fuel-Optimal Guidance for End-to-End Human-Mars Entry, Powered-Descent, and Landing Mission*.

[92] O. L. Mangasarian, *Nonlinear Programming*. Society for Industrial and Applied Mathematics, 1994.

[93] *Multi-parametric Linear Programming*, ch. 2, pp. 19–43. John Wiley and Sons, Ltd, 2020.

[94] J. Z. Ben-Asher, *Numerical Techniques for the Optimal Control Problem*, ch. 6, pp. 161–178. January 2010.

[95] G. Smirnov. 01 2002.

[96] F. Fahroo and I. M. Ross, "Direct trajectory optimization by a chebyshev pseudospectral method," *Journal of Guidance, Control, and Dynamics*, vol. 25, no. 1, pp. 160–166, 2002.

[97] A. E. Bryson. Routledge, 2018.

[98] R. W. Beard, G. N. Saridis, and J. T. Wen, "Approximate solutions to the time-invariant hamilton-jacobi-bellman equation," vol. 96, no. 3, pp. 589–626, 1998.

[99] P. Lu, "Predictor-corrector entry guidance for low lifting vehicles," *Journal of Guidance, Control, and Dynamics*, vol. 31, no. 3, pp. 1067–1075, 2008.

[100] K. M. Smith, "Predictive lateral logic for numerical entry guidance algorithm," in *26th AAS/AIAA Space Flight Mechanics Meeting*, AAS Paper 2016-1182, 2016.

[101] A. R. Klumpp, "A manually retargeted automatic descent and landing system for lem," in *Proceedings of AIAA/JACC Guidance and Control Conference*, (Seattle, WA), pp. 713–727, 1966.

[102] F. V. Bennett, "Apollo lunar descent and ascent trajectories," Technical Memorandum X-58040, NASA, 1970.

[103] P. Lu, B. J. Griffin, G. A. Dukeman, and F. R. Chavez, "Rapid optimal multiburn ascent planning and guidance," *Journal of Guidance, Control, and Dynamics*, vol. 31, no. 6, pp. 1656–1664, 2008.

[104] P. Lu and B. Pan, "Highly constrained optimal launch ascent guidance," *Journal of Guidance, Control, and Dynamics*, vol. 33, no. 2, pp. 404–414, 2010.

[105] M. Baldwin and P. Lu, "Optimal deorbit guidance," *Journal of Guidance, Control, and Dynamics*, vol. 35, no. 1, pp. 93–103, 2012.

[106] P. Lu, S. Forbes, and M. Baldwin, "A versatile powered guidance algorithm," in *AIAA Guidance, Navigation, and Control Conference*, (Minneapolis, MN), AIAA Paper 2012-4843, 8 2012.

[107] P. Lu and R. Callan, "Propellant-optimal powered descent guidance revisited," *Journal of Guidance, Control, and Dynamics*, vol. 46, no. 2, pp. 215–230, 2023.

[108] S. A. Sandoval, P. Lu, J. T. Hwang, J. R. Rea, and R. R. Sostaric, "Multiple optima in abort ascent during lunar powered descent," in *SciTech Forum and Exposition*, AIAA, Paper 2022-0949, 2022.

[109] S. A. Sandoval and P. Lu, "Powered descent guidance for a crewed lunar landing mission," in *AAS Guidance and Control Conference, Breckenridge, CO*, AAS Paper 20–044, 2020.

[110] D. J. Jezewski, "An optimal, analytic solution to the linear- gravity, constant-thrust trajectory problem," *Journal of Spacecraft and Rockets*, vol. 8, no. 7, pp. 793–796, 1971.

[111] B. Pan, Z. Chen, P. Lu, and B. Gao, "Reduced transversality conditions in optimal space trajectories," *Journal of Guidance, Control, and Dynamics*, vol. 36, no. 5, pp. 1289–1300, 2013.

[112] I. M. Ross, Q. Gong, M. Karpenko, and R. J. Proulx, "Scaling and balancing for high-performance computation of optimal controls," *Journal of Guidance, Control, and Dynamics*, vol. 41, no. 10, pp. 2086–2097, 2018.

[113] B. Pan, Z. Chen, P. Lu, and B. Gao, "Reduced transversality conditions in optimal space trajectories," *Journal of Guidance, Control, and Dynamics*, vol. 36, no. 5, pp. 1289–1300, 2013.

[114] J. S. Gray, J. T. Hwang, J. R. R. A. Martins, K. T. Moore, and B. A. Naylor, "OpenMDAO: An open-source framework for multidisciplinary design, analysis, and optimization," *Structural and Multidisciplinary Optimization*, vol. 59, pp. 1075–1104, April 2019.

[115] L. S. Pontryagin, V. G. Boltyanskii, Q. V. Gramkreledze, and E. F. Mishchenko, *The Mathematical Theory of Optimal Processes*. New York: Intersciences, 1962.

[116] A. V. Rao, "A survey of numerical methods for optimal control," in *AAS/AIAA Astrodynamics Specialist Conference*, (Pittsburgh, PA), AAS Paper 09-334, 8 2009.

[117] J. S. Gray, J. T. Hwang, J. R. R. A. Martins, K. T. Moore, and B. A. Naylor, "Openmdao: an open-source framework for multidisciplinary design, analysis, and optimization," *Structural and Multidisciplinary Optimization*, vol. 59, no. 4, pp. 1075–1104, 2019.

[118] J. T. Hwang and D. Munster, "Solution of ordinary differential equations in gradient-based multidisciplinary design optimization," in *2018 AIAA/ASCE/AHS/ASC Structures, Structural Dynamics, and Materials Conference*, (Kissimmee, FL), AIAA Paper 2018-1646, 2018.

[119] "Apollo 11 lunar module / easep," NSSDCA/COSPAR ID 1969-059C, NASA, 1969.

[120] A. D. Cianciolo, R. A. Dillman, A. J. Brune, R. A. Lugo, T. P. Polsgrove, T. K. Percy, S. G. Sutherlin, and A. M. Cassell, "Human mars entry, descent, and landing architecture study: Deployable decelerators," in *SPACE and Astronautics Forum and Exposition*, AIAA, 2018.

[121] C. Wan, G. Jing, R. Dai, , and J. Rea, "Fuel-optimal guidance for end-to-end human-mars entry, powered-descent, and landing mission," *IEEE Transactions on Aerospace and Electronics Systems*, vol. 58, no. 4, pp. 2837–2854, 2022.

[122] W. H. Press, S. A. Teukolsky, W. T. Vetterling, and B. P. Flannery, *Numerical Recipes: The Art of Scientific Computing*, ch. 10. New York: Cambridge University Press, 2007.

[123] L. Perko, *Differential Equations and Dynamical Systems*, ch. 2. New York: Springer, 3 ed., 2001.

[124] W. Rudin, *Principles of Mathematical Analysis*, p. 89. New York: McGraw Hill Inc., 3 ed., 1976.

[125] L. Hood, G. Bennett, and J. J. Parish, "Model fidelity studies for rapid trajectory optimization," in *SciTech Forum and Exposition*, AIAA, 2019.

[126] D. Schuster, "Cfd2030 grand challenge: Cfd-in-the-loop monte carlo simulation for space vehicle design," in *AIAA*, Paper 2021-0957, 2021.

[127] T. W. Simpson and J. R. R. A. Martins, "Multidisciplinary design optimization for complex engineered systems: Report from a national science foundation workshop," *Journal of Mechanical Design*, vol. 133, no. 10, pp. 101002–1–101002–10, 2011.

[128] H. L. Justin, "Mars global reference atmospheric model 2010 version: Users guide," Technical Memo 2014-217499, NASA, 2014.

[129] C. J. Cerimele, E. A. Robertson, R. R. Sostaric, and J. A. Garcia, "A rigid mid lift-to-drag ratio approach to human mars entry, descent, and landing," in *Guidance, Navigation, and Control Conference*, AIAA, 2017.

[130] J. J. Breanna, C. J. Cerimele, S. J. Stachowiak, R. R. Sostaric, D. A. Matz, and P. Lu, "Mid-lift-to-drag ratio rigid vehicle control system design and simulation for human mars entry," in *Guidance, Navigation, and Control Conference*, AIAA, 2018. AIAA Paper 2018-0615.

[131] J. J. Breanna, E. M. Braden, R. R. Sostaric, C. J. Cerimele, and P. Lu, "Entry, descent, and landing performance for a mid-lift-to-drag ratio vehicle at mars," *Advances in the Astronautical Sciences*, vol. 164, pp. 285–297, 2018.

[132] I. M. Ross, "Enhancements to the dido optimal control toolbox," 2020.

[133] I. M. Ross and F. Fahroo, "Pseudospectral knotting methods for solving optimal control problems," *Journal of Guidance, Control, and Dynamics*, vol. 23, no. 3, pp. 397–405, 2004.